

Hydrogeology and water resources of the Salt Basin, New Mexico and Texas

Edited by Stacy Timmons and Laila Sturgis



OPEN-FILE REPORT

Open-File Report 618—Hydrogeology and water resources of the Salt Basin, New Mexico and Texas

Edited by Stacy Timmons and Laila Sturgis

Copyright © 2022

New Mexico Bureau of Geology and Mineral Resources

A research division of New Mexico Institute of Mining and Technology

Dr. Stephen G. Wells, *President, New Mexico Tech*

Dr. Nelia W. Dunbar, *Interim Vice President for Research, New Mexico Tech*

Dr. J. Michael Timmons, *Interim Director and State Geologist, New Mexico Bureau of Geology*

Science Editor: Shari Kelley

Graphics/Mapping/Data Support: Luna Brett, Ethan Mamer, Cris Morton, Kitty Pokorny, Laila Sturgis, and SayoStudio, including Claire Agosti, Nicolle Fuller, and Trinkia Kensill

Copyediting: Carrin Rich

Layout and Design: Lauri Logan

Publications Program Manager: Barbara J. Horowitz

Printed in the United States

Cover Photo:

View to the east of the Guadalupe Mountains from the Salt Flat playas located northeast of Dell City, Texas. *Photo by Shari Kelley*

Project Funding:

Funding for this project was provided by the U.S. Department of the Interior Bureau of Reclamation through Cooperative Agreement R19C00082 with New Mexico Institute of Mining and Technology.

Suggested Citation:

Timmons, S., and Sturgis, L., eds., 2022, Hydrogeology and water resources of the Salt Basin, New Mexico and Texas: New Mexico Bureau of Geology and Mineral Resources Open-File Report 618, 154 p.

CONTRIBUTORS:

Dr. Daniel Cadol, Earth and Environmental Science, NMT

Beth Ann Eberle, Earth and Environmental Science, NMT; MS complete in 2021

Elizabeth Evenochek, Earth and Environmental Science, NMT; MS complete in 2021

Marissa Fichera, Hydrogeology, NMBGMR

Dr. Shari Kelley, Geophysics, NMBGMR

Dr. Talon Newton, Hydrogeology, NMBGMR

Dr. Mark Person, Earth and Environmental Science, NMT

Laila Sturgis, Hydrogeology, NMBGMR

Stacy Timmons, Hydrogeology, NMBGMR

ACKNOWLEDGMENTS

The editors and authors of this report have many team members and staff to thank for this work. The research team at New Mexico Tech is especially grateful for the support of the U.S. Bureau of Reclamation staff throughout this project, especially Sarah Branum and Dagmar Llewellyn for their reviews of the draft report. The team at the New Mexico Interstate Stream Commission (ISC) and collaborating consultants from S.S. Papadopoulos & Associates (SSPA) were incredible to work with, especially John Longworth at the ISC and Gilbert Barth and Jessica Rodgers at SSPA. Reviews and collaboration by USGS staff, including Jeff Pepin and Andre Ritchie, were also very helpful in improving the details related to the geophysical studies and the modeling sections, respectively.

The fieldwork and data collection could not have been accomplished without the cooperation of the many land owners and well owners who granted access to wells for measurement or sampling.

This research would not have been as organized or successful without the team at the New Mexico Bureau of Geology, especially Kitty Pokorny for data management, Bonnie Frey and Dustin Baca for lab sample analyses, and the field data collection efforts of Scott Christenson, Ethan Mamer, Marissa Fichera, and Trevor Kludt.

The students who worked on this project endured long weekly meetings and completed their research during a pandemic. Elizabeth Evenochek and Beth Ann Eberle were essential members of the research team. Thank you for your endurance and hard work.

CONTENTS

Technical Summary	1	Chapter 4: Water Budget	61
Chapter 1: Overview of the Salt Basin	13	Dan Cadol and Beth Ann Eberle	
Marissa Fichera, Shari Kelley, Stacy Timmons, Laila Sturgis and Elizabeth Evenocheck		Precipitation	61
Hydrogeology	13	Runoff	62
Water Use	20	Recharge	64
Groundwater Level Observations	22	Chloride mass balance method	65
Chapter 2: Geophysics	23	Recharge results and discussion	72
Shari Kelley		Evapotranspiration	77
Geophysical Methods	24	Agricultural consumption methods	77
AMT survey	24	Agricultural consumption discussion and results	79
TEM survey	27	Chapter 5: Modeling	83
Geophysics Results	27	Elizabeth Evenocheck, Mark Person and Marissa Fichera	
AMT results: Dimensionality	27	Hydrogeologic Model	83
AMT results: Geologic context	27	Model framework	83
AMT results: Water quality	30	Recharge and evapotranspiration	87
AMT results: One-dimensional inversions	32	Historic pumping	87
AMT results: Comparison to USGS data	35	Model calibration	88
TEM results	35	Historical transient model	91
TEM data collected at AMT sites	37	Pumping scenario results	95
Geophysics Discussion	38	Model discussion	99
Geophysics Conclusions	39	Groundwater Storage	105
Recommendations for future work	39	Estimates based on model	105
Chapter 3: Hydrogeochemical Data	41	Storage calculation results	110
Talon Newton		Model Calibration: Last Glacial Maximum Simulation	113
Water Quality and Major Ion Chemistry	41	Paleo-recharge estimates	113
Water Types	47	Last glacial maximum model approach ...	114
Environmental Tracer Analysis	48	Results	116
Stable isotopes of water	48	Discussion and conclusions	116
Tritium and carbon-14	51	Effects of Fluid Density Variations on Groundwater Flow and Saline Water Migration	121
Discussion: Water Sources, Geochemical Processes, and Flowpaths	53	Introduction	121
Conclusions	59	SEAWAT cross-sectional model setup ...	124
		FEMOC NW–SE cross-sectional model setup	127

SEAWAT model results	128
FEMOC model results	129
Discussion	132
Conclusions	133
References	135
Appendices (online only)	
Appendix 1. Geophysics	
1.1. Locations of geophysics measurements	
1.2. Dimensionality of phase tensors and shift corrections	
1.3. One dimensional resistivity model	
1.4. Resistivity logs	
A. Alpha Federal	
B. Turner State 1	
C. Lois Spanel	
Appendix 2. Water data	
2.1. Locations	
2.2. Surface water data	
2.3. Well data	
2.4. Groundwater levels	
2.5. Water chemistry	
Appendix 3. Evenocheck 2021 thesis	
Appendix 4. Eberle 2021 thesis	

Figures

TS-1. Location map of study area	2	2-7. Cross sections showing 1-D models calculated using WinGLink	34
TS-2. Measured water table elevations in the Dell City area compared to the modeled groundwater pumping over time	8	2-8. Comparison of the USGS AMT data collected in the Cornudas Mountain area with data collected during this NMT study	36
TS-3. Hypothetical well field locations in the Salt Basin included in the MODFLOW model scenarios	10	2-9. Resistivity contours in ohm-m from TEM stations on the east side of the study area between Dog Canyon on the north and the Salt Flats on the south	37
1-1. Generalized geologic map of the Salt Basin study area	14	2-10. Resistivity contours from a TEM station coincident with AMT station SB27	37
1-2. Cross section across buried Ancestral Rocky Mountains structures, modified from Black (1976)	16	3-1. Map indicating the hydrogeologic regions used to discuss water chemistry results	42
1-3. Key structural geologic features impacting groundwater flow of the Salt Basin	17	3-2. TDS concentrations in mg/L for groundwater samples	44
1-4. Regional map of the approximate groundwater potentiometric surface	18	3-3. Sulfate (SO ₄) concentrations in mg/L for groundwater samples	44
1-5. Map of estimated depth to water in feet below land surface	19	3-4. Chloride (Cl) concentrations in mg/L for groundwater samples	45
1-6. Schematic block diagram of the Salt Basin; view from Texas, facing northeast ..	20	3-5. Iron (Fe) concentrations in mg/L for groundwater samples	45
1-7. Historical groundwater pumping as reported by the Texas Water Development Board in Culberson and Hudspeth counties from 1980 to 2019	21	3-6. Manganese (Mn) concentrations in mg/L for groundwater samples	46
1-8. Dell City water table observations from 1948 through 2022	22	3-7. Nitrate (NO ₃) concentrations in mg/L for groundwater samples	47
2-1. Range of typical electrical conductivities (or resistivities) of common subsurface materials	23	3-8. Fluoride (F ⁻) concentrations in mg/L for groundwater samples	48
2-2. Map showing the locations of the AMT and TEM measurement sites and other data available from oil wells	24	3-9. Piper diagram showing groundwater in the study area grouped by hydrogeologic region	49
2-3. Field configuration for AMT data collection	25	3-10. Dominant water types for samples with complete ion chemistry	50
2-4. An example of static shift in the apparent resistivity curves	26	3-11. Isotopic composition of groundwater in the study area, categorized by hydrogeologic region	51
2-5. A portion of the resistivity curves from oil wells in the eastern and central parts of the study area	28	3-12. Spatial distribution of δD for groundwater	52
2-6. Resistivity based on 1-D models for stations within 10 km of oil wells drilled in the Salt Basin	31	3-13. Spatial distribution of δ ¹⁸ O for groundwater	52
		3-14. Spatial distribution of tritium in groundwater	53

<p>3-15. Spatial distribution of carbon-14 activity in groundwater in percent modern carbon (PMC) 53</p> <p>3-16. Schematic Piper diagram showing different possible geochemical processes to explain observed groundwater compositions 54</p> <p>3-17. The cation deficit, $(Ca + Mg) - (HCO_3 - SO_4)$, plotted as a function of the sodium-chloride cation surplus $(Na - Cl)$ is used to assess the occurrence of cation exchange 55</p> <p>3-18. $(Ca + MG) / SO_4$ data that has not been corrected for cation exchange plotted as a function of relative sulfate concentration 56</p> <p>3-19. $(Ca + MG) / SO_4$ data that has been corrected for cation exchange plotted as a function of relative sulfate concentration 57</p> <p>3-20. Chloride concentrations plotted as a function of relative sulfate concentrations shows mixing of high-chloride water mainly in the Salt Flats region 58</p> <p>4-1. Long-term average runoff/rainfall ratios of monitored watersheds at Walnut Gulch, plotted against the drainage area of the watershed 64</p> <p>4-2. Scatter plot of Salt Basin chloride and bromide groundwater sample data 68</p> <p>4-3. Recharge fraction for groundwater samples using the chloride mass balance method 70</p> <p>4-4. Recharge volumes based on the recharge regions shown in Figure 4-3 and spatially variable end-member estimates (Table 4-8) 75</p> <p>4-5. Irrigated land assessment using normalized difference vegetation index (NDVI) data 78</p> <p>4-6. NDVI maps of the Dell City area for every other year in the satellite record 79</p>	<p>4-7. Evapotranspiration from the agricultural areas of the Salt Basin using the method of this study over the growing season (March through October), over the full year, and using the OpenET model ensemble for the full calendar year 81</p> <p>4-8. Irrigated acreage in the agricultural areas of the Salt Basin using the method of this study compared against the reported acreage of Groeneveld and Baugh (2002) 81</p> <p>5-1. Current model grid outline with all boundary conditions symbolized by color of grid cell. Diffuse recharge depression-focused recharge, evapotranspiration specified-flux boundaries, general-head boundaries, and no-flow boundaries are shown 84</p> <p>5-2. Maps of final model geologic zonation in Layers 1 through 6 86</p> <p>5-3. Observed versus computed water levels for the three predevelopment steady-state recharge model scenarios 89</p> <p>5-4. Observed and modeled predevelopment water table contour map 90</p> <p>5-5. Distribution of depression-focused recharge in streamflow routing segments in the predevelopment steady-state model .. 92</p> <p>5-6. Computed versus observed carbon-14 ages for the three preliminary predevelopment steady-state model scenarios 93</p> <p>5-7. Observed versus computed well hydrographs in the Salt Basin 93</p> <p>5-8. Initial, 1948, and final, 2020, transient model water table contours 94</p> <p>5-9. Computed changes in evapotranspiration, pumping, total recharge, and net storage within the Salt Basin between 1948 and 2020 95</p> <p>5-10. Measured water table elevations in the Dell City area compared to the modeled groundwater pumping over time 96</p> <p>5-11. Location of pumping wells and hypothetical well fields 97</p>
--	---

5-12. Drawdown contours for the additional pumping in model Scenarios 1 and 2	99	5-26. Idealized simulation of variable-density groundwater flow in an arid, hydrologically closed basin	122
5-13. Comparison of (A) the annual subsurface flux of water across the state line from New Mexico to Texas, and (B) the difference in flux from the historical model for each of the well field locations pumping scenarios	100	5-27. Salinity of Salt Basin wells along cross sections A-A' and B-B'. See Figure 5-25 for the location of the Salt Basin profiles..	123
5-14. Water levels for the historical transient model and the six pumping simulations ...	103	5-28. Hydraulic conductivity distribution used in east-west 6-layer MODFLOW (A) and 23-layer SEAWAT (B) model grids ...	124
5-15. Study domains corresponding to existing groundwater storage estimates	106	5-29. Location of NW-SE hydrostratigraphic cross section and corrected carbon-14 age dates	125
5-16. Distribution of TDS data from groundwater wells with known well depths across the Salt Basin study area ...	108	5-30. FEMOC finite element mesh and hydrostratigraphic units used in FEMOC model	126
5-17. Conceptual schematic of the multi-step process of developing a TDS surface including (a) geologic formation assignment, (b) well water quality designation, (c) elevation point placement, and (d) interpolation process result	109	5-31. Plan-view and cross-sectional schematic diagrams showing boundary conditions imposed along the land surface	127
5-18. Contoured surface representing the estimated treatable groundwater base elevation in meters above mean sea level	111	5-32. Computed heads and concentrations from multiple SEAWAT model scenarios .	129
5-19. Specific yield values used in groundwater storage estimation, based on model-calibrated specific yield values	112	5-33. Location of pumping wells and salinity trends over time for wells near Dell City..	130
5-20. Base map of Salt Basin showing stream bed hydraulic conductivity and recharge zones	114	5-34. Computed groundwater concentrations after 50 years, 100 years, and 200 years of pumping	131
5-21. Comparison of estimated modern and last glacial maximum recharge for Cloudcroft, New Mexico, and Dell City, Texas	115	5-35. FEMOC model output including simulated (a) equivalent freshwater hydraulic heads, (b) salinity, (c) groundwater age, (d) temperatures, and (e) stream functions	132
5-22. Simulated heads and flooded cells in Layer 1 for last glacial maximum simulation Runs 1 through 6	118		
5-23. Simulated heads and flooded cells in Layer 1 for last glacial maximum simulation Runs 7 through 11	119		
5-24. Graphic comparison of vertical anisotropy (A and B) and horizontal hydraulic conductivity (C and D) values in layer 1 for Runs 1 and 10	120		
5-25. Base map showing the location of north-south (B-B') and west-east (A-A') salinity profiles, halite salt deposits, and well locations having salinity data	121		

Tables

TS-1. Water chemistry summary	6	5-4. Net changes to the flow budget for the historical transient model from 1948 to 2020	96
1-1. Primary water-bearing units of the Salt Basin	15	5-5. Years and pumping rates of extra pumping for Scenario 1	98
1-2. Salt Basin water use in New Mexico	21	5-6. Years and pumping rates of extra pumping for Scenario 2	98
2-1. Comparison of TDS values in water wells near AMT/TEM sites	32	5-7. Comparison of subsurface water flux across the state line from New Mexico into Texas for the six pumping scenario models	101
2-2. Comparison of rock unit depths in oil wells to AMT data	33	5-8. Summary of estimated recoverable groundwater storage values calculated previously and in this study	113
3-1. Statistics for water chemistry constituents	43	5-9. Modern and last glacial maximum recharge estimates for Cloudcroft, New Mexico	115
4-1. Estimated average annual precipitation and runoff volumes	63	5-10. Modern and last glacial maximum recharge estimates for Dell City, Texas ..	115
4-2. Recharge estimates for Salt Basin using end-member (chloride mass balance) analysis	71	5-11. Description of last glacial maximum model parameters	117
4-3. Recharge volume estimates in acre-ft/yr for mountainous zones	73	5-12. Simulated lake levels, errors in simulated versus observed lake levels, and sum of flooding errors for Layer 1	118
4-4. Recharge fraction estimates (unitless) for mountainous zones	73	5-13. Summary of hydraulic conductivity and vertical anisotropy ranges for Layers 1–6, model runs 1 and 9–11	119
4-5. Recharge volume estimates in acre-ft/yr for lowland zones	73	5-14. Comparison of hydraulic conductivity ranges between MODFLOW and SEAWAT model runs	125
4-6. Recharge fraction estimates in acre-ft/yr for lowland zones	73	5-15. Hydraulic conductivity used in the FEMOC model	128
4-7. Recharge estimates using meteoric and end-member compositions	74	5-16. Transport parameters held constant in the FEMOC model runs	128
4-8. Possible recharge estimates with spatial variation using comparison to groundwater	75	5-17. Temporal records of salinity for wells within 10 km of Dell City, Texas	131
4-9. Influence of runoff/rainfall ration on recharge estimation	76	5-18. Statistical analysis of well salinity data to the east and west of Dell City	131
4-10. Summary of basin-wide recharge estimates	76		
4-11. Annual irrigated acreage in Dell City	80		
5-1. Best-fit hydraulic conductivities and vertical anisotropies assigned to geologic zones	85		
5-2. Average hydraulic conductivities and vertical anisotropies for three levels of recharge rates	89		
5-3. Diffuse recharge polygons and net fluxes from final predevelopment steady-state model	92		

UNIT ABBREVIATIONS

acre-ft	acre-feet
acre-ft/yr	acre-feet per year
cm	centimeter
ft	feet
ft/yr	feet per year
g/L	grams per liter
Ga	billion years
ha	hectare
HK	hydraulic conductivity
Hz	hertz
in.	inches
in./yr	inches per year
J/kg-°C	joules per kilogram per Celsius degree
ka	thousand years
kg/m ³	kilograms per cubic meter
km	kilometer
kPa	kilopascal
m	meter
m/yr	meters per year
Ma	million years
mi	miles
meq/L	milliequivalents per liter
mg/L	milligrams per liter
mm/mo	millimeters per month
mS/cm	millisiemens per centimeter
nm	nanometers
ohm-m	ohm-meter
ohm-m ² /m	ohm-meter squared per meter
PMC	percent modern carbon
ppt	parts per thousand
sq. mi.	square miles
TU	tritium units
VA	vertical anisotropy
W/m-°C	watts per meter per Celsius degree

TECHNICAL SUMMARY

INTRODUCTION

The Salt Basin is a hydrologically closed, semiarid basin shared across the southern region of New Mexico and westernmost Texas (Figure TS-1). Water resources in the southwestern United States are limited, and they are becoming further strained due to increasing aridity and rising temperatures in the face of climate change. Even with significant changes to current water use and robust conservation, exploration of new or alternative water resources may be necessary as water shortages occur in the Southwest. Historically, in New Mexico water resource exploration efforts have occurred in basins with limited groundwater pumping or population. The Salt Basin has been one such region of exploratory interest for several decades.

The process of determining a firm water budget in this region has long eluded and challenged researchers and consultants. Data density in some areas is too sparse to draw reliable conclusions, especially with regard to the subsurface. One of the biggest obstacles to fully quantifying the water resources in the region is simply its remoteness and isolation, in addition to limited data availability and groundwater access.

PURPOSE AND SCOPE OF THIS PROJECT

Beginning in 2019, the New Mexico Bureau of Geology and Mineral Resources (NMBGMR) and the New Mexico Institute of Mining and Technology (NMT) initiated research to assess the water resources of the Salt Basin region of southern New Mexico and westernmost Texas. This project was funded by the U.S. Bureau of Reclamation and was conducted in coordination with two graduate students at NMT, the U.S. Geological Survey (USGS), the New Mexico Interstate Stream Commission (NMISC), and consultants with the NMISC. The current study was initiated as a result of NMISC considering potential groundwater export from the New Mexico portion of the basin to other regions of New Mexico, particularly during times of reduced surface water availability.

The purpose of this project was to assess the water resources and evaluate the sustainability of pumping 100,000 acre-ft/yr in the Salt Basin region. In particular, the project's scope addressed the Salt Basin regional water availability by (1) identifying and attempting to address data gaps where there is currently little or no information about the groundwater system; (2) refining estimates of the regional water budget, including groundwater recharge, storage, evapotranspiration, and pumping; (3) building and updating the hydrogeologic framework and numerical hydrologic model; and (4) running specific pumping scenarios in the revised model. These efforts focus attention on the region's capacity to sustain current groundwater withdrawals in the Salt Basin and implications for future development in New Mexico. Additional techniques applied in this study included electromagnetic geophysical measurements to better characterize the subsurface of the Salt Basin and to evaluate use of these methods in identifying saline or brackish aquifers.

In the first year of this study, the research team compiled previous data and reports to build the data release report NMBGMR Open File Report 608 (Kelley et al., 2020). Kelley et al. (2020) included an overview of the Salt Basin geology, a description of the geophysical and geochemical studies

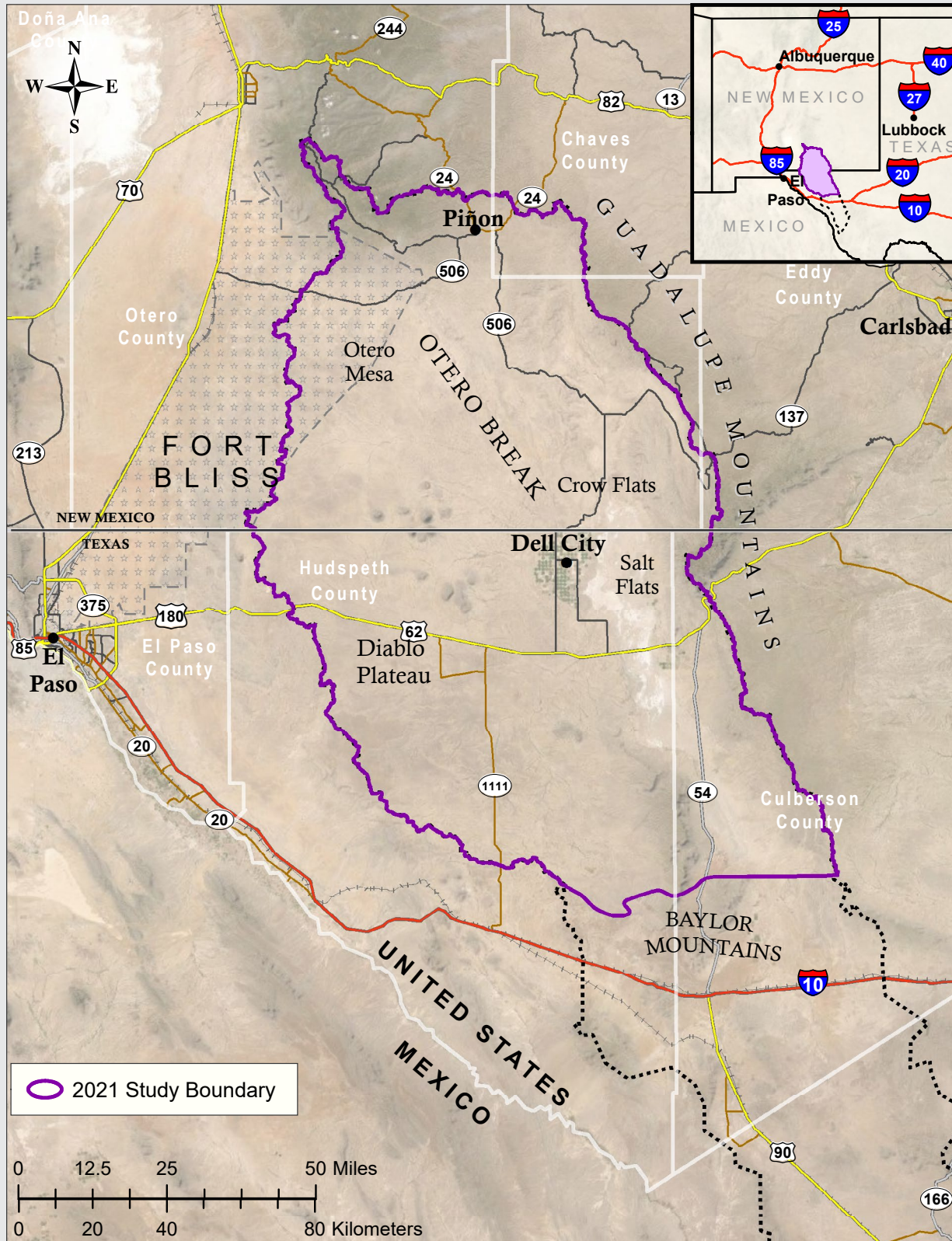


Figure TS-1. Location map of study area. The Salt Basin of New Mexico and westernmost Texas covers approximately 5,000 square miles. The study boundary was designated based on the surface water divide, except for the region around the Baylor Mountains, which corresponds to a groundwater divide (Nielson and Sharp Jr., 1985).

completed by others, a review of the previous estimates for recharge, and discussion of the existing hydrologic models of the region. From this data summary, in the second year of this study, data gaps were identified and efforts were taken to fill them. The research team collected 13 new water chemistry samples, inventoried 20 wells in New Mexico, conducted geophysical surveys, and applied new recharge estimations, along with estimating groundwater storage and water use. Two student master's theses were completed on portions of this research. This report is the final summary and synthesis of the work completed.

DESCRIPTION OF THE STUDY AREA

The Salt Basin is a 5,000-sq. mi., hydrologically closed, semiarid basin stretching from southern New Mexico into westernmost Texas (Figure TS-1). The Salt Basin lies within Hudspeth and Culberson Counties in Texas and within Otero, Chaves, and Eddy Counties in New Mexico. The westernmost portion of the Salt Basin is managed by the U.S. military at Fort Bliss. The largest population center is Dell City, Texas, which is located near the New Mexico–Texas border. The population of Dell City Census County Division climbed to 1,355 residents by 1960 but had dwindled to 615 residents in 2020, according to the U.S. Census Bureau (1960, 2021). The population within the Dell City limits was reported as 245 residents in the 2020 U.S. Census update.

The economy of this rural region is largely dependent on ranching. In some areas, like Dell City, Texas, farming and agriculture using groundwater resources are predominant. Water resources in this region are primarily provided by groundwater wells, and there is very limited surface water. The main surface water drainages include the ephemeral streams of the Sacramento River, Piñon Creek, and Cornucopia Draw from the north, with smaller intermittent arroyos in the central and southern regions of the Salt Basin.

Precipitation rates in the Salt Basin region vary depending upon location and elevation. In the higher elevations of the Sacramento Mountains, annual average precipitation is approximately 25 in./yr (660 mm/yr; PRISM, 2014). At lower elevations in the central part of the Salt Basin, precipitation averages around 9 in./yr (247 mm/yr). Temperature also varies spatially. Dell City's average temperature from 1981 to 2010 was about 16.4°C (61.5°F), while the Sacramento Mountains averaged about 7.1°C (44.8°F; PRISM, 2014).

Vegetation in the upper elevations above 6,000 ft, such as in the southern Sacramento Mountains, is dominated by piñon–juniper forest. In lower elevations comprising much of the Salt Basin, the vegetation zone is dominantly Chihuahuan desert, with mesquite, creosote, yucca, and grasses.

On the surface, the Salt Basin appears to be a broad, expansive, relatively flat and simple basin. However, the basin is structurally and geologically complex in the subsurface. There have been numerous periods in the geologic history of the Salt Basin and southwestern United States in which the region underwent faulting and folding (315–310 Ma), transitions of sea level (300–280 Ma), and further deformation and folding (around 65–50 Ma and 30–20 Ma). More geologically recent events, approximately 38–35 Ma, caused igneous rock to intrude into older sedimentary rocks in the western Salt Basin. This complex geologic history has resulted in extensive fracture networks and compartmentalization of aquifers, particularly in the limestone and dolomite layers, that have had a profound effect on water quality, water age, and flowpaths within the hydrogeologic system in the Salt Basin.

SUMMARY OF RESULTS

We have determined that the Salt Basin is unlikely to sustainably maintain withdrawals of 100,000 acre-ft/yr. However, the region may have the capacity to sustain 35,000 to 84,000 acre-ft/yr in total use. Based on estimates of historical pumping, the aquifer is already being pumped in excess of the available groundwater recharge. Groundwater level declines since the 1950s are upwards of ~50 to 65 ft (15 to 20 m) related to pumping in the vicinity of Dell City, Texas. The groundwater level declines suggest that Dell City pumping exceeds the local aquifer's capacity to transmit and recharge water.

Additional pumping of 100,000 acre-ft/yr would result in changes in storage within the broader, regional aquifer system. We estimate that at least 2.65 million acre-ft have already been mined from the aquifer. All the water in an aquifer cannot realistically be removed from the rock formation that makes up that aquifer. As part of this project, we estimated the amount of recoverable (extractable) groundwater currently in aquifer storage for the Salt Basin in New Mexico and Texas at approximately 34.5 million acre-ft. With limited well coverage in New Mexico, estimating the recoverable volume is limited. Our methods provide estimates that there are about 6.35 million acre-ft of recoverable groundwater in the New Mexico portion of the Salt Basin.

Additionally, water quality in many of the wells in the Salt Basin does not meet drinking water standards and in some areas is not suitable for livestock or irrigation of certain crops.

Approximately how much recharge is estimated to occur in the Salt Basin?

Recharge to the Salt Basin occurs primarily through two processes. First, recharge occurs in higher elevation regions such as the Sacramento Mountains in the form of diffuse recharge. This process allows some portion of the precipitation to infiltrate directly into the groundwater due to lower rates of evaporation and transpiration typically found at higher elevations. Second, channel-focused recharge occurs as precipitation runs off the landscape and collects in drainages such as the Sacramento River and smaller ephemeral arroyos and drainages during snowmelt or storm events. Accurately measuring or estimating these two types of recharge processes continues to challenge the hydrologic research community, especially in semi-arid, topographically diverse regions like the Salt Basin.

Utilizing both new and historical stable isotope data and groundwater ages, including tritium and carbon-14, we find that most recharge to the aquifer is derived from the Sacramento Mountains. Pairing these data with the geochemical results, we find there is limited recharge beyond the higher elevation region in the Sacramento Mountains, although there is some recharge through fractured carbonates in the Eightmile Draw area in the southwestern portion of the Salt Basin. With variability in the age results, we infer that the fractured nature of the aquifer allows faster recharge to the aquifer in regions where focused precipitation runoff occurs. In other regions, such as the expansive flat landscape in the low elevations of the Salt Basin, very little recharge seems to occur, as reflected by the lower tritium and lower percent modern carbon results (from carbon-14).

Results of this project covering the Salt Basin of New Mexico and Texas and including both diffuse and focused recharge yield an estimated range of recharge rates from about 35,000 to 84,000 acre-ft/yr, with a most likely rate of 57,000 acre-ft/yr or lower. This range is derived from a chloride mass balance method used in conjunction with a runoff estimation model developed at New Mexico Tech (called PyRANA). Recharge estimates were also evaluated using a detailed groundwater model developed for this project. When the model was tested with recharge rates of 40,000, 60,000, and 80,000 acre-ft/yr, the observed head distributions from wells were able to be matched to a very high degree ($R^2 > 0.99$).

by the model output in all three cases by adjusting aquifer hydraulic conductivity values. The 60,000 acre-ft/yr recharge test case had the lowest root mean square error between observed and computed head values, while the 40,000 acre-ft/yr test case had the mean error closest to zero. This range is the best estimate we can provide using all the data and tools currently available.

What is the estimated amount of evapotranspiration that occurs in this region?

In this study, temperature-based Blaney-Criddle (1962) crop transpiration depth estimates were combined with estimates of irrigated acreage derived from satellite remote sensing to produce estimates of annual volumetric evapotranspiration from all agricultural fields in the basin, primarily located around Dell City and outlying areas to the east. The average annual evapotranspiration from these fields totaled 96,750 acre-ft/yr between 1984 and 2019, including winter months. This estimate can be bracketed at the low end by only considering the growing season months, with an average of 76,670 acre-ft/yr during the same years. An ensemble of energy-balance-derived evapotranspiration estimates has recently become available from the OpenET consortium but only for the years 2016 to 2020. This product produced an annual average of 106,000 acre-ft/yr of total transpiration from these fields, similar to our 12-month Blaney-Criddle estimate of 107,000 acre-ft/yr from 2016 to 2019. The growing season estimate for these 4 years was 85,000 acre-ft/yr, indicating higher recent water consumption than the average over the period of record. Most of this agricultural evapotranspiration is derived from pumped groundwater.

How is water used in the Salt Basin and what is it used for?

Prior to the discovery of usable quantities of groundwater in 1947 accessed by wells and pumping, water use in the Salt Basin was typically limited to goat and sheep ranching. Groundwater use for irrigation of cotton, tomatoes, onions, and alfalfa developed rapidly in the 1950s in the Dell City area and continues to be the primary use of water in the basin. The outlying areas use lesser amounts of water for livestock and domestic and municipal uses. Unfortunately, metered well use data is typically not available for the Salt Basin. The New Mexico Office of the State Engineer reports municipal water use for the small community of Piñon and provides estimates of irrigation water use for the New Mexico portion of the basin from 1985 to 2015. The Texas Water Development Board provides countywide water use data from 1980 to 2019. These basin-wide water use datasets were correlated to historical reports of irrigated acreage, historical air photo analysis, and satellite imagery to estimate annual groundwater pumping from 1947 to 2019 for use in the groundwater modeling simulations. This estimate ranges from a maximum of 143,000 acre-ft/yr in 2014 to a minimum of 25,000 acre-ft/yr in 1947, with an average pumping rate of approximately 90,000 acre-ft/yr. These rates represent the total volume of water pumped and not the consumptive use of the water, which would account for the water that percolates back down through the soil to potentially recharge the aquifer (return flow).

What is the estimated amount of water stored in the Salt Basin?

Recoverable groundwater storage describes an estimate of how much groundwater can feasibly be removed, which is about half of the total groundwater in storage. The total groundwater storage is equivalent to the amount of water in the pores of the rock formation, whereas the recoverable groundwater storage is the fraction of total groundwater able to be extracted. This estimate fundamentally depends on the interconnection of the pore spaces, or the permeability. An aquifer can experience a decrease in permeability from effects such as groundwater depletion, aquifer compaction,

and mineral precipitation. When there is a decrease in effective permeability, this can also decrease the recoverable groundwater in storage. Our estimates in this report do not take into account reduction in permeability or the effects on recoverable storage estimate.

In this study, we estimated the “recoverable” groundwater storage in the Salt Basin of New Mexico and Texas at approximately 34.5 million acre-ft as of approximately current day (2021). For the New Mexico portion of the Salt Basin, we estimate there is approximately 6.35 million acre-ft, or about 18% of the estimated recoverable groundwater volume for the entire basin. The New Mexico recoverable storage estimate is smaller because we have sparse well control; additional subsurface geologic and hydrologic data are needed to make a more accurate estimate. Unlike some other studies, this storage estimate was derived for the entire Salt Basin aquifer system in New Mexico and Texas, covering approximately 3.3 million acres of land surface. Recoverable storage was calculated using the depths and extent of aquifer-bearing geologic formations and using a boundary where total dissolved solids (TDS) in groundwater are less than 3,000 mg/L. These estimates are weakest where there are few wells and more robust where there is a higher density of wells with samples and depth information.

What is the water quality of the Salt Basin?

Combining the new data with historical data, we find that generally the Salt Basin has good to poor water quality, depending on the location and depth. Almost all of the water quality samples indicate water with elevated hardness, with much groundwater having high levels of TDS, fluoride, and nitrates, among other constituents. TDS concentrations and other constituents for groundwater in the basin are typically above standards for drinking water (Table TS-1) but within the tolerance levels for some crops and livestock. Sulfate concentrations are particularly high, with most locations above the recommendations for drinking water and in some cases for cattle.

Primary drinking water maximum contaminant levels (MCLs) are legally enforceable standards that apply to public water systems to protect public health. However, these standards are not enforceable for privately owned wells. The U.S. Environmental Protection Agency (EPA) secondary drinking water MCLs are non-enforceable standards for constituents that do not pose significant health risks but may affect aesthetic considerations, such as taste, color, and odor. Because these standards are not enforceable for private water sources, the following information is provided to inform readers about the general water quality within the Salt Basin.

Table TS-1. Statistics for selected chemical constituents in groundwater and EPA primary and secondary drinking water maximum contaminant levels (MCLs), where applicable. Statistics were calculated after removing all duplicate analyses, using only the most recent values. Values for analyses that showed non-detects were entered as half the detection limit. The number of non-detects is shown. All concentrations are in mg/L.

	Ca	Mg	Na	HCO ₃	Cl	SO ₄	TDS	F	Fe	Hardness	Mn	NO ₃
Minimum	10.4	3	4.7	33	1.8	14.5	99.6	0.05	0.0001	115	0.0005	0.005
Maximum	16000	9000	43000	1093	71000	51000	160981	16	370	72500	0.588	233
Mean	364.2	210.4	553.6	257.6	1007.3	1154.1	3167.7	2.1	5.75	1963.5	0.0269	25.87
Standard Deviation	997.3	823.5	3268.2	95	5844.5	2796.2	11595.7	1.9	42.55	5698.3	0.0764	40.74
n*	352	349	314	368	379	377	332	305	150	309	120	304
# Non-detects	0	0	0	0	0	0	0	2	76	0	81	28
EPA Primary MCL								4				44.2
EPA Secondary MCL					250	250	500	2	0.3		0.05	

* n = number of samples

Groundwater in the Sacramento River region, which is the primary recharge zone, exhibits the lowest TDS concentrations in the Salt Basin, ranging from 253 to 993 mg/L. Sulfate concentrations range from 22 to 513 mg/L. Many of the groundwater samples in this region exceed secondary EPA MCLs for drinking water but do not exceed primary EPA MCLs. Available data indicate that all water in this region is suitable for livestock (TDS <6,000 mg/L) and irrigation (TDS <2,100 mg/L). However, the number of wells sampled in the region is limited, and there are large spatial data gaps. Therefore, there may be areas where groundwater quality deviates from that described above.

For the Shiloh Draw Region, groundwater TDS concentrations range from 99 to 3,100 mg/L, and sulfate concentrations range from 14 to 1,732 mg/L. This region has better quality water than most other areas in the Salt Basin. Most groundwater in this region is suitable for drinking, livestock, and irrigation, although some samples exceed TDS and sulfate secondary drinking water standards. There are a few wells that exceed the primary EPA standards for fluoride, which can have health implications. Again, groundwater quality data is scarce in this region. More groundwater samples need to be collected.

Groundwater TDS and sulfate concentrations in the Eightmile Draw Region range from 590 to 3,327 mg/L and 74 to 1,490 mg/L, respectively, with a rough apparent direct correlation with depth (higher TDS concentrations at greater depths). Therefore, much of the groundwater in this region exceeds EPA secondary MCLs for drinking water, and some of it is also insufficient for irrigation (TDS >2,100 mg/L). Most concerning is the presence of groundwater that exceeds primary EPA MCLs for fluoride (4 mg/L) and nitrate (44 mg/L as nitrate or 10 mg/L as nitrogen), both of which could have significant health implications. Well coverage in this region is poor, and therefore more wells need to be sampled in this area to get a better idea about the spatial distribution of water quality.

For the Salt Flats region, where a large number of wells have been sampled by the Texas Water Development Board, TDS concentrations in groundwater range from 329 to 160,981 mg/L, with a rough inverse correlation with depth. While mixing of high-chloride, high-TDS water is observed in the Salt Flats region, the higher TDS water located at shallow depths is due to evaporation. It is clear that much of the groundwater in this region exceeds secondary EPA drinking water MCLs, and much of it is not suitable for livestock or irrigation. However, groundwater around the Dell City area is apparently suitable for agriculture. There are many wells in this region that produce water that exceeds primary EPA standards for nitrate and fluoride and should not be consumed by humans.

How has past pumping from Dell City affected groundwater flow patterns, water levels, or aquifers in the region?

Groundwater in this region is mainly found in the Victorio Peak / Bone Springs formations in the Dell City area and in the Yeso Formation in the northern part of the basin. Much of the groundwater is found and moves within carbonate bedrock in fractures, faulted zones, and dissolution features. Groundwater movement into the basin from surrounding basins is difficult to resolve, particularly along the Sacramento River drainage, along the subtle groundwater divide between the Peñasco Basin and the Salt Basin, and along the southern border of the Salt Basin.

Using groundwater level measurements from wells measured as part of this study along with historical groundwater levels, we developed a potentiometric surface to estimate groundwater flow conditions. Groundwater in the Salt Basin generally moves from the southern Sacramento Mountains toward the south, with a historical natural discharge location around the playas (or salt flats) in the east-central part of the basin. Groundwater generally moves from west to east in the western portion of the

Salt Basin, also historically discharging naturally at the playas, and more recently groundwater is pumped from irrigation wells around Dell City, Texas. Groundwater depths range from less than 50 ft to over 2,100 ft below land surface.

While detailed pumping records are difficult to find for this basin, the Texas Water Development Board has carefully tracked groundwater elevation and water chemistry changes annually since 1947 in many wells around Dell City. Figure TS-2 plots the observed water table elevation and the modeled pumping amounts together over time, showing that the two trends are closely tied. From 1947 to 1978, while groundwater use was being rapidly developed, the water table declined at a rate of 1.25 ft/yr. From 1979 to 1994, the number of irrigated acres and groundwater pumping rate declined, and the water table began rising at a rate of approximately 0.30 ft/yr. Pumping increased again from 1995 to 2019, and the water table has been steadily declining at a rate of 1.08 ft/yr over this time period.

The fact that groundwater levels in this region, especially around Dell City, have been declining since irrigation began suggests that a substantial amount of groundwater has been removed from storage and is not being replaced by current rates of recharge. The amount of consumptive groundwater use, while not the same every year, is more than the balance of recharge to the basin over the period of time that groundwater levels have declined.

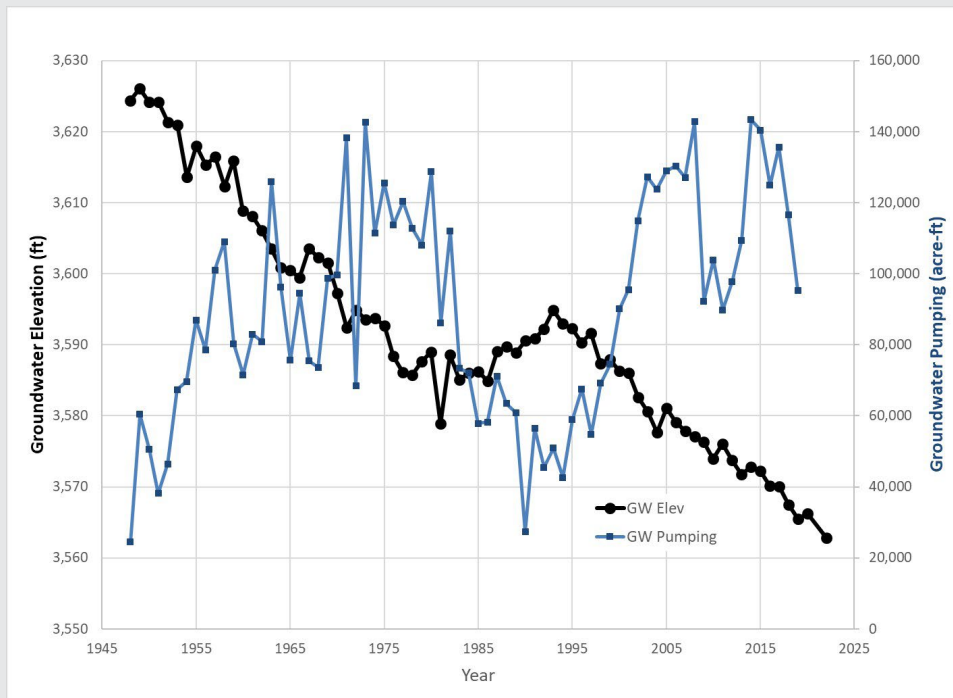


Figure TS-2. Measured water table elevations (left axis) in the Dell City area compared to the modeled groundwater pumping over time (right axis). The water table in Dell City has been closely monitored since groundwater development first began in the region in 1947 and has been steadily declining at a rate of 1.25 feet per year (1947–1977) to 1.08 feet per year (1995–2020). The exception to this trend is a short time from approximately 1978 to 1994 when pumping rates decreased and the water table began rising at 0.30 feet per year.

If 100,000 acre-ft/yr were pumped from the Salt Basin annually for the next several decades, how would that affect the basin over time?

After collecting numerous datasets and evaluating and running modeling scenarios with the information described above, we determined that this is an unrealistic number to evaluate. The Salt Basin is unlikely to sustainably maintain 100,000 acre-ft/yr of pumping in addition to the current water use in the basin because the amount of recharge to the region is too low. One supporting indicator is the measured aquifer level decline due to the region's principal aquifer stress—pumping in Dell City, Texas. We estimate that decades-long pumping of approximately 80,000 to 106,000 acre-ft/yr from the Dell City region has led to aquifer mining in the Salt Basin, where groundwater is being removed at a faster rate than it is recharging.

Therefore, given these values it is reasonable to conclude the basin cannot sustainably support consumptive groundwater withdrawals of 100,000 acre-ft/yr and maintain long-term aquifer levels. Rather, the aquifer and region may have the capacity to sustain somewhere between 35,000 to 84,000 acre-ft/yr in total consumptive use, if future climate conditions are not much different from the past. However, one caveat to tracking this is maintenance of groundwater level monitoring in the region, which is minimal at this time.

Continued pumping of over 100,000 acre-ft/yr would result in changes in storage within the confined and unconfined aquifer system. We estimate that at least 2.65 million acre-ft have already been mined from the unconfined aquifer. As noted above, we estimate there is about 34.5 million acre-ft of groundwater remaining, according to the modeled results. Most of this groundwater storage, according to our methods of analysis using well data, is found in the Texas portion of the Salt Basin, with about 18% of the recoverable groundwater in New Mexico.

This study was not able to investigate future hydrologic conditions, such as effects of climate change, which are likely to affect a variety of factors related to the overall water budget. The most obvious factor is rising temperatures due to climate change. Increased temperature would cause increased rates of evaporation and transpiration in the Salt Basin watershed. This reduces amounts of aquifer recharge even if precipitation rates remain at historical levels. Therefore, it is reasonable to conclude that the region is likely to see reduced groundwater recharge in the foreseeable future. Any planning work that utilizes this report's findings needs to evaluate this aspect of the region's water budget.

What were the pumping locations and scenarios evaluated? What are the limitations of the model?

Six hypothetical pumping scenarios were performed using the historical transient model. Three well field locations were considered for this study (Piñon Creek, Crow Flats, and Otero Break; Figure TS-3), with two pumping schemes (Scenario 1 and Scenario 2) for each location, totaling six pumping simulations. In any simulation only one of the well fields was pumped at a time, using one of the two pumping scenarios. Scenario 1 applied an additional pumping of up to 127,072 acre-ft, and Scenario 2 was up to 66,345 acre-ft in total. The hypothetical locations provide opportunities to examine effects of spatial and geologic contrasts and to evaluate the simulated response.

The hypothetical pumping scenarios were not run into the future because of the many unknowns, including projected temperature increases and uncertainty regarding future pumping stresses (Gutzler, 2005). Examining hypothetical pumping scenarios under historical conditions provided insights with less uncertainty regarding the context of developing predictions of future conditions.

With the different model scenarios evaluated in this study, what effects to groundwater flow across the state line are expected?

For the historical transient run, the sum total flux of water crossing the New Mexico state line into Texas was about 3 million acre-ft/yr between 1948 and 2020, with an average annual flux of approximately 44,000 acre-ft/yr. Six different well field simulations were created within this historical model (meaning these models did not project pumping rates into the future but instead added additional pumping to the historical record). For the purpose of this study, these well field simulations only pump when certain conditions are met, such as target low flow rates in the Pecos River (Scenario 1 simulations) or target high rainfall amounts (Scenario 2 simulations). The Scenario 1 simulations pump 127,000 acre-ft over 6 consecutive years of particularly low flow in the Pecos River (1969–1973). The Scenario 2 simulations pump 66,000 acre-ft of water over 8 non-consecutive years of high rainfall (1972–2014). Due to the on–off nature of this scenario, single year effects to state line flux were minimal, with the largest single year effect of 3,372 acre-ft from the Crow Flats Scenario 1 simulation, but the average annual change over all 6 simulations was only 412 acre-ft/yr. However, when examining the long-term effect of these simulations, the decrease to state line flow is more significant. The Crow Flats Scenario 1 simulation, for example, pumped a cumulative total of 127,072 acre-ft of water over the model period, which resulted in a total reduction of 67,625 acre-ft of flow across the state line, showing that over half of the well field pumping came directly from water that would otherwise flow into Texas. Well field location does play a role in the effects seen at the state line, such as the Piñon Creek Scenario 1 simulation, which also pumped 127,072 acre-ft of water (over the total model period) but only showed a cumulative decrease of 8,125 acre-ft of water to Texas.

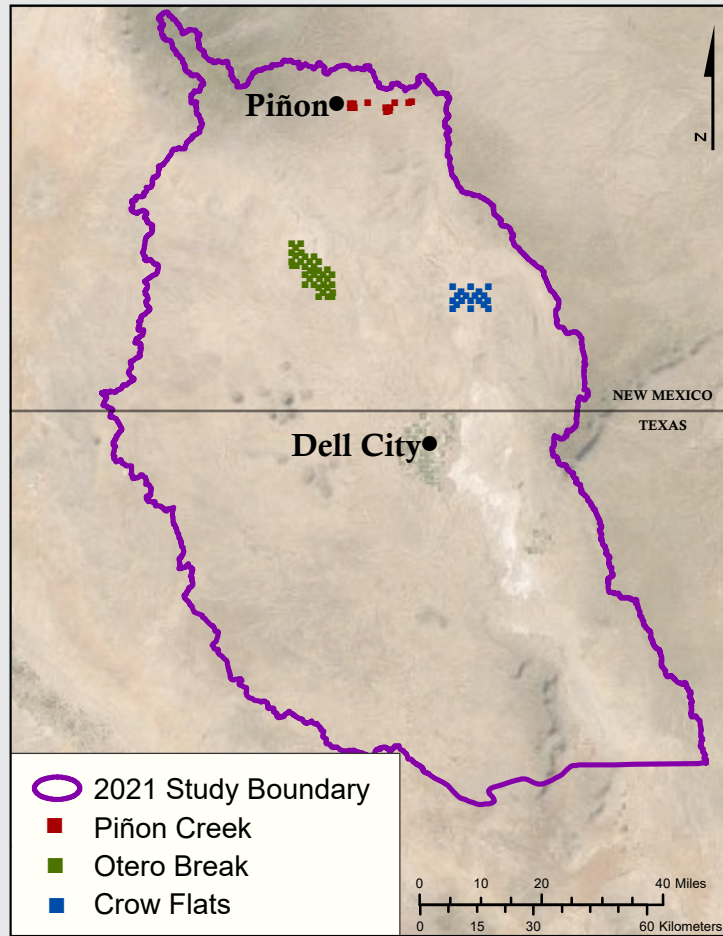


Figure TS-3. Hypothetical well field locations in the Salt Basin included in the MODFLOW model scenarios.

What are some highlights of the new geophysical research from this project?

Land-based geophysical measurements were incorporated into the Salt Basin groundwater study to further investigate aquifer properties. The geophysical surveys measure both natural and induced electrical and magnetic signals to explore the subsurface. Audio-magnetotelluric (AMT) data were collected at 28 sites in the study area. The AMT technique utilizes naturally occurring electromagnetic

waves generated by lightning (high frequency) and the interaction of solar winds with the Earth's magnetosphere (low frequency). Transient electromagnetic (TEM) data were collected at 12 sites. The TEM method measures the electrical resistivity of the subsurface using an applied current. The subsurface resistivity measured by both methods is affected by rock type, porosity, and groundwater salinity. Saline water, clays, and mineralized rocks conduct electric currents well (i.e., are conductive), whereas fresh water, dry anhydrite, and bedrock with little permeability or porosity are poor conductors (i.e., are resistive).

This study focused on Crow Flats and Otero Mesa in New Mexico. Crow Flats is underlain by gypsum playa deposits. The water table is close to the surface, and AMT and TEM data indicate that the shallow groundwater is conductive, consistent with the high TDS content of the groundwater measured during previous water quality studies. The geologic and hydrologic interpretation of the AMT data from Otero Mesa was more challenging because, as mentioned above, many factors besides TDS affect the resistivity of the subsurface. We found that limestone in the shallow subsurface (<1,000 ft) is resistive and probably contains fresh water. The interpretation is trickier at depths below 1,000 ft, where at many sites a conductive zone is recorded in the AMT data. Is the conductive zone due to a clay-rich rock type (Abo Formation) or brackish water? Luckily, several exploratory oil wells have been drilled in the Salt Basin, and geophysical well logs and rock cuttings from those wells are on file at the NMBGMR. Careful examination of the logs and cuttings revealed that in some instances, the conductive zone correlates with the Abo Formation. However, in other cases, the conductive zone is in the overlying Yeso Formation, a unit that contains anhydrite (a dehydrated form of gypsum), which is not conductive unless the calcium sulfate goes into solution. Thus, using evidence derived from the oil wells and AMT data, we hypothesize that brackish aquifers can be identified in the Yeso Formation using this combined approach. This investigation was reconnaissance in nature; the AMT sites were scattered over an area of about 100 sq. mi. Given our encouraging results, future work could conduct more focused experiments near the oil wells to test the interpretation.

What data gaps remain an issue in the Salt Basin region?

The Salt Basin region has been studied for decades and a substantial amount of historical data exists for several locations in the basin. However, exploration of these data through the modeling effort in this project highlighted some of the limitations that exist due to lack of spatially distributed data or poor data quality. As with any model, the Salt Basin model would benefit from additional information, including continued or expanded monitoring of groundwater levels, aquifer parameter characterization, and salinity measurements. Extension of modeling efforts to include age data constraints or simulation of density-dependent flows would improve the numerical representation of the Salt Basin and potentially improve simulated predictions.

Future work toward resolving past, present, and future recharge rates is essential in this region and could aid in water planning and decision making. Additional geologic and geophysical studies could provide model layer refinements and improve representations of the complex Salt Basin subsurface. Future modeling work could be refined to more accurately project effects from pumping under future climate conditions with likely increasing aridity and evapotranspiration rates and with reduced recharge rates. Chloride mass balance method recharge estimates developed in this study provided another method to quantify a major Salt Basin water budget component and would be improved with additional sampling to better characterize the end-member inputs.



Wind Mountain, one of several Cenozoic intrusions in the Cornudas Mountains. *Photo by Shari Kelley*

CHAPTER 1: OVERVIEW OF THE SALT BASIN

HYDROGEOLOGY

Marissa Fichera, Shari Kelley and Stacy Timmons

Surficial geology of the region includes Permian through Quaternary units (Figure 1-1) that overlie intensely faulted Pennsylvanian strata and Precambrian basement at varying depths. The geology of the study area can be broken into four general rock types based on corresponding depositional time periods and environments, from oldest to youngest: (1) Paleozoic sandstones and limestones deposited in a marine environment, (2) shelf-to-basin Permian limestones deposited in shallow-to-deep marine environments, (3) Cretaceous sandstones and limestones deposited in a shallow marine environment, and (4) Cenozoic intrusions and Neogene alluvial deposits. Thick sequences of faulted, fractured, and karstic Permian limestones make up the primary aquifer units in the area, followed by Salt Basin Graben basin-fill and Cretaceous limestones of the Diablo Plateau (Figure 1-1). A diagrammatic cross section showing the complex shelf and basin geology is presented in Figure 1-2. A summary of the primary water-bearing units is presented in Table 1-1.

Structural features (i.e., faults and fractures) in the Salt Basin have significant effects on the groundwater flow system. Structural features produced during multiple tectonic episodes are superimposed upon one another, causing major structural trends to be reactivated (George et al., 2005; Kelley et al., 2020). Consequently, high-permeability limestones in the region exhibit high densities of faults and fractures along directional trends and create preferential groundwater flowpaths (Mayer and Sharp, 1998). Hydrologically significant structural features mentioned in this report include the Otero Break and the Salt Basin Graben. The Otero Break is a broad, northwest-southeast-trending fault and fracture zone

extending from the Sacramento Mountains to the Salt Flats near Dell City, Texas (Figure 1-3; Mayer and Sharp, 1998). The high density of fractures within the karstic limestones (Yeso Formation and San Andres Limestone, Table 1-1) creates a high-transmissivity conduit of fresh water from the Sacramento Mountains to Dell City, Texas (Mayer and Sharp, 1998). The Salt Basin Graben is a north-south-trending horst-and-graben structure developed during Basin-and-Range extension (Goetz, 1980; Figure 1-1). Infill material consists of unconsolidated sand, playa deposits, and carbonate rock deposited by ancestral drainages within the Salt Basin (Angle, 2001; Table 1-1). The structure itself extends from the Crow Flats region south approximately 200 mi into Texas; however, physiographic subdivisions exist (Angle, 2001). The sub-basin relevant to this study, referred to as the Salt Flat, has a southern boundary defined by the Victorio Flexure and relatively thin basin-fill (Gates et al., 1978). A groundwater divide is also present in the same location (Nielson and Sharp, 1985). Countless additional structures exist (Kelley et al., 2020); however, their influence on groundwater flow is not explicitly investigated in this report. The structural geology and facies complexity beneath the surface of the Salt Basin is nicely illustrated in a cross section constructed by Black (1976) using seismic and well data (Figure 1-2). A Proterozoic-basement-cored Ancestral Rocky Mountain highland that is oriented roughly north-south underlies the central Salt Basin. The Permian Abo Formation lapped across the highland and thus has variable thickness or is absent.

The Permian carbonates of the Victorio Peak and Bone Spring Limestones are the primary aquifer units in the basin. The Victorio Peak is the shelf-margin facies equivalent of the basin-facies Bone Spring (Hayes, 1964). The Bone Spring pinches out beneath the Victorio Peak northwest of the Delaware Basin margin, and where the two are stacked, the limestones collectively constitute a major water-bearing unit

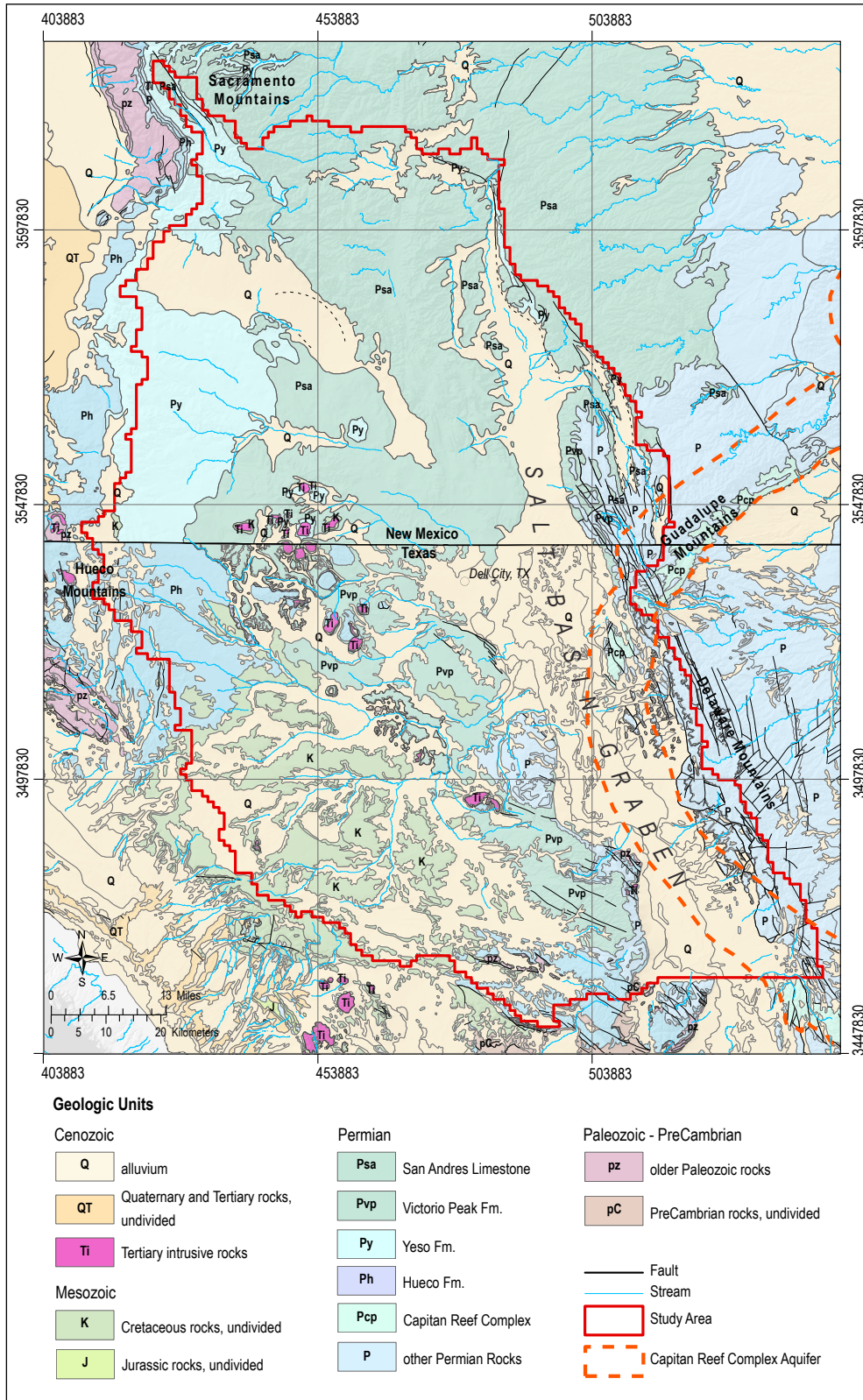


Figure 1-1. Generalized geologic map of the Salt Basin study area. This map is a modified compilation of the 1:500,000-scale geologic maps of New Mexico (Scholle, 2003) and Texas (Barnes, 1992). Digital map files for Texas were obtained from the USGS Texas Water Science Center (2014) Geologic Database of Texas. Geologic units were correlated across the state line as best as possible; however, some discrepancies are apparent (e.g., Permian Yeso Fm. [Py] mapped in New Mexico merges with Permian Hueco Fm. [Ph] mapped in Texas near the Hueco Mountains). Despite this, mapped lithology stays generally consistent from New Mexico to Texas.

Table 1-1. Primary water-bearing units of the Salt Basin

Age	Unit	Location	Physical and Lithologic Characteristics	Water-Bearing Characteristics
Neogene	Alluvial and Bolson Deposits	Crow Flats in New Mexico, Dell Valley in Texas	Unconsolidated clay, silt, sand, and gravel derived from weathering and erosion of local rock and deposited by ancestral drainages within the Salt Basin; commonly 1,000 to 2,000 ft thick. Interbedded carbonate, gypsum, and saline deposits in the playas are derived from evaporation of groundwater originating in the Permian strata of the surrounding highlands.	Supplies moderate to large quantities of fresh to saline water to the northern parts of the Salt Basin, mostly in fine-grained lacustrine and alluvial deposits.
Cretaceous	Cox Sandstone	Diablo Plateau in Texas	Mostly quartz sandstone with some pebble conglomerate and siltstone, shale, and limestone; very fine- to medium-grained; commonly less than 200 ft thick but can be as much as 700 ft thick.	Supplies small to moderate quantities of fresh to moderately saline water in eastern and southern Wild Horse Flat.
Permian Shelf-Margin Facies	Capitan Limestone	Southern tip of study area, Guadalupe Mountains, Capitan Peak	The Capitan Formation is a high-permeability, massive white limestone formed in a wide reef zone. In the southern Guadalupe Mountains it ranges in thickness from 1,000 to 2,000 ft. Only the westernmost portion of this formation is included in the study area.	Capitan and Goat Seep Limestones supply moderate to large quantities of fresh to slightly saline water in the Beacon Hill area. The Capitan also supplies moderate to large quantities of fresh to slightly saline water to the Apache Mountain area. The Delaware Mountain Group supplies small quantities of slightly to moderately saline water along the eastern side of the northern Salt Basin and foothills of the Delaware Mountains.
Permian Shelf-Margin Facies	Goat Seep Limestone, undifferentiated limestones and sandstones, including the Delaware Mountain Group	Apache Mountain area	The Goat Seep Limestone contains massive, thick-bedded reef limestone and dolomite. It is exposed in the Guadalupe Mountains and ranges from 560 to 1,200 ft thick. The Delaware Mountain Group (Brushy Canyon, Cherry Creek Canyon, and Bell Canyon formations) are sandstones and limestones with some siltstones; the group is exposed in the Delaware Mountains, where it is 600 to 1,000 ft thick. Permian gypsum deposits of the Guadalupe and Delaware Mountains contribute significant amounts of calcium sulfate to the groundwater system.	
Permian Shelf Facies	San Andres Limestone and Yeso Formation	Sacramento Mountains, comprises much of the north and west basin regions	The shallow water platform carbonate of the San Andres Limestone and the underlying Yeso Formation grade into the Victorio Peak Limestone (shelf-margin facies), which then transitions to the Bone Spring Limestone (basin facies). The Victorio Peak Limestone is characterized by white dolomite and limestone, which transition to the black and dark grey cherty limestone and thin beds of siliceous shale of the Bone Spring Formation. The transition between the San Andres Formation and Victorio Peak Formation is poorly defined and has led to the difference in unit assignment across the state line, with the New Mexico portion mapped primarily as the San Andres Formation and the Texas portion labelled as the Victorio Peak Formation.	Where the Bone Spring and Victorio Peak units are stacked, the limestones collectively constitute a major water-bearing unit. This aquifer is the primary source of water for Dell City, Texas.
Permian Shelf-Margin Facies	Victorio Peak Limestone	Diablo Plateau, Sierra Diablo Mountains, Guadalupe Mountains		
Permian Basin Facies	Bone Spring Limestone	Sierra Diablo Mountains		
Permian Shelf Facies	Hueco Limestone	Hueco Mountains	The lower Hueco Formation consists of fine-crystalline limestone interbedded with shale and minor sandstone.	Source of fresh water (King and Harder, 1985) based on drill-stem tests. These authors provide an example from a well in Hudspeth County, Texas.

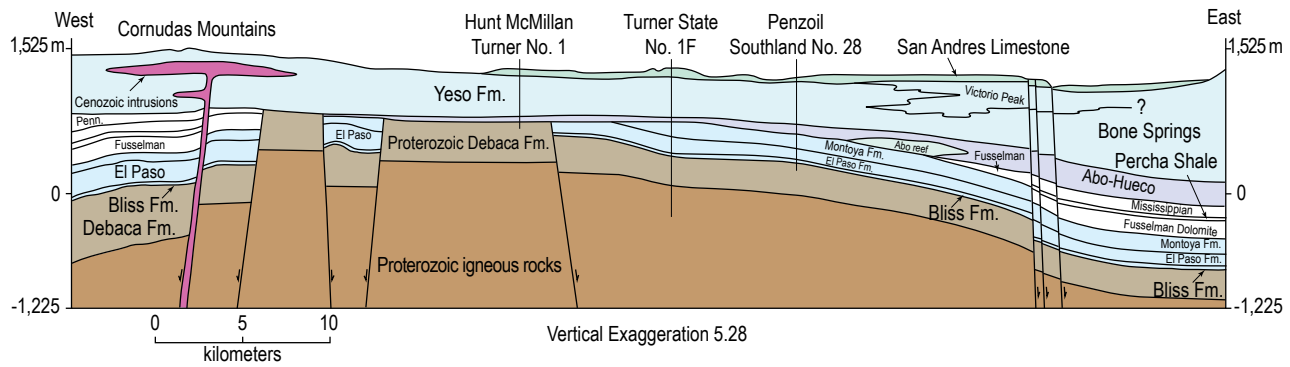


Figure 1-2. Cross section across buried Ancestral Rocky Mountains structures, modified from Black (1976). Location of cross section line is on Figure 2-2. Brown = Proterozoic rocks; dark blue = Cambro-Ordovician sedimentary rocks; white = Silurian to Pennsylvanian sedimentary rocks; blue = Permian sedimentary rocks; red = middle Cenozoic intrusive rocks. Oil wells are shown as vertical lines. Elevation as meters above or below sea level (at 0) are noted on the vertical axes.

referred to as the Bone Spring–Victorio Peak Aquifer (see Figure 1-2). This aquifer is an important source of potable groundwater in the region and is the principal source of water for Dell City, Texas. Victorio Peak Limestone is characterized by white limestones and dolomites, while Bone Spring Limestone consists of black to dark gray cherty limestone with thin interbedded layers of black or brown siliceous shale (Ashworth, 1995).

The high-permeability Capitan Limestone constitutes one of the most prolific aquifer units where it is present in the subsurface; however, only the westernmost portion of it is included in the Salt Basin study area. It crops out in the Guadalupe Mountains and is the rock unit that forms Capitan Peak, the highest point in Texas.

Additional sources of groundwater in the basin include the Hueco Limestone and to a very minor extent the Abo Formation (Huff and Chace, 2006). The San Andres Limestone and the Yeso Formation serve as aquifers in the northern part of the Salt Basin, which grade southeastward into the Victorio Peak and Bone Spring Limestones. The Yeso Formation is also important hydrologically, as it contains abundant evaporites (primarily anhydrite/gypsum), contributing to increased TDS concentrations in the groundwater of the region. The Abo Formation can also behave as a confining unit along with Cretaceous shales in the southern region of the Salt Basin.

Groundwater in the Salt Basin originates and is recharged from the high elevations of basin-bounding mountain ranges (primarily the Sacramento Mountains and, to a lesser extent, the Guadalupe Mountains, Hueco Mountains, Delaware Mountains, and Baylor Mountains) as precipitation and travels down-gradient toward low-elevation playas in the center of the basin (Figures 1-3 and 1-4). Groundwater generally moves from west to east in the western portion of the Salt Basin, historically discharging naturally at the playas, and more recently groundwater is pumped from irrigation wells around Dell City. The southeastern boundary of the study area is likely an area of subsurface discharge via the highly transmissive Capitan Formation, where groundwater flows preferentially south and east through a network of solution-enlarged fractures toward Balmorhea, Texas (Land and Veni, 2018).

The Salt Basin is a hydrologically closed basin (Duffy and Al-Hassan, 1988). Prior to pumping, diffuse and channel-focused recharge was balanced by evapotranspiration in lowland playas. Evapoconcentration of groundwater has resulted in salinities as high as 139 g/L (ppt) near the playas.

Based on well records, accessible groundwater depths range from less than 50 ft to over 2,100 ft below land surface (Figure 1-5). Shallow groundwater levels below the salt playas or “salt flats” have been observed, as this was the natural discharge point

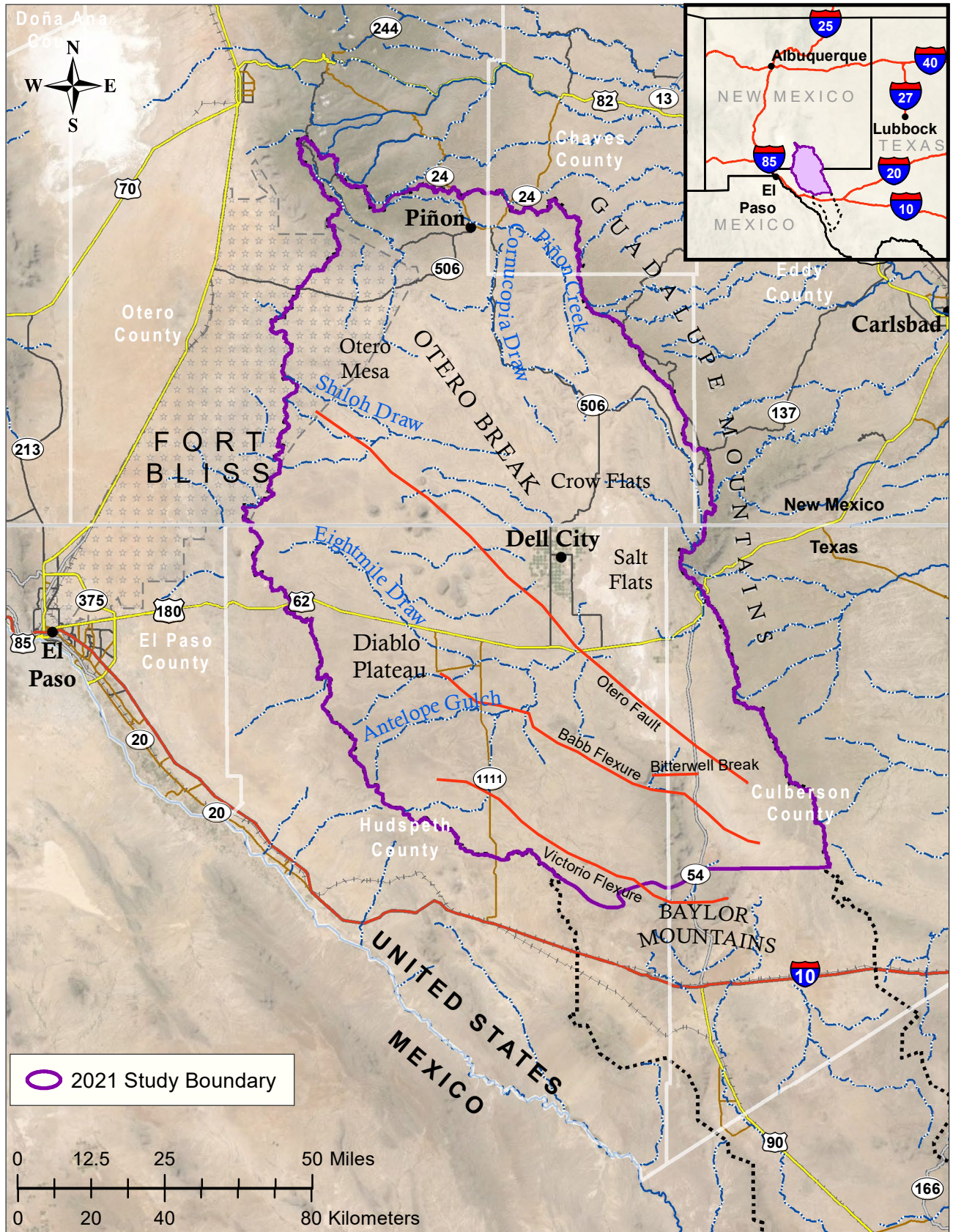


Figure 1-3. Key structural geology features impacting groundwater flow of the Salt Basin include the Otero Break, Babb Flexure and Otero Fault, Crow Flats, and Victorio Flexure.

for this basin until pumping began in the Dell City region. Much of the groundwater is found and moves in carbonate bedrock materials within fractures, faulted zones, and dissolution features.

A three-dimensional block diagram shown in Figure 1-6 depicts the land surface of the Salt Basin with the various aquifer units, including the San Andres Limestone and Yeso Formation inter-fingering with the Victorio Peak to Bone Spring Limestones.

Additionally, disruption of these formations and the aquifer by faults and intrusive igneous units further complicate the groundwater flowpaths and geochemical interpretations in this region. The aquifer system in this region appears to be compartmentalized, as groundwater is found largely in fractures, fault zones, and other openings and is disconnected and disrupted in various ways along its flowpath.

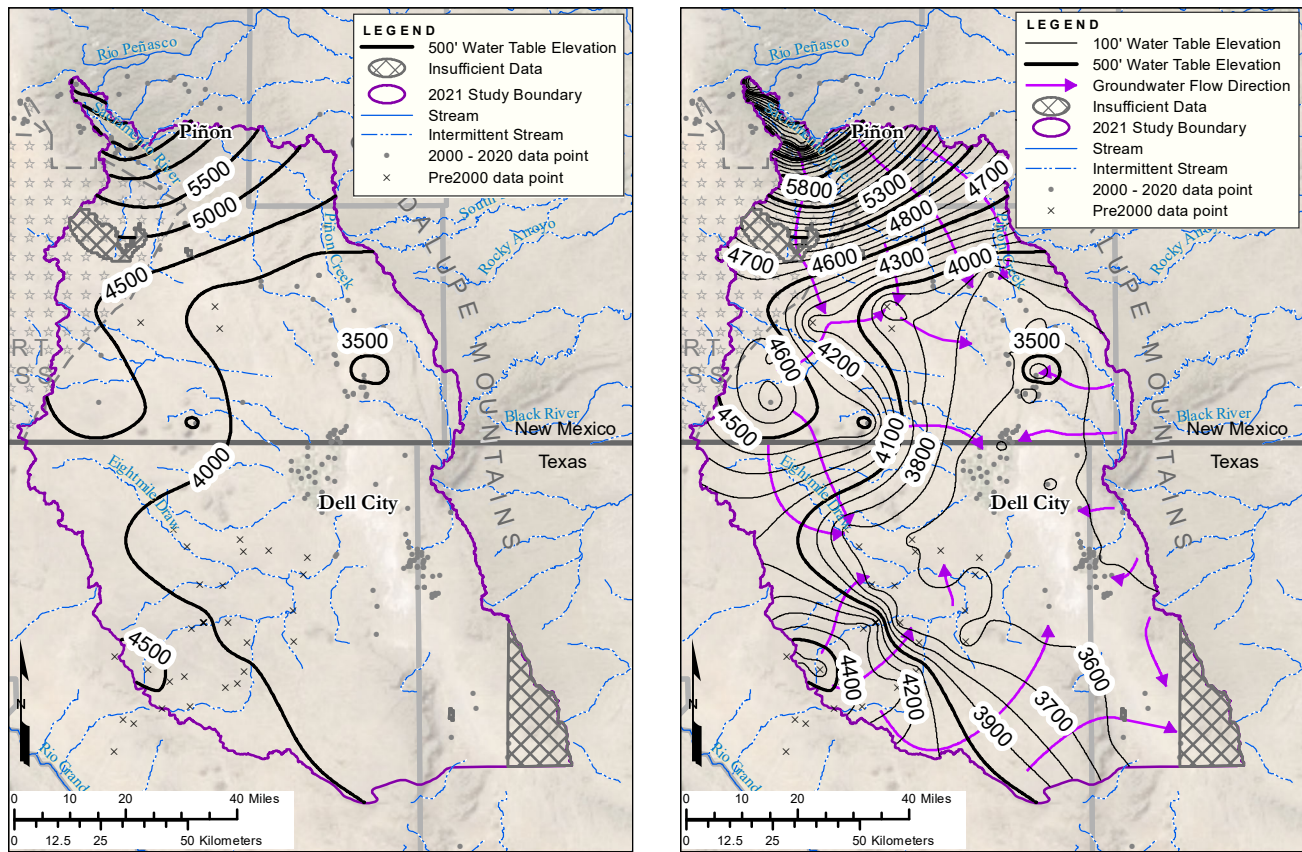


Figure 1-4. Regional map of approximate groundwater potentiometric surface. Groundwater generally flows from the higher-elevation mountain ranges toward the low-elevation salt flats in the center of the basin. Groundwater contours were developed for this project using groundwater level data from a range of sources, including current measurements (2000–2020 data points) and a few sources measured prior to 2000. Measurements made while a well was pumping were removed. Water level elevations were calculated from water depth measurements and used as point-elevation inputs for the ESRI Topo-to-Raster tool, which interpolated a potentiometric surface. The potentiometric surface was “smoothed out” using the Focal Statistics tool with a 500-m-by-500-m cell rectangular neighborhood and mean statistics type.

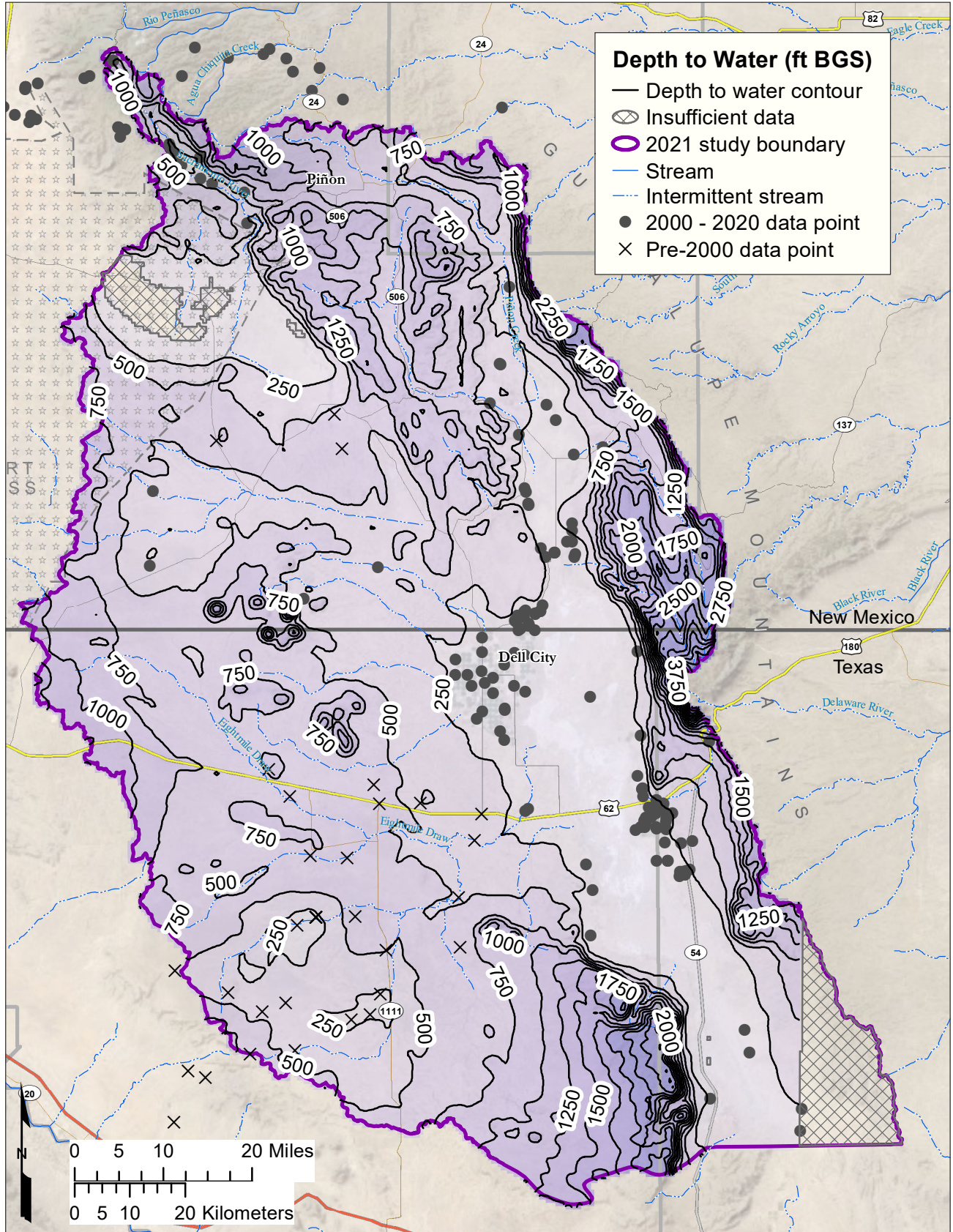


Figure 1-5. Map of estimated depth to water in feet below ground surface (BGS). This map was developed using the groundwater potentiometric surface compared to the land surface digital elevation model.

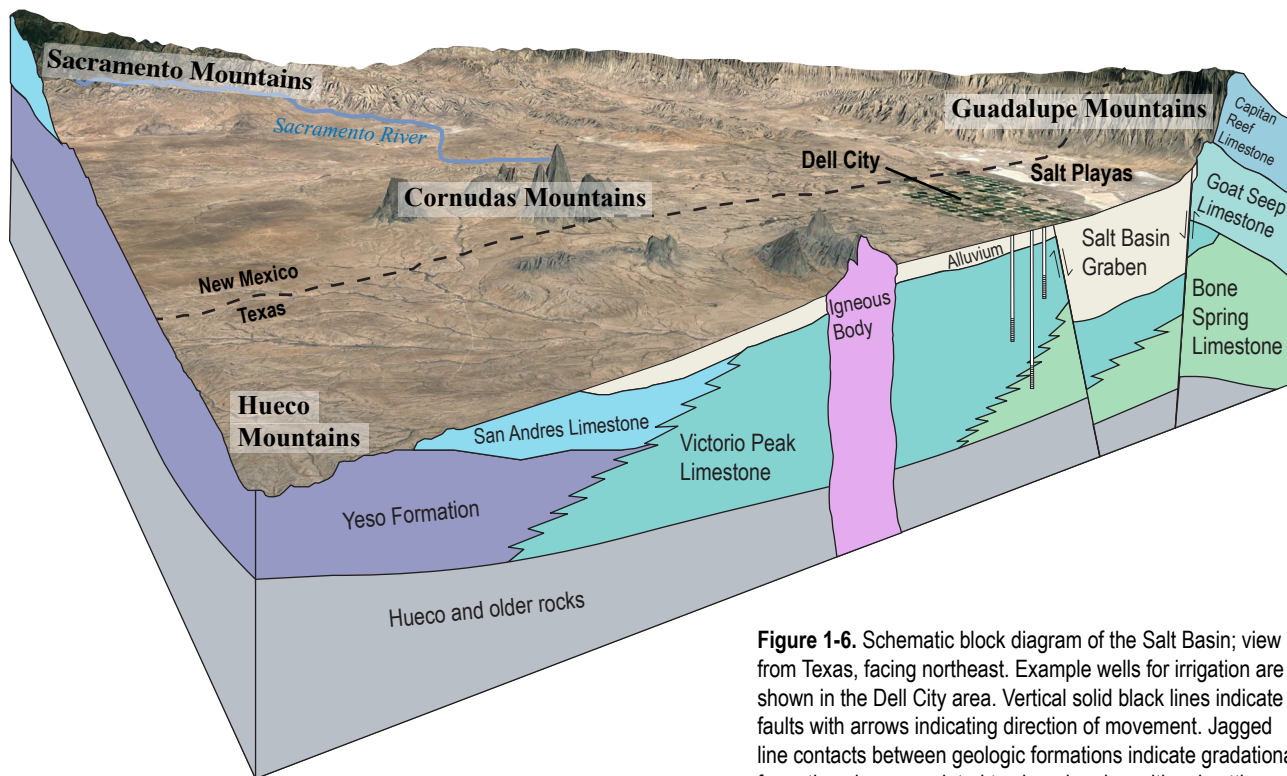


Figure 1-6. Schematic block diagram of the Salt Basin; view from Texas, facing northeast. Example wells for irrigation are shown in the Dell City area. Vertical solid black lines indicate faults with arrows indicating direction of movement. Jagged line contacts between geologic formations indicate gradational formation changes related to changing depositional settings.

WATER USE

Laila Sturgis

Water use in the Salt Basin was historically limited to sheep and goat farming until groundwater resources were discovered and developed in the late 1950s. The Dell City area currently consists of 40,000 acres of irrigable land in Texas and extends northward into Otero County, New Mexico, where it is referred to as Crow Flats (Ashworth, 1995). The primary crops grown in this region are cotton, onions, tomatoes, and, to a lesser extent, alfalfa and chile. The population of Dell City climbed to 950 by the early 1960s but had dwindled to 526 residents in 2019 (U.S. Census Bureau, 2021). Despite the shrinking population, Dell City remains the largest urban center in the Salt Basin. Other towns to note in the basin include Piñon and Timberon in New Mexico; El Paso is the nearest major city and is outside the basin. Most the Salt Basin land in New Mexico is federally owned and administered by the U.S. Bureau of Land Management (BLM) and is leased for cattle ranching supported by privately owned and operated wells.

Water use for the state of New Mexico is published by the New Mexico Office of the State Engineer (NMOSE) every 5 years and includes agricultural and municipal water use estimates specifically for the Salt Basin (Wilson, 1992; Wilson and Lucero, 1997; Wilson et al., 2003; Longworth et al., 2008; Longworth et al., 2013; Magnuson et al., 2018). In particular, the reports confirm that all irrigated agriculture in the New Mexico portion of the Salt Basin is supplied from groundwater, with no surface water diversion rights. The total number of irrigated acres has slowly declined over the reporting period (Table 1-2). Water use from the Piñon Water Users Association (WUA) is also included in the NMOSE reports and shows that water use for this community has also steadily declined since reporting began in 1990.

In addition to reporting water withdrawals, the NMOSE calculated groundwater depletions for 1990, 1995, and 2000. These values are comparable to the calculated agricultural consumptive use data for the entire basin but on a much smaller scale, as most of the irrigation happens on the Texas side of the basin. A brief summary of the methods used to calculate

Table 1-2. Specific water use for the New Mexico portion of the Salt Basin, as reported by the New Mexico Office of the State Engineer (2021)

Report Year	Irrigated Acres	Agricultural Use Withdrawals (acre-ft)	Agricultural Use Depletions (acre-ft)	Piñon WUA Withdrawal (acre-ft)	Piñon WUA Depletions (acre-ft)
1985	2,636	10,129			
1990	2,360	8,772	6,742	44.32	22.16
1995	2,475	10,017	8,088	50.75	25.38
2000	2,127	7,275	5,964	33.38	16.69
2005	2,167	8,111		Not reported	
2010	683	2,430		24	
2015	295	985		10	

depletions for agricultural use is presented here, but more details can be found in Wilson et al. (2003). The first step of making these estimates was determining the number of irrigated acres by analyzing multiple data sources, including hydrographic surveys, aerial photos, and water rights permits. These acres were then separated by type of irrigation (flood, sprinkler, or drip). Local precipitation and temperature records were tabulated to determine the length of the growing season. Effective rainfall and theoretical consumptive use or evapotranspiration of water by individual crops was calculated using the Blaney-Criddle (1950, 1962) method. The consumptive irrigation requirement (CIR) for each crop is computed by subtracting the effective rainfall from the consumptive use. The total quantity of water depleted on a farm or irrigation project is the sum of the individual crop CIRs minus any incidental depletions such as weather, biological, or economical losses to crops.

The Texas Water Development Board provides a similar annual summary of groundwater diversions for the state, but the data are designated by county and by aquifer. Therefore, Table 1-2 does not include subtotals for the Texas portion of the basin. Hudspeth County and Culberson County historical pumping data are presented in Figure 1-7. The project study area includes many of the pumping wells in Hudspeth County but only captures the western portion of Culberson County, so the data presented in Figure 1-7 overestimate use in the study area. The primary source of groundwater in Hudspeth County and for Dell City is the Bone Spring–Victorio Peak Aquifer, which shows a trend of increased use in the 1990s but overall has remained fairly consistent at 30,000 to 50,000 acre-ft of withdrawals per year. The primary source of groundwater for Culberson County is the West Texas Bolson Aquifer, which has

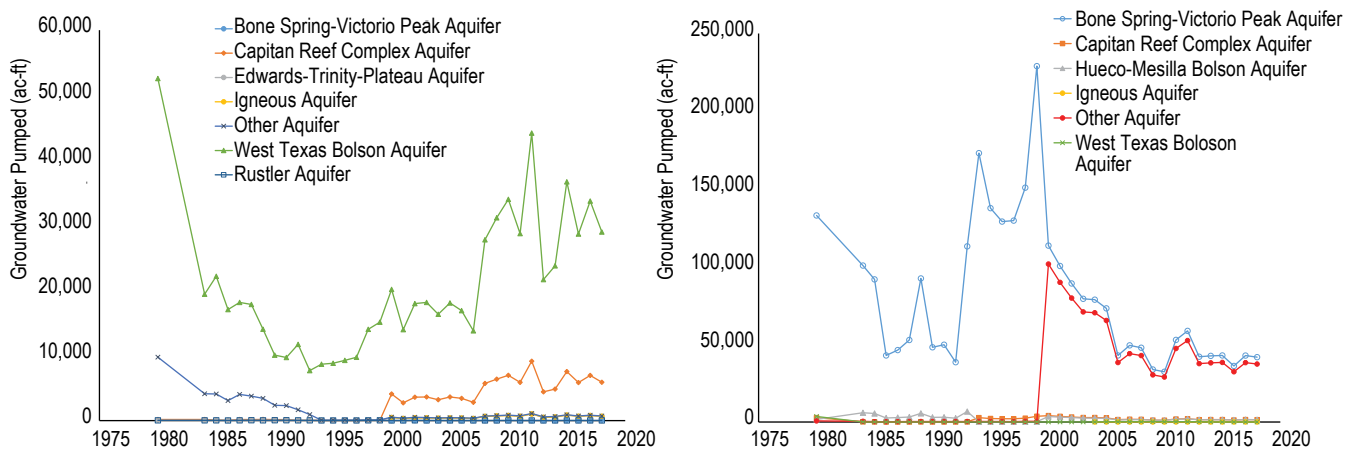


Figure 1-7. Historical groundwater pumping as reported by the Texas Water Development Board in (L) Culberson County and (R) Hudspeth County from 1980 to 2019. The study area covers a significant portion of Hudspeth County, but only the western portion of Culberson County. The wells in Dell City are typically completed in the Bone Spring–Victorio Peak Aquifer, where pumping rates have ranged from 40,000 acre-ft/yr to 230,000 acre-ft/yr. County boundaries are shown in Figure TS-1.

shown increased withdrawals since 1980, but the data are not refined enough to draw conclusions about Salt Basin water use.

The two report categories described above provide insight on regional trends and some annual pumping ranges, but they do not capture enough detail to create an accurate pumping history for the basin. These values then had to be estimated, as described in Chapter 5 of this report.

GROUNDWATER LEVEL OBSERVATIONS

Stacy Timmons and Elizabeth Evenocheck

As important as it is to try to more accurately estimate or measure the different features of the water budget, sometimes reflecting on current

conditions can shed light on the reality of the groundwater system. There are several sites in the Salt Basin region where periodic and invaluable groundwater level measurements have been captured. When we review the history of groundwater level trends in the central part of the Salt Basin, specifically around Dell City, we can see that over the past several decades, groundwater elevations have been declining (Figure 1-8). The wells in the Dell City area are completed in the unconfined Bone Spring and Victorio Peak Limestones. This decline in water levels is on the order of 15 to 20 m (50 to 65 ft) since the 1950s when pumping began. This graph also shows that groundwater level declines slowed significantly in the period of time around the 1980s, which were notably wetter years in this region. Without pumping records to compare from these wells, we can hypothesize that perhaps pumping was less during these wetter years, and groundwater was used as much as in the decades before or following the 1980s.

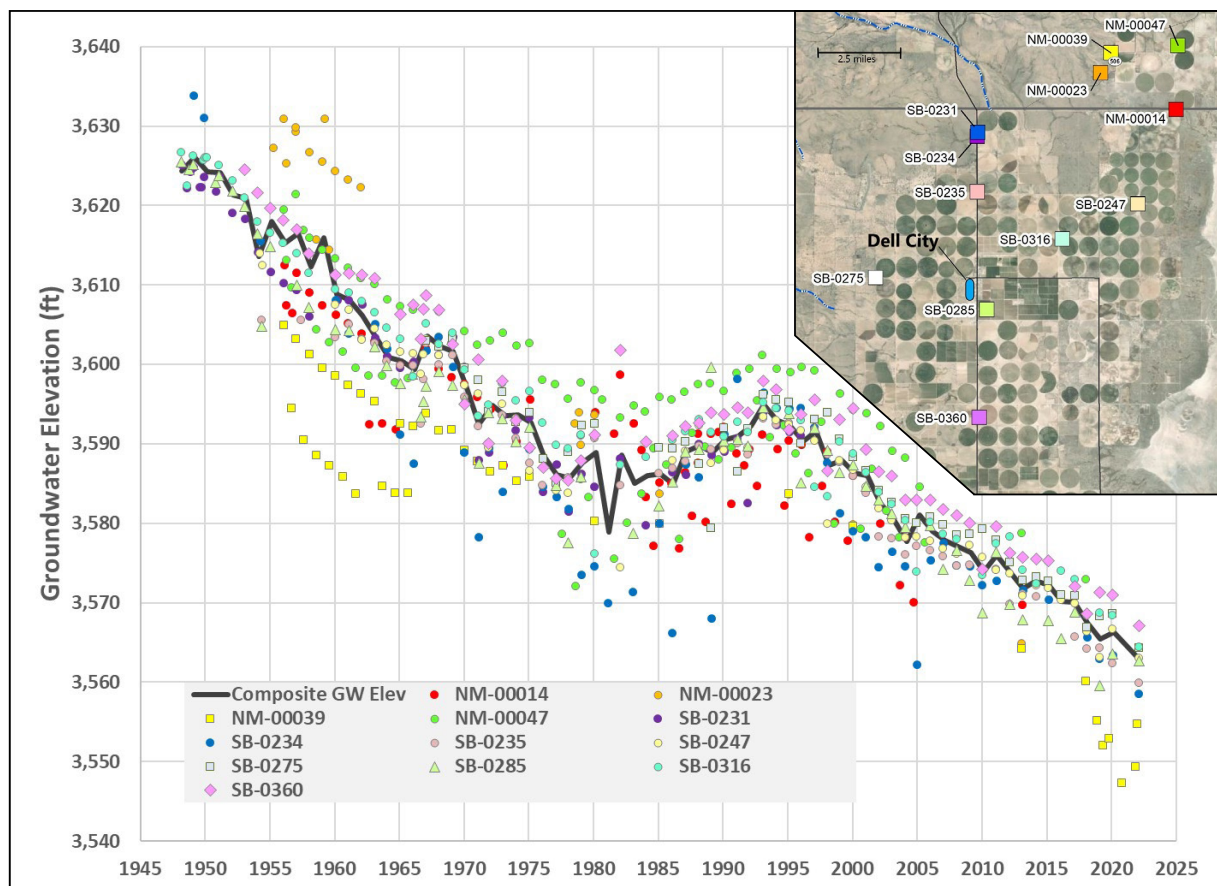


Figure 1-8. Dell City water table observations from 1948 through 2022 show a 50–65-ft decline over this time period. The water table in Dell City has been closely monitored since groundwater development first began in the region in 1947 and has been steadily declining at a rate of 1.25 ft/yr (1947 to 1977) to 1.08 ft/yr (1995 to 2020). The exception to this trend is a short time from approximately 1978 to 1994 in which pumping rates decreased and the water table began rising at 0.30 ft/yr.

CHAPTER 2: GEOPHYSICS

Shari Kelley

To learn more about the subsurface of the basin, we collected audio-magnetotelluric (AMT) data at 28 sites and transient electromagnetic (TEM) data at 12 sites in the New Mexico portion of the Salt Basin. Both of these methods measure subsurface electrical resistivity, which is affected by rock type, porosity and its connectivity, and groundwater salinity (Figure 2-1). Saline water, clays, and mineralized rocks all conduct electric currents well (i.e., are conductive), whereas fresh water, anhydrite, and unaltered bedrock with little permeability or porosity are poor conductors of electrical currents (i.e., are resistive). Sedimentary rocks containing saline pore fluids can have bulk formation resistivities of less than 10 ohm-m (Figure 2-1) based on Archie's law, as follows:

$$\sigma = \sigma_{fluid} \phi^m$$

where σ is bulk electrical conductivity, σ_{fluid} is fluid electrical conductivity, ϕ is porosity, and m is the cementation factor. Formation resistivity (ρ) is the inverse of electrical conductivity ($\rho = 1/\sigma$).

The AMT field sites were chosen based on four criteria. The sites were located: (1) on BLM land; (2) far from cultural noise sources such as power transmission lines, pipelines, fences, buildings, and water storage tanks; (3) at least 100 m from a road (mostly well-maintained Otero County roads); and (4) along transects that cross the known orientations of important geologic structures in the region, based on previous seismic surveys (e.g., Black, 1976). The locations of the sites are presented in map form in Figure 2-2, and the UTM NAD83 coordinates associated with each site are listed in Appendix 1.1. These data supplement the results of an earlier AMT study conducted by the USGS in the Cornudas Mountains of New Mexico (Klein and Rodriguez, 1997); the USGS data were collected at eight sites in and around the Cornudas Mountains to map the subsurface extent of the intrusions in that area as part of a mineral resource assessment.

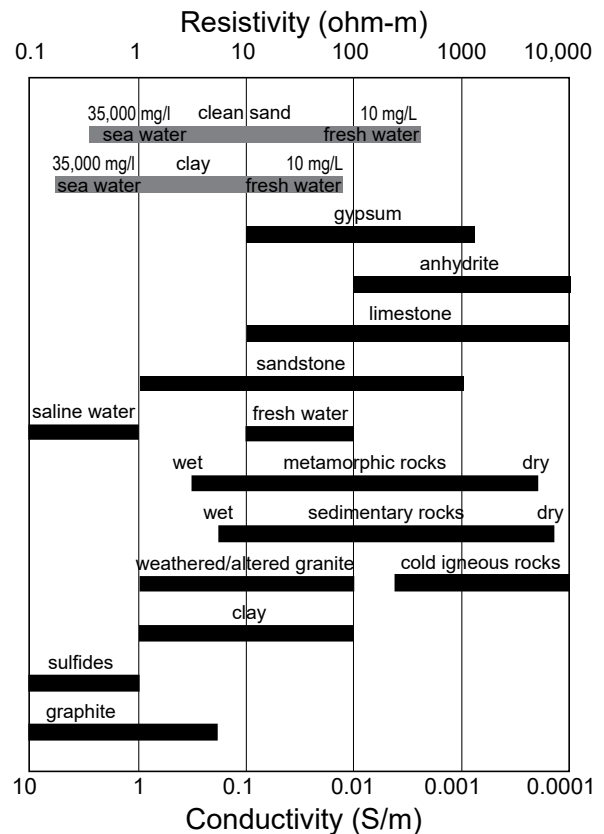


Figure 2-1. Black bars illustrate the range of electrical conductivities (or resistivities) of common subsurface materials (after Lowrie, 2007; Guinea et al., 2012; Peacock et al., 2015; Caselle et al., 2019). Wet and dry refer to pores or fractures that are filled with water or air. The gray bars represent end-member formation resistivity conditions for fresh (10 mg/L) and seawater (35,000 mg/L) in clean sand or clay using a cementation factor of 2 and porosity of 0.3 in Archie's Law for sand and a clay resistivity of 10 ohm-m for the Glover correction.

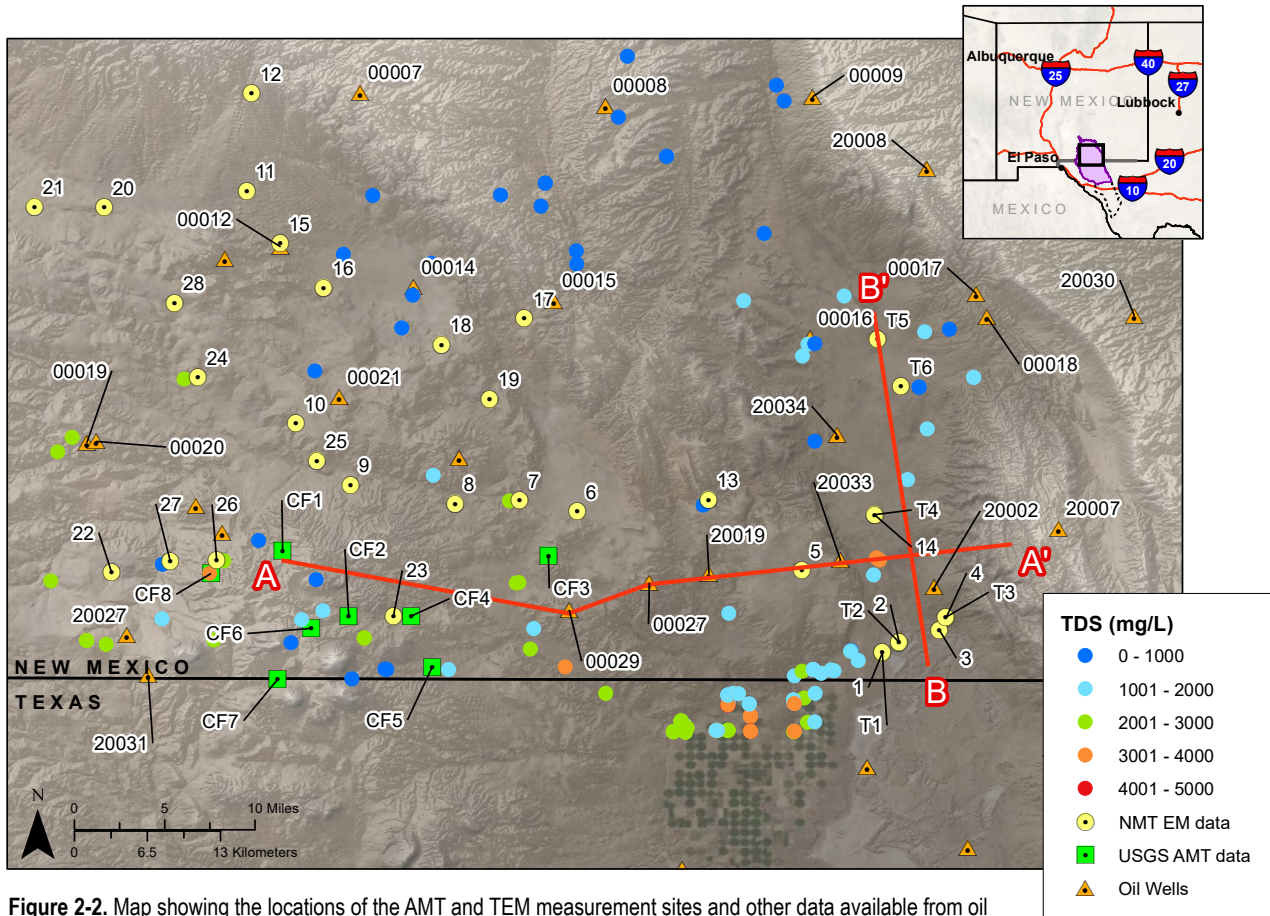


Figure 2-2. Map showing the locations of the AMT and TEM measurement sites and other data available from oil wells. The letter T is used to designate the TEM stations in Crow Flats. Oil wells are labeled using the last five digits of the API number. EM = electromagnetic; TDS = total dissolved solids in mg/L. Cross-section lines for Figure 1-2 (A-A') and Figure 2-9 (B-B') are marked.

Several of the stations were located in the general vicinity of water and oil wells to provide ground truth for the interpretation of the geophysical data. We analyzed driller’s logs, resistivity logs, and some well cuttings from oil wells in the study area to account for the electromagnetic response of clay- and anhydrite-rich rock units such as the Abo and Yeso formations. Only three resistivity logs are available for the study area: one from the eastern margin and two from the central part of the area of investigation. Cuttings from petroleum wells are available at the NMBGMR in Socorro, New Mexico, and well logs are available both at the NMBGMR petroleum records library and on the Oil Conservation Division web page (<https://ocdimage.emnrd.nm.gov/imaging/WellFileCriteria.aspx>).

GEOPHYSICAL METHODS

AMT survey

AMT theory is based on Maxwell’s equations of electromagnetism (EM; Simpson and Bahr, 2005; Chave and Jones, 2012). The AMT technique utilizes naturally occurring electromagnetic waves generated by lightning (high frequency) and by the interaction of solar winds with the Earth’s magnetosphere (low frequency; Simpson and Bahr, 2005). These natural magnetic field variations induce eddy currents in the Earth’s crust that can be measured at the surface to better understand subsurface electrical resistivity. Low frequency (long period) signals penetrate deeper than high frequency (short period) waves. Therefore, measuring signals over a large frequency range can

provide resistivity information to depths from a few tens of meters to more than 1 km. The AMT field setup uses induction coils to measure the Earth's magnetic field as a function of time, and an array of electrodes captures subsurface electrical responses to magnetic field variations. Because the electric (E) and magnetic (H) fields are measured in orthogonal directions, the data have four components that are generally presented in the form of the impedance tensor, Z (Chave and Jones, 2012), which has both real and imaginary terms. The real component is used to calculate apparent resistivity, and the imaginary terms are used to derive the phase. These data are measured in the time domain but are converted to the frequency domain using Fourier transform methods. Apparent resistivity and the phase are plotted as a function of frequency and are modeled together to estimate the subsurface resistivity structure using inversion methods.

In our study, we collected AMT data at 28 stations using a Zonge GDP32-24 data logger and Zonge ANT-6 induction coils that work in the frequency range of 0.1 to 10,240 Hz to measure horizontal magnetic fields. The induction coils were buried in shallow (about 0.3 to 0.4 m) trenches that were oriented along north-south and east-west lines (Figure 2-3). Electric fields were measured using an L-shaped electrode array with 40-m dipoles and three silver-silver chloride SRE-011-SPB electrodes buried in small holes with bentonite and salty water (Figure 2-3). The site was surveyed and staked to ensure the precise north-south and east-west orientations of the wires. The electrical array and induction coils were oriented north-south and

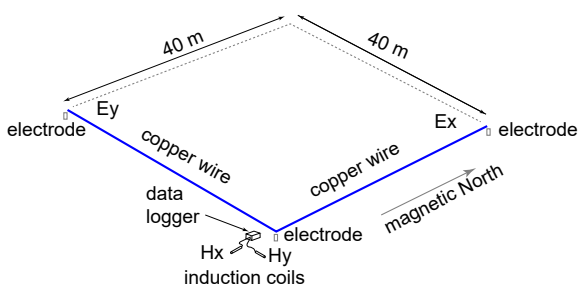


Figure 2-3. Field configuration for AMT data collection.

east-west using magnetic north. Data were collected using a variable sample-rate time schedule of 192 to 8192 Hz for 2 minutes, 3 to 256 Hz for 10 minutes, and .0938 to 8 Hz for 20 minutes, which allowed for sampling of the AMT response across a wide frequency range to attain resistivity information at a series of depths.

The data were analyzed in the field, first applying a Fourier transform to the data and then evaluating the resulting spectra and calculated apparent resistivity curves and phases using Zonge software (MacInness, 2010a, 2010b, 2014). If the curves were complete and relatively free of noise, the equipment was moved to a new station. Two sites, SB14 and 16, yielded noisy data during the initial run. The equipment was checked and additional water was placed on the electrodes. The second experiment at each of these sites gave results similar to the initial run. Consequently, only the most robust data in the middle of each of the apparent resistivity curves was used for these sites. The noise was likely anthropogenic.

Once back in the office, the quality of the data was improved by removing low-coherence data and obvious human-made noise. EM-community-standard .EDI files were created using Zonge software, which were then imported into the computer program WinGLink to make static shift corrections. Static shift is caused by distortion arising from near-surface conditions that can sometimes affect the signal measured by the electrodes, which causes a shift of the apparent resistivity curves to higher or lower values (Figure 2-4; Pellerin and Hohmann, 1990; Chave and Jones, 2012). TEM, which is described in more detail in the next section, can be used to correct for static shift since this method does not rely on electrodes to estimate resistivity structure (Pellerin and Hohmann, 1990). Many of the stations overlie limestone with a thin alluvial cover. We found that the TEM signal dissipated rapidly with depth in the limestone, so this method indicated that the subsurface was resistive (>100 ohm-m). In every situation where a static shift was observed in the AMT data, the low conductivity values associated with lower resistivity curve (e.g., the 30 to 60 ohm-m values on the blue Z_{xy} curve in Figure 2-4) were inconsistent with the rapid dissipation of the signal observed using TEM. Thus, we shifted the lower curve up to match the upper curve at shallow depths

(high frequencies). WinGLink was also used to create one-dimensional (1-D) resistivity models and cross-sectional diagrams based on the 1-D models.

MTPy (Krieger and Peacock, 2014) was used to calculate phase tensors in order to assess the dimensionality of the resistivity structure in the subsurface. Phase tensors are described in detail in Caldwell et al. (2004) and Bibby et al. (2005). The shallow subsurface of the study area is layered, but the deeper structure is complex because of Ancestral Rocky Mountain faulting (Black, 1976). Plots of phase tensors and ellipticity are commonly used to evaluate and visualize this dimensionality (Figure 2-4; Appendix 1.2; Caldwell et al., 2004; Bibby et al., 2005; Booker, 2014). Phase tensors are

plotted graphically as circles or ellipses by comparing principal axes of the tensor. Circles represent 1-D structure, slightly skewed ellipses represent 2-D structure, and strongly elliptical shapes represent 3-D structure. In addition to providing insight into the complexity of the subsurface, dimensionality helps determine the appropriate inverse modeling scheme.

In this study, we only consider 1-D models, making note of stations that indicate 2-D and 3-D subsurface structure and removing higher dimensional data from the curves so that all the cross-sectional models are based only on 1-D data. 3-D modeling was not included in the scope of work, given the reconnaissance nature of this study and the large distance between stations (5 to 20 km).

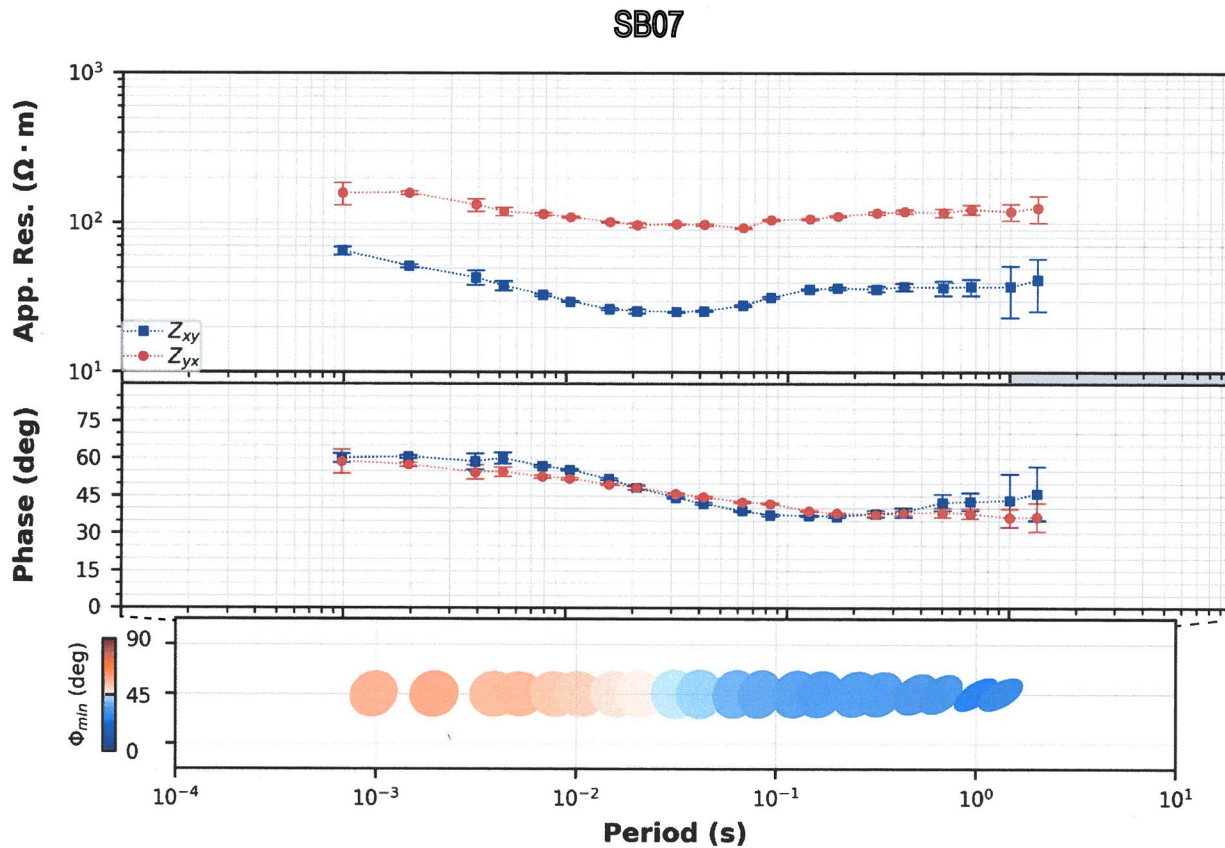


Figure 2-4. An example of static shift in the apparent resistivity curves. In this case, the blue xy mode was shifted up to match the red yx mode. The x-axis for the upper panel is depicted at the bottom of the lower panel but is expanded, as illustrated by the dashed lines. The bottom panel provides information about the dimensionality of the subsurface resistivity structure in terms of phase tensors (colors indicate skew angle). Non-skewed circles indicate 1-D stratified layers, whereas skewed ellipses represent more complex 2-D or 3-D resistivity structures.

TEM survey

The TEM method is a time-domain, surface-based geophysical technique that measures the electrical resistivity of the subsurface using an applied current. A transmitter box attached to a power source sends a current into a loop of copper wire that is laid on the ground surface. Investigation depth is a function of the effective loop area and input signal magnitude. The current is rapidly shut off and on, which induces a set of downwardly diffusing eddy currents into the subsurface. These currents produce small secondary magnetic fields of opposite polarity in a vertically leveled magnetic induction coil placed in the center of the transmitter loop. Decaying magnetic fields recorded at early times contain information about the shallow subsurface, while decaying magnetic fields at later times are associated with subsurface characteristics at greater depths. The secondary magnetic field is dissipated more rapidly by resistive layers and is sustained for longer time periods by conductors. Consequently, slope changes on plots of the secondary magnetic field strength as a function of time indicate layering in the resistivity of the earth. Thus, the method can determine distinct resistivity values at different depths for a given sounding. In practice, this measurement is done rapidly and repeatedly via a transmitted square wave. The frequency of the square wave is adjusted to find the optimal recording characteristics for a given setting. The transmission and removal of current through the copper loop is cycled many times (typically 1,024 cycles), and the responses from the earth are stacked (usually 10 times) to yield an average TEM decay curve.

We used a 100-m-by-100-m square loop at six AMT stations that had large static shifts (SB5, 7, 15, 17, 19, 27) and at six additional localities along a north-south line in Crow Flats along the eastern edge of the study area. A 10.5-ampere current was pulsed through this loop using a Zonge ZT-30 transmitter and two 24-volt batteries. Vertical magnetic fields were measured near the center of the loop using a Zonge TEM/3 induction coil. Data were recorded and viewed in the field using a Zonge GDP32-24 multi-channel receiver. Data were collected using frequencies of 8 to 64 Hz (most at 8 Hz), 32 to 2048 cycles (depending on the frequency used), and 10 data stacks. The TEM configuration available for this work can typically image resistivity below

100 ohm-m, with rapid current dissipation of the fields beyond this threshold.

The TEM data were processed using the Zonge TEMAVGW software package (MacInnes, 2010b). The data were then modeled to estimate resistivity as a function of depth using the Zonge STEMINV smooth-model inversion package (MacInnes and Raymond, 2009). Optimal solutions are acquired when using smoothing factors ranging from 1 to 6 and a maximum number of allowable iterations of 32; most models converge in fewer than ten iterations. During this study, we modified this technique, first running the model using a smoothing factor of 1, then using this model as the starting point for a model with a smoothing factor of 3. This approach yielded optimal inversion solutions that balanced model roughness and data fitting. This inversion method is 1-D, which is required for TEM applications. AMT dimensionality in the shallow subsurface was confirmed to be 1-D, thereby indicating the 1-D assumption implicit in using TEM is applicable to the shallow subsurface of the study area. The 1-D inversion results for stations along the Crow Flats transect were contoured by hand to create a 2-D cross section of the subsurface.

GEOPHYSICS RESULTS

AMT results: Dimensionality

2-D and 3-D structures impacted the AMT data collected at several sites. Appendix 1.2 shows the dimensionality of the data for each station calculated from phase tensors using MTpy after low-coherence data and anthropogenic noise were removed from the data. Another line of evidence for 2-D and 3-D structure in the subsurface is the slight separation of the apparent resistivity curves at depth after making static shift corrections (Appendix 1.2). All 3-D points were removed prior to inversion. Some slightly 2-D points were retained in this preliminary evaluation of the data.

AMT results: Geologic context

The first step in assigning geological meaning to the interpretation of the AMT data is to compare the rock units identified on geophysical well logs (Figure 2-5) and listed on oil well completion records to the 1-D inversion results from AMT sites located

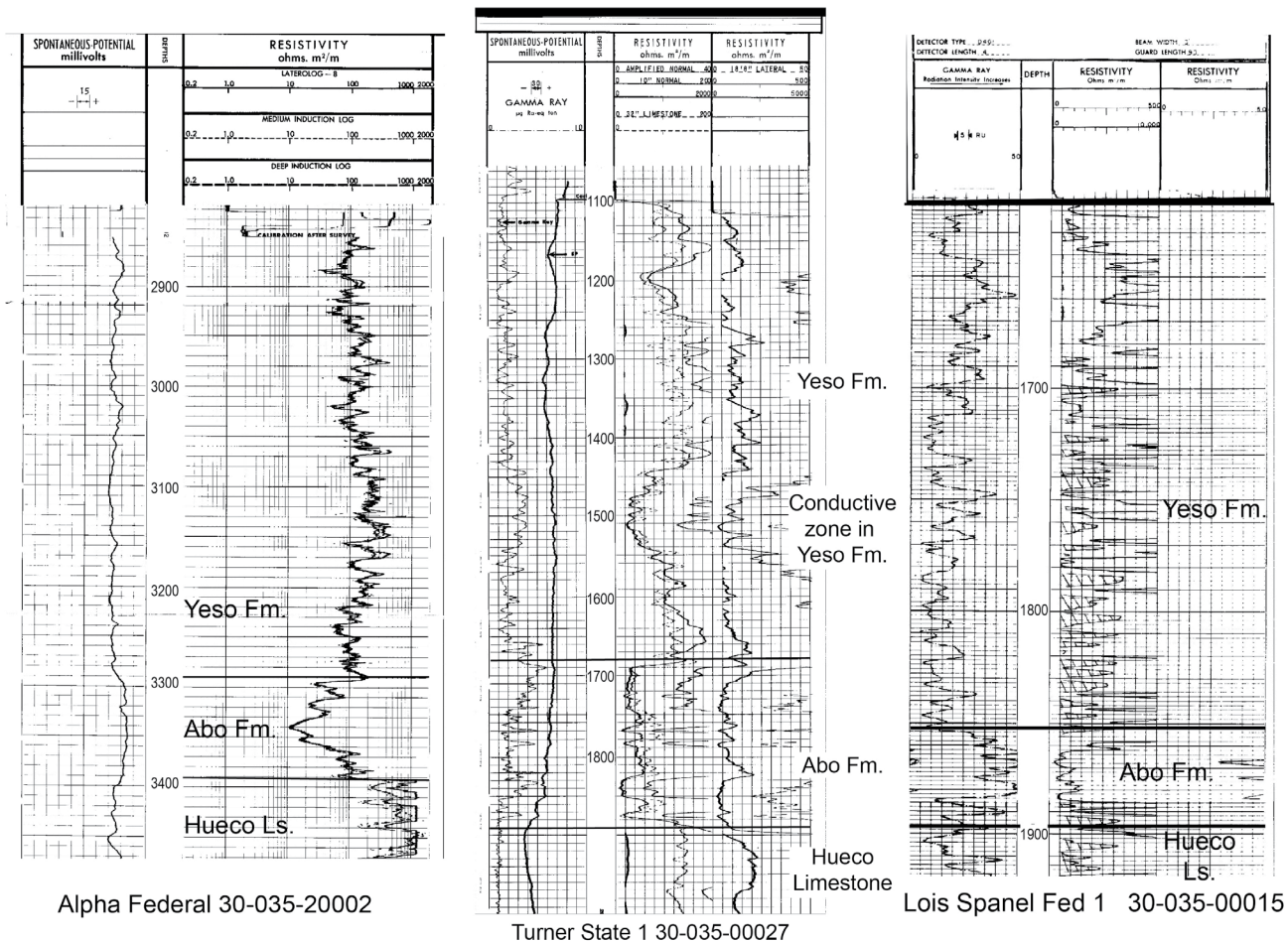


Figure 2-5. A portion of the resistivity curves from oil wells in the eastern and central parts of the study area illustrating the resistive nature of the Yeso Formation and Hueco Limestone and the more conductive nature of the mud-rich Abo Formation.

near the oil wells (Figure 2-2). Cuttings of Paleozoic sedimentary rocks from three wells were examined to tie the geology to the resistivity logs and the AMT data. In addition, to establish information about the resistivity structure of the deep subsurface, cuttings from the Proterozoic basement were also examined.

The Permian rock units in the shallow subsurface of the Salt Basin are, from youngest to oldest: San Andres Limestone, Hondo (or Glorieta) Sandstone, Yeso Formation, and Abo Formation/Hueco Limestone. Both the San Andres Limestone and the Hondo Sandstone are thin, resistive units that typically do not show up on well logs or in well reports, but these units can be identified in well cuttings.

Yeso Formation

The Yeso Formation has a relatively uniform thickness across the region (365 m to the west, 426 m to the east). A silty sandstone interval, locally called the Drinkard Member, divides the Yeso Formation into upper and lower units (Donegan, 1961). The upper Yeso Formation is primarily composed of dolomite and sandstone near the top and anhydrite near the base. The lower Yeso Formation is sandstone with thin dolomite and anhydrite beds toward the top and massive anhydrite beds toward the bottom.

Two recent laboratory and field studies have focused on measuring the electrical properties of gypsum and anhydrite in hopes of using EM methods to locate evaporite mineral resources (Guinea et al.,

2012; Caselle et al., 2019). The measured electrical resistivity of gypsum in these field-based studies spans several orders of magnitude (10 to 1,200 ohm-m), depending on the purity of the deposit. Caselle et al. (2019) found that gypsum-saturated water in the laboratory has a conductivity of 2.15 mS/cm (4.65 ohm-m) and that saturated gypsum that is 80% pure at a field site in Italy has a measured resistivity of 150 ohm-m. Anhydrite has higher resistivity values, up to 10,000 ohm-m for a pure deposit (Guinea et al., 2012). The tidal-flat, shelf-margin depositional environment of the Yeso Formation suggests that the Yeso anhydrite is likely not pure; examination of well cuttings discussed below verifies this hypothesis.

The resistivity logs in Figure 2-5 and Appendix 1.4 indicate that the Yeso Formation has a variable resistivity response, depending on geographic location in the Salt Basin. The resistivity measured in the Yeso Formation in the Alpha Federal well (20002 on Figure 2-2) on the east side of the basin varies between 2 and 400 ohm-m²/m. Well cuttings and the driller's log for this drill hole were used to annotate the full resistivity log (see Appendix 1.4A). An interval of dolomite and limestone with gypsum and trace anhydrite at 1,250 to 1,560 ft (380 to 475 m) has a resistivity of 10 to 90 ohm-m²/m. The rock types in the Yeso Formation transition to a red siltstone at 1,608 ft (~490 m) with a resistivity of 2 to 10 ohm-m²/m (Appendix 1.4A). Below 1,750 ft (530 m), the dolomite, limestone, red siltstone, and calcite with trace anhydrite and black shale average about 100 ohm-m²/m. Unfortunately, we do not have any deep AMT data near this well for comparison.

The resistivity measurements in Turner State 1 (00027 on Figure 2-2, about 17 km northwest of Dell City) also have a range of values, in this case from 20 to more than 200 ohms-m²/m. Examination of the cuttings from this well reveals that the 20 to 40 ohm-m²/m conductive zone in this well at approximately 1,500 ft (460 m) corresponds with an interval containing abundant anhydrite that appears to be saturated, whereas the more resistive interval above with values of 120 to 200 ohm-m²/m (Figure 2-5, Appendix 1.4B) is dominated by dolomite with minor sandstone. XRD analysis verified the presence of anhydrite. The interval below the conductive zone with values of 100 to 180 ohm-m²/m is composed of alternating layers of dolomite, red siltstone, and anhydrite. In this particular well, the anhydrite

interval in the Yeso Formation appears to be quite conductive (Figure 2-5, Appendix 1.4B). We have no AMT data for comparison with the log measurements in this well because this area is on private land.

The wrap-around on the Lois Spanel Fed 1 (00015 on Figure 2-2) resistivity log (Figure 2-5) in the north-central part of the study area near AMT site 17 makes determination of the exact resistivity values on this log challenging, but the maximum values indicated by the hatched pattern on the log are on the order of 500 ohm-m²/m, and the lowest values are 50 ohm-m²/m. The entire resistivity log of Lois Spanel Fed 1 in Appendix 1.4C, which is annotated using cuttings and the driller's log, is regrettably of poor quality. The driller's log reports the presence of anhydrite in the Yeso Formation between 1,200 and 1,862 ft (365 to 567 m). Analysis of the cuttings reveals alternating dolomite, anhydrite, and siltstone beds (Appendix 1.4C), which is consistent with the alternating high and low resistivity spikes on the log (Figure 2-5). A drill-stem test reported on this resistivity log indicates fresh water at 2,600 to 2,680 ft (792 to 817 m) in the Fusselman Dolomite.

Abo Formation

The Abo Formation in the Salt Basin has a lower and an upper unit separated by Hueco Limestone (Donegan, 1961). The lower Abo, which is called the Powwow Conglomerate, is composed of an interval of red beds, conglomerate, and sandstone that is 0 to 60 m thick. The upper Abo is made up of red beds, sandstone, siltstone, and evaporite to the west that gradually becomes dominated by dolomite with red and green shale toward the south and east. The Hueco Limestone grades laterally into the Abo Formation toward the east and thins northward (Donegan, 1961). All three resistivity logs in Figure 2-5 show that the Abo Formation has lower resistivity values compared to the immediately overlying Yeso Formation and the immediately underlying Hueco Limestone.

Older units

The older Paleozoic rock units and Proterozoic basement rocks penetrated by the three wells with resistivity logs are generally resistive. Exceptions are the Powwow Conglomerate, the top of the Mississippian, the Percha Shale, and the Bliss Sandstone. Powwow Conglomerate is variably

resistive and conductive in the Lois Spanel Fed 1 well, as should be expected given the presence of resistive sandstone and conglomerate and conductive red beds. The unconformity at the top of the Mississippian that developed during Ancestral Rocky Mountain deformation is commonly associated with a conductive layer, probably related to residual clays that accumulated as the result of weathering. The Percha Shale is generally conductive. The Bliss Sandstone is relatively conductive compared to the carbonates of the El Paso Formation above and the Proterozoic basement (diabase) below because of the presence of glauconitic cement. The Hueco Limestone in both the Alpha Federal and Lois Spanel Fed 1 drill holes is variably resistive and conductive, particularly in the Lois Spanel Fed 1 well. Donegan (1961) notes that a basin facies in the Hueco may occur in southeastern Otero County, so the more conductive intervals in the Hueco might be shale. The low conductivity interval at the base of the Montoya Formation in the Turner State well is due to dissolution (vugs) and alteration (iron-stained fracture surfaces and trace pyrite).

The cross section in Figure 1-2 was modified from Black (1976) based in part on examination of the Proterozoic basement during this study. The Proterozoic basement in the Salt Basin includes three diverse terranes: (1) the Debaca Group, characterized by metasedimentary and metavolcanic rocks; (2) the Panhandle Igneous Complex (Southern Granite-Rhyolite Province) and the Franklin Mountains Rhyolite; and (3) the Plutonic Province (Denison and Hetherington, 1969; Barnes et al., 2002). In addition, the possible influence of these varied basement rocks on the interpretation of the AMT data was evaluated through the inspection of cuttings.

Previous work reported by Denison and Hetherington (1969) on ~650 m of basement rocks penetrated in Turner State (00027 on Figure 2-2) documents subhorizontal Proterozoic Debaca Group marbles intruded by diabase sills that sit on 1.35 to 1.40 Ga Southern Granite-Rhyolite Province quartz syenite and granite. Examination of cuttings as part of the current study from the McMillan Turner 1 borehole (00029 on Figure 2-2), which went through 112 m of Proterozoic basement, indicates the presence of altered rhyolite starting at a depth of 552 m. The top of a diabase (likely a sill associated with the Debaca Group) is at 572 m, and rhyolite porphyry

that resembles the Proterozoic Thunderbird Rhyolite in the Franklin Mountains is present between 628 m and total depth at 664 m. Cuttings from the Southland 28 borehole (20019 on Figure 2-2) were also included in the current investigation. These cuttings indicate that the well penetrated into the Cambrian Bliss Sandstone at 780 m, a red Proterozoic quartzite or rhyolite at 805 m, and marble between 826 m and total depth. The top of the Debaca Group is at the same elevation in both the Southland 28 and Turner State 1F boreholes, but top of this unit is about 450 m higher in the McMillan Turner 1, indicating the existence of a buried down-to-the-east Ancestral Rocky Mountain fault to the east of this well. All rock units encountered in these wells that penetrate the basement are resistive rock types. Small amounts of pyrite and chalcopyrite were observed in the marble in the Southland 28, which could enhance the conductivity of this unit.

Quaternary playas

Four of the AMT sites are located on Pleistocene to recent playa deposits at the south end of Crow Flats on the east side of the study area. Daniel B. Stephens and Associates (DBS&A; 2010b) determined the average composition of the playa deposits in nine auger holes in Texas, just south of the state line. These researchers found the deposits are 90% sulfate, 3% carbonate, 2% halides, and 5% quartz and other insoluble material. Boyd (1982) sampled fluids from 63 auger holes in the playa deposits in New Mexico and Texas and measured major element geochemistry on 44 of the samples. The brines in the shallow subsurface (<3 m) have TDS values of 35,000 to 300,000 mg/L, and the main constituents are Na⁺ and Cl⁻; the concentration varies widely over short lateral distances (Boyd, 1982). As a consequence of the high salinity of the fluids in the playa deposits, these deposits are very conductive.

AMT results: Water quality

The next step in interpreting the AMT data, this time in a hydrogeologic context, is to compare the results with water quality data. As discussed in more detail later in this report, TDS data were compiled from the literature, and new water quality data from 13 wells were collected as part of this study. A total of 161 TDS measurements lie within the boundaries of Figure 2-2; 102 have well-depth information, and the name of the formation screened is identified in 40 of

the wells (20 have repeat measurements). Note the general increase in TDS values toward the south, with lower values in the northern highlands and higher values around Dell City. Wells with TDS data near Dell City that are completed in the Bone Spring–Victorio Peak Aquifer are 46 to 518 m deep and have TDS values that range from 1,090 to 4,674 mg/L (fresh to slightly brackish). TDS concentrations in wells with repeat measurements in this area generally increase through time. Two 100-m wells completed in the Yeso Formation near oil well 00016 on the west side of Crow Flats ~5 km west of TEM station T5 have TDS concentrations of 820 to 1,170 mg/L. A third Yeso Formation well is located 9 km south of station SB05; this well is 101 m deep and has a TDS concentration of 1,200 mg/L. This TDS measurement

is consistent with the shallow resistive layer in the 1-D model for SB05 illustrated in Figure 2-6 (Appendix 1.3). Nine wells that draw water from alluvium in Crow Flats are only 24 to 101 m deep and have TDS concentrations of 400 to 2,170 mg/L.

Table 2-1 summarizes the TDS concentrations in water wells near AMT or TEM sites compared with the resistivity values derived from the 1-D model inversions of the AMT data (see next section) at the depth of the bottom of the well (presumably the screened interval). In general, the correlation between the TDS values from water wells and the calculated resistivity is weak, except for the regional sites, where the expected correlation is observed. The groundwater in the vicinity of the AMT/TEM sites

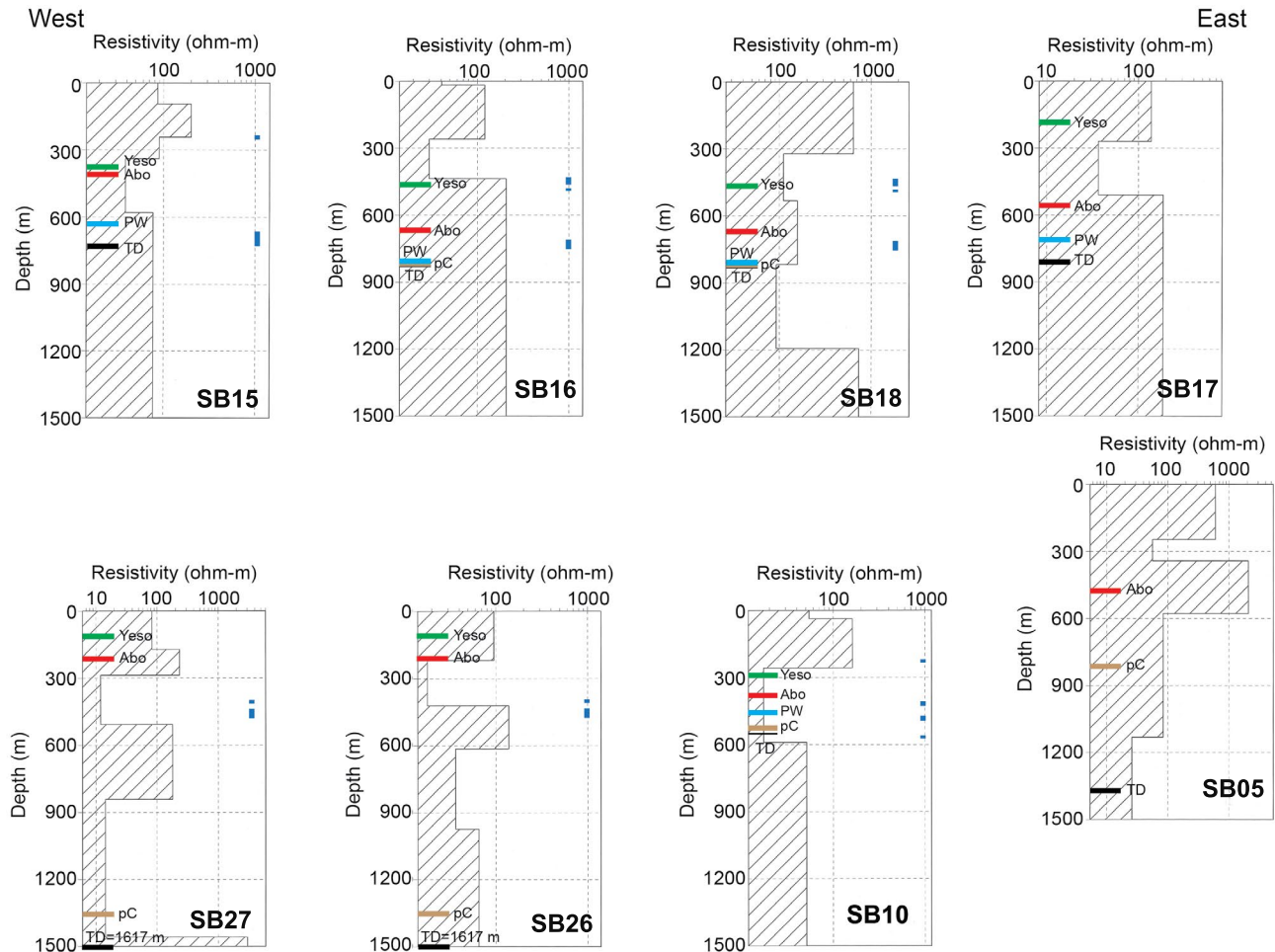


Figure 2-6. Resistivity based on 1-D models for stations within 10 km of oil wells drilled in the Salt Basin. The blue dots on the right side are water-bearing intervals recorded on the well completion forms. SB refers to the AMT station numbers on Figure 2-2. The four stations along the top of the figure (SB15-18) are in the northern part of the study area. The three stations along the bottom of the figure (SB10, 26, 27) are located in the southwestern part of the study area, and SB05 is in the eastern part of the study area. Yeso is the top of the Yeso Formation, which is usually a limestone; Abo is the top of the Abo Formation; PW is the Powwow Conglomerate, which marks the top of the section disturbed by Ancestral Rocky Mountains deformation; pC = top of the Proterozoic basement; and TD = total depth of the well.

Table 2-1. Comparison of TDS values in water wells near AMT/TEM stations and calculated resistivity from 1-D models

AMT station	Distance from water well (km)	Well depth (m)	TDS (mg/L)	1-D resistivity at well depth (ohm-m)
Regional Salt Basin sites				
7	0.7	198 (Bone Spring)	2710	190
13	0.7	146	785	1700
24	1.1	171	2743	150
Cornudas				
CF2	1.9	91	1767	>1000
CF2	2.3	94	2530	>1000
CF5	1.2	213	1915	1000
CF6	1	106	1257	1000
CR8/SB26	1.4/0.5	117	2740	97
SB27	0.6	61	853	82
Crow Flats				
14	4	27	1210	2
14	4	42	3300	2
T6	1.4	34	692–733	20

is fresh to slightly brackish (<3,000 mg/L), except for one well near site 14 in Crow Flats that is mildly brackish. No water wells are present within the very conductive playa deposits. Interestingly, large irrigation wells drilled in the alluvial deposits on the elevated ground about 1.6 to 1.8 km to the west of SB01, which is on the playa and has both TEM and AMT data indicating very conductive material at depth (Figure 2-6), are producing water capable of growing crops. One well 2 km west of SB01 produces water with a TDS of 1,272 mg/L, and another 2.5 km to the west that is 30 m deep has water with TDS values ranging from 981 to 1,120 mg/L.

AMT results: One-dimensional inversions

The formation tops listed in well completion records are plotted on the 1-D AMT inversion results in Figure 2-6. Note that the top of a low-resistivity interval is commonly detected by the AMT data at a depth of ~300 m below ground surface across the study area. Station SB15 is very close to the Hurley 1 well (00012 on Figure 2-2), and the low-conductivity interval coincides closely with the upper red beds of the Abo Formation. Similarly, the conductive interval in SB26 and SB27 closely aligns with the top of the Abo Formation in the nearby McMillan 1A (00028 on Figure 2-2). The correlation of the conductive interval with the Abo Formation is

generally not as good as the distance between the sounding sites and the oil wells increases (Figure 2-6 and Table 2-2) because of facies changes, structural complexity in the subsurface, and the possible presence of high-TDS fluids.

Cross sections created in WinGLink that include all the AMT data are presented in Figure 2-7. Two of the profiles, E-W3 and E-W4, overlap and cross the Ancestral Rocky Mountain highland beneath stations 6, 7, and 8. The rocks in the subsurface are resistive carbonates, sandstones, and basement rocks (Figure 1-2). The highland extends northward across E-W2 beneath SB24, 25, 10, 18, 19, and 17, and the high may continue even farther north to SB20 and SB15 on E-W1. On the north-south profile, SB11 and SB09 mark the northern and southern extent of the resistive rocks. Station 23 in the Cornudas Mountains will be discussed in the next section. Stations SB 21, 22, 26, and 27 on the west end of the east-west profiles 1 and 4 are generally more conductive and the Yeso Formation is at the surface, in contrast to areas to the east where San Andres Limestone is at the surface. Many of the stations across the Salt Basin have conductive zones at depths of 300 to 600 m in the subsurface that in places appear to correlate to the Abo Formation but elsewhere may correspond to discontinuous saline aquifers within the Yeso Formation.

Table 2-2. Comparison of rock unit depths in oil wells to conductive layers in AMT data (NA = data not available)

Region	API	Well Name	AMT station	Distance AMT site from well (km)	Yeso top (m)	Abo top (m)	Powwow base (m)	Basement top (m)	Well TD (m)	Top AMT conductive interval (m)	Base AMT conductive interval (m)	Resistivity (ohm-m)	Water-bearing intervals (m)
North-central	30-035-20012	Hurley 1	15	0.1	380	418	641 on Miss.	NA	741	340	520	39	244-250; 670-741
	30-035-00014	Liberian State	16	6.8	465	663	819 on gabbro	819	823	260	440	30	441-454 (fresh); 475-478 (fresh); 719-755 (sulfur)
	30-035-00015	Lois Spanel Fed 1	17	2.8	Py 177	564	712 on Miss.	NA	817	270	510	37	DST 792-817 (fresh)
	30-035-00014	Liberian State	18	5.5	465	663	819 on gabbro	819	823	320	532	110	441-454 (fresh); 475-478 (fresh); 719-755 (sulfur)
Southwest	30-035-20018	George J Ablah 1	26	2.4	NA	NA	NA	1362	1617	217; 612	412; 972	17; 36	442-472; now a water well
	30-035-00028	McMillan A1	26	5	116	211	NA	NA	1589	217; 612	412; 972	17; 36	396; 1567-1570; 1579-1582
	30-035-00028	McMillan A1	27	5.2	116	211	NA	NA	1589	286; 841	506; 1456	12; 14	396; 1567-1570; 1579-1582
	30-035-00021	Ann Spanel	10	4	291	376	475	556	571	257	589	17	219-222; 421-442; 492-512; 553-556
East	30-035-20033	Mescalero 28 Fed 1	5	3	NA	469	NA	831	1409	247	342	56	NA

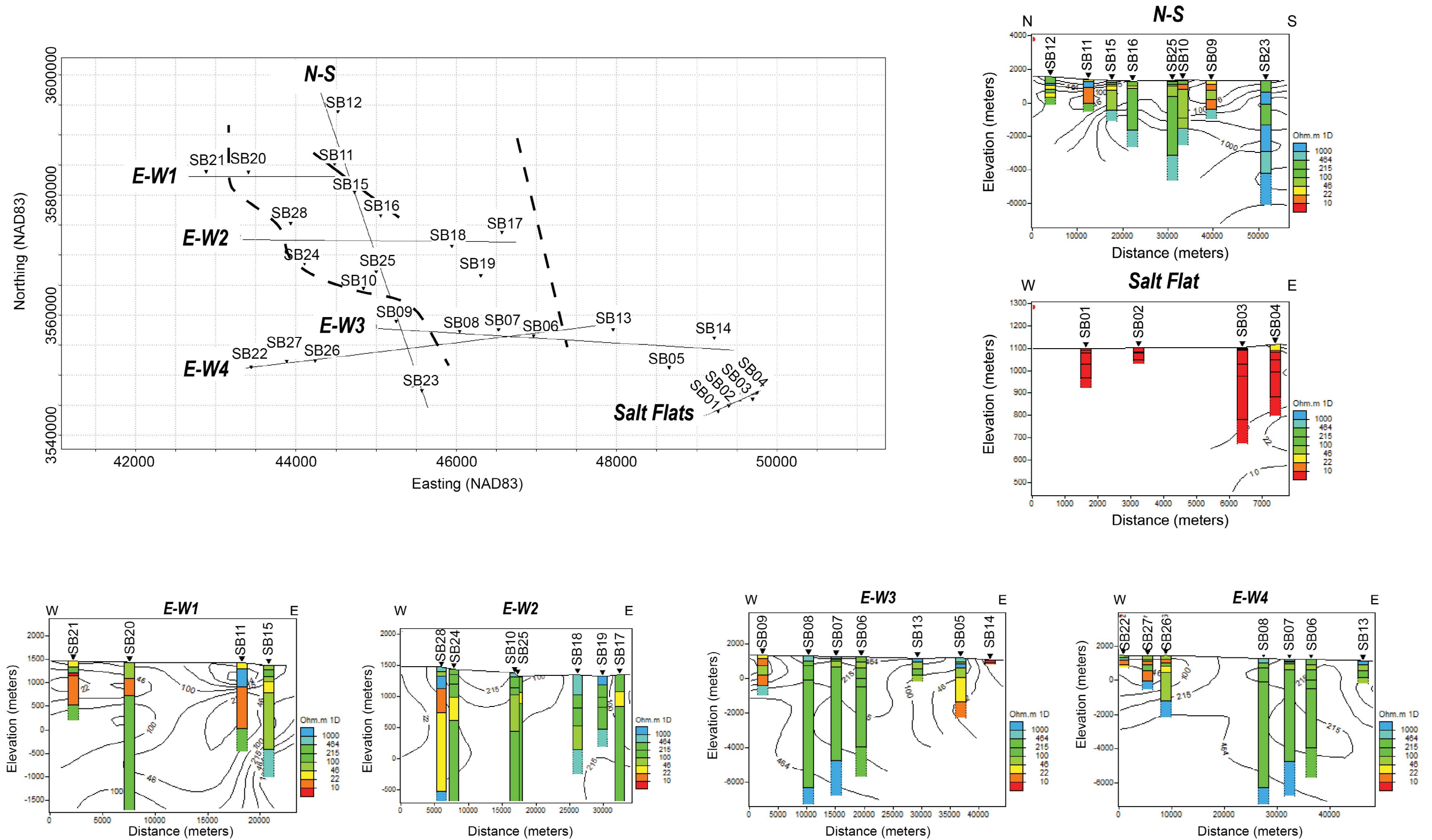


Figure 2-7. Cross sections showing 1-D models calculated using WinGLink. The very deep soundings below stations SB06, SB07, and SB08 on the E-W3 and E-W4 profiles correspond to a Proterozoic-cored highland associated with Ancestral Rocky Mountain deformation. Dashed lines on the location map mark the western, eastern, and northern soundings on the highland based on the AMT response.

The AMT data from stations SB1, 2, and 3 collected on the playa deposits at the south end of Crow Flats indicate conductive materials in the subsurface, consistent with the observations of Boyd (1982) mentioned earlier in this report, and do not reveal the depth to bedrock below the playas. Station SB4 is on an alluvial fan on the east side of the playa. A shallow, slightly resistive layer that correlates with the gravel deposits observed at the surface is underlain by conductive material that likely corresponds to older playa deposits. AMT data from Station SB5 on the east end of the E-W3 profile shows that the resistive San Andres Limestone exposed at the surface continues in the subsurface, where it is underlain by resistive Yeso Formation to depths of 1,000 m. The resistive material is underlain by a conductor, which might be saline water derived from Crow Flats 4.5 km to the east.

AMT results: Comparison to USGS data

To expand the coverage of AMT data in the Salt Basin, the data from this study are compared to previously published AMT data collected by Klein and Rodriguez (1997) in the vicinity of the Cornudas Mountains in Figure 2-8. Cenozoic syenitic intrusions enriched in rare earth elements that have pushed upward through Permian and Cretaceous units are exposed in the Cornudas Mountains; because the intrusions are unaltered and resistive, Klein and Rodriguez (1997) experimented with using the AMT method to identify mineral exploration targets associated with the intrusions in the subsurface. With the exception of CF5 and CF3 (see Figure 2-2 for location of CF3), these authors found conductive material at depths of less than 20 m that they attribute to weathered rock and soil (not shown on Figure 2-8 because this layer is too thin), a 100- to 400-m-thick resistive zone associated with carbonates and anhydrite, and another conductive zone they attribute to shale or mud (i.e., the Abo Formation in McMillan 1A). The change in thickness of the resistive layer toward the east between CF8 and CF1 (Figure 2-8) was interpreted to be due to flexure or intrusion. The presence of a fourth resistive layer below the conductive layer at depth was recorded in the AMT data for CF5 and CF3, suggesting a change in structure east of the Cornudas Mountains (Klein and Rodriguez, 1997).

The depth of investigation, which is controlled by the frequency range of the AMT induction coils and data logging configuration used during data collection, is 20 to 400 m in the USGS study, as compared to 2,500 to 4,000 m in this study. The USGS data were acquired across a range of frequencies between 4.5 and 27,000 Hz, whereas the NMT data were collected over a frequency range of about 0.1 to 8192 Hz. This difference led to higher-resolution shallow data in the USGS study but a greater depth of investigation in the NMT study.

The stations in the current study along the northern transect in Figure 2-8 are in Yeso Formation, and the 1-D models show generally resistive material in the shallow subsurface and more conductive material at depth; the conductive layer interpreted by the USGS researchers to be a shale could be the Abo Formation. In contrast, measurements at station SB26 indicate quite resistive rocks at depth and may indicate the presence of an intrusion. The USGS 1-D models from the southern profile again have a pattern of generally resistive values in the shallow subsurface and more conductive values at depth. Measurements at SB23 in this study indicate a resistive feature that extends to great depth and is likely an intrusion.

TEM results

TEM data were collected at six sites along a north-south profile between the mouth of Dog Canyon on the north, through Crow Flats, to the playa to the south in an effort to map the alluvial fan and playa deposits along the east side of the study area. In addition, we collected TEM data from six sites throughout the study area to determine AMT static shift corrections.

North-south profile

Two playa-deposit stations on the southern end of the transect, along the east side of the study area in Crow Flats (T1, T2), were evaluated northeast of Dell City (Figures 2-2 and 2-9). The apparent resistivity below these two sites is low (1 to 2 ohm-m), and the conductive layer associated with the playa sediments appears to persist to depths of up to 200 m. Station T3 is located on an alluvial fan on the east side of the playa. The upper 20 m are slightly resistive, consistent with the gravel deposit observed at the surface, but

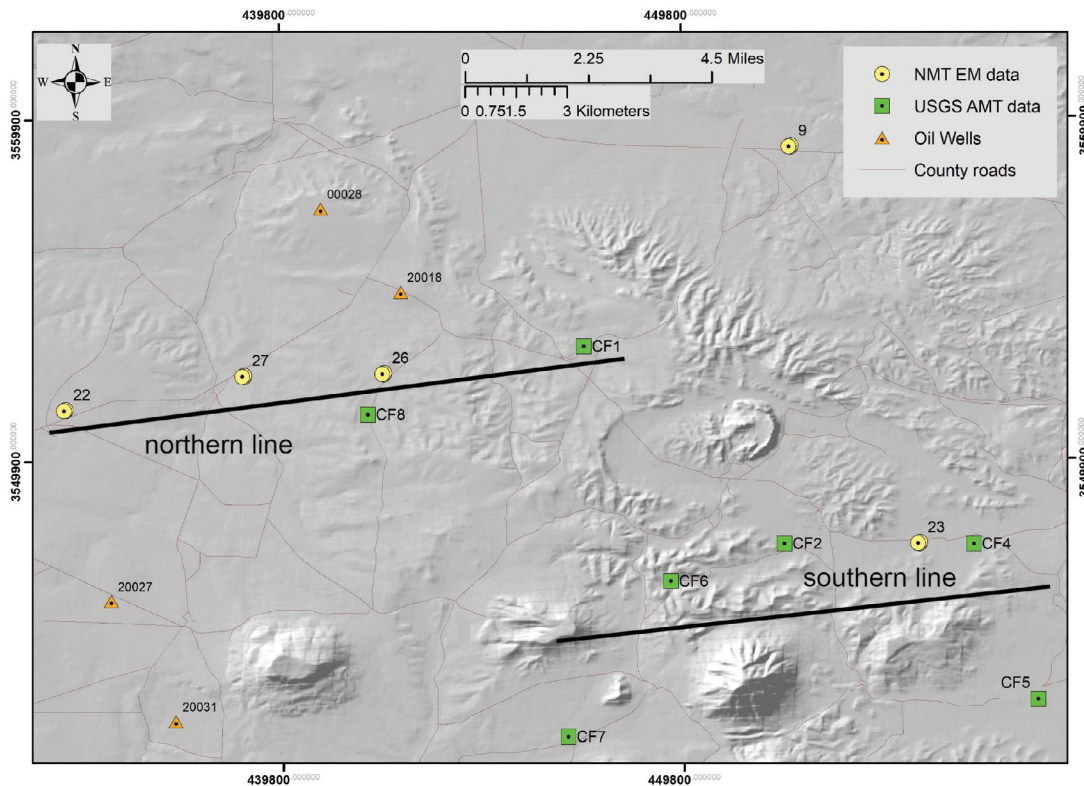
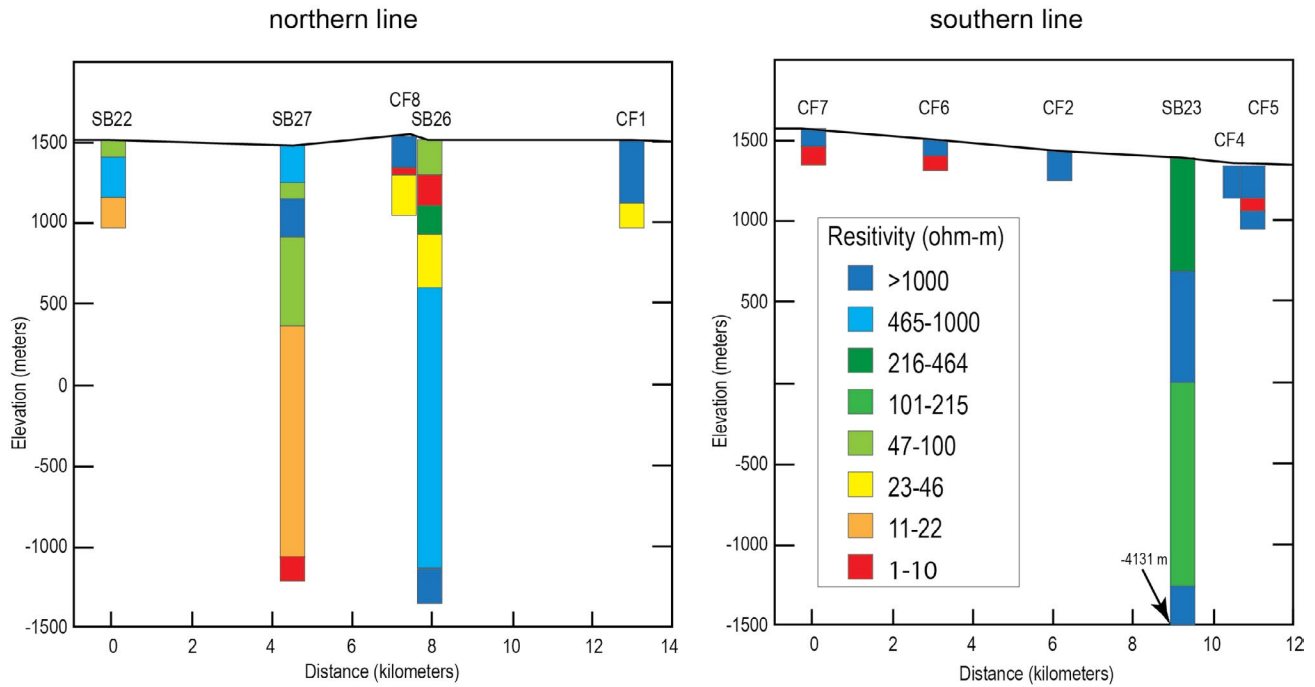


Figure 2-8. Comparison of the USGS AMT data (CF, green squares) collected in the Cornudas Mountain area with data collected during this NMT study (SB, yellow circles).

overall the underlying material is conductive. Station T4 is located farther north on Crow Flats (Figures 2-2 and 2-9) and is also underlain by conductive alluvium, which at the surface contains more sand compared to areas to the south. TEM stations T1–T3 coincide with AMT stations SB01, SB02, and SB04, and TEM station T4 is located at the site of AMT station SB14. Both methods yielded similar results, even though the AMT data for SB14 in northern Crow Flats contained considerable anthropogenic noise.

Station T6 near the north end of the profile is on the Dog Canyon alluvial fan, which is sourced in the Guadalupe Mountains. The fan appears to be relatively conductive (10 to 20 ohm-m) and is approximately 100 to 150 m thick. More resistive bedrock (350 to 400 ohm-m) lies below the fan (Figure 2-9).

Station T5 at the north end of the profile is in an area with karstic subsidence cracks clearly visible at the surface. Like Station T6, conductive alluvium is present to depths of about 100 m, but the underlying material is 50 to 100 ohm-m (Figure 2-8), which could be indicative of collapsed bedrock filled with air or water in the subsurface.

TEM data collected at AMT sites

TEM data from six of the AMT sites were collected in areas underlain by limestone bedrock with a thin alluvial cover. At five of the six sites, the presence of resistive San Andres Limestone in the shallow subsurface caused the TEM signal to dissipate rapidly with depth, so the signal penetrated less than 100 m. The exception is the data collected at SB27, which has Yeso Formation in the shallow subsurface, allowing the signal to penetrate to depths of about 400 m (Figure 2-10). In this case, both the AMT and TEM data show a resistive unit above a conductive unit, and in both 1-D models, the depth to the top of the conductive layer is similar (~200 m). However, TEM data collected above the San Andres Limestone generally do not correlate at all with the AMT data. The Zonge TEM system in general is insensitive to subsurface structure at depths of less than 50 m. In the case of the Salt Basin, the AMT method is the better tool to use in the limestone terrains.

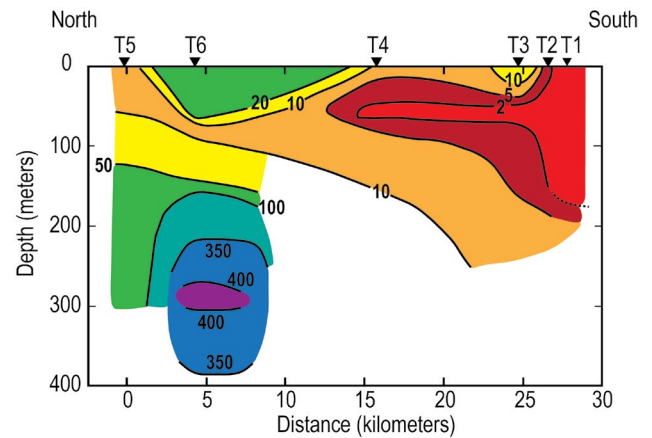


Figure 2-9. Resistivity contours in ohm-m from TEM stations on the east side of the study area between Dog Canyon on the north and the Salt Flats on the south. The TEM stations are denoted by the inverted triangles along the top of the cross section. The cross section is located on Figure 2-2 (B-B').

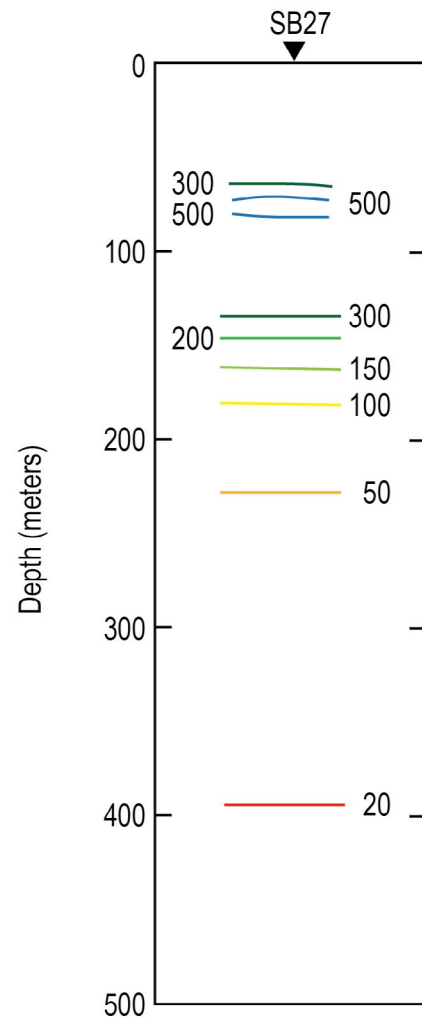


Figure 2-10. Resistivity contours from a TEM station coincident with AMT station SB27. The location of SB27 is shown in Figure 2-2 and Figure 2-8.

GEOPHYSICS DISCUSSION

Analysis of resistivity logs and associated well cuttings from three wells drilled in the eastern half of the study area provides valuable insight needed to discern whether the conductive intervals at depths of 300 to 600 m in the subsurface detected in the AMT surveys are related to rock properties or to the occurrence of high-TDS fluids. Another important line of inquiry is exploring the connection between water quality in both water and oil wells and the AMT data. A few oil wells have been converted to water wells upon abandonment, and the presence of water-bearing units noted on driller's logs has been incorporated into the interpretation of the AMT data.

Many of the Late to Early Paleozoic rocks in the subsurface of the Salt Basin are generally resistive. These rock units are dominantly composed of carbonates (dolomite and limestone) and include, from youngest to oldest, San Andres Limestone, carbonates within the Yeso Formation and Hueco Limestone, Mississippian limestone below the weathered zone related to the Ancestral Rocky Mountain unconformity, Silurian Fusselman Dolomite, and the Ordovician Montoya and El Paso formations. Sandstone and conglomerate in the Powwow Conglomerate are also resistive. The resistivity of the Bliss Sandstone is intermediate at 40 to 100 ohm-m/m² due to glauconitic cement. The metasedimentary rocks and mafic intrusions in the Proterozoic Debaca Formation and the Proterozoic granite and syenite are generally resistive, except where altered or mineralized.

The most consistently conductive unit in the Salt Basin is the mud-rich upper part of the Abo Formation, which is 5 to 60 m thick in the wells with resistivity logs. Resistivity values obtained from geophysical logs are as low as 10 ohm-m/m² in Alpha Federal, 20 to 40 ohm-m/m² in Turner State, and 40 to 50 ohm-m/m² in Lois Spanel Fed 1. Red beds within the Powwow Conglomerate are also conductive, as is the Percha Shale. Interestingly, a red siltstone in the Yeso Formation in the Alpha Federal well is quite conductive (2 to 10 ohm-m/m²).

The Yeso gypsum- and anhydrite-bearing intervals have a wide range of resistivity values, and the overall volume of these evaporites within the Yeso section varies with geographic position in the basin. The amount of anhydrite is highest in the Lois

Spanel Fed 1 in the north-central part of the basin. The resistivity of the anhydrite intervals in the Lois Spanel Fed 1 well is hard to quantify because of the poor quality of the geophysical log, but the lowest resistivity values in the complexly intercalated section of dolomite and anhydrite appear to be about 50 ohm-m/m². Anhydrite is common throughout the examined interval (375 to 560 m). In contrast, the easternmost well, Alpha Federal, has only trace amounts of anhydrite and an interval of gypsum that occurs at depths of 400 to 475 m. The resistivity of the gypsum and anhydrite interval in Alpha Federal is 15 to 90 ohm-m/m². Dolomite with gypsum is present at depths of 325 to 380 m and dolomite ± siltstone with abundant anhydrite are found at depths of 425 to 475 m in Turner State. The resistivity of the upper interval is generally greater than 200 ohm-m/m², but one 3-m-thick interval at a depth of 366 m is as low as 120 ohm-m/m². Remarkably, given that the dominant rock type in the lower interval is dolomite (based on cuttings), the conductivity of this section is unusually low at about 40 ohm-m/m². In contrast, the values at the top and bottom of this interval are 400 and 280 ohm-m/m², respectively, which is more typical for dolomite. This unusual resistivity signature may be related to an aquifer within fractured dolomite containing layers of anhydrite; the intercalated anhydrite is dissolving and elevating the TDS of the fluid. In other words, this conductive zone within resistive rock may be evidence of the presence of an aquifer with elevated TDS due to dissolution of anhydrite. As mentioned earlier, dry calcium sulfate is very resistive, but fluids saturated with calcium sulfate are conductive (Caselle et al., 2019).

Attempts to connect AMT and TEM data to water quality data from water wells was generally unsuccessful because most water wells are too shallow and quality measurements are biased toward drinkable water. Only regional AMT sites 7, 13, and 24 displayed the expected trend of higher TDS and lower modeled resistivity. Water-bearing intervals near AMT sites are presented in Figure 2-6 and Table 2-2. The nature of the water found in oil wells 20012 near site 15, 00028 near sites 26 and 27, and 00021 near site 10 is not stated in oil-well records, and water information is not available for 20033, thus limiting comparison to the AMT data. The indication of fresh water in 00014 is consistent with the greater-than-100 ohm-m values derived from 1-D modeling of SB16 and SB18. Similarly, fresh water near the bottom

of Lois Spanel Fed 1 (00015) matches the greater-than-100 ohm-m values derived from the 1-D model of SB17. The quality of the water and the depth of the water in the converted oil-to-water well at 20018 is not known, so the encountered water-bearing units cannot be directly compared to the modeled results.

GEOPHYSICS CONCLUSIONS

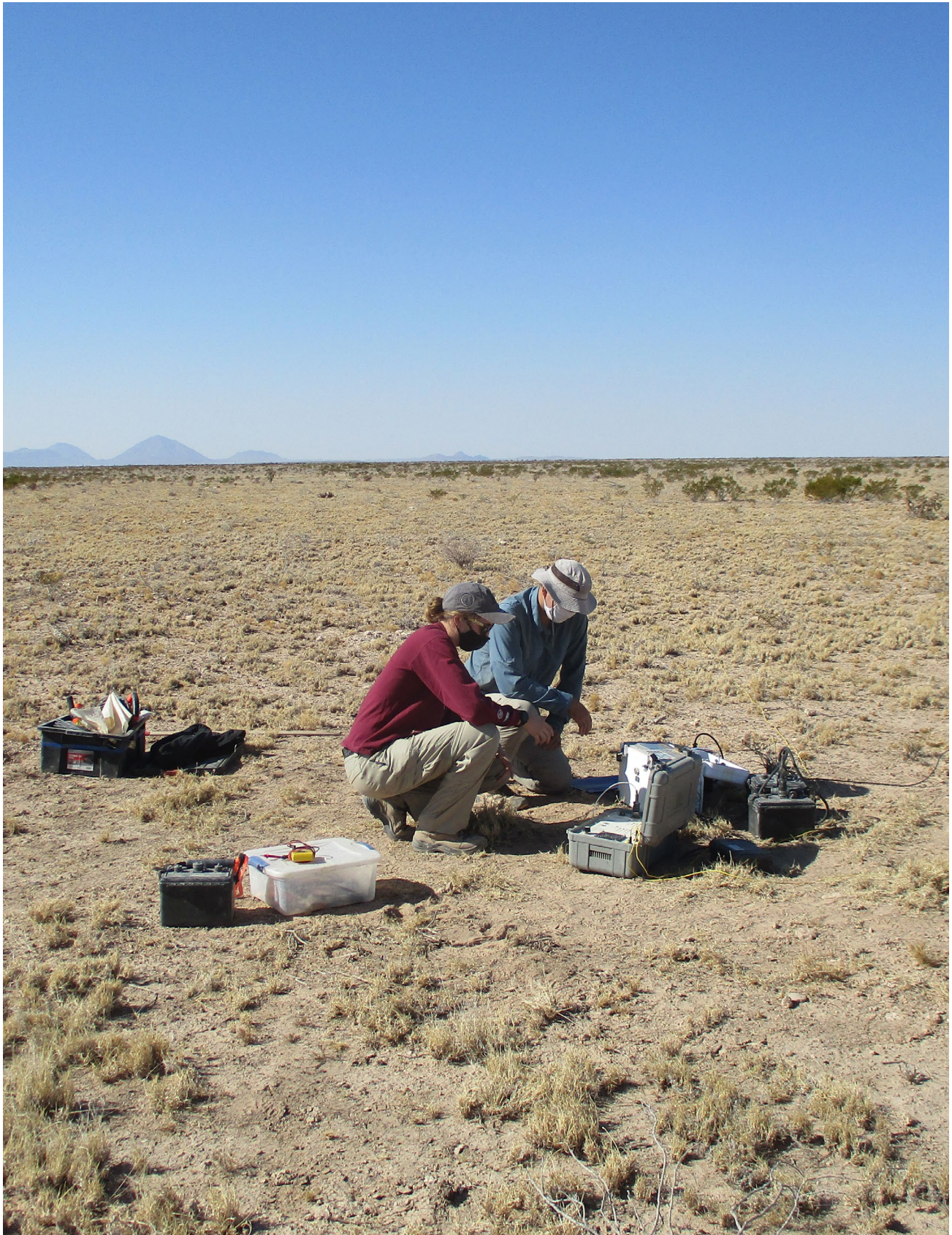
The AMT method proved to be useful in exploring the subsurface of the Salt Basin to depths of 1.5 to 3 km. Several of the AMT stations lie above a buried north-south-trending Ancestral Rocky Mountain highland that is covered by moderately deformed Permian sedimentary rocks (Figure 1-2). The highlands appear to be resistive features in the deep subsurface that are surrounded by more conductive features to the east, west, and north. Many of the 1-D models of the AMT data reveal a conductive interval at depths of 300 to 600 m that generally does not correlate with the main, fairly continuous conductive rock unit in the section, the Abo Formation (Figure 2-5 and Figure 2-6). The Percha Shale is another continuous conductor that typically lies at greater depths of 750 to 1,450 m. Other conductive units that are discontinuous are red beds in the Powwow Conglomerate, possible shales in the Hueco Limestone, and a siltstone within the Yeso Formation. The analysis of resistivity logs, particularly in the Turner State well, suggests that the interval detected in the AMT data may be related to discontinuous lenses of high-TDS water associated with dissolution of anhydrite within the Yeso Formation, which has complex facies changes and karstic features that disrupt aquifers. The examination of well cuttings in conjunction with resistivity logs aided in identifying rock units in the Salt Basin that are generally resistive and units that are relatively conductive. Anomalous conductive layers within the Yeso Formation are possibly high-TDS aquifers.

TEM measurements in conductive deposits located in Crow Flats on the east side of the study area and in the Yeso Formation on the west side produced models of the shallow subsurface conductivity structure to depths of about 400 m that correlate favorably with inversion results from the AMT measurements. The results from TEM station T5 indicate that this method can be used to estimate depth to bedrock. The TEM input signal in areas underlain by the San Andres Limestone at or near

the surface dissipates too rapidly to provide detailed information; our results demonstrate that TEM data in these instances simply record the fact that the limestone is a resistive unit.

Recommendations for future work

1. Collect AMT data along north-south and east-west 10-km-long profiles using a 0.5 km spacing in the vicinity of the three oil wells with resistivity logs to provide ground truth for the interpretation of data and to get a better idea of the continuity of resistors and conductors. Surveys of this nature will test the utility of using AMT to locate saline aquifers in the Salt Basin.
2. Meticulous analysis of well cuttings compared to geophysical logs has the potential to further improve the hydrogeologic model presented later in this report. Invaluable information about porosity and other hydrogeologic parameters could be obtained by measuring hydrologic parameters using cuttings.



Researchers from the USGS and New Mexico Tech collecting TEM data in the northern Salt Basin. *Photo by Shari Kelley*

CHAPTER 3: HYDROGEOCHEMICAL DATA

Talon Newton

Historical hydrogeochemical data were analyzed in conjunction with new samples collected for this study. Historical data came from multiple sources and spanned more than 80 years. Over 800 groundwater samples from nearly 400 water wells throughout the Salt Basin have been collected and analyzed throughout the basin's groundwater development history. NMBGMR staff collected 13 new water samples in 2020. Sample locations for historical water chemistry data and samples collected for this study are shown in Figure 3-1. These data are compiled in Appendix 2.5. The full dataset consisted of analyses of groundwater, spring, precipitation, and perennial stream water samples. Water samples collected for this study were analyzed for major ions (calcium, chloride, carbonate, bicarbonate, bromide, potassium, magnesium, sodium, and sulfate), temperature, pH, and the stable isotopes of water ($\delta^{18}\text{O}$, δD). A subset of well samples was also analyzed for $\delta^{13}\text{C}$, carbon-14, and tritium. The different constituents included in the historical water chemistry datasets vary quite a bit across different studies and data sources. This section presents the entire hydrogeochemical dataset (including historical data collected from other sources) and discusses its implications for identifying important controlling hydrogeochemical processes and for identifying different groundwater sources and flowpaths.

Figure 3-1 shows four different hydrogeologic regions (Sacramento River, Shiloh Draw, Eightmile Draw, and Salt Flats) that were delineated primarily based on the potentiometric surface contours. The Sacramento River region appears to be comprised of groundwater that originates as precipitation in the high Sacramento Mountains and is characterized by steep hydraulic gradients. While, according to the potentiometric surface map, much of the groundwater from the Shiloh Draw region appears to come from the Sacramento River region, there may be

some groundwater coming from the west into this region. Groundwater in the Eightmile Draw region appears to be sourced from the southwest and may be sourced from Cretaceous rocks and Victorio Peak Limestone. The large Salt Flats region is characterized by very flat hydraulic gradients and appears to have groundwater from all the other hydrogeologic regions flowing into it, as well as some coming from the Guadalupe Mountains to the east. Because these regions appear to be associated with different water sources according to the implied flowpaths, these hydrogeologic regions form the framework under which much of the water chemistry interpretations are evaluated. It is important to understand that the implied flowpaths are based on the potentiometric surface contours that likely represent horizontal flowpaths. Deeper, regional flowpaths induced by the large elevation difference between the Sacramento Mountains and the rest of the basin may complicate some of the water chemistry trends presented in this section.

WATER QUALITY AND MAJOR ION CHEMISTRY

Selected constituents from the entire groundwater chemistry dataset were examined to assess general water quality and spatial distribution within the study area. Table 3-1 shows statistics for major ions, fluoride, iron, hardness, and nitrate, as well as primary and secondary EPA drinking water maximum contaminant levels (MCLs) where applicable. Primary drinking water MCLs are legally enforceable standards that apply to public water systems to protect public health. However, these standards are not enforceable for private wells. EPA secondary drinking water MCLs are non-enforceable standards for constituents that do not pose significant health risks but which may affect aesthetic considerations, such as taste, color, and odor. Because these standards

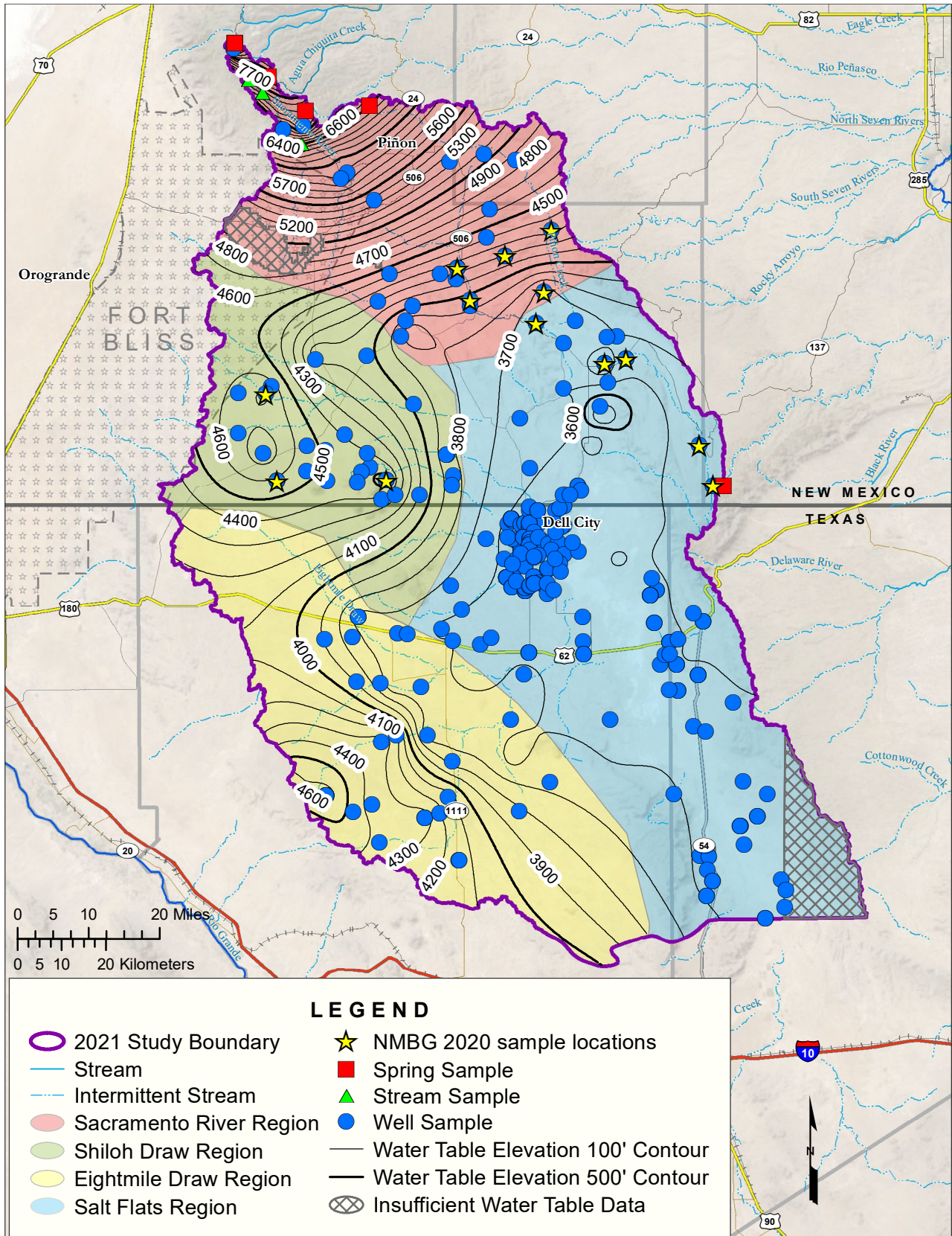


Figure 3-1. Map indicating the hydrogeologic regions used to discuss water chemistry results and the locations of sites with samples that have complete ion chemistry analysis, including spring, well, and stream locations. The 13 wells sampled as part of this study are indicated by yellow stars.

are not enforceable for domestic water sources, the following information is provided to inform readers about the general water quality within the Salt Basin.

Figure 3-2 shows that most groundwater within the Salt Basin is characterized by TDS concentrations that are well above the 500 mg/L secondary MCL. The freshest water occurs in the Sacramento River region, which is close to the recharge zone in the high Sacramento Mountains. Most groundwater throughout the basin shows TDS concentrations of 3,000 mg/L or less. In general, water with TDS concentrations less than 1,000 mg/L is suitable for drinking. Groundwater with TDS concentrations less than 3,000 mg/L is generally suitable for applying to most crops. Water with TDS concentrations higher than 3,000 mg/L may be harmful to many crops. The high TDS concentrations observed in the Salt Basin are mainly due to the soluble minerals that make up the rocks (carbonates and evaporites) and the relatively long residence times of groundwater. The highest TDS values are observed in the Salt Flats region, where playas are present. TDS concentrations in these areas are likely increased to a larger degree due to evaporation of shallow groundwater.

Figure 3-3 shows that most groundwater within the basin is characterized by sulfate concentrations well above the 250 mg/L secondary MCL. Again, the lowest sulfate concentrations occur in the Sacramento River region. The primary source of sulfate is gypsum/anhydrite. The general observed trend of increasing sulfate concentrations is primarily due to water/mineral interactions, discussed in more detail below.

Groundwater chloride concentrations (Figure 3-4) in the Sacramento River region are mostly very low (<10 mg/L) and are observed at much higher values throughout the rest of the basin, with the highest chloride concentrations observed in the Salt Flats region. For the Salt Flats region, where a large number of wells have been sampled by the Texas Water Development Board, chloride concentrations in groundwater range from 5.2 to 71,000 mg/L, with a rough inverse correlation with depth. The water located at shallow depths with very high chloride concentrations is mostly due to evaporation. Groundwater in the Shiloh Draw region exhibits relatively low chloride concentrations (<200 mg/L). Most groundwater samples collected in the Eightmile Draw region are also fairly low, but a few wells show chloride concentrations above 500 mg/L. The major source of chloride is likely the Yeso Formation and Cretaceous rocks to the southwest.

Most groundwater samples in the study area exhibit very low iron concentrations, much lower than the secondary MCL of 0.3 mg/L (Figure 3-5). In fact, over half of the results showed values below the detection limit (Table 3-1). However, a few groundwater samples exhibit much higher iron concentrations. The two points that show the highest iron concentrations (370 mg/L each) are located close to each other in the Salt Flats region. These two wells also exhibit the lowest pH values (4.9 and 5.4, data not shown). These samples were collected by USGS in 1991, and we do not have field notes about these two well samples. It is possible that these iron concentrations are errors or are due to old and rusty

Table 3-1. Statistics for selected chemical constituents in groundwater, with EPA primary and secondary drinking water MCLs where applicable. Statistics were calculated after removing all duplicate analyses, using only the most recent values. Values for analyses that showed non-detects were entered as half the detection limit. The number of non-detects is shown. All concentrations are in mg/L.

	Ca	Mg	Na	HCO ₃	Cl	SO ₄	TDS	F	Fe	Hardness	Mn	NO ₃
Minimum	10.4	3	4.7	33	1.8	14.5	99.6	0.05	0.0001	115	0.0005	0.005
Maximum	16000	9000	43000	1093	71000	51000	160981	16	370	72500	0.588	233
Mean	364.2	210.4	553.6	257.6	1007.3	1154.1	3167.7	2.1	5.75	1963.5	0.0269	25.87
Standard Deviation	997.3	823.5	3268.2	95	5844.5	2796.2	11595.7	1.9	42.55	5698.3	0.0764	40.74
n*	352	349	314	368	379	377	332	305	150	309	120	304
# Non-detects	0	0	0	0	0	0	0	2	76	0	81	28
EPA Primary MCL								4				44.2
EPA Secondary MCL					250	250	500	2	0.3		0.05	

* n = number of samples

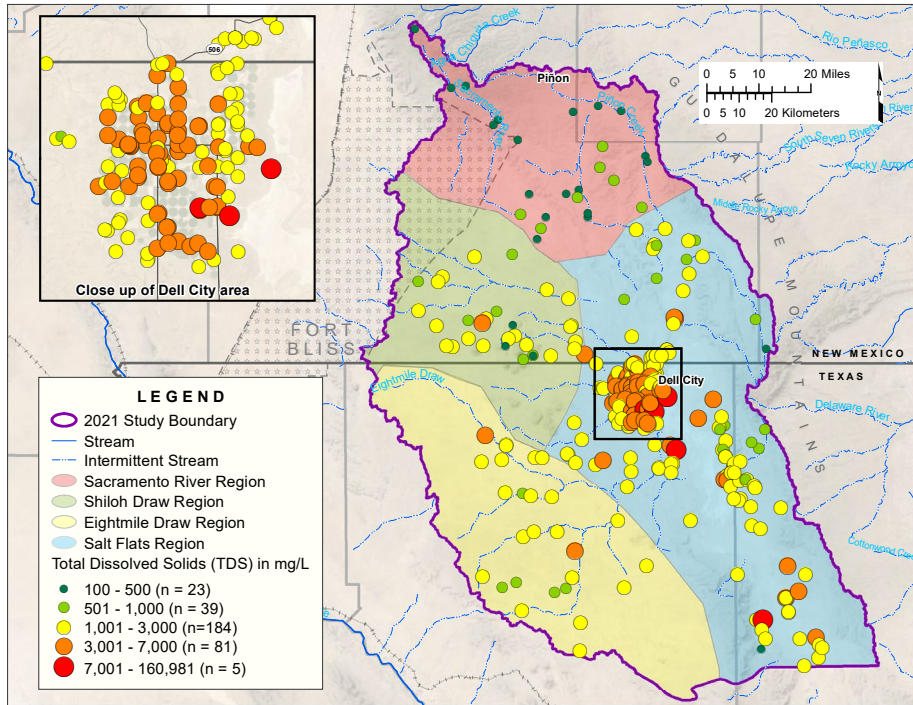


Figure 3-2. TDS concentrations in mg/L for groundwater samples. TDS has an MCL of 500 mg/L for drinking water, and the USGS considers water between 1,000 mg/L and 3,000 mg/L to be slightly saline. Over 3,000 mg/L is typically not economically feasible to treat for human consumption. Poultry and livestock maximum limits on TDS are 5,000 and 7,000 mg/L, respectively. Agricultural limits on the TDS of irrigation water vary by crop, but typically need to be below 2,000 mg/L for long-term irrigation use. Only the most recent data point for a given well is shown.

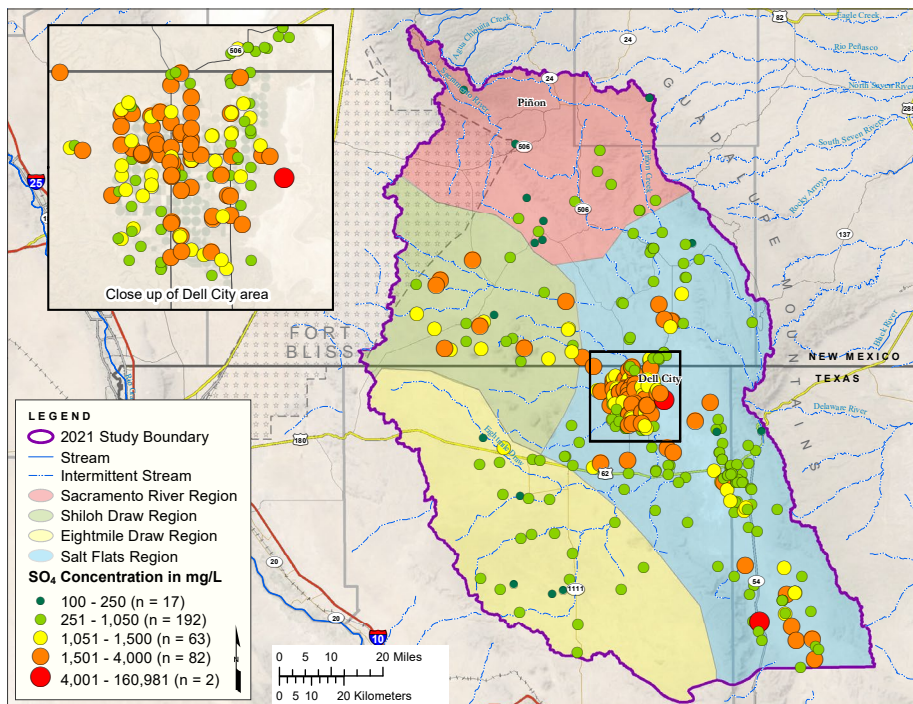


Figure 3-3. Sulfate (SO₄) concentrations in mg/L for groundwater samples. The EPA secondary MCL for SO₄ in drinking water is 250 mg/L. Poultry also require water supplies at 250 mg/L or below. Livestock can tolerate SO₄ in the 300–1,050 mg/L range if they are fed a low-sulfate diet, but it may have laxative effects in animals not accustomed to the water. Concentrations above 1,500 may cause serious health issues in cattle.

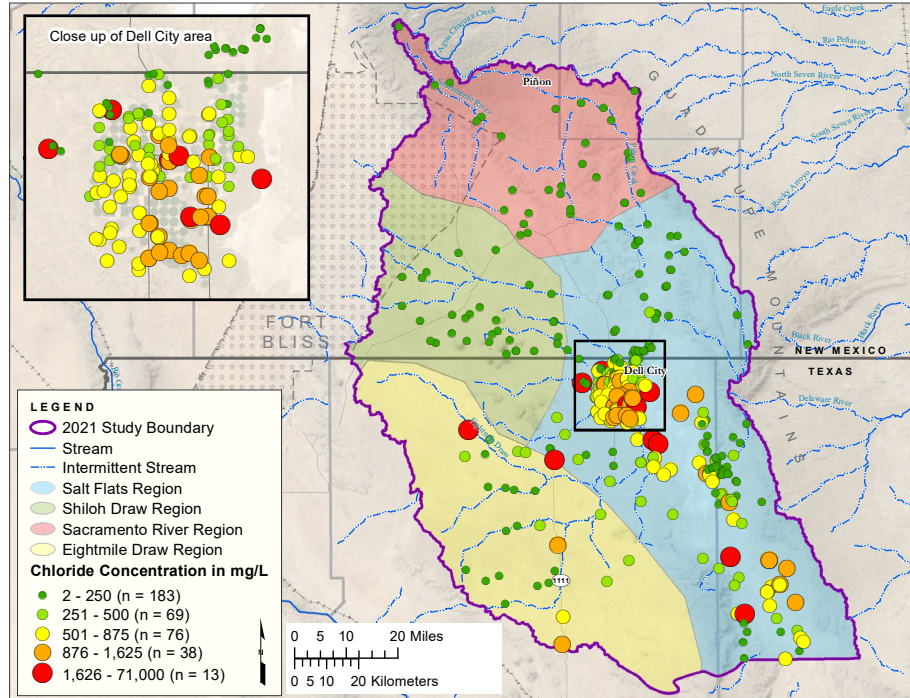


Figure 3-4. Chloride (Cl) concentrations in mg/L for groundwater samples. The EPA secondary MCL for Cl is 250 mg/L for drinking water. Poultry and livestock maximum limits are similar at 250 mg/L and 300 mg/L, respectively. Agricultural limits on the Cl of irrigation water vary by crop, with onions tolerating up to 350 mg/L, tomatoes up to 875 mg/L, and cotton up to 1,625 mg/L for long-term use.

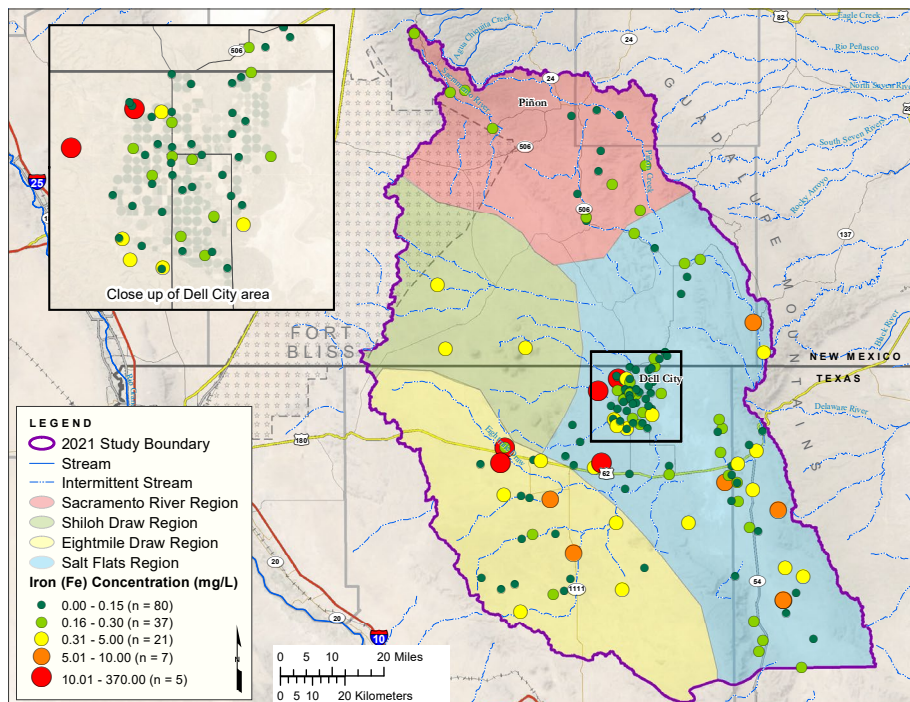


Figure 3-5. Iron (Fe) concentrations in mg/L for groundwater samples. The EPA drinking water secondary MCL for Fe is 0.3 mg/L, which is also considered the safe upper limit for poultry and livestock. Crops can tolerate 5.0 mg/L Fe in irrigation water for long-term supply and up to 10 mg/L in short-term supply.

well casings. It is unclear why a few other water samples collected in the Eightmile Draw and Salt Flats regions exhibit relatively high iron concentrations. Possible geologic sources of iron are Cenozoic intrusive rocks and possibly the Abo Formation.

Figure 3-6 shows the spatial distribution of manganese concentrations in groundwater. The large majority of water samples exhibit concentrations well below the secondary MCL for manganese of 0.05 mg/L. Over 75% of the water samples showed no detectable manganese (Table 3-1). A few wells located in the Salt Flats region produced water samples with manganese concentrations that exceed the secondary MCL.

Nitrate concentrations in groundwater in the Salt Basin (Figure 3-7) are mostly well below the primary MCL of 44.2 mg/L. (We report nitrate as NO₃ in this study; the MCL for nitrate as N is 10 mg/L). Most elevated nitrate concentrations in groundwater may be related to anthropogenic sources such as septic tanks, fertilizers, and animal waste. Several wells in the study area show nitrate concentrations exceeding the EPA primary MCL.

While elevated nitrate concentrations in groundwater are usually interpreted as caused by anthropogenic contamination, many wells in the Salt Basin exhibiting high nitrate concentrations also appear to be old groundwater, according to tritium and carbon-14 concentrations (discussed below), and do not appear to be impacted by other anthropogenic contaminants. Walvoord and Phillips (2004) identified a large reservoir of bioavailable nitrogen as nitrate being stored in deep vadose zones in arid regions, including the Chihuahuan desert. This nitrate has been accumulating in subsoil regions throughout the Holocene. Therefore, it is possible that high nitrate concentrations in groundwater in many areas of the Salt Basin are due to episodic Holocene recharge events that flushed vadose zone nitrate into the groundwater system. This mechanism of nitrate contamination in groundwater has also been suggested for areas in Australia by C. J. Barnes et al. (1992). While many of the wells in the Dell City area that produce water with high nitrate concentrations may be due to anthropogenic activities such as irrigation and leakage from septic tanks, it is possible that in several areas, high nitrate

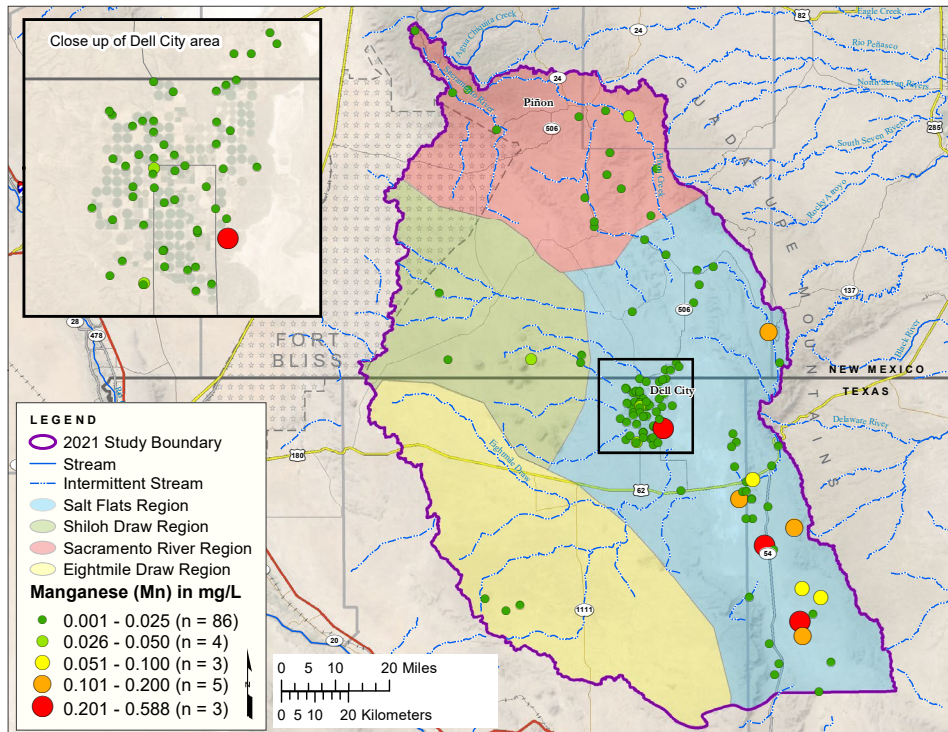


Figure 3-6. Manganese (Mn) concentrations in mg/L for groundwater samples. The EPA drinking water secondary MCL for manganese is 0.05 mg/L, which is also the recommended upper limit for livestock and poultry. For agricultural applications, manganese should be below 0.2 mg/L for long-term application and is acceptable up to 10.0 mg/L for short-term use.

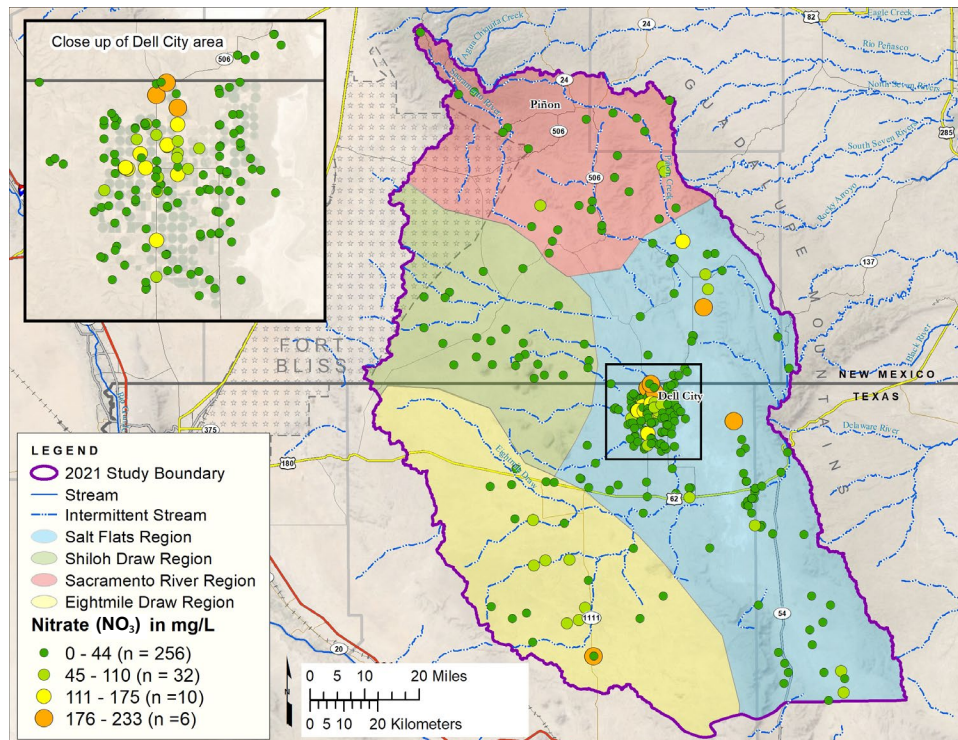


Figure 3-7. Nitrate (NO₃) concentrations in mg/L for groundwater samples. Nitrate concentrations can be reported in two different ways: as the measured nitrate (NO₃) ion, shown here, or as the amount of nitrogen in the nitrate ion. The safety limits described here are reported in nitrate ions for consistency. The EPA drinking water primary MCL for nitrate is 44.2 mg/L. Poultry can tolerate nitrate up to 110 mg/L, while concentrations above 175 mg/L have increasingly negative effects on cattle.

concentrations are due to natural nitrate sources that are stored in the vadose zone. This hypothesis should be studied further to identify mechanisms by which nitrates from surface are sequestered into the vadose zone of the Salt Basin.

The term *hardness* refers to the amount of dissolved magnesium and calcium. Very hard water is defined by USGS as water with a hardness greater than 180 mg/L. Almost all wells in the Salt Basin produce very hard water (Table 3-1; Appendix 2), which is expected due to the primary aquifers being composed of limestone and dolomite. Hard water can be problematic, as it leaves scaly deposits inside pipes, water heaters, and tanks.

While the majority of wells in the study area appear to produce water with fluoride concentrations well below the secondary MCL (Figure 3-8), several water samples exhibit fluoride concentrations that exceed the primary MCL of 4 mg/L and may pose health risks if used as drinking water. The main geologic source of fluoride is likely Cenozoic intrusive rocks in the western part of the Basin.

WATER TYPES

The Piper diagram (Figure 3-9) is a graphical way of categorizing natural waters according to their relative concentrations of major cations (left ternary diagram) and anions (right ternary diagram). By plotting chemical compositions on a Piper diagram, waters can be assigned a water type that is based on the dominant cation(s) and anion(s). By projecting cation and anion composition onto the diamond portion of the Piper diagram, the different water types can be compared to each other. Trends observed for data plotted on the diagram can then be interpreted to indicate specific physical and geochemical processes such as mixing, dissolution, cation exchange, and more. Water types for samples with complete major ions are identified in Figure 3-10, with our inferred hydrogeologic regions. Waters from the Sacramento River region plot along a linear trend from calcium-bicarbonate type to calcium-sulfate type on the Piper diagram. This trend is also seen spatially on Figure 3-10, where calcium-bicarbonate waters are located at higher elevations and up-gradient, while the calcium-sulfate waters are located down-gradient at

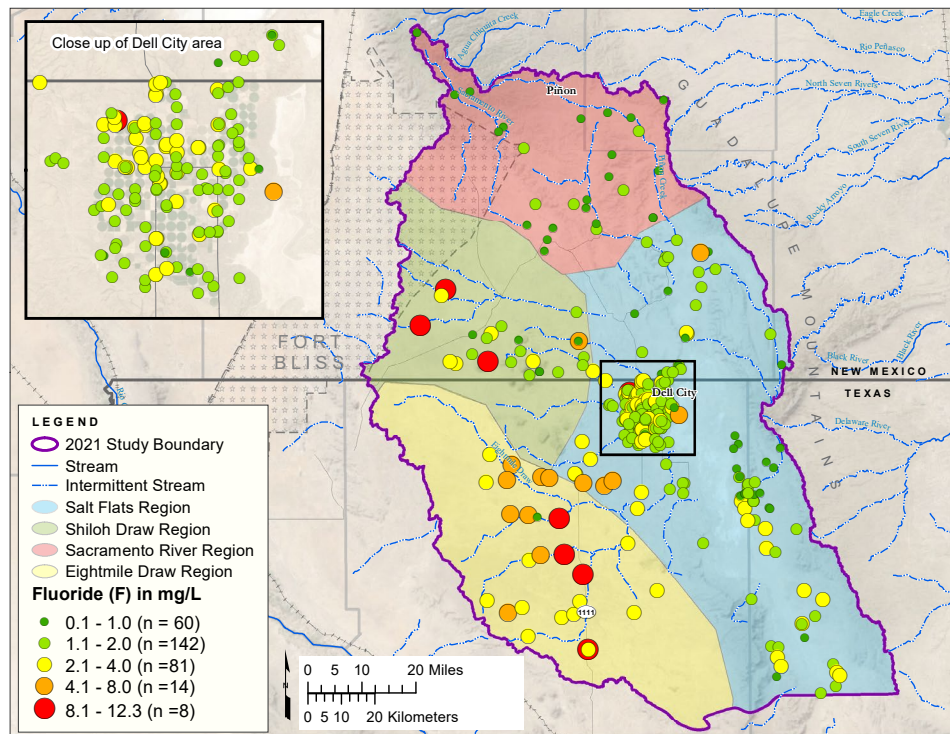


Figure 3-8. Fluoride (F⁻) concentrations in mg/L for groundwater samples. Only the most recent data point for a given well is shown. The EPA has both primary and secondary MCLs for fluoride in drinking water for public water systems (4 mg/L and 2 mg/L, respectively). Poultry and livestock follow these same guidelines for maximum acceptable levels in their water.

lower elevations. This trend is indicative of a process called dedolomitization, which has been documented in the Sacramento Mountains and the Salt Basin by various researchers (Newton et al., 2012; Morse, 2010; Sigstedt, 2010) and is discussed in more detail below. Water types in the Shiloh Draw region are mostly calcium-sulfate type water, possibly related to flow down gradient from the Sacramento River region. However, a few wells show relative increases in sodium and chloride (Figure 3-9 and 3-10), which likely indicates a different water source from the west. Waters in the Eightmile Draw region show very different chemical composition with higher relative concentrations of sodium and chloride; these likely represent a different water source coming from the Victorio Peak Limestone and Cretaceous rocks in the southwest. Waters in the Salt Flats region exhibit a variety of water types that are likely due to the mixing of various water types from the other regions. The mixing and water/mineral interactions that are apparent from these observations are discussed below.

ENVIRONMENTAL TRACER ANALYSIS

Stable isotopes of water

The stable isotopes of oxygen and hydrogen are useful tools for tracing the hydrologic cycle. The isotopic composition of a water sample refers to the ratio of heavier isotopes to lighter isotopes (*R*) for the hydrogen and oxygen that make up water molecules. Because these stable isotopes are part of the water molecule, small variations in these ratios act as labels that allow tracking of waters with different stable isotopic signatures. All isotopic compositions in this report are presented as relative concentrations (δ), which is the per mil deviation of the *R* of a sample from the Vienna Standard Mean Ocean Water (VSMOW) *R*, as shown in the equation below:

$$\delta = \frac{R_{sample} - R_{standard}}{R_{standard}} * 1000\text{‰}$$

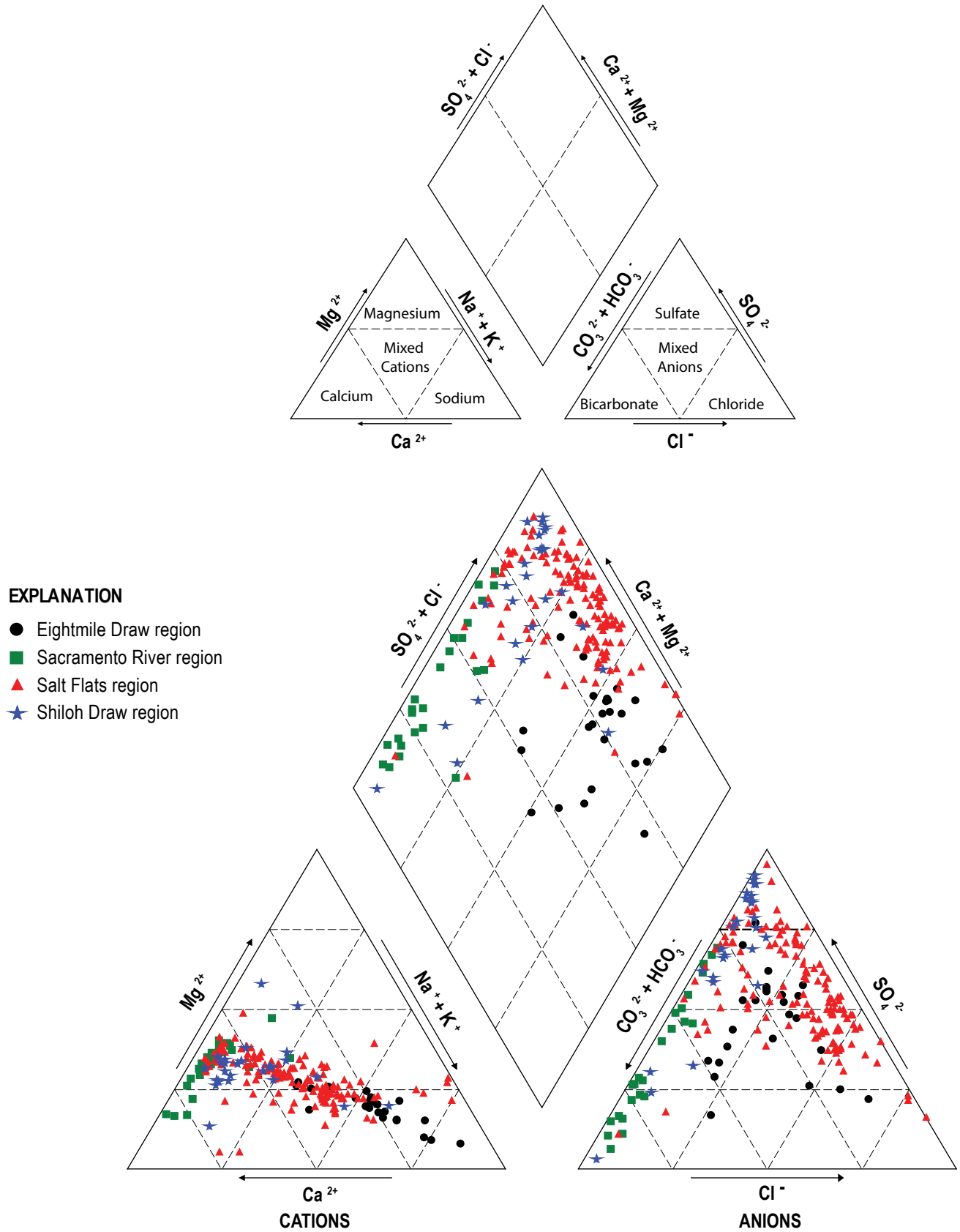


Figure 3-9. Piper diagram showing groundwater in the study area grouped by hydrogeologic region. The example Piper diagram in the upper right corner shows how water types are defined.

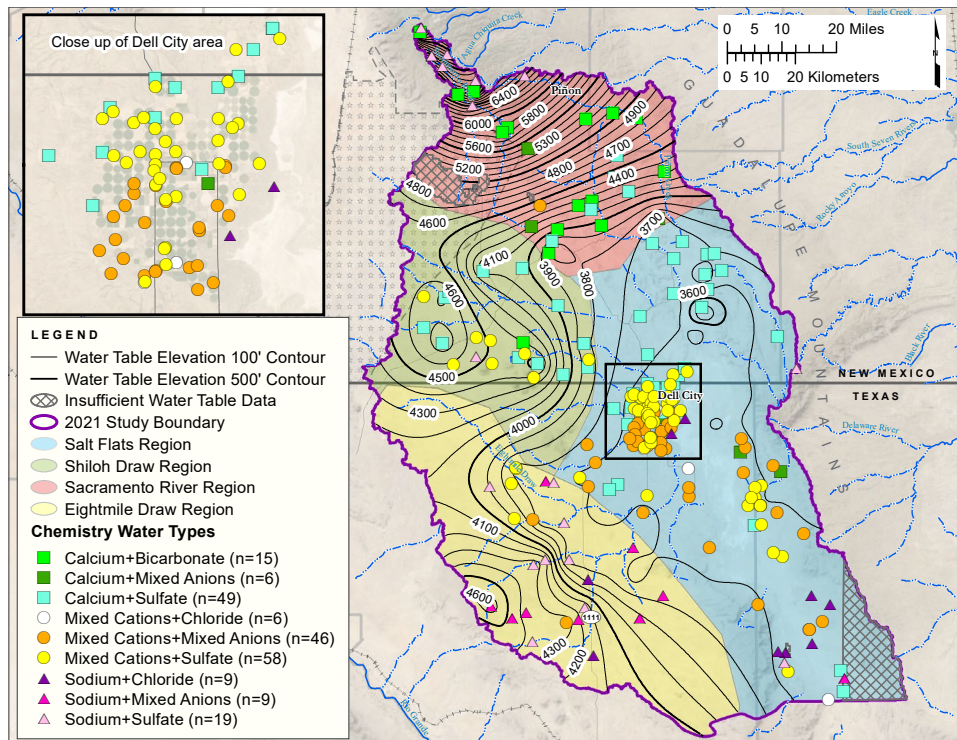


Figure 3-10. Dominant water types for samples with complete ion chemistry. Regional similarities in water types can be observed. The dominant water type in the Sacramento River region, which includes the primary recharge zone, is calcium-bicarbonate. Dedolomitization results in this water evolving to a calcium-sulfate water type, which can be seen down-gradient in the Shiloh Draw region and the northern part of the Salt Flats region. Groundwater high in chloride and sodium can be seen in the Eightmile Draw region, where it flows to the northeast to mix with groundwater in the Salt Flats region.

It is useful to plot stable isotope data on a δD -versus- $\delta^{18}O$ graph, as shown Figure 3-11. In general, most precipitation plots on or near the global meteoric water line (GMWL) with a slope of 8 and a deuterium excess (y-intercept) of 10, as demonstrated by Craig (1961). However, the linear trend that characterizes local precipitation in a specific area may deviate from the GMWL with a similar slope but a different deuterium excess and is referred to as a local meteoric water line (LMWL). Stable isotopes of water can also be useful for identifying water that has undergone evaporation. Isotopically lighter water molecules evaporate at a slightly higher rate than isotopically heavier water molecules, resulting in isotopic fractionation and thus causing the residual water to become heavier and evolve along an evaporation line that usually has a slope between 4 and 6.

Newton et al. (2012) estimated a LMWL based on the isotopic composition of precipitation samples collected in several areas in the southern Sacramento

Mountains at different times in 2007 and 2008. Newton et al. (2012) also demonstrated that water from most springs and wells in the Sacramento Mountains and along the Pecos Slope plotted either along an evaporation line or between the evaporation line and the LMWL, indicating mixing of focused recharge through mountain streams, where this water is evaporated to some degree, and diffuse recharge, which is precipitation that infiltrates past the root zone without undergoing evaporation. Most data points representing groundwater in the Salt Basin plot between the LMWL and the evaporation line defined by Newton et al. (2012; Figure 3-11), suggesting that much of the groundwater in the study area may originate from the Sacramento Mountains. However, the large variability in stable isotope data may also be due to mixing of different water sources in a complex hydrogeologic system. Some groundwater samples from the Salt Flats and Shiloh Draw regions plot below the evaporation line and lie along the GMWL. These waters may represent a different groundwater

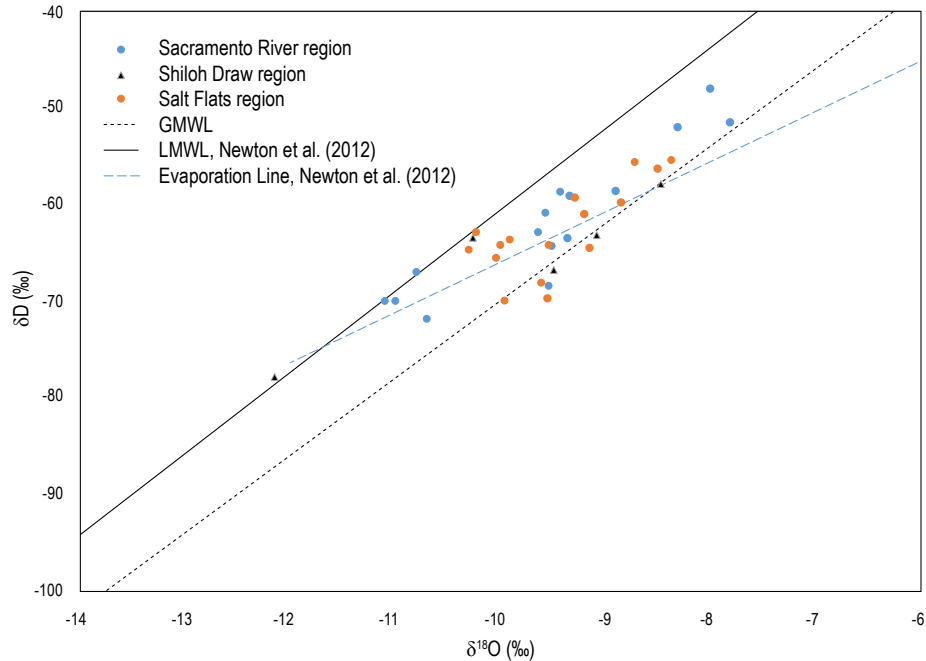


Figure 3-11. Isotopic composition of groundwater in the study area, categorized by hydrogeologic region. There is no data for groundwater in the Eightmile Draw region. The global meteoric water line (GMWL), the local meteoric water line (LMWL) defined by Newton et al. (2012), and the Sacramento Mountains evaporation line defined by Newton et al. (2012) are also shown.

source from an area (likely to the southwest) where precipitation is better characterized by the GMWL than the Sacramento Mountains LMWL.

The spatial distribution of δD (Figure 3-12) and $\delta^{18}O$ (Figure 3-13) in groundwater shows the lightest isotopic compositions along the Sacramento River at high elevations in the Sacramento Mountains. Throughout the rest of the basin, no real spatial trend can be identified. However, groundwater in the Eightmile Draw region exhibits groundwater with the heaviest $\delta^{18}O$ values, which may represent a different water source coming from the Victorio Peak Limestone and Cretaceous rocks in the southwest. Unfortunately, no δD data exist for that region; therefore, it is difficult to conclusively interpret these data.

Tritium and carbon-14

Tritium (3H), a radioactive isotope of hydrogen with a half-life of 12.4 years, is produced naturally in the atmosphere by cosmic radiation and enters the hydrologic cycle via precipitation as part of a water molecule. Tritium concentration is measured in tritium units (TU), where one TU indicates

a tritium-hydrogen atomic ratio of 10^{-18} . The tritium content of precipitation varies spatially and temporally, with average values in the southwestern United States and Mexico ranging from 2 to 10 TU (Eastoe et al., 2012). Between 1991 and 2005, the tritium content of precipitation in Albuquerque, New Mexico, ranged from 4.5 to 19.1 TU, with an average of 8.8 TU (IAEA/WMO, 2017). Newton et al. (2012) observed tritium concentrations in precipitation in the Sacramento Mountains in southern New Mexico to range from 3 to 10 TU. For groundwater samples collected over the last 20 years, the general interpretation of tritium in groundwater is: (1) tritium concentrations between 5 and 10 TU represent modern water that is less than 10 years old; (2) tritium concentrations between 1 and 5 TU indicate a mixture of modern recharge and “tritium dead” water that is over 50 years old; and (3) groundwater with tritium concentrations of 1 TU or less indicates that most recharge is over 50 years old. Due to testing of thermonuclear devices beginning in 1953, tritium concentrations in precipitation increased drastically above background levels, with peak concentrations ($>3,000$ TU) in 1962 and 1963 (Solomon and Sudicky, 1991). Since then,

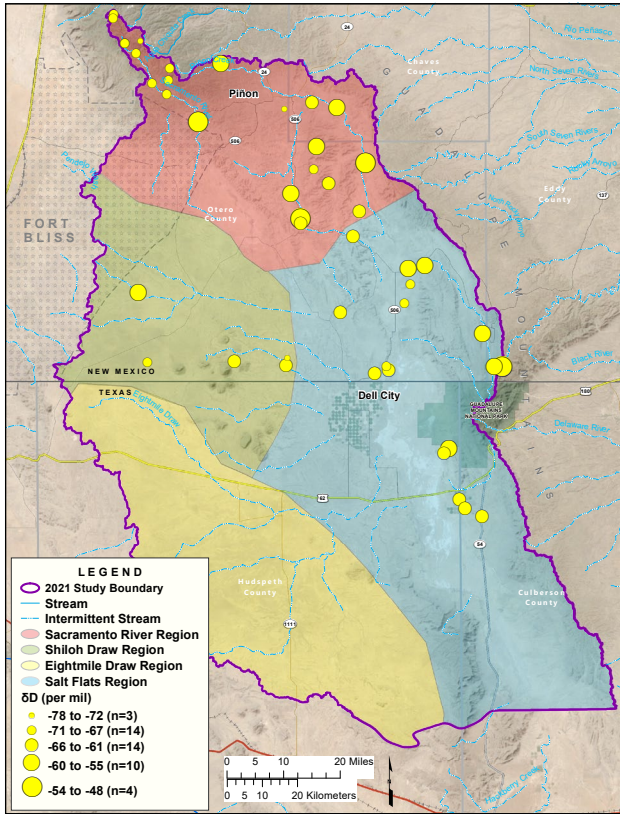


Figure 3-12. Spatial distribution of δD for groundwater. Only the most recent data point for a given well is shown.

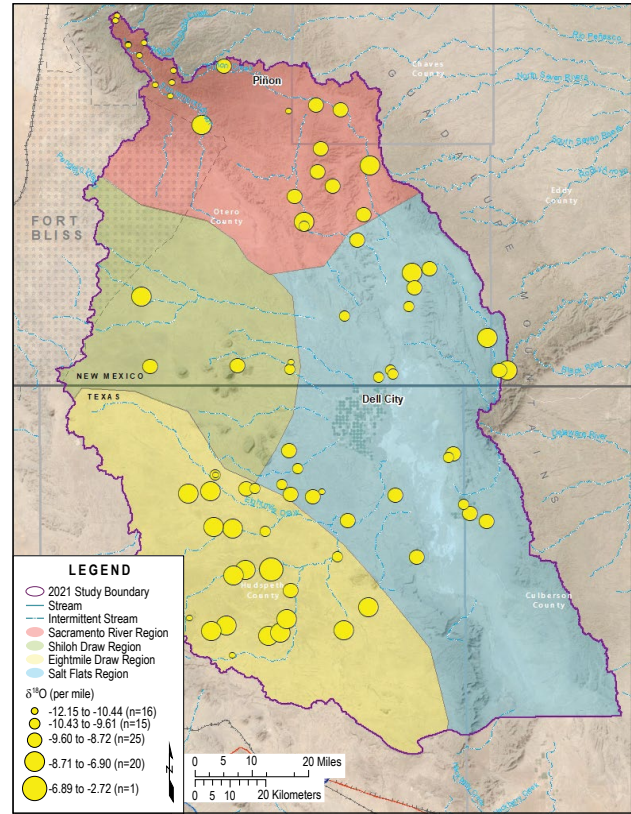


Figure 3-13. Spatial distribution of $\delta^{18}O$ for groundwater. Only the most recent data point for a given well is shown.

tritium concentrations in precipitation have decreased back to pre-1953 values. For many years after this increase in tritium activity in precipitation, the “bomb pulse” could be detected in groundwater. These days, the bomb pulse cannot be detected in groundwater due to radioactive decay of tritium.

Figure 3-14 shows the spatial distribution of tritium in groundwater. Groundwater in the Sacramento River region at high elevations shows tritium concentrations between 3 and 6 TU, indicating a significant amount of modern recharge. In the general down-gradient direction to the south, tritium concentrations decrease substantially, with values of less than 1 TU in the southern portion of the Sacramento River region, the Shiloh Draw region, and the northern portion of the Salt Flats region. These samples were collected between 2006 and 2020 by researchers at NMBGMR and Sigstedt (2010). Interestingly, all the samples from wells located within the Eightmile Draw region and the western edge of the Salt Flats region were sampled between 1986

and 1988 by the Texas Water Development Board. Two samples in the southern portion of the Eightmile Draw region, which exhibit tritium activities of 32 and 21.4 TU, and the sample in the center of the same region with a tritium concentration of 13.7 TU definitely indicate an input of bomb pulse tritium from the 1960s. The other relatively high tritium concentrations in this area are also likely indicative of some proportion of recharge that is 20 to 30 years old.

Atmospheric CO_2 gas, which has an approximate carbon-14 activity of 100 percent modern carbon (PMC; Fritz and Fontes, 1980) is incorporated into the groundwater system as bicarbonate ($H^{14}CO_3^-$) during infiltration of recharge through the vadose zone (Kalin, 2000). As the infiltration crosses the water table, the dissolved inorganic carbon is isolated from the modern carbon-14 input from the atmosphere and soil zone reservoirs. As the water travels along a flowpath in the aquifer system, the carbon-14 decays with time. As a result, the

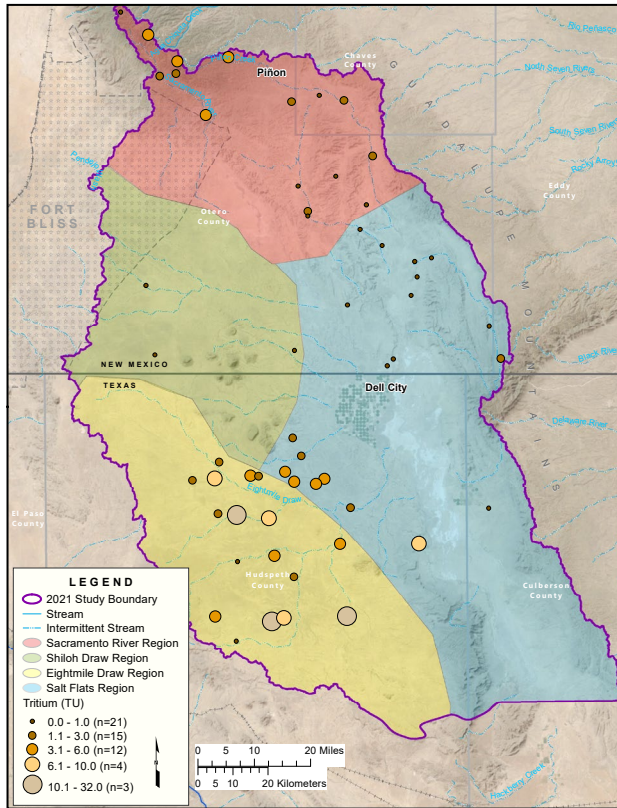


Figure 3-14. Spatial distribution of tritium in groundwater. Units are tritium units (TU).

amount of carbon-14 measured in the groundwater along a flowpath gives an age or the approximate time that has passed since the water recharged the aquifer system. In general, lower PMC indicates older groundwater. However, to properly quantify groundwater age, it is usually necessary to correct the measured carbon-14 activity to account for hydrogeologic processes such as carbonate dissolution, isotopic exchange, and mixing of older and younger waters (Fontes and Garnier, 1979). The carbon-14 data presented in Figure 3-15 have not been corrected, and only general trends are discussed. Sigstedt (2010) and Eberle (2021) have applied different corrections that are discussed in more detail below.

The spatial distribution of carbon-14 activity (Figure 3-15) is similar to that for tritium (Figure 3-14). The highest carbon-14 activities are observed at higher elevations in the Sacramento River region, where recharge is clearly occurring, and they decrease significantly in the general down-gradient

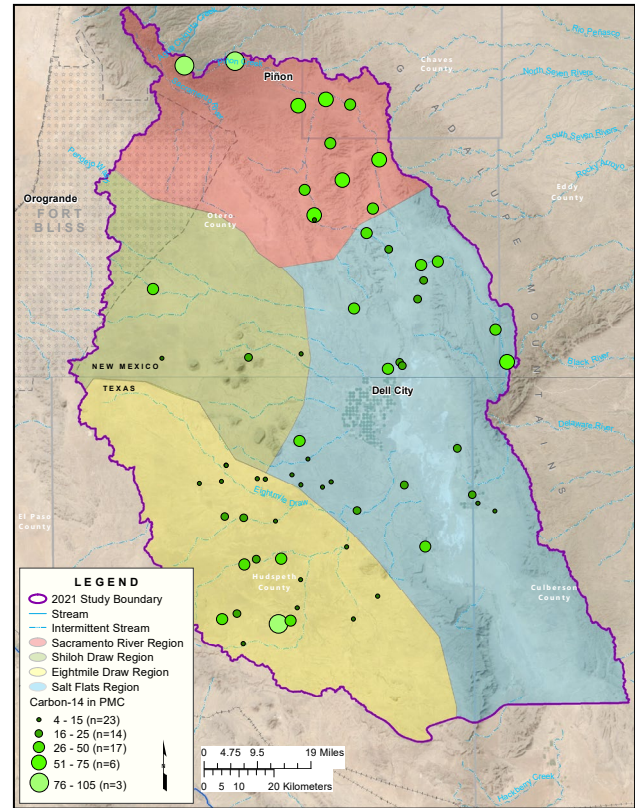


Figure 3-15. Spatial distribution of carbon-14 activity in groundwater in percent modern carbon (PMC). These values have not been corrected for hydrogeologic processes such as carbonate dissolution, isotopic exchange, or mixing.

direction to the south, indicating older water. Again, the wells in the Eightmile Draw region and the western edge of the Salt Flats region were sampled in the 1980s by the Texas Water Development Board. The data sample exhibiting a carbon-14 activity of 90.8 PMC likely represents bomb pulse carbon from the 1960s, again indicating that young meteoric waters are entering the groundwater system in this area.

DISCUSSION: WATER SOURCES, GEOCHEMICAL PROCESSES, AND FLOWPATHS

The example Piper diagram in Figure 3-16 shows the possible hydrologic processes that can explain the distribution of water types shown in Figure 3-10. The dedolomitization pathways shown have been well documented in the southern Sacramento Mountains and the Pecos Slope to the north of the study area (Newton et al., 2012; Morse, 2010), as well as in the

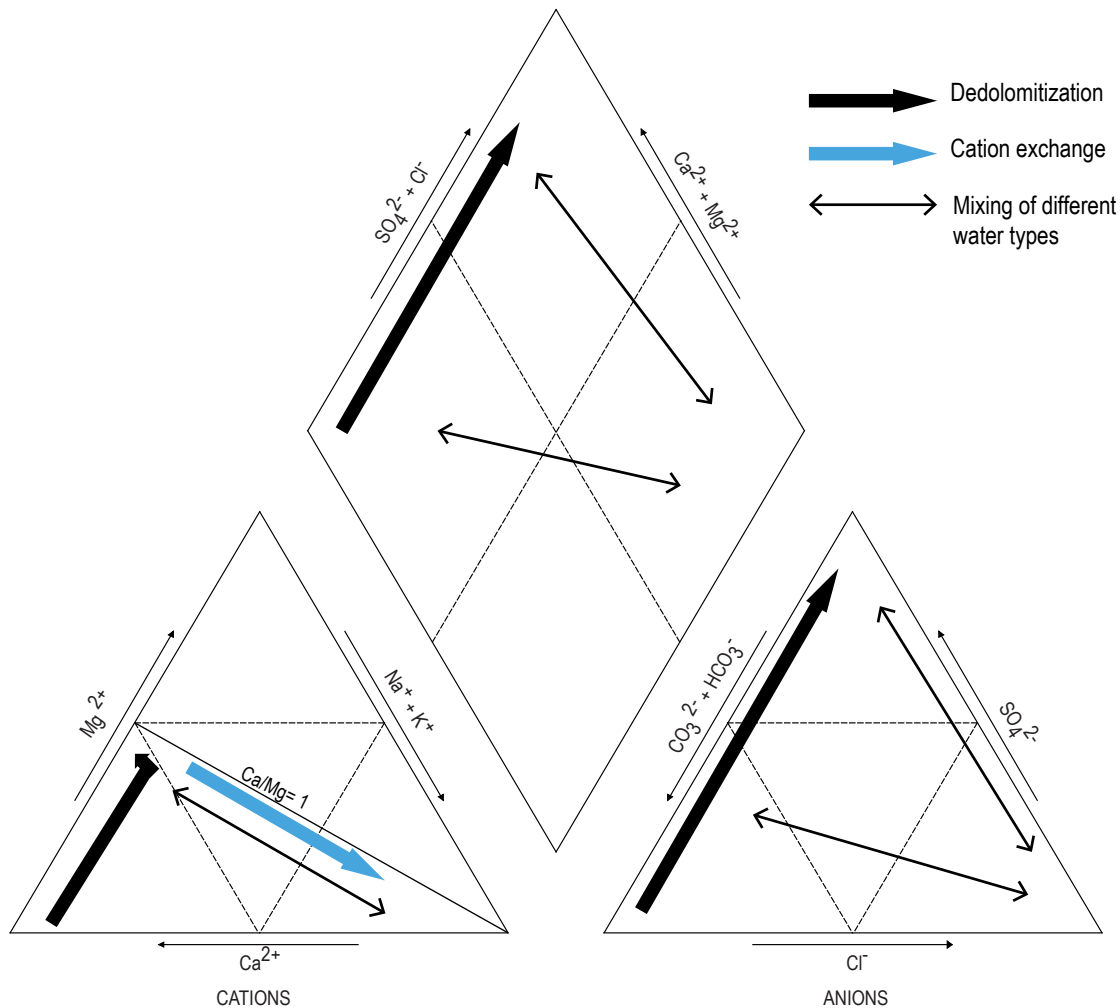


Figure 3-16. Schematic Piper diagram showing different possible geochemical processes to explain observed groundwater compositions. The Ca/Mg = 1 line represents the ratio that is approached during dedolomitization.

northern portion of the Salt Basin by Sigstedt (2010). Dedolomitization occurs when the dissolution of gypsum or anhydrite and the associated increase in sulfate concentration causes dissolution of dolomite and precipitation of calcite. A solution in equilibrium with calcite and in the presence of gypsum and dolomite will become saturated to supersaturated with respect to calcite due to the addition of calcium ions from the dissolution of gypsum. As the dissolution of gypsum continues, the common ion effect causes calcite to precipitate, which removes carbonate from the system and forces the dissolution of dolomite (Back et al., 1983). Dedolomitization usually causes groundwater to evolve from calcium-bicarbonate water type to calcium-sulfate water type. The line labeled $Ca/Mg = 1$ shows the calcium/magnesium ratio that is approached as

dedolomitization progresses (Figure 3-16, compare with Figure 3-9). Data in Figure 3-9 show a linear trend that falls just below this line. Dedolomitization helps explain this trend. However, the linear trend may also indicate cation exchange, where dissolved magnesium and calcium are exchanged for sodium that is adsorbed to clay minerals in the aquifer. This process results in a decrease in relative calcium and magnesium concentrations and an increase in sodium concentrations in groundwater. The other process that probably plays a role in controlling groundwater chemistry is mixing of different water types or sources. It is likely that all three of these processes are occurring.

The plot shown in Figure 3-17 graphically assesses the occurrence of cation exchange based on stoichiometry. Most of the data are clustered around

the $-1:1$ line, indicating that cation exchange is occurring. Groundwater in the Shiloh Draw region and the Eightmile Draw region exhibits the largest degree of cation exchange. Interestingly, many data points representing groundwater in the Salt Flats region plot along the $-1:1$ line in the upper left quadrant of the graph; this indicates reverse cation exchange, where dissolved sodium is exchanged for calcium and magnesium that are adsorbed to minerals in the aquifer. This process has been observed in some hydrologic systems (Zaidi et al., 2015; Sajil Kumar and James, 2016), but it is rare. Evidence of reverse cation exchange suggests that groundwater that has undergone cation exchange, resulting in an increase in sodium concentrations, has moved into a different aquifer or facies that exhibits a significantly lower cation exchange capacity. This process should be studied further in this system.

As dedolomitization progresses, the molar ratio, or $(Ca + Mg) / SO_4$, approaches 1 (Richter and

Kreitler, 1986). Figure 3-18 shows $(Ca + Mg) / SO_4$ plotted as a function of relative sulfate concentration. Because dedolomitization is driven by the dissolution of gypsum, the relative increase in sulfate makes a good proxy to assess the degree to which this process has progressed. As expected, almost all groundwater samples from the Sacramento River region plot along a trend that approaches $(Ca + Mg) / SO_4 = 1$. Many points from the Shiloh Draw Region also plot along this trend. With the exception of a few wells within the Eightmile Draw and Salt Flats regions that show a $(Ca + Mg) / SO_4$ ratio of less than 1, most other data from these regions plot beneath the dedolomitization trend but above the $(Ca + Mg) / SO_4 = 1$ line.

Figure 3-19 shows the same plots as Figure 3-18 but with data that have been corrected for the cation exchange process. The sodium excess ($Na - Cl$, meq/L) term added to the $(Ca + Mg, meq/L)$ term show that the water chemistry prior to cation exchange was represented. This correction pulls

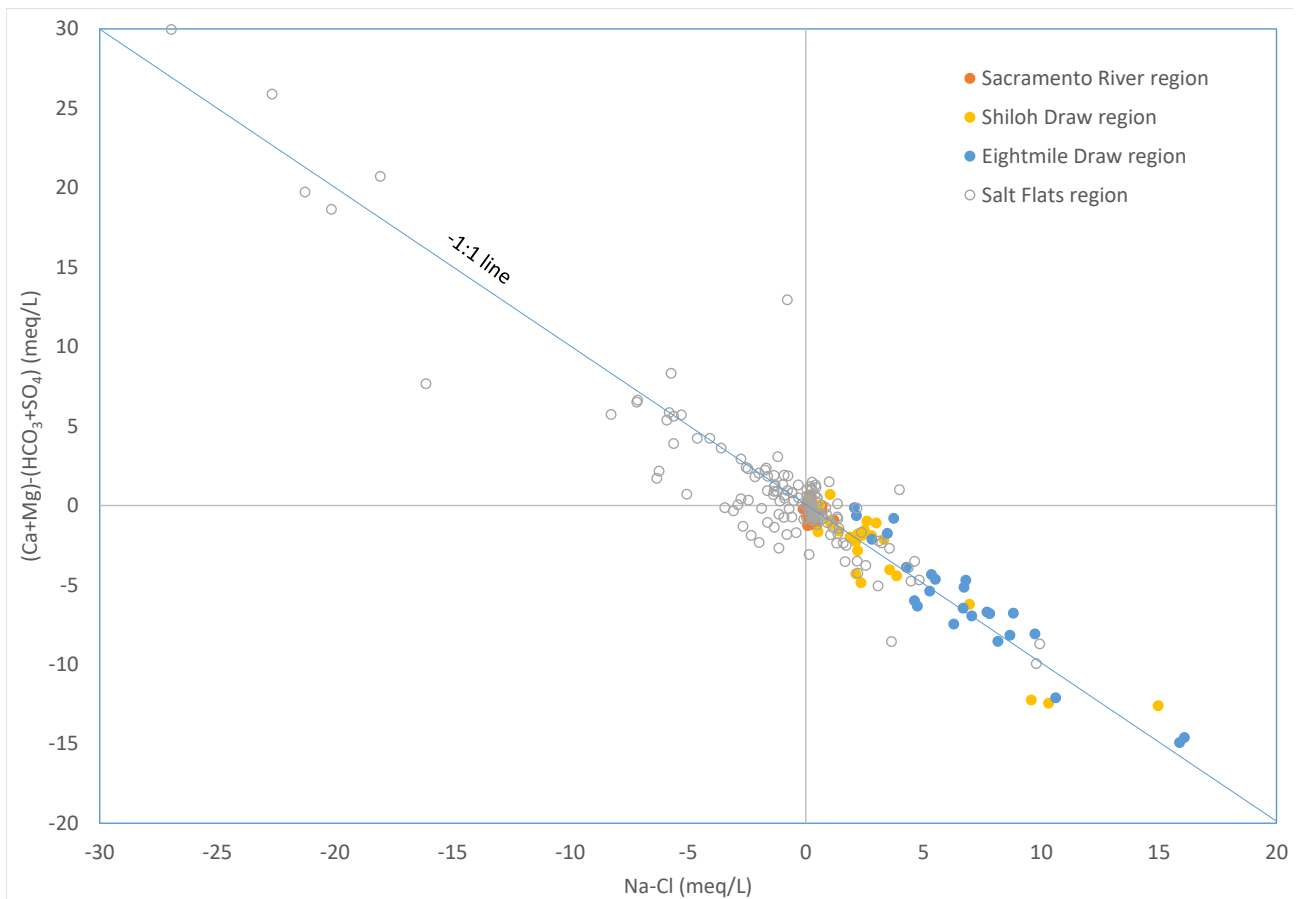


Figure 3-17. The cation deficit, $(Ca + Mg) - (HCO_3 + SO_4)$, plotted as a function of the sodium-chloride cation surplus ($Na - Cl$) is used to assess the occurrence of cation exchange. Data that plot on or near the line with a slope of -1 indicate that the cation exchange is occurring. The unit meq/L is the amount of millimoles per liter multiplied by the valence of the ion.

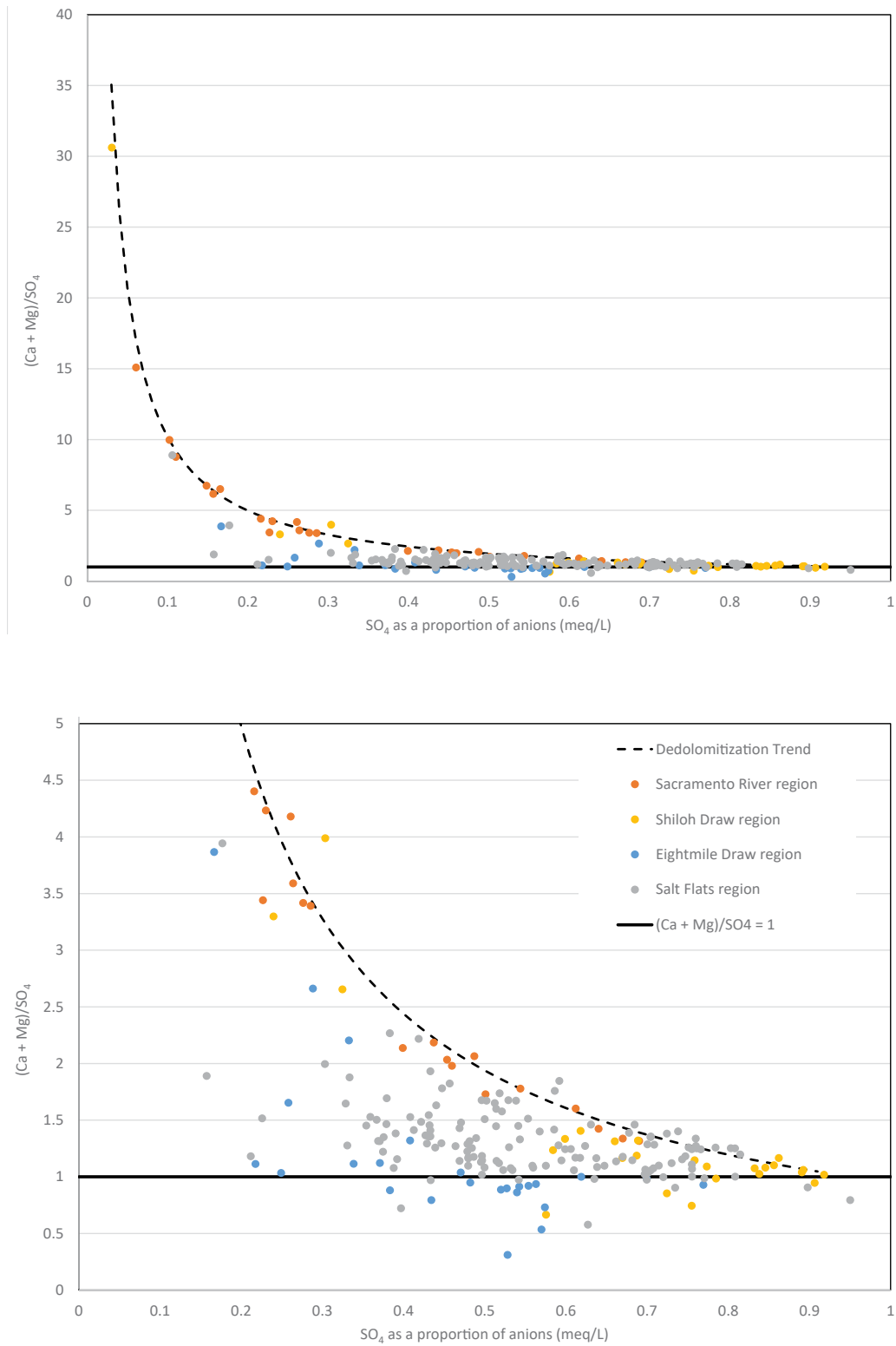


Figure 3-18. (Ca + Mg) / SO₄ plotted as a function of relative sulfate concentration. The dedolomitization trend was fit to data from the Sacramento River region, where dedolomitization is known to be occurring. This trend approaches a (Ca + Mg) / SO₄ ratio of 1 as dedolomitization progresses. The lower graph is zoomed in for more detail. These data have not been corrected for cation exchange.

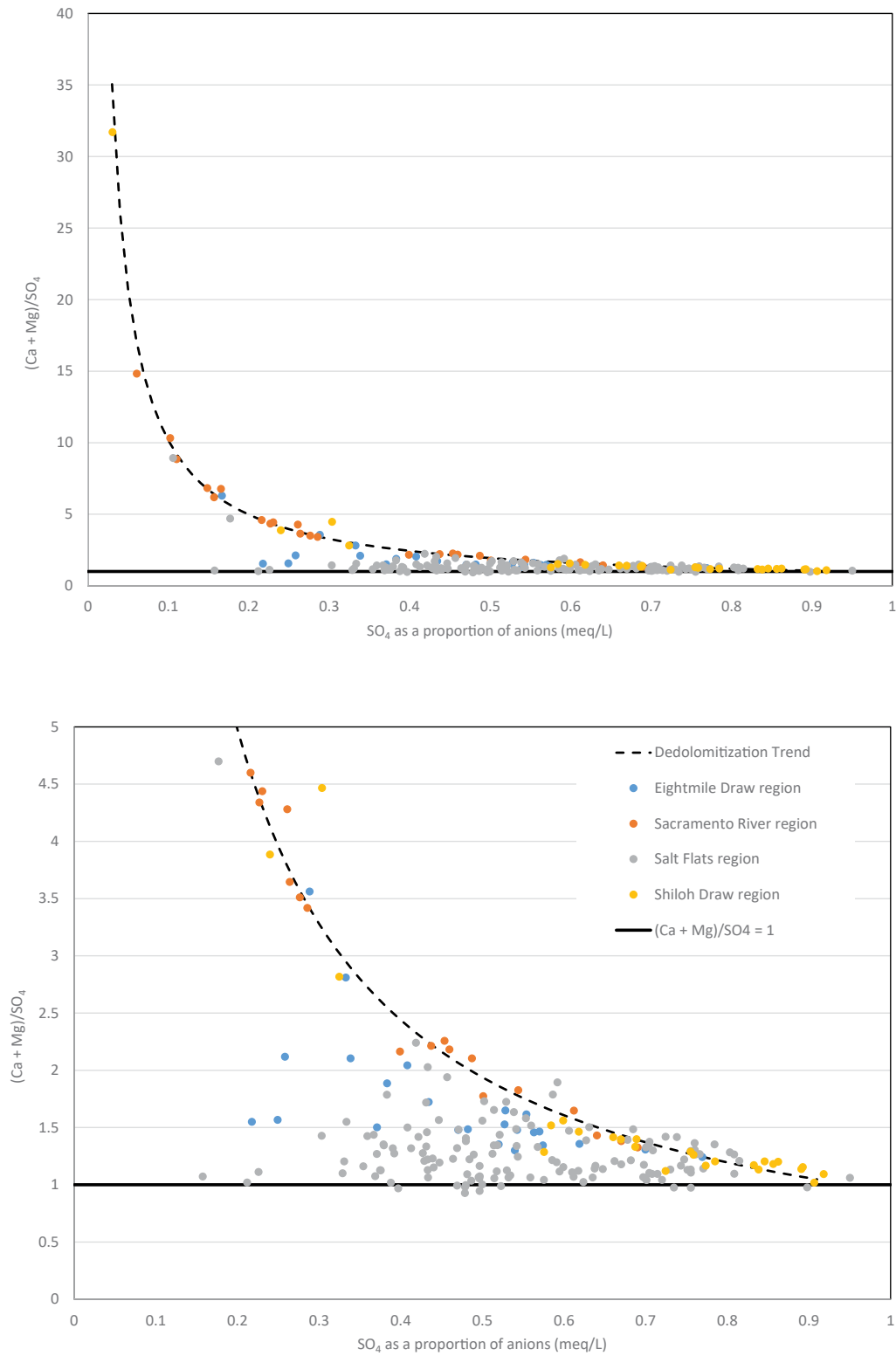


Figure 3-19. $(Ca + Mg) / SO_4$ plotted as a function of relative sulfate concentration. The dedolomitization trend was fit to data from the Sacramento River region, where dedolomitization is known to be occurring. This trend approaches a $(Ca + Mg) / SO_4$ ratio of 1 as dedolomitization progresses. The lower graph is zoomed in for more detail. These data have been corrected for cation exchange.

almost all data points that showed a $(Ca + Mg) / SO_4$ ratio of less than 1 up to equal to 1 or above. This correction also resulted in most of the points from the Shiloh Draw region that plotted below the dedolomitization trend lining up along the dedolomitization trend. These points mostly occur at the lower portion of the dedolomitization trend, suggesting that much of the groundwater in the Shiloh Draw region comes from the Sacramento River region, where dedolomitization is in progress. Dedolomitization continues to progress

in the Shiloh Draw region. Cation exchange clearly also plays a role in controlling the groundwater chemistry in this region.

To assess processes affecting the water chemistry for groundwater in the Eightmile Draw and Salt Flats regions, which mostly do not plot along the dedolomitization trend in Figure 3-19, we plotted chloride concentrations as a function of relative sulfate concentrations (Figure 3-20). From these plots, it is clear that high-chloride waters with chloride

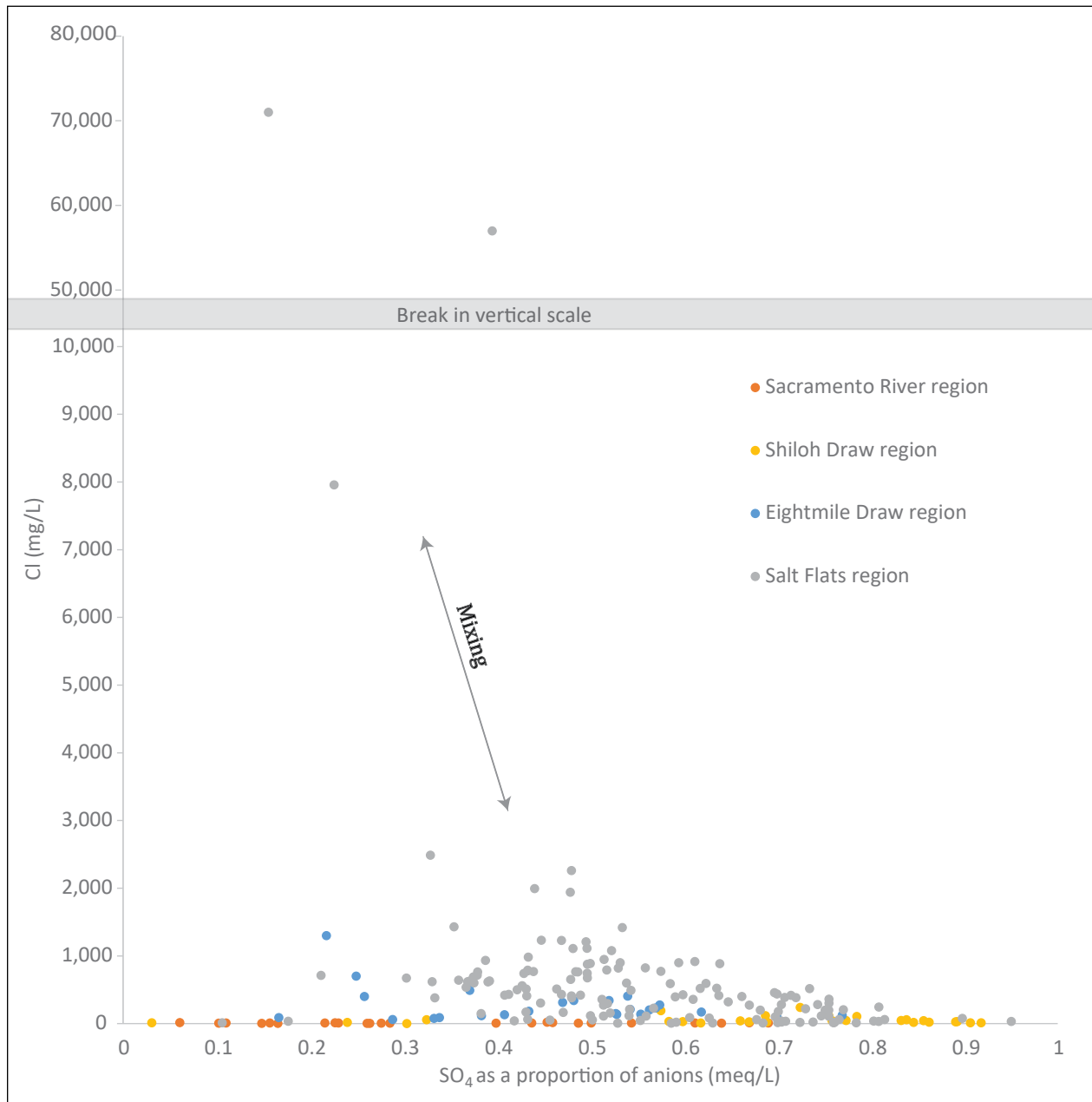


Figure 3-20. Chloride concentrations plotted as a function of relative sulfate concentrations shows mixing of high-chloride water mainly in the Salt Flats region.

concentrations as high as 7,000 mg/L and relative sulfate concentrations between 0.1 and 0.35 mg/L are mixing with groundwater that has undergone dedolomitization, which is significantly affecting the groundwater chemistry in the Eightmile Draw and Salt Flats regions.

CONCLUSIONS

General spatial trends observed in the water chemistry (Figures 3-2 through 3-8), tritium (Figure 3-14), and carbon-14 (Figure 3-15) show a progression in water chemistry evolution and groundwater age in the general down-gradient groundwater flow direction. However, no clear flowpaths can be identified or used to assess groundwater flow velocity or recharge rates. The complexity of the system, which makes it difficult to use water chemistry to identify actual flowpaths, is likely due to the compartmentalized nature of the fractured aquifer system in the carbonate bedrock. Water flows at variable rates, and with zones of limited aquifer connectivity, within permeable fractures, fault zones, and dissolution features. The influence of this fracture system is especially pronounced in the Eightmile Draw region, where we see clear evidence in the tritium data (Figure 3-14) for active recharge in this area. In semiarid regions like the Salt Basin, groundwater recharge is generally limited to high elevations in the mountains, in this case the Sacramento Mountains. Therefore, the identification of this low-elevation area as a recharge zone is significant and warrants further research to better quantify this water budget component.

While cation exchange and mixing of different water sources affect groundwater chemistry in the Salt Basin, dedolomitization is the primary process that controls it. Specifically, dedolomitization dominantly controls groundwater chemistry in the Sacramento River and Shiloh Draw regions. In the Shiloh Draw region, much of the groundwater chemistry appears to be due to the progression of dedolomitization of groundwater coming from the Sacramento River region in the north. However, there does appear to be groundwater flowing from the west and southwest (likely recharge through local fracture systems) that is also undergoing dedolomitization. Dedolomitization also affects groundwater chemistry in the Eightmile Draw region. However, there appears to be addition of high-chloride water mixing into the system as well as cation exchange that increases

sodium concentrations. Groundwater chemistry in the Salt Flats region appears to be a mixture of groundwater flowing from the north, west, and southwest, with the high-chloride end-member having a significant effect. Interestingly, an apparent decrease of cation exchange capacity within this region has resulted in reverse cation exchange, in which dissolved sodium is exchanged for magnesium and calcium that is adsorbed to clay minerals in the aquifer.



Field irrigated using a center-pivot well in Crow Flat. The Brokeoff Mountains and the Guadalupe Mountains are in the background.
Photo by Shari Kelley

CHAPTER 4: WATER BUDGET

Dan Cadol and Beth Ann Eberle

This multipart study used independent methods to investigate and further refine the components of the water budget in the Salt Basin aquifer system. Water inflows to the aquifer include (1) diffuse recharge, which falls as precipitation, then percolates through the soil and past the rooting zone; (2) focused recharge (or channel-focused recharge), which is surface runoff that concentrates in ephemeral channels and seeps through the channel bed as flow conveyance loss or accumulates in playas and infiltrates to the water table; and (3) subsurface groundwater inflows into the Salt Basin, primarily from the Peñasco Basin. Water outflows from the aquifer include (1) evaporation from playas (especially the Salt Flats) at times and locations where the water table is within the capillary rise of the surface; (2) net evapotranspiration losses (consumptive use) from irrigation water that is pumped from the aquifer and applied to agricultural fields; and (3) subsurface groundwater outflows, which are also likely, as exemplified by the hypothesized flowpath from the Salt Basin to springs near Balmorhea, Texas (Land and Veni, 2018). The following sections provide a brief description of the methods and results of this investigation as they relate to the overall water cycle.

Recharge was estimated by Eberle (2021) through a chloride mass balance analysis of both new and historic groundwater geochemical data. This technique relies on measurements of the concentration of atmospherically deposited chloride in groundwater, and it infers the amount of evapotranspiration necessary to have concentrated chloride to the extent observed. In locations where soil moisture rarely or never becomes recharge, such as the creosote-dominated lowlands of the Salt Basin, this method should only be applied to the fraction of precipitation that becomes runoff and is concentrated in ephemeral channels, where it infiltrates and may percolate below the rooting zone and eventually to the aquifer.

Therefore, this method was combined with a stochastic estimate of runoff produced by rainfall in a New-Mexico-specific Python-based model (Python Recharge Assessment for New Mexico Aquifers [PyRANA]; Xu, 2018). The PyRANA model also produces an estimate of diffuse recharge using a soil water balance (Ketchum, 2016); this was used to help define geographic locations in the basin where diffuse recharge through the rooting zone is more or less likely. Because the soil water balance model is highly sensitive to the soil water holding capacity, which is difficult to parameterize accurately in karst terrain, we also relied on elevation thresholds defined in past studies (Rawling and Newton, 2016), vegetation distribution, and PRISM precipitation thresholds to identify probable areas of diffuse recharge. Eberle (2021) also estimated crop consumptive evapotranspiration through historical satellite photo analysis and Blaney-Criddle evapotranspiration rate estimation, as described in the Evapotranspiration section of this chapter.

PRECIPITATION

PRISM Climate Group data were used for all precipitation estimates related to runoff and recharge. Prior research (Xu, 2018) suggests that an adjustment for daily monsoon season precipitation may be appropriate due to a scale mismatch between the small footprint of convective storms and the relatively large spacing between rain gauges in the network used by the PRISM regression algorithm. Xu (2018) calculated a monsoon season correction factor for daily PRISM precipitation based on data from the Walnut Gulch experimental station in southeastern Arizona and applied it to data from New Mexico. This correction increased values for large rainfall days by a factor of 1.47 and reduced low precipitation days by 1.6 mm depth (Xu, 2018). At the high end, this adjustment pattern accounts for the likelihood

of PRISM training gauges missing the high-intensity core of thunderstorms. At the low end, it corrects an artifact of PRISM spreading or smoothing the rainfall signal too broadly, presumably because the interpolation parameters are adjusted for other regions where rainstorms have larger footprints. However, long-term (annual or longer) PRISM values agreed well with the rain gauge network at Walnut Gulch, suggesting these two factors balance out over many storms, as would be expected for a well-calibrated regression model such as PRISM. Daily PRISM data were used to estimate runoff in New Mexico using PyRANA, so the monsoon season adjustment was used in this application. All other applications in this project considered long-term average precipitation, so unadjusted PRISM annual averages were used. This also helped to maintain continuity across the state border in this study region, since daily 800-m resolution PRISM data had not been purchased for Texas.

As mentioned above, precipitation data were used in two primary ways. First, annual average precipitation estimates were used with groundwater chloride data to directly estimate recharge in regions where diffuse recharge is expected to take place (Sacramento Mountains and high Guadalupe Mountains), as identified by elevation and PyRANA output. Second, daily precipitation data were used in a stochastic regression algorithm (Xu, 2018) to estimate daily runoff at a 250-m grid resolution in New Mexico during the period of 2000 to 2013.

RUNOFF

A module within PyRANA estimates surface runoff using an algorithm trained on data from the USDA Agricultural Research Station at Walnut Gulch, Arizona (Xu, 2018). This procedure estimates precipitation intensity as a probabilistic function of daily precipitation depth. Intensity is a function of both precipitation depth and duration, meaning intensity cannot be known from just the daily depth of rainfall. But there is an observed positive relationship between the two at Walnut Gulch, with a statistically normal distribution of residuals within bins of precipitation depth values, allowing probabilistic estimation of intensity. The procedure then considers the observed probability of a runoff event occurring as a function of the daily rainfall depth in the Walnut Gulch monitoring network.

Finally, it uses both precipitation depth and intensity in a regression to predict surface runoff at the 250-m grid scale. This procedure was applied to precipitation data in the New Mexico portion of the Salt Basin, and these daily runoff estimates were summed to annual totals which were averaged over the PyRANA analysis period of 2000 to 2013. Because PyRANA has only been parameterized to run within New Mexico, the runoff estimates needed to be extended into Texas. For this we used a regression of average annual runoff calculated by PyRANA against elevation from the USGS and mean annual precipitation from PRISM, with each 250-m grid cell serving as a data point. Calculations and raster handling were performed using R statistical software (R Core Team, 2018). This regression analysis produced the model

$$RO = 12.08 - (0.01607 \cdot Elev) - (0.000697 \cdot P) + (0.000044 \cdot Elev \cdot P)$$

where RO is mean annual runoff in mm, $Elev$ is elevation in m, and P is mean annual precipitation in mm. The R^2 of this model was 0.80 on the training dataset from the southern New Mexico portion of the Salt Basin south of the Sacramento Mountains. This equation was used to estimate mean annual runoff in the Texas portion of the basin. This runoff estimate is expected have the same characteristics of the original PyRANA runoff estimate: (1) it only considers runoff at scales larger than a 250-m grid cell (i.e., any local hillslope runoff that infiltrates before leaving the grid cell would not be measured as runoff); (2) it is only valid at time scales of a decade or longer because of the non-linear relationship between precipitation depth and runoff depth and the stochastic estimation of rainfall intensity based on daily precipitation depth; and (3) it is only valid for hydrometeorological settings similar to Walnut Gulch, where nearly all runoff is produced by localized, monsoon-season, convective storms. The Salt Basin does match this hydroclimatological setting reasonably well. In the recharge analysis that follows, regression estimates of runoff were only used in the Texas portion of the basin. The original PyRANA runoff estimates, which were used to train the regression, were used in New Mexico.

In this study, we evaluated the PyRANA runoff model against a broader dataset of runoff from Walnut Gulch than that used to train the model. The analysis conducted by Xu (2018) focused on three watersheds gauged by flumes that also had rain

gauges within the watershed or near the outlet. These sites were selected for completeness of the detailed daily data and for their basin sizes, which bracketed the size at which focused recharge was expected to commence in channels (10 to 100 ha). We do not expect small watersheds to contribute to focused recharge due to the associated short duration of flow and small channel width. This threshold is expected to be greater than 10 ha based on observations at the Jornada Experimental Range (Reuter et al., 2021). It may even be greater than 100 ha in some cases. Scanlon (1991) observed chloride bulges representing over 8,000 years of chloride accumulation under channels draining 550 ha and 2,100 ha near Camp Rice Arroyo, immediately south of the Salt Basin. This suggests even channels with relatively large drainage areas might contribute little to focused recharge in certain circumstances.

Further long-term runoff data from Walnut Gulch from a broader range of basin sizes are available for comparison with the analysis by Xu (Stone et al., 2008). When we plot these, we find that the smallest watershed analyzed by Xu (a drainage area of 1.9 ha) produced less runoff per rainfall input than other basins of that size over the analysis period of 2000 to 2015 (Figure 4-1). As a result, the basin-wide runoff/rainfall ratios estimated with this method may underestimate the runoff fraction for small watersheds (<100 ha), but it appears to function as intended at the ~100 to 1000 ha watershed scale (Figure 4-1). The trained PyRANA algorithm estimated runoff/rainfall ratios from 2% to 3% for the analyzed basins in Walnut Gulch. It produced a similar range of runoff/rainfall ratios when applied in the Salt Basin (Table 4-1).

The basin scale at which this algorithm is calibrated is important for the focused recharge estimation. Once the channel network accumulates sufficient flow for channel bed infiltration to regularly push water below the rooting zone and allow percolation to the water table, that point marks the basin size and runoff volume that are relevant for estimating focused recharge (discussed in the Recharge section). Channels draining basins of a scale at which infiltration is too limited to percolate past the rooting zone will retain water and reduce the runoff fraction of larger downstream channels, as represented by the decreasing runoff fraction in larger basins in Figure 4-1, but this water will be retained in the rooting zone and transpired by bankside vegetation rather than contributing to groundwater recharge. Any dissolved chloride will accumulate under the channel rather than being flushed into the groundwater—an effect that is of great importance to the chloride mass balance method of recharge estimation (see Chloride mass balance method section of this chapter). If this area threshold at which bed infiltration regularly percolates to the aquifer is indeed between 10 and 100 ha, the long-term Walnut Gulch data suggest that 3.5% to 5% of precipitation can be expected to become runoff that feeds focused recharge, which is greater than predicted by the PyRANA algorithm. However, if the threshold is between 100 and 1,000 ha, which may be the case in the Salt Basin according to the Scanlon (1991) study, then 2% to 3.5% of precipitation (the same range found by the algorithm; Table 4-1) would be expected to become runoff that feeds focused recharge. Therefore, we continue to use the trained PyRANA algorithm as the baseline “best-estimate” runoff fraction in this study, but we also consider a uniform

Table 4-1. Average annual precipitation and runoff volumes estimated for lowland, ephemeral sub-watersheds (Figure 4-4) of the Salt Basin, with calculated runoff/rainfall ratio.

Sub-Watershed Name	Area (km ²)	PRISM Mean Annual Precipitation (mm)	PyRANA Mean Annual Runoff (mm)	Best-Estimate Runoff/Rainfall Ratio	Low Uniform Runoff/Rainfall Ratio	High Uniform Runoff/Rainfall Ratio
North Draw	885	280	6.7	0.024	0.02	0.05
Piñon Wash	1830	376	7.9	0.021	0.02	0.05
Sacramento Lowlands	1550	361	8.8	0.024	0.02	0.05
Big Dog Canyon	431	344	10.9	0.032	0.02	0.05
Shiloh Draw	1010	328	9.4	0.029	0.02	0.05
Southern Watersheds	7880	281	7.3	0.026	0.02	0.05

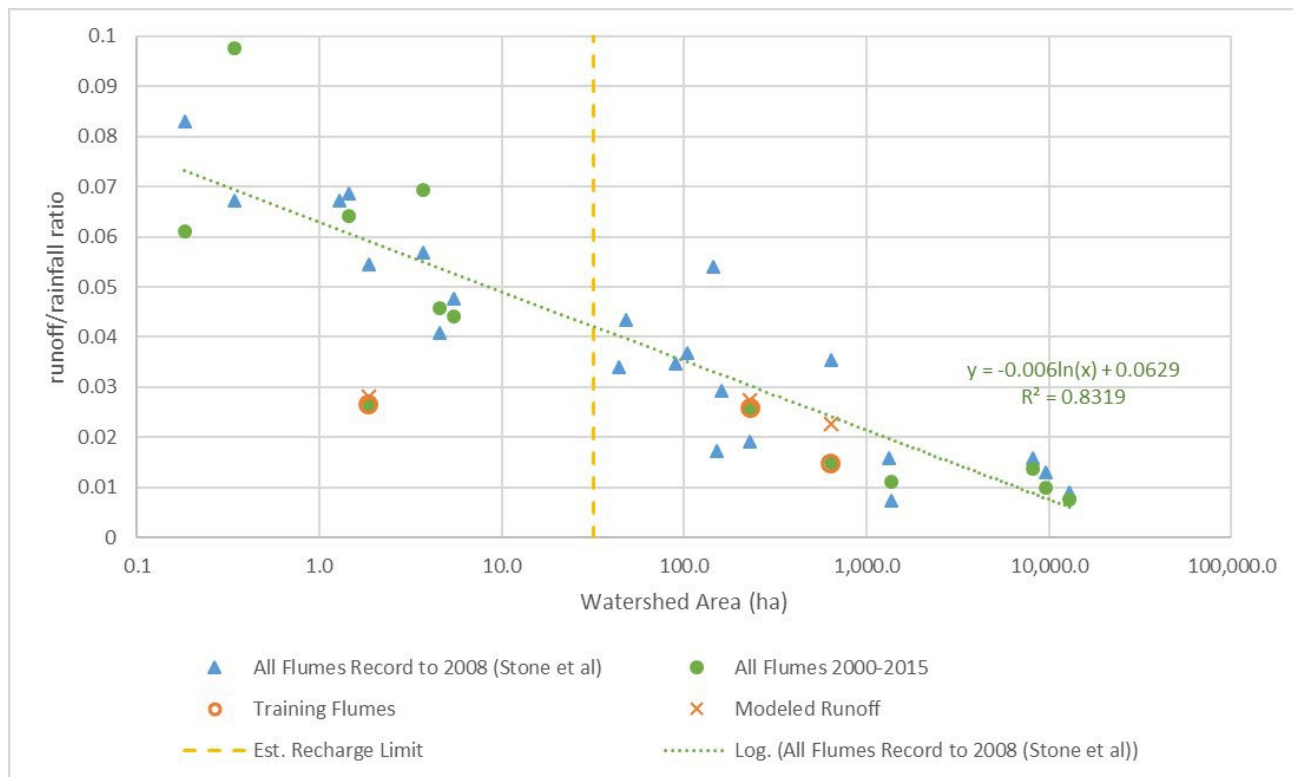


Figure 4-1. Long-term average runoff/rainfall ratios of monitored watersheds at Walnut Gulch, plotted against the drainage area of the watershed. Blue triangles indicate long-term data from Stone et al. (2008). Green circles indicate data from 2000 to 2015, the time period analyzed by Xu (2018). Orange circles mark the watersheds analyzed by Xu to produce the PyRANA runoff algorithm used in this study. Orange Xs indicate the modeled runoff/rainfall ratios at these three sites using the PyRANA algorithm. The vertical dashed yellow line is a rough approximation of the lower limit of watershed area that produces focused recharge that connects to the aquifer, as opposed to being fully consumed by near-channel evapotranspiration after infiltration. The actual limit may be anywhere from 10 ha to 1,000 ha and should vary with channel-bed saturated hydraulic conductivity.

2% runoff fraction and a uniform 5% runoff fraction in our analyses (Table 4-1). We discuss the effects of runoff/rainfall ratio in the Recharge section.

RECHARGE

Our conceptual model of recharge in the Salt Basin can be divided into two major pathways: diffuse recharge in the mountainous uplands and focused recharge (also referred to in this report as channel-focused recharge) in the basin lowlands. In the diffuse recharge pathway, precipitation or snowmelt saturates the soil and sediment of the rooting zone, predominantly in ponderosa pine forests but possibly also in piñon-juniper woodlands, and enables water to percolate below the depth of roots. This process is most prevalent in the Sacramento Mountains and possibly the high elevations of the Guadalupe Mountains, but it is a significant source of recharge in spite of its small spatial extent. These recharge events

when soil is saturated are relatively limited in time and are modeled to occur only a few times a year or less, depending on assumptions about soil thickness and rooting depth. The thin soils and underlying karstic bedrock of the Sacramento and Guadalupe Mountains promote this form of recharge. Once the water has moved past the rooting zone, it may follow an exclusively subsurface flowpath through the mountain block and into the aquifers underlying the central Salt Basin. Groundwater may re-emerge as baseflow in a perennial river; however, the only example of this in the Salt Basin is the Sacramento River and its small spring-fed tributaries at the north margin of the Salt Basin watershed. Recharged water that reemerges as streamflow will typically re-infiltrate into the subsurface as the Sacramento River leaves the mountain front and transitions from a gaining to a losing river. Water may emerge and infiltrate multiple times along its flowpath, although in the Salt Basin this process is only expected to occur

along the corridor of the Sacramento River valley within the Sacramento Mountain block. The flow in the river may be supplemented by overland flow from a fraction of precipitation events or snowmelt that does not infiltrate into the soils, but the fate of this water will be similar, infiltrating into the channel bed at or near the mountain front. With the exception of water that is transpired by stream-adjacent riparian vegetation, most of this surface water will eventually reach the central basin aquifer. Of the total precipitation falling on these mountainous areas, most will be transpired by vegetation, with a small amount evaporated from the ground or channel surface and the remainder recharging the basin aquifer. The fraction that becomes recharge can be estimated with the chloride mass balance method (see next section and Rawling and Newton, 2016). Although the mountainous uplands represent a small proportion of the total area of the Salt Basin, these processes make them an important source of recharge.

The second recharge pathway we conceptualize is focused recharge in the ephemeral channels of the remainder of the basin. Precipitation that falls on the creosote-dominated hillslopes and plains of the low-lying areas may either infiltrate or run off as overland flow. In areas with significant surface sediments, the water that infiltrates is unlikely to be able to percolate beyond the deep-rooted creosote, which is able to exert an unusually high tension on the soil to extract water (Scanlon, 1991; Sandvig and Phillips, 2006; Reuter et al., 2021). Infiltration is typically stored for eventual transpiration by the desert vegetation, thus no diffuse recharge occurs in these areas. The runoff, however, concentrates into ephemeral channels. During flow events, infiltration through the channel bed can push water below the rooting depth of the channel-adjacent vegetation, from whence it may percolate downward and accrete to the underlying water table. If surface flow continues to a downstream playa, the finer-grained surface sediment relative to the active channel bed will reduce infiltration and retain water near the surface, but it is still possible for some recharge to occur here before the water is evaporated, especially if there are preferential flowpaths.

With focused recharge, the duration of flow and the hydraulic conductivity of the bed material are the primary controls on the amount of bed infiltration. The amount of bed infiltration necessary to push

water past the rooting zone of channel-adjacent vegetation depends on channel width and the rooting depth of vegetation. Hence, small channels draining small watersheds are less likely to produce focused recharge than larger channels draining extensive fluvial networks. As described in the previous section, the scale at which focused recharge begins is important for our analysis of aquifer recharge. But constraints on this scale are limited, and local conditions play an important role.

We expect focused recharge to be the most important source of recharge in the lowland portions of the Salt Basin. However, a possible exception to the lack of diffuse recharge in the lowlands would be locations where the surface sediments are thin and underlain by fractured or karstic bedrock. An extended rainfall event may saturate this thin soil and enable fracture flow. However, this requires saturation of the soil, which is expected to be kept at low moisture content by any desert vegetation. Enhancement of focused recharge is more likely to occur where flows cross exposed bedrock, perhaps even in very small channels or hillslopes. Additionally, if water ponds at the surface, any fracture or karst conduit that is unobstructed by sediment from previous flow events would rapidly convey the water into the subsurface and past the influence of the rooting zone.

All of these recharge paths will convey dissolved chloride and bromide from wet and dry atmospheric deposition along with the water. The following section outlines the fluxes and reservoirs of chloride and describes its use in estimating recharge.

Chloride mass balance method

Chloride, along with bromide, is delivered to the land surface from the atmosphere both during rainstorms that wash dust from the atmosphere (wet deposition) and between storms as dust settles to the land surface (dry deposition; Wood, 1999). One important source of atmospheric chloride is the evaporation of sea spray, which leaves tiny salt crystals suspended in air currents. Because chloride is non-reactive and stays in solution, it travels along the hydrological pathways described in the previous section. As water is evaporated along any flowpath, chloride concentrations increase proportionally. Given an initial and final chloride concentration, the fraction of water evaporated from the system (or alternatively,

the fraction of water remaining) can be calculated. To do so, the method must differentiate between atmospheric chloride and chloride from mineral dissolution within the aquifer.

The atmospheric deposition rate is dependent on atmospheric conditions, and consequently it has varied from the Pleistocene to the Holocene (Zhu and Liu, 2003). For the Holocene (less than 12,000 years ago), the steady-state atmospheric chloride deposition flux in the study area has been estimated to be 0.55 mg/L (Rawling and Newton, 2016). Chloride in groundwater can also derive from mineral or sedimentary sources typically manifesting as brines. The sedimentary sources of chloride typically have much lower bromide concentrations than atmospheric sources.

On the hydrologic pathway of mountainous diffuse recharge (described in the previous section), chloride accumulates on the land surface and on the canopy during periods of dry deposition. Rainfall, carrying wet depositional chloride with it, dissolves the available chloride accumulations on the surfaces it interacts with. The portion of rainfall that is intercepted by the canopy and does not drip to the land surface evaporates following the storm and precipitates its chloride on the vegetation. This storage is only temporary, however, as subsequent storms that fill canopy storage will flush the retained chloride. Water that infiltrates into the soil transports chloride in solution as it percolates toward the water table. Any water that is evaporated from the soil or extracted by roots for transpiration will leave behind its chloride content, increasing the concentration in the remaining soil water. The abundance of water in the high mountains and the solubility of chloride ensure that all atmospheric chloride is eventually delivered to the water table. In the Sacramento Mountains, runoff from either storm overland flow or springs and baseflow also conveys the chloride load down gradient toward the main channel and eventually to the losing reaches of the Sacramento River at the mountain front. In the high Guadalupe Mountains, there is likely to be frequent-enough flow to convey all atmospheric chloride to the mountain front aquifer as well. Evapotranspiration along the riparian zones of both mountainous areas serves to further concentrate chloride. The mixing of focused recharge and diffuse recharge in the aquifer results

in a concentration of chloride that is representative of total evaporation losses from the entire mountainous watershed.

On the focused recharge hydrologic pathway in the central basin lowlands (described in the previous section), chloride likewise accumulates on the land surface during periods of dry deposition. Water that infiltrates into the soil at the start of a storm dissolves much or all of this dry deposition and delivers it to the root zone. If the water is unable to infiltrate past the root zone but is transpired by desert vegetation, the chloride will accumulate in the soil at the most common depth of infiltration. These “bulges” of chloride in the soil profile have been observed under many vegetation communities typical of the Salt Basin (Sandvig and Phillips, 2006). In creosote settings, the accumulations appear to represent the entire chloride load deposited on the landscape during the Holocene (Phillips et al., 1988; Walvoord and Phillips, 2004). Chloride bulges have also been observed beneath small channels (Scanlon, 1991; Reuter et al., 2021), indicating further chloride storage in the smallest-order portions of the channel network. Hence, a significant portion of the atmospheric chloride may not reach the aquifer and should not be included in the chloride mass balance analysis.

Surface runoff in the larger-order channels of the basin lowlands, in contrast, does contribute to recharge (i.e., through channel-bed infiltration that escapes the rooting zone) and conveys some portion of the chloride deposited at the surface. As runoff flows over the surface, it may or may not encounter additional chloride. Previous rain in the area may have flushed the dry deposition into the soil with it during the initial phase of rapid, sorptivity-controlled infiltration. Alternatively, the runoff may flow into areas outside the storm footprint, in which case surface accumulations of chloride may be incorporated into the flow. Additionally, flow that passes through the soil and re-emerges farther down a hillslope would be expected to accumulate chloride previously deposited in the soil. For these reasons, the degree to which surface runoff mimics the typical atmospheric chloride concentration is presently unknown. To investigate this issue, we analyzed flash-flood runoff samples from the Arroyo de los Pinos near Socorro, New Mexico, for chloride and bromide concentration on the rising and falling limb of the flow event and found concentrations

similar to those of meteoric waters (see Results and Discussion section of this chapter). In any case, once the runoff focuses in channels, any evapotranspiration along the flowpath serves to concentrate the chloride. However, preferential flowpaths such as karst conduits rapidly convey the surface water to depth, where the concentration should no longer be subject to alteration by evaporation.

For both major pathways (mountain-block recharge and ephemeral channel-focused recharge), there remains the complication of non-atmospheric chloride. Sedimentary sources of chloride, as well as connate water from the time of marine deposition, can produce brines that mix with meteoric waters and increase the chloride concentration. Fortunately, these brines typically have a much higher Cl/Br ratio than meteoric waters. Correction of total groundwater chloride concentration to the atmospheric contribution can be accomplished by utilizing both chloride and bromide data in a mixing model that assumes a particular sedimentary brine chloride concentration and Cl/Br ratio.

This model, as well as the resulting estimate of the fraction of the initial meteoric water that contributed to recharge, is sensitive to the estimate of meteoric water concentration, which depends on both the estimate of wet and dry deposition and on precipitation amount. It is also sensitive to the chloride concentration and Cl/Br ratio of the assumed brine end-member. We explored a range of end-member compositions to evaluate the uncertainty of the resulting recharge estimate.

We used a two-end-member chloride mixing model developed for the region by Rawling and Newton (2016). The first freshwater end-member explored in our work, following Rawling and Newton (2016), was assumed to have a chloride concentration of 0.55 mg/L, which was the highest value consistent with their groundwater data from the Sacramento Mountains, and a Cl/Br ratio of 65, which was the lowest value observed in their spring and groundwater samples. We tested higher atmospheric concentrations as well because areas with lower annual precipitation may be expected to dilute the atmospheric chloride flux less, and the 0.55 mg/L estimate was for the highest-precipitation portion of the Salt Basin. For comparison, measured bulk precipitation chloride concentration (both

wet and dry combined) was 0.27 mg/L in Santa Fe, New Mexico (Anderholm, 1994), and 3.4 mg/L in Socorro, New Mexico (Rawling and Newton, 2016).

The initial brine end-member explored in our work was also from Rawling and Newton (2016), at a value of 10,000 mg/L chloride and Cl/Br ratio of 9,000. These values were selected in consideration of a brine found during well drilling near Cloudcroft, New Mexico, that had 130,000 mg/L chloride and no detectable bromide (Rawling and Newton, 2016). These values do not match the Cloudcroft brine because the values were modified downward to provide a mixing curve that cleanly delineated the Sacramento Mountain data. We also explored brine end-members from groundwater samples collected near the Salt Flats and Dell City. As with the atmospheric end-member, it is possible that different brine end-members should be considered in different geographic portions of the Salt Basin.

The chloride mass balance method, when assuming conservation of chloride and only local atmospheric sources of chloride, can be summarized with the equality

$$R(C_{gw}) = P(C_{atm})$$

where R is mean annual recharge, C_{gw} is mass concentration of chloride in groundwater, P is mean annual precipitation, and C_{atm} is mass concentration of chloride in meteoric waters. Solving for the fraction of precipitation that becomes recharge (R_{frac}), which is the ratio of recharge to precipitation, gives $R_{frac} = C_{atm}/C_{gw}$. If the concentrations are equal, the interpretation would be that no water evaporates. For each doubling of C_{gw} , the estimate of R_{frac} will be halved (for constant C_{atm}).

The presence of sedimentary chloride brines and the resulting mixing can be accommodated by considering an adjusted chloride concentration that only includes the chloride in the groundwater from atmospheric sources (C_{gw-adj}). The calculated mixtures of the two end-members produce a curve when chloride concentration is plotted against the Cl/Br ratio (Figure 4-2). Because evaporation increases chloride concentration while leaving Cl/Br ratio unchanged, groundwater samples in theory plot to the right of this mixing curve. For each groundwater sample, an unevaporated mixture of the two end-members can be found with an equal Cl/Br ratio

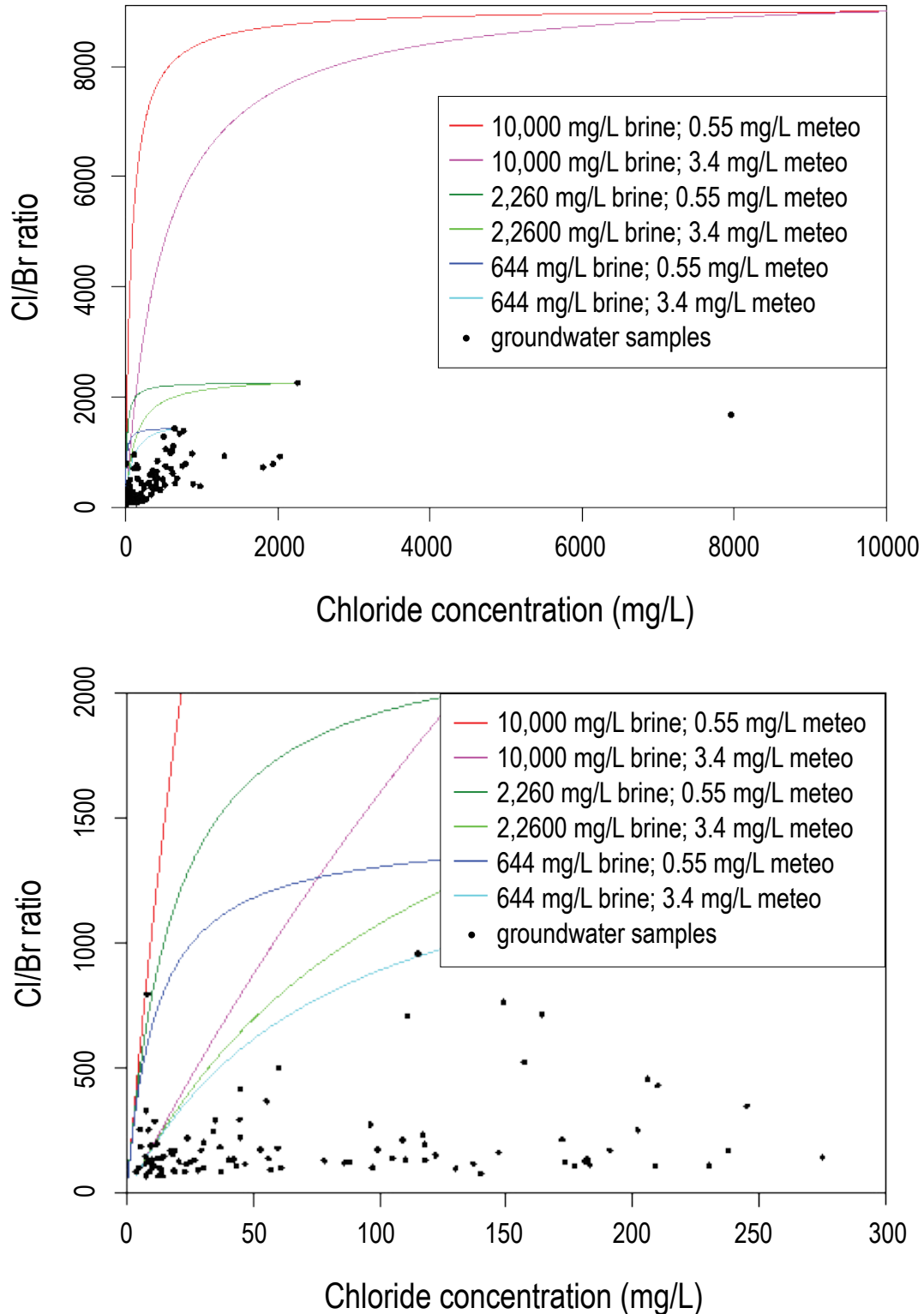


Figure 4-2. Scatter plot of Salt Basin chloride and bromide groundwater sample data. Six different meteoric-brine chloride mixing curves are shown, crossing two meteoric (labeled as “meteo” on graph) water values with three brine water values. The meteoric end-members are: 0.55 mg/L chloride and 65 Cl/Br ratio (after Rawling and Newton, 2016), and 3.4 mg/L chloride (reported for Socorro, New Mexico) and 65 Cl/Br. The brine end-members are: 10,000 mg/L chloride and 9,000 Cl/Br ratio (after Rawling and Newton 2016); 2,260 mg/L chloride and 2,260 Cl/Br ratio (highest Cl/Br groundwater sample within Salt Flats); and 664 mg/L chloride and 1,431 Cl/Br ratio (highest Cl/Br sample near Dell City). The lower plot is zoomed in to show more detail.

to the sample and a lower (or equal) chloride concentration, which we define as the mixing concentration (C_{mix}). Because evaporation has driven a chloride concentration change from this C_{mix} to the measured C_{gw} , the ratio of these values gives the recharge fraction

$$R_{frac} = C_{mix}/C_{gw}$$

just as the ratio of atmospheric and groundwater chloride concentrations gave the recharge fraction in the idealized non-mixing case. We can also calculate the chloride concentration in groundwater from strictly atmospheric sources as

$$C_{gw-adj} = (C_{gw}/C_{mix})C_{atm}$$

The value of C_{mix} is highly sensitive to the initial estimate of C_{atm} used in the mixing model, particularly at low Cl/Br ratios. As the Cl/Br ratio increases, sensitivity to the estimate of brine chloride concentration (C_{brine}) increases.

There are many ways to write the relationship between chloride concentration and Cl/Br ratio in the mixing model. One convenient form, which calculates chloride concentration as a function of Cl/Br ratio and the properties of the two end-members, is

$$C_{mix} = \frac{Br_2 - Cl_2 \left(\frac{Br_2 - Br_1}{Cl_2 - Cl_1} \right)}{\frac{1}{Cl/Br} - \left(\frac{Br_2 - Br_1}{Cl_2 - Cl_1} \right)}$$

where C_{mix} is the chloride concentration of the unevaporated mixture, Cl/Br is the Cl/Br ratio of the mixture and subsequent groundwater sample, Cl_1 and Br_1 are the chloride and bromide concentrations of the meteoric water end-member, and Cl_2 and Br_2 are the chloride and bromide concentrations of the brine end-member. Using this equation, the original unevaporated chloride concentration C_{mix} for any groundwater sample can be found given the groundwater Cl/Br ratio, assuming it is a mixture of only the meteoric and brine end-members.

As part of our sensitivity analysis, we explored three different brine mixing members: (1) the 10,000 mg/L chloride and 9,000 Cl/Br ratio end-member of Rawling and Newton (2016); (2) a 2,260 mg/L chloride and 2,260 Cl/Br ratio end-member from the dataset near the Salt Flats (the concentration and ratio have the same value because bromide concentration

was measured to be 1.0 mg/L); and (3) a 664 mg/L chloride and 1,431 Cl/Br ratio end-member from the dataset near Dell City (Figure 4-2). We also explored the simple case of no sedimentary chloride. Likewise, we explored four different concentrations of chloride in meteoric waters: 0.55 mg/L (following Rawling and Newton, 2016), 0.75 mg/L, 1.0 mg/L, and 3.4 mg/L (the reported bulk chloride value in meteoric waters near Socorro, New Mexico, from Popp et al., 1984).

Certain groundwater data points were inconsistent with particular mixing curves. One sample from the Piñon Draw sub-watershed had an unexpectedly high Cl/Br ratio (795) for its chloride concentration (7.95 mg/L) and plotted to the left of all but one chloride mixing curve (i.e., the lowest meteoric concentration and highest brine concentration tested). Mathematically, points left of the curve produce recharge fraction estimates that exceed 100%. Therefore, this sample was considered to be an outlier but for unknown reasons and was not included in the analysis. A similar issue arose for mixing curves that used the highest chloride meteoric water end-member we tested (3.4 mg/L). Numerous points plotted left of the mixing line, generating recharge fraction estimates significantly above 100% (Figure 4-2). These points were all from either the Sacramento Mountains or Piñon Draw watershed, suggesting that 3.4 mg/L is not a plausible value of meteoric waters in those recharge zones—a finding consistent with Rawling and Newton's (2016) Sacramento Mountains analysis. Meteoric end-member values of 1.0 mg/L and lower did not produce recharge fraction estimates exceeding 100%. A final incompatibility occurred for the mixing curve using the brine end member with the lowest chloride concentration (664 mg/L) and Cl/Br ratio. Two data points had Cl/Br ratios higher than this end-member, which resulted in slightly negative estimates of recharge fraction. Both of these negative estimates were set to zero.

Rather than applying a single average recharge fraction to the entire Salt Basin, we divided the Salt Basin into sub-watersheds with consistent groundwater chloride concentrations (Figure 4-3). The sub-watershed divisions generally followed surface water divides (USGS HUC-10 delineations), but some surface watersheds were merged into broad areas with generally similar chloride and surface processes, and one surface watershed (North Draw)

was divided along a mapped groundwater divide (Figure 4-3). We also separated the two mountainous regions, where diffuse recharge is likely, into separate recharge zones based on our conceptual model of the hydrologic flowpaths. Within each sub-watershed or region, an average value of R_{frac} was found for all groundwater samples that were amenable to chloride mass balance analysis (i.e., had detectable bromide).

The mountainous polygons considered the total precipitation rate to be the source potential of recharge. The mean annual precipitation volume (mean depth multiplied by polygon area) was multiplied by the recharge fraction to estimate total annual volumetric recharge. For the lowland polygons, total precipitation volume would not be representative of the source of potential recharge due to the limited diffuse recharge characteristic of this environment (Sandvig and Phillips, 2006) and the expected accumulation of chloride in the rooting zone of the desert vegetation. Therefore, the mean annual runoff volume for each lowland polygon, as estimated by PyRANA (see Runoff section above), was multiplied by the recharge fraction to estimate average annual groundwater recharge volume. To provide constraints on uncertainty, we also calculated recharge using runoff volumes derived from uniform runoff/rainfall ratios of 2% and 5% across all lowland sub-basins. The total annual recharge volume from the chloride mass balance method is the sum of the recharge rates from each sub-basin polygon.

The use of runoff volume as the recharge fraction multiplier in the lowlands is a novel approach. It assumes that runoff has similar chloride concentration as the typical meteoric waters. To test this assumption, we analyzed runoff samples from a late-monsoon-season flash flood in Arroyo de los Pinos—an ephemeral watershed near Socorro, New Mexico, where meteoric chloride has been reported to have bulk concentrations of 3.4 mg/L (Popp et al., 1984). Chloride concentration in the rising limb of the flood was 2.1 mg/L, while three samples from the falling limb of the flood ranged from 1.5 to 1.7 mg/L. Even using a more sensitive bromide analytical method, all the runoff samples were non-detects at the 0.01 mg/L level. This indicates a Cl/Br ratio of greater than 150 for the falling limb and greater than 210 for the rising limb—both higher than the assumed ratio for precipitation in the Sacramento Mountains, which was 65 (Rawling and Newton, 2016). These higher Cl/Br ratios may be due to the preferential uptake of bromide by vegetation from soil moisture (Davis et al., 1998) that contributes to runoff, though subsequent death and decay of vegetation at the ground surface would be expected to make the bromide available again for dissolution in runoff (Gerritse and George, 1988). It is uncertain how closely Salt Basin ephemeral runoff should be expected to match these waters from Arroyo de los Pinos, though the two basins have similar vegetation cover, lithology, and mean annual precipitation.

Table 4-2. Recharge estimates for the Salt Basin using meteoric and brine end-member compositions of 0.55 mg/L and 10,000 mg/L, respectively, from Rawling and Newton (2016). For Sacramento Mountains and Guadalupe Mountains, total precipitation (acre-ft/yr) was used instead of PyRANA runoff as the source of potential recharge. In the subtotals and totals, recharge fraction is a weighted mean, weighted by watershed area.

Watershed	Area (acres)	Runoff or *Precipitation (acre-ft/yr)	Average Corrected Recharge Fraction	Recharge Volume (acre-ft/yr)
North Draw	218,743	4,792	0.051	245
Piñon Wash	453,280	11,678	0.162	1,898
Sacramento Lowlands	384,093	11,040	0.100	1,099
Big Dog Canyon	106,587	3,826	0.054	206
Shiloh Draw	250,092	7,747	0.023	176
Southern Watersheds	1,946,923	46,572	0.019	885
Sacramento Mts.	39,618	*86,386	0.302	26,081
Guadalupe Mts.	29,120	*48,430	0.099	4,805
Mountain Area Subtotal	68,738	*134,817	0.216	30,885
Lowland Area Subtotal	3,359,718	85,654	0.051	4,509
Total Salt Basin	3,428,456	220,471	0.054	35,395

Recharge results and discussion

The chloride mass balance method used 139 groundwater well samples that had analytical results for both chloride and bromide. We produced an average brine-adjusted recharge fraction over the aerial extent of each recharge area (Figure 4-3) for each of the 16 chloride mixing model end-member combinations. The average corrected recharge fractions for the meteoric and brine end-members proposed by Rawling and Newton (2016) are shown in Table 4-2, along with the resulting estimate of volumetric annual groundwater recharge in each polygon. The two recharge regions with primarily diffuse recharge are the Sacramento Mountains and Guadalupe Mountains, and all of the annual precipitation was considered as the source water for potential recharge. Recharge from these two mountain blocks dominates the estimated total for this scenario, with ~31,000 acre-ft/yr of the total 35,000 acre-ft/yr coming from these two zones, and 26,000 acre-ft/yr of that is from the Sacramento Mountains alone. This is because the lowland watersheds are assumed to receive only focused recharge (i.e., water and chloride that infiltrate in the hillslopes and flats do not pass beyond the rooting zone), and the recharge fractions resulting from this particular end-member mixing curve produce generally low recharge fraction estimates.

The assumption of negligible diffuse recharge at the 250-m grid scale is supported by chloride profile analyses conducted under small (<1 m wide) ephemeral channels in nearby creosote-dominated landscapes in the Jornada Experimental Range near Las Cruces, New Mexico (Reuter et al., 2021), and in the Hueco Bolson near Fort Hancock, Texas, just south of the Salt Basin (Scanlon, 1991). But it is possible that enhanced flow in karst conduits could enable some recharge from hillslope-scale runoff. A study of unsaturated flow in fissures near Van Horn, Texas, in the southern Salt Basin showed that water potentials were higher and chloride concentrations were lower than in surrounding sediments (Scanlon et al., 1997). But the continued presence of a chloride bulge, though slightly diminished, suggests that even in this favorable location for recharge, not enough water passes beyond the root zone to transport the atmospheric chloride. Therefore, the results presented here limit the possible recharge volume to that of runoff, as estimated by the empirical

PyRANA algorithm. We note that if this assumption is violated, recharge volumes would be higher than estimated here.

We analyzed the sensitivity of the recharge estimates to meteoric water and brine chemistry. Greater concentrations of chloride in meteoric waters lead to greater estimates of recharge (Table 4-3), leading eventually to estimates of recharge fractions that exceed 100% (Table 4-4). For the tested mixing curves, the mountainous areas produce the majority of recharge. However, it is not assured that the end-members will be spatially uniform across the Salt Basin. It is reasonable to suspect that meteoric waters will have higher chloride concentrations in the lowlands where mean annual precipitation depths are lower.

For the lowland watersheds, where runoff is the source of recharge, the initial chloride concentration has additional uncertainty. We tentatively assume it is the same as rainfall, which is consistent with rainfall being the source of runoff and with our analysis of runoff water from near Socorro, New Mexico, but it is possible that as the water runs off the landscape it picks up additional chloride deposited on the soil surface. If the chloride concentration of runoff is actually higher than in rainfall, then our estimates would be lower than actual recharge in these portions of the basin, or we should prefer the higher estimates of meteoric chloride concentration in the range of values explored (Table 4-5). Given the spatial proximity of these basins to the two lower-concentration brine end-members and the greater distance from Cloudcroft, where the higher chloride brine was observed, it is also reasonable to prefer the lower brine concentration values in this analysis. All of the groundwater samples from the lowland watersheds had high enough chloride concentration to at least be conceptually compatible with all four meteoric chloride concentrations explored in this analysis, meaning there were no recharge fraction estimates exceeding 100% (Table 4-6). The highest average was 37%. The procedure for averaging recharge fractions across multiple recharge polygons in this report was to produce a weighted arithmetic mean that was weighted by polygon area.

The highest total estimate for recharge in the Salt Basin that used spatially uniform end-members and did not produce recharge regions with recharge fractions above unity was for the 1.0 mg/L meteoric

Table 4-3. Recharge volume estimates (in acre-ft/yr) for the mountainous recharge zones only for a range of possible mixing end-members. Red text indicates recharge fractions exceeding 100% due to incompatibility of the mixing curve with sample data.

		Brine			
		10,000 mg/L	2,260 mg/L	644 mg/L	No mixing with brine
Meteoric					
0.55 mg/L		30,885	32,668	34,227	9,378
0.75 mg/L		42,114	44,536	46,632	12,789
1.0 mg/L		56,149	59,364	62,106	17,052
3.4 mg/L		190,793	201,263	208,911	57,976

Table 4-4. Recharge fraction estimates (unitless) for the mountainous recharge zones only for a range of possible mixing end-members. Red text indicates recharge fractions exceeding 100% due to incompatibility of the mixing curve with sample data.

		Brine			
		10,000 mg/L	2,260 mg/L	644 mg/L	No mixing with brine
Meteoric					
0.55 mg/L		0.216	0.228	0.239	0.067
0.75 mg/L		0.295	0.311	0.325	0.092
1.0 mg/L		0.393	0.415	0.433	0.122
3.4 mg/L		1.335	1.406	1.458	0.415

Table 4-5. Recharge volume estimates (in acre-ft/yr) for the lowland recharge zones only for a range of mixing members.

		Brine			
		10,000 mg/L	2,260 mg/L	644 mg/L	No mixing with brine
Meteoric					
0.55 mg/L		4,509	5,390	6,005	1,895
0.75 mg/L		6,149	7,148	7,935	2,585
1.0 mg/L		8,198	9,344	10,320	3,446
3.4 mg/L		27,855	30,319	32,330	11,717

Table 4-6. Recharge fraction estimates (unitless) for the mountainous recharge zones only for a range of mixing members.

		Brine			
		10,000 mg/L	2,260 mg/L	644 mg/L	No mixing with brine
Meteoric					
0.55 mg/L		0.051	0.062	0.069	0.021
0.75 mg/L		0.070	0.082	0.091	0.029
1.0 mg/L		0.093	0.107	0.119	0.038
3.4 mg/L		0.315	0.345	0.369	0.130

Table 4-7. Recharge estimates for the Salt Basin using meteoric and brine end-member compositions of 1.0 mg/L and 644 mg/L, respectively. For Sacramento Mountains and Guadalupe Mountains, total precipitation (in acre-ft/yr) was used instead of PyRANA runoff as the source of potential recharge. In the subtotals and totals, recharge fraction is a weighted mean weighted by watershed area.

Watershed	Area (acres)	Runoff or *Precipitation (acre-ft/yr)	Average Corrected Recharge Fraction	Recharge Volume (acre-ft/yr)
North Draw	218,743	4,792	0.098	469
Piñon Wash	453,280	11,678	0.320	3,741
Sacramento Lowlands	384,093	11,040	0.190	2,102
Big Dog Canyon	106,587	3,826	0.101	388
Shiloh Draw	250,092	7,747	0.043	332
Southern Watersheds	1,946,923	46,572	0.071	3,288
Sacramento Mts.	39,618	*86,386	0.613	52,960
Guadalupe Mts.	29,120	*48,430	0.189	9,146
Mountain Area Subtotal	68,738	*134,817	0.433	62,106
Lowland Area Subtotal	3,359,718	85,654	0.119	10,320
Total Salt Basin	3,428,456	220,471	0.125	72,426

end-member and the 644 mg/L brine end-member. These assumptions produce an estimate of 72,000 acre-ft/yr of recharge, again dominated by the mountain blocks, which contribute 62,000 acre-ft/yr (Table 4-7).

Because the end-members may vary spatially, we attempted to select end-member combinations for each delineated recharge area (Figure 4-4) that lead to higher-end, but still plausible, estimates of recharge (Table 4-8). The total recharge estimate of 57,000 acre-ft/yr was not as heavily dominated by the Sacramento Mountains, which contributed 29,000 acre-ft/yr, as the previous estimates with spatially uniform end-members, though it still contributed over half of the total.

We next explored the influence of uncertainty in the runoff/rainfall ratio in the lowland portion of the basin, where focused recharge in ephemeral channels is dominant. For this comparison, we used the spatially varying end-member scenario (Table 4-8) as our baseline and replaced the PyRANA-derived runoff estimates with uniform 2% and 5% runoff/rainfall values (Table 4-9). Mountain area recharge estimates were unchanged since these did not rely on runoff estimates. Assuming uniform runoff at 2% of mean annual precipitation reduced recharge estimates for the lowland areas from 18,500 acre-ft/yr to 14,900 acre-ft/yr, while assuming 5% runoff increased lowland recharge to 37,300 acre-ft/yr, nearly as much as the mountainous areas.

As discussed in the Runoff section, the long-term average fraction of rainfall that becomes focused-recharge-feeding runoff is a key uncertainty in this analysis. Tables 4-2, 4-7, and 4-8 all present runoff and recharge figures that assume the PyRANA-derived runoff/rainfall ratios of 2% to 3.5% are accurate. If the algorithm underestimates runoff, either due to the unusually low runoff ratio at the smallest training site during the period of analysis or due to an overestimation of the contributing area at which focused recharge to the aquifer commences, then values in the 3.5% to 5% range (i.e., ~1.5 times higher) may be more appropriate. Indeed, the issue is likely to vary spatially. If a localized watershed has more exposed bedrock than the training sites in Walnut Gulch and/or the channel bed is more highly conductive and can convey water to the aquifer during short runoff events, then the fraction of precipitation that becomes recharge-contributing runoff will be higher. Given the research of Scanlon (1991) at the southern edge of the Salt Basin suggesting limited focused recharge for 550 ha to 2,100 ha watersheds, we do not think this issue will be present at all watersheds. But it is likely to be present in certain areas, such as near the bedrock exposures of the Cornudas Mountains.

Finally, we explored the effect of using chloride concentrations and Cl/Br ratios similar to those found in the runoff at Arroyo de los Pinos near Socorro for the lowland area sub-basins. Recall that

Recharge Volume (acre-ft/year and percent of total)

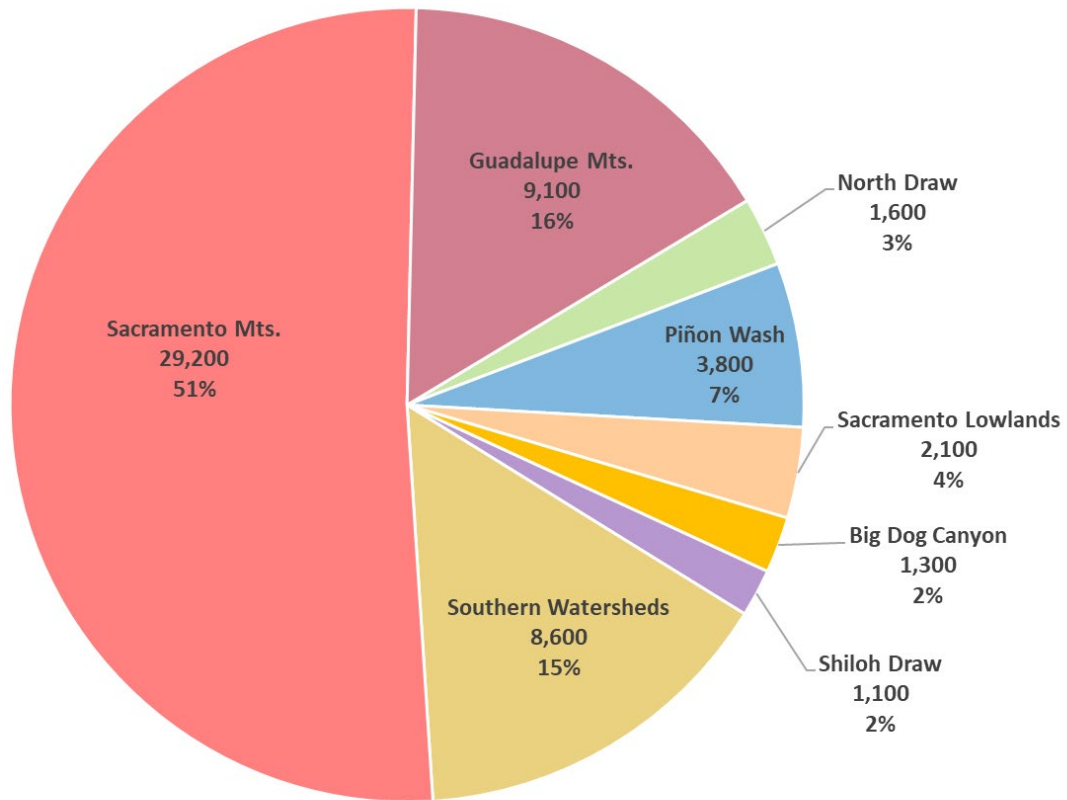


Figure 4-4. Recharge volumes and percentages based on the recharge regions shown in Figure 4-3 and spatially variable end-member estimates (Table 4-8).

Table 4-8. A possible combination of spatially varying end-members and the resultant average corrected recharge fractions for groundwater samples within each recharge watershed, with annual volumetric recharge estimates.

Watershed	Meteoric end-member (mg/L)	Brine end-member (mg/L)	Average Corrected Recharge Fraction	Recharge Volume (acre-ft/yr)
North Draw	3.4	644	0.331	1,600
Piñon Wash	1	644	0.320	3,800
Sacramento Lowlands	1	644	0.190	2,100
Big Dog Canyon	3.4	644	0.344	1,300
Shiloh Draw	3.4	644	0.145	1,100
Southern Watersheds	3.4	644	0.184	8,600
Sacramento Mts.	0.55	644	0.338	29,200
Guadalupe Mts.	1	644	0.189	9,100
Mountain Area Subtotal			0.275	38,300
Lowland Area Subtotal			0.215	18,500
Total Salt Basin			0.216	56,800

Table 4-9. Influence of runoff/rainfall ratio on recharge estimation. Mountain area recharge is unaffected by change since total precipitation is used for those areas where diffuse recharge is expected.

Watershed	Average Corrected Recharge Fraction	PyRANA Runoff Recharge Volume (acre-ft/yr)	2% Runoff Recharge Volume (acre-ft/yr)	5% Runoff Recharge Volume (acre-ft/yr)
North Draw	0.331	1,600	1,300	3,300
Piñon Wash	0.320	3,800	3,600	9,000
Sacramento Lowlands	0.190	2,100	1,800	4,300
Big Dog Canyon	0.344	1,300	800	2,100
Shiloh Draw	0.145	1,100	800	2,000
Southern Watersheds	0.184	8,600	6,600	16,600
Sacramento Mts.	0.338	29,200	29,200	29,200
Guadalupe Mts.	0.189	9,100	9,100	9,100
Mountain Area Subtotal	0.275	38,300	38,300	38,300
Lowland Area Subtotal	0.215	18,500	14,900	37,300
Total Salt Basin	0.216	56,800	53,200	75,600

the analyzed runoff had a chloride concentration of 2.1 mg/L on the rising limb of the flash flood and 1.5 to 1.7 mg/L on the falling limb. Bromide was not detected with an analytical sensitivity of 0.01 mg/L. For reference, the total lowland recharge was 6,000 acre-ft/yr when using Cl = 0.55 mg/L and Cl/Br = 65—the expected meteoric waters in the Sacramento Mountains—and Cl = 644 mg/L and Cl/Br = 1431 for the brine. When using a meteoric end-member of Cl = 1.5 mg/L and Cl/Br = 150 (the lowest possible ratio given the non-detect of bromide at 0.01 mg/L sensitivity), the lowlands were estimated to produce 6,600 acre-ft/yr of recharge (with the same brine end-member). Recharge estimates decreased rapidly with higher Cl/Br ratios. When using Cl = 2.1 mg/L and Cl/Br = 210—values from the rising limb of the runoff event—lowland recharge was estimated to be 6,300 acre-ft/yr. These are all significantly lower than the highest lowland recharge scenario tested, 32,300 acre-ft/yr, which came from a meteoric-end member of Cl = 3.4 mg/L and Cl/Br = 65. Clearly, both the chloride concentration and the Cl/Br ratio of

the runoff (i.e., meteoric) end-member in the focused lowland recharge analysis exert significant influence on the estimated recharge.

In summary, both the mixing model end-members and the fraction of rainfall that becomes runoff in aquifer-recharging channels had significant influence within our uncertainty estimates on total aquifer recharge and the spatial distribution of recharge. Varying both factors led to total recharge estimates for the basin that varied from 35,000 to 84,000 acre-ft/yr (Table 4-10). Future work to constrain these estimates would improve the certainty of the recharge estimates. This work could include runoff sampling in the Salt Basin to constrain the runoff end-member, stream gauging to develop local runoff/rainfall relationships, and coring of the channel network to extract chloride profiles under a range of channel sizes and lithologic conditions to investigate focused recharge distribution. Additional groundwater samples with both chloride and bromide analyses would also help constrain the recharge fraction.

Table 4-10. Summary table of basin-wide recharge estimates in acre-ft/yr depending on chloride mass balance (CMB) end-member assumptions and runoff/rainfall ratio. The “low uniform” meteoric and brine end-member compositions are 0.55 mg/L and 10,000 mg/L, respectively (see Table 4-2), while the “high uniform” meteoric and brine end-member compositions are 1.0 mg/L and 644 mg/L, respectively (see Table 4-7). The “mixed” end members are listed in Table 4-8.

	Low uniform CMB end-members	Mixed CMB end-members	High uniform CMB end-members
2% runoff/rainfall (uniform)	34,800	53,200	71,000
PyRANA runoff (spatially variable)	35,400	56,800	72,400
5% runoff/rainfall (uniform)	40,500	75,600	84,100

EVAPOTRANSPIRATION

Agricultural consumption methods

Consumptive use is the difference between the volume of pumped irrigation water and the infiltrated water that percolates back down through the soil to recharge the aquifer (Ashworth, 1995; Mayer and Sharp, 1998). In other words, it is the amount of pumped water that is applied to the fields by center-pivot or flood irrigation that is then transpired by the vegetation or evaporated from the soil surface. To estimate this total volume of evapotranspiration, we first estimated a rate (depth) of evapotranspiration for each month using the Blaney-Criddle method (e.g., Allen and Pruitt, 1986). The rate found by this method is intended to describe evapotranspiration from a well-watered crop, such as alfalfa, and is most reliable during growing season. To determine the area of active irrigation each year, we used Landsat multispectral satellite imagery (USGS, 2021) analyzed in Google Earth Engine, a cloud-based platform that provides access to geospatial databases and simplifies analyses using high-performance parallel computing (Gorelick et al., 2017). We then multiplied the total depth of evapotranspiration during the growing season (March through October) by the irrigated acreage for that year to find the total volume of consumptive use for the year.

The Blaney-Criddle method was used to calculate a reference crop evapotranspiration (ET_o). This method was chosen because it is commonly used by the New Mexico Office of the State Engineer to estimate evapotranspiration and because the data requirements are very simple, as they are based solely on temperature and sunlight hours. The Blaney-Criddle method is most reliably applied at the monthly time scale. Daily minimum and maximum temperatures are averaged to find the daily mean, and the daily means are averaged to find the monthly mean temperature (T_{mean}). Reference crop evapotranspiration is then estimated as

$$ET_o = p(0.457 \cdot T_{mean} + 8.128)$$

where p is the mean daily percentage of annual daytime hours for that month (e.g., each day in January represents 0.24% of the annual daylight hours at 30°N latitude), T_{mean} is in degrees Celsius, and ET_o is in mm/day. The maximum and minimum temperature data were downloaded from a NOAA

network weather station in Dell City, Texas, with daily data for January 1, 1984 to December 31, 2019 (National Centers for Environmental Information, 2021). The result, ET_o , for each month is a reference transpiration rate that is only achieved if the crop is healthy and well-watered. We assume that the farmers of the area strive for this state during the growing season, and so we consider the summed ET_o for the 8 months between March 1 and October 31 to be a reasonable measure of total evapotranspiration during the irrigation season. During the remainder of the year, crops will probably not transpire at the reference rate due to senescence, harvesting, and lack of irrigation. For comparison we also calculated a full year reference evapotranspiration. This full year value was more directly comparable with the ensemble cumulative annual evapotranspiration product produced by the OpenET consortium (discussed below).

To estimate the area of active agriculture, we used the Normalized Difference Vegetation Index (NDVI; USGS, 2021) data provided within Google Earth Engine as the ‘Tier 1, 8-day NDVI composite’ images from Landsat 5, 7, and 8. NDVI is a spectral difference ratio used to identify vegetation, calculated as

$$(NIR - red) / (NIR + red)$$

where NIR is the near-infrared band (845 to 885 nm wavelength) reflectance and red is the visible red band (630 to 680 nm wavelength) reflectance. For most of the analysis period, extending from 1984 to 2019, Landsat satellites passed over the Salt Basin every 8 to 16 days. Return times were shorter for time periods when two Landsat satellites were active. Each satellite overpass provided a snapshot of the vegetation if there were no clouds to interfere. We focused our analysis on the growing season, which we defined as March through October based on both visual inspection of the Landsat imagery and the characteristic planting and harvesting dates for cotton and alfalfa in New Mexico, the most common agricultural products of Dell City, Texas (Bjorklund, 1957; NM MEP, 2018).

Our mapping of irrigated agriculture necessitated developing a representative growing-season NDVI map across Dell City and outlying agricultural areas (Figure 4-5). To filter out the effects of clouds, harvesting, and other transient low-NDVI events, we

stacked the scenes from all overpasses for a given growing season and found the 85th-percentile NDVI value at each pixel of the scene. This means that as long as one-fifth of the overpasses were cloud-free, which is usually the case in this arid environment, we retrieved data representing the vegetation for that pixel. NDVI varies over the growing season in both agricultural fields and native vegetation. The variability is often greater in native vegetation due to temporary green-up after a rainfall event. We used the 85th-percentile NDVI for each pixel instead of the maximum value because we wanted to avoid the influence of very short-term green-up, which can bring non-irrigated land into the range of NDVI values typically associated with irrigation in this environment. We also wanted to exclude poorly

watered agricultural fields, which may have had some growth in spite of being fallow in that year.

Once we had the 85th-percentile-filtered scene, representing typical growing season greenness for each pixel while avoiding cloud influence, we set a simple threshold NDVI value of 0.5 to distinguish irrigated agriculture from other land covers (Figure 4-5). The threshold of 0.5 was chosen to be slightly lower than the NDVI of a manually selected field within the Salt Basin domain that was identified to be an active agricultural field with lower-than-average greenness. We tested this threshold value by comparing our estimates of irrigated acreage with those of Groeneveld and Baugh (2002), as reported in Hutchison (2006), and we found the comparison to be consistent.

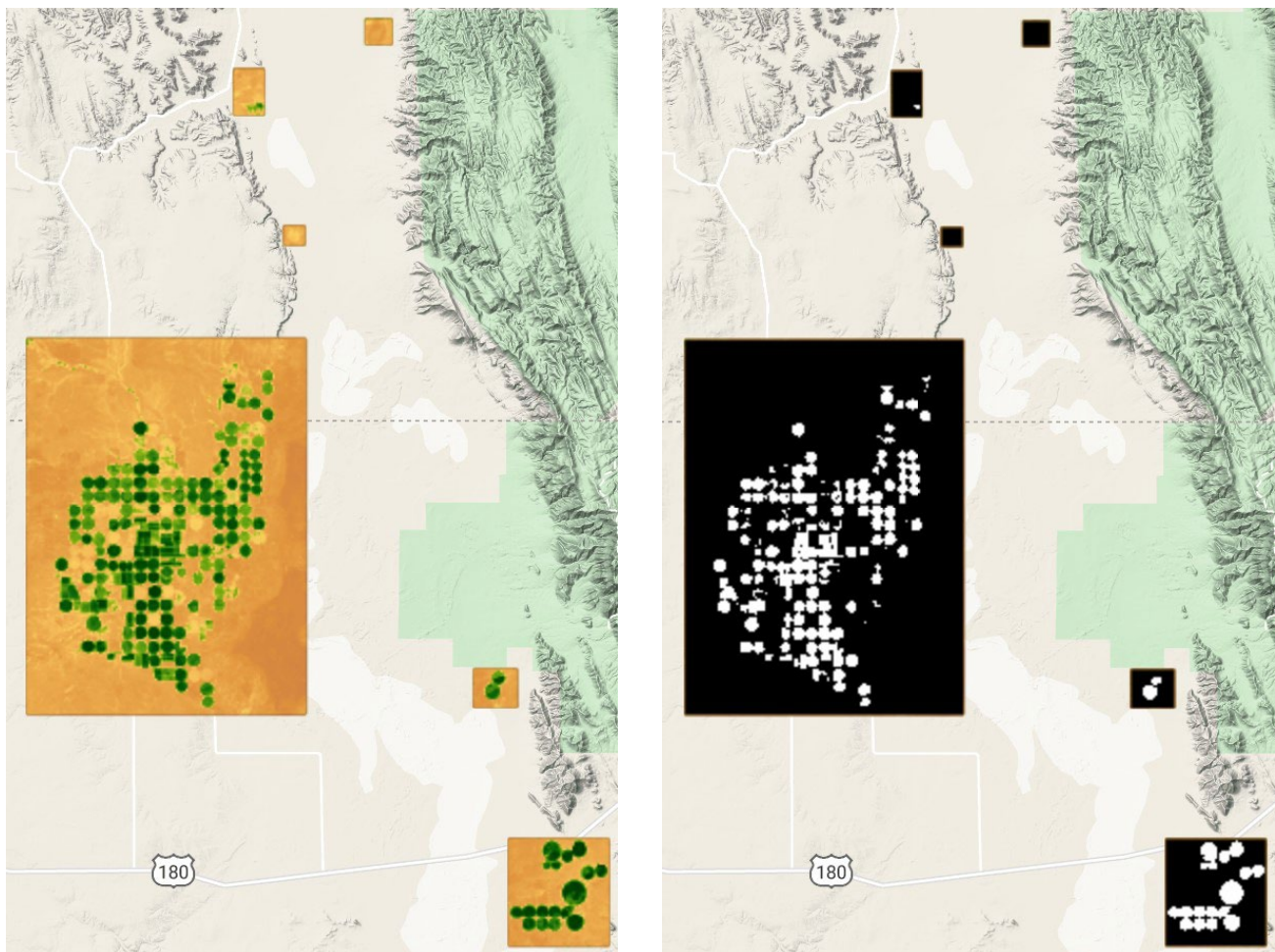


Figure 4-5. Irrigated land assessment using normalized difference vegetation index (NDVI) data. On the left, the Google Earth Engine 85th-percentile-filtered growing season scene for 2019. On the right, the areas identified as active irrigation based on an NDVI threshold of 0.5 (shown in white).

To determine the total agricultural consumptive use, we multiplied this area of active irrigation with the cumulative reference crop evapotranspiration estimated by the Blaney-Criddle method for the growing and irrigation season of that year.

Agricultural consumption discussion and results

The estimated reference crop evapotranspiration during the growing season (March through October) using the Blaney-Criddle method over the time period 1984 to 2019 averaged 1.29 m/yr, with a minimum value of 1.25 m/yr and a maximum value of 1.33 m/yr (Table 4-11). The value was very stable through time and had a standard deviation of only 0.025 m/yr in our dataset. If the entire year was considered, the Blaney-Criddle method produced a total annual reference evapotranspiration of 1.63 m/yr on average (minimum = 1.57 m/yr, maximum = 1.68 m/yr, standard deviation = 0.03 m/yr).

The actively irrigated areas calculated in Google Earth Engine using Landsat NDVI data were a much more variable driver of annual consumptive loss (Figure 4-6), averaging 7,300 ha with a minimum of 4,738 ha in 1992 and a maximum of 10,660 ha in 2004 (Table 4-11). The standard deviation in the 1984 to 2019 annual time series was 1,500 ha.

The product of the growing season reference evapotranspiration and the active agricultural acreage gives our estimate of consumptive use. The mean annual value was 76,670 acre-ft/yr, with a minimum of 49,250 acre-ft/yr in 1992 and a maximum of 112,070 acre-ft/yr in 2004 (Table 4-11).

These volumes of evapotranspiration increase if we include winter season evaporation. The average Blaney-Criddle estimate of total evapotranspiration including winter was 1.63 m/yr in our study period, and the average estimate of volumetric water loss was 96,750 acre-ft/yr. It is debatable whether these winter losses should be considered consumptive use. Water is not being applied, so the evaporation is likely supplied by natural precipitation. However, if soil moisture that was delivered during irrigation season is slowly being evaporated in the winter, these losses could be considered part of agricultural consumptive use. The role of precipitation complicates this debate as well as the attribution of winter transpirative losses to groundwater consumption.

As an independent source of evapotranspiration data, we downloaded estimates of total evapotranspiration (which may be less than reference evapotranspiration) from the newly launched OpenET web data interface (openetdata.org).

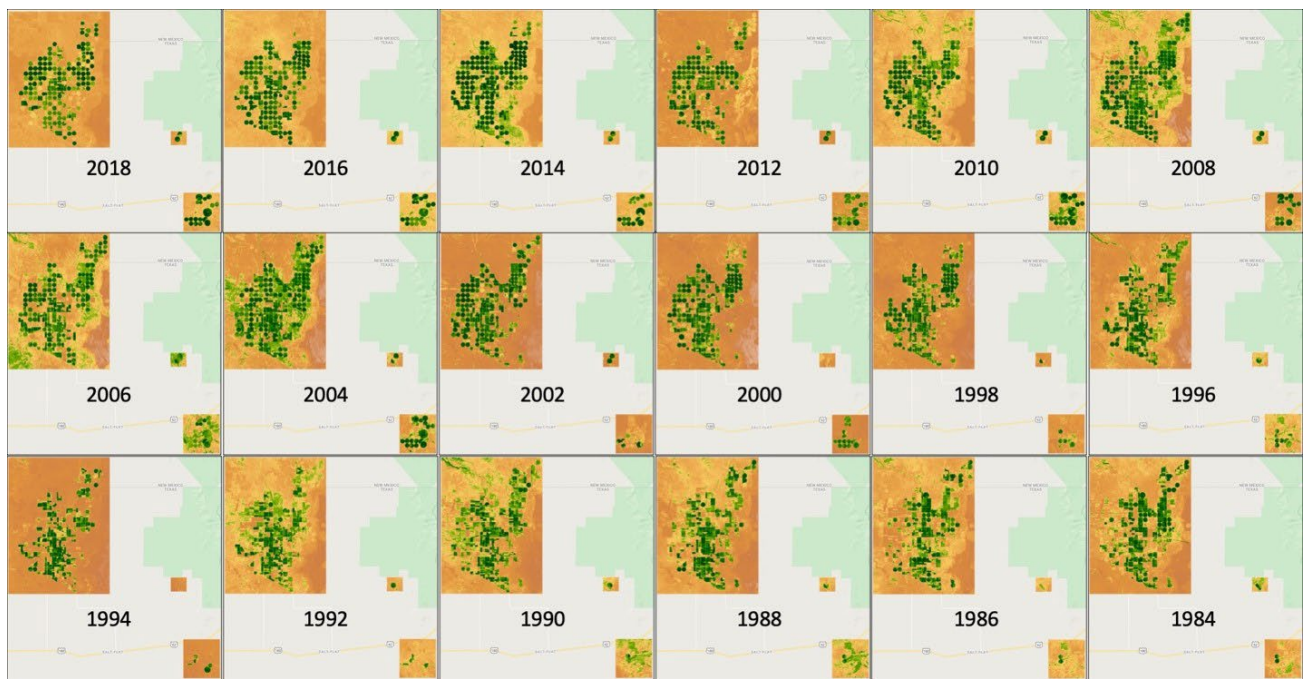


Figure 4-6. NDVI maps of the Dell City area for every other year in the satellite record. The NDVI values are the 85th-percentile-filtered growing season values. The color ramp scales from dark green for an NDVI of 1 to dark orange for an NDVI of 0. The prevalence of flood versus center-pivot irrigation techniques can be seen to vary through time, as can the intensity of irrigation in outlying areas farther east from the main Dell City area.

Table 4-11. Annual irrigated acreage in the Dell City, Texas, area, including outlying irrigated areas and growing season (March through October) Blaney-Criddle reference evapotranspiration based on Dell City temperature data for the years 1984 to 2019. Volume of annual consumptive use is the product of the two.

Year	Irrigated area (ha)	Growing Season Reference ET (m)	Agricultural consumptive use (acre-ft/yr)
1984	7,006	1.26	71,517
1985	5,622	1.25	57,220
1986	5,693	1.25	57,572
1987	6,937	1.25	70,577
1988	6,222	1.25	62,883
1989	5,683	1.31	60,343
1990	6,247	1.27	64,534
1991	5,935	1.25	60,163
1992	4,738	1.28	49,251
1993	4,806	1.29	50,266
1994	5,210	1.32	55,734
1995	5,555	1.29	58,277
1996	6,448	1.28	66,916
1997	5,884	1.29	61,673
1998	7,012	1.31	74,267
1999	7,675	1.29	80,378
2000	7,644	1.33	82,357
2001	8,039	1.31	85,732
2002	8,467	1.33	91,600
2003	8,760	1.32	93,512
2004	10,660	1.30	112,073
2005	8,267	1.28	86,028
2006	8,275	1.30	86,982
2007	9,616	1.29	100,891
2008	9,199	1.28	95,261
2009	7,065	1.33	76,060
2010	7,849	1.33	84,479
2011	5,537	1.33	59,776
2012	6,878	1.33	74,271
2013	8,894	1.30	93,720
2014	9,064	1.30	95,690
2015	9,592	1.30	101,455
2016	8,665	1.28	89,825
2017	8,722	1.28	90,570
2018	7,319	1.31	77,742
2019	7,770	1.28	80,537

OpenET calculates evapotranspiration using six different energy budget methods or their derivatives: METRIC (Allen et al., 2005), DisALEXI (Anderson et al., 2007), SEBAL (Bastiaanssen et al., 1998), JPL-Preistly-Taylor (Fisher et al., 2008), SIMS (Melton et al., 2012), and SSEBop (Senay et al., 2013). It then produces an ensemble estimate using all of the models that work with the given satellite image. Using the Landsat data record, we produced monthly evapotranspiration estimates, currently only for the time period from 2016 through 2020. We extracted the OpenET time series for the main Dell City agricultural area as well as the eastern outlying areas. The average annual evapotranspiration estimated by the OpenET ensemble was 106,000 acre-ft/yr during the 2016 through 2020 time period, similar to our average full-year estimate of 107,000 acre-ft/yr over these years and larger than our growing season average of 85,000 acre-ft/yr (Figure 4-7). Groeneveld and Baugh (2002) also produced estimates of irrigated acreage and consumptive use. Our growing season estimate of evapotranspiration agrees well with their estimate over the time period of overlap between the datasets (Figure 4-7).

The main driver of variability in our estimate of growing season evapotranspiration is the irrigated acreage. We compared our analysis with reported active agricultural acreage from Groeneveld and Baugh (2002) and found good agreement for the time periods that the studies overlapped (Figure 4-8). Both methods used Landsat imagery, so it is not surprising they agree, but our method was automated and controlled by two adjustable parameters (percentile NDVI value for the growing season to represent typical greenness for each pixel and NDVI threshold), while the Groeneveld and Baugh (2002) study delineated fields by hand.

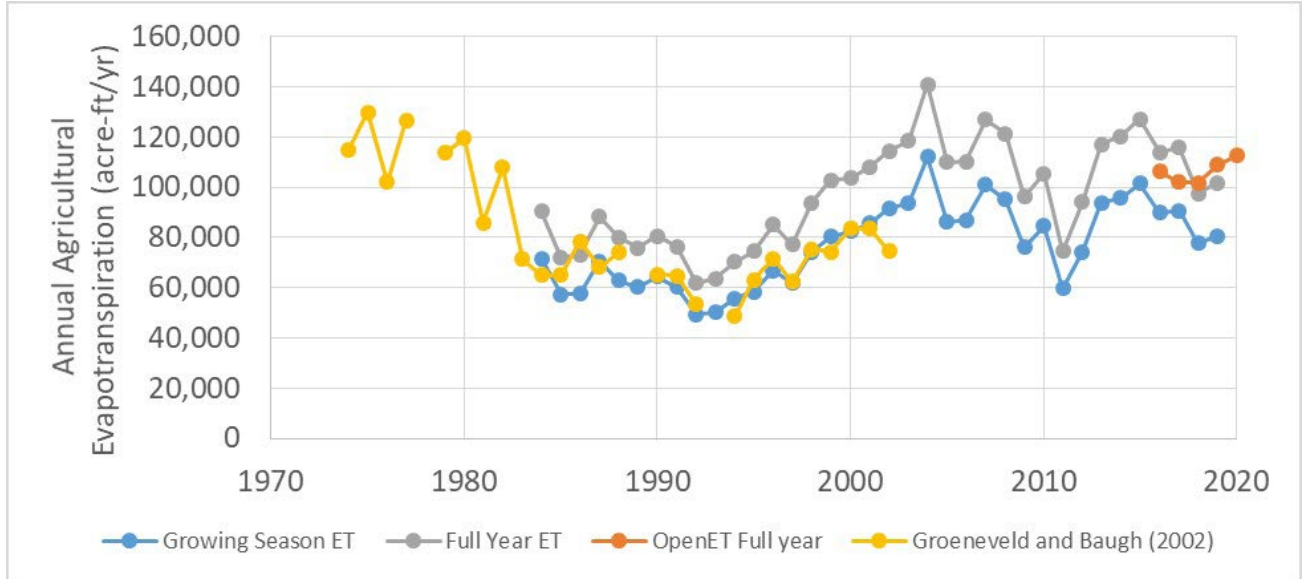


Figure 4-7. Evapotranspiration from the agricultural areas of the Salt Basin using the method of this study over the growing season (March through October), over the full year, and using the OpenET model ensemble for the full calendar year.

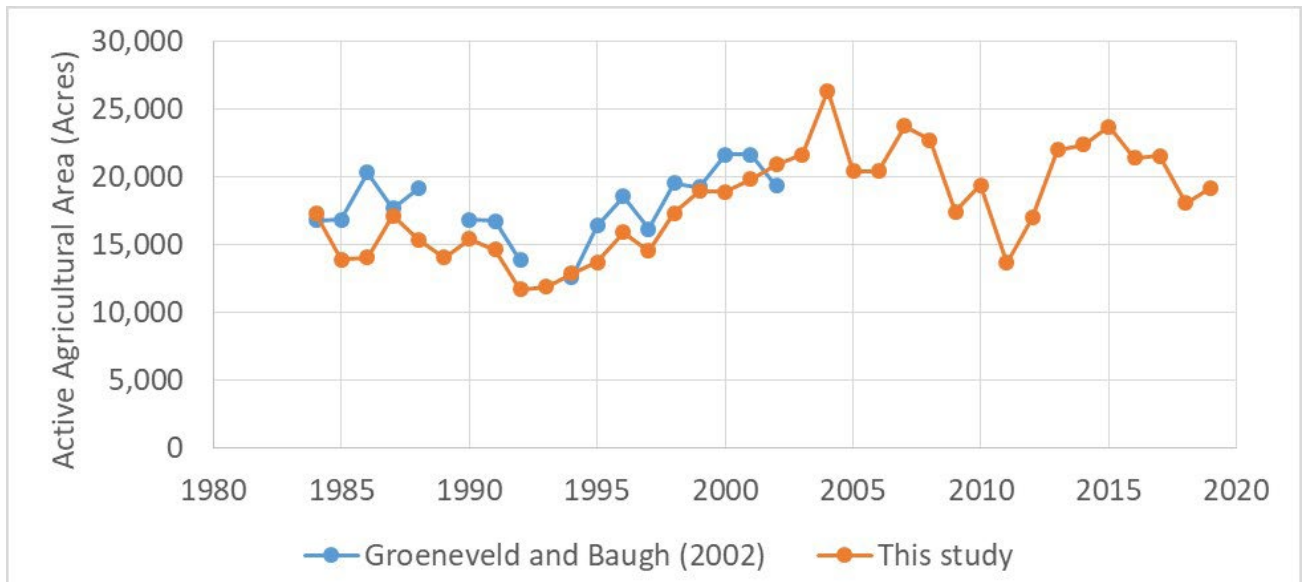
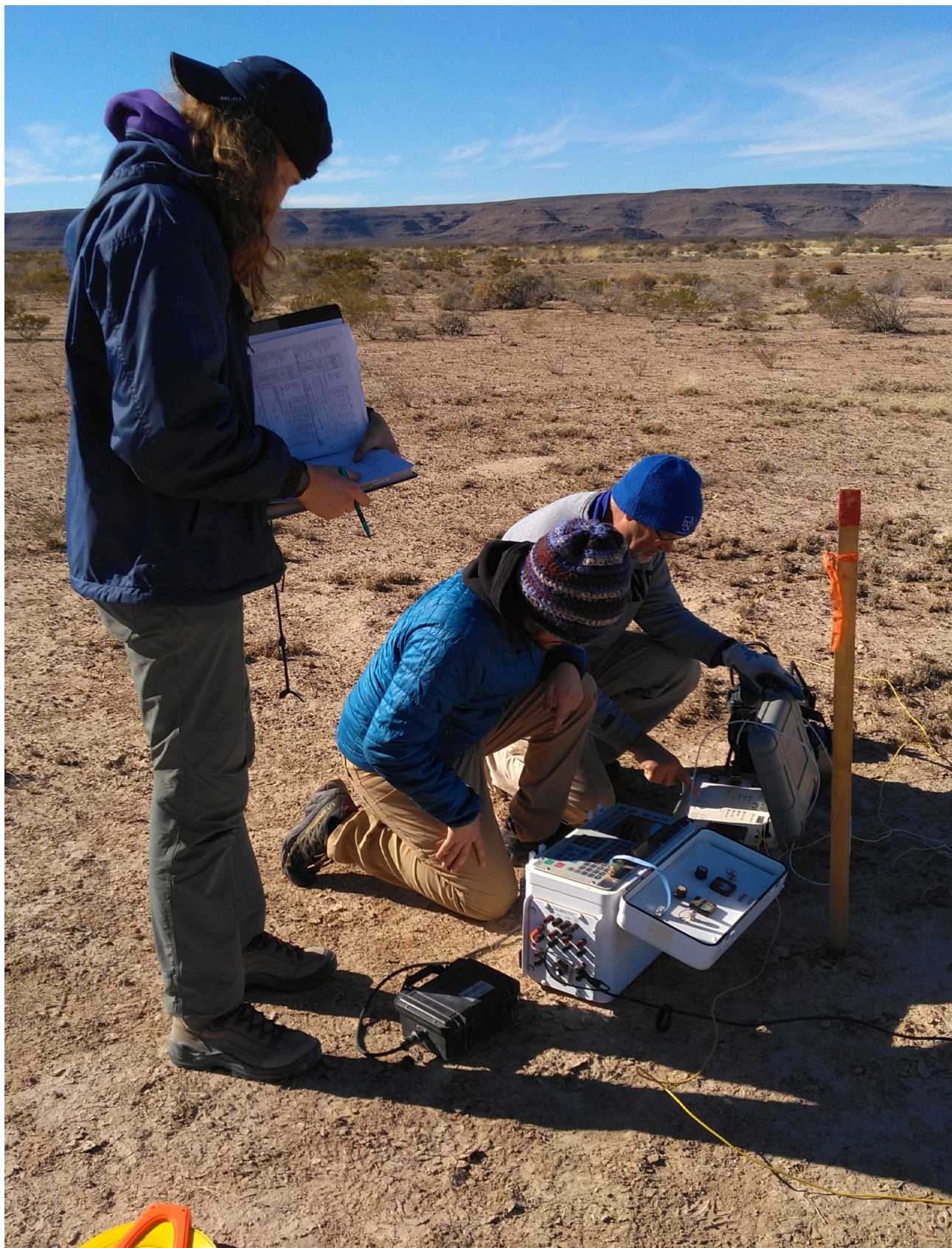


Figure 4-8. Irrigated acreage in the agricultural areas of the Salt Basin using the method of this study compared against the reported acreage of Groeneveld and Baugh (2002).



New Mexico Tech hydrology professor Mark Person with New Mexico Tech graduate students Liz Evenocheck and Dolan Lucero collecting TEM data in Crow Flat. Photo by Shari Kelley

CHAPTER 5: MODELING

HYDROGEOLOGIC MODEL

Elizabeth Evenocheck and Mark Person

To better understand the water budget within the Salt Basin and to determine the effects of groundwater pumping at hypothetical well fields, a series of groundwater flow models were constructed. These include both predevelopment steady-state and transient groundwater flow models. The predevelopment steady-state model was constructed to estimate hydraulic conductivity values, streambed conductance, recharge, evapotranspiration, and underflow. This model and a historical transient model were adjusted based on computed residuals as well as groundwater storage. The transient model was also used to evaluate changes in the Salt Basin water budget due to 72 years of pumping, as well as the effects of introducing three hypothetical well fields that consider two pumping scenarios in the New Mexico portion of the Salt Basin. The models were developed using the Groundwater Modeling System (GMS) software package, which includes a pre- and post-processor for MODFLOW. MODFLOW was developed by the USGS and the specific formulation used in this study was MODFLOW-NWT (Harbaugh, 2005; Niswonger et al., 2011). MODFLOW-NWT uses a Newton-Raphson matrix solver for MODFLOW-2005 that models groundwater flow in unconfined geologic units (Niswonger and Prudic, 2005). The governing groundwater flow equation solved in MODFLOW is given by:

where h is the freshwater hydraulic head; S_s is specific storage; K_x , K_y , and K_z are the hydraulic conductivity values in the x , y , and z directions, respectively; Q_p is groundwater pumping; R is total recharge (diffuse, channel-focused recharge along ephemeral stream channels and arroyos as well as trans-basin inflow); and ET is evapotranspiration. For this study, it is assumed that the coordinate system is aligned with the principal directions of hydraulic conductivity in the x , y , and z directions (i.e., there are no off-diagonal terms represented in the hydraulic conductivity tensor). It is further assumed that fluid density is constant ($1,000 \text{ kg/m}^3$); this assumption is violated near the lowland playa deposits. For the upper water table aquifer (Layer 1), specific storage is replaced by S_y/b , where S_y is specific yield and b is the unconfined aquifer thickness. Details of how recharge (R) and evapotranspiration (ET) were calculated are described below.

Model framework

The model has six layers with a model grid of finite difference cells that are 1,000 m by 1,000 m. The active cells create a grid of 176 rows and 135 columns. Figure 5-1 shows the model outline. Upland diffuse recharge and ephemeral stream networks are also shown in Figure 5-1. Layer 1 is represented as unconfined aquifer with a saturated thickness between 0 and 550 m. Layers 2 through 6 are assigned a layer type of confined. With the exception of a Cretaceous shale unit in the southern Salt Basin, confining units such as the Abo and Yeso formations were lumped in with aquifers and represented by high values of

$$S_s \frac{\partial h}{\partial t} = \frac{\partial}{\partial x} \left[K_x \frac{\partial h}{\partial x} \right] + \frac{\partial}{\partial y} \left[K_y \frac{\partial h}{\partial y} \right] + \frac{\partial}{\partial z} \left[K_z \frac{\partial h}{\partial z} \right] - Q_p(x, y, z) + R(x, y, z) - ET(x, y, z)$$

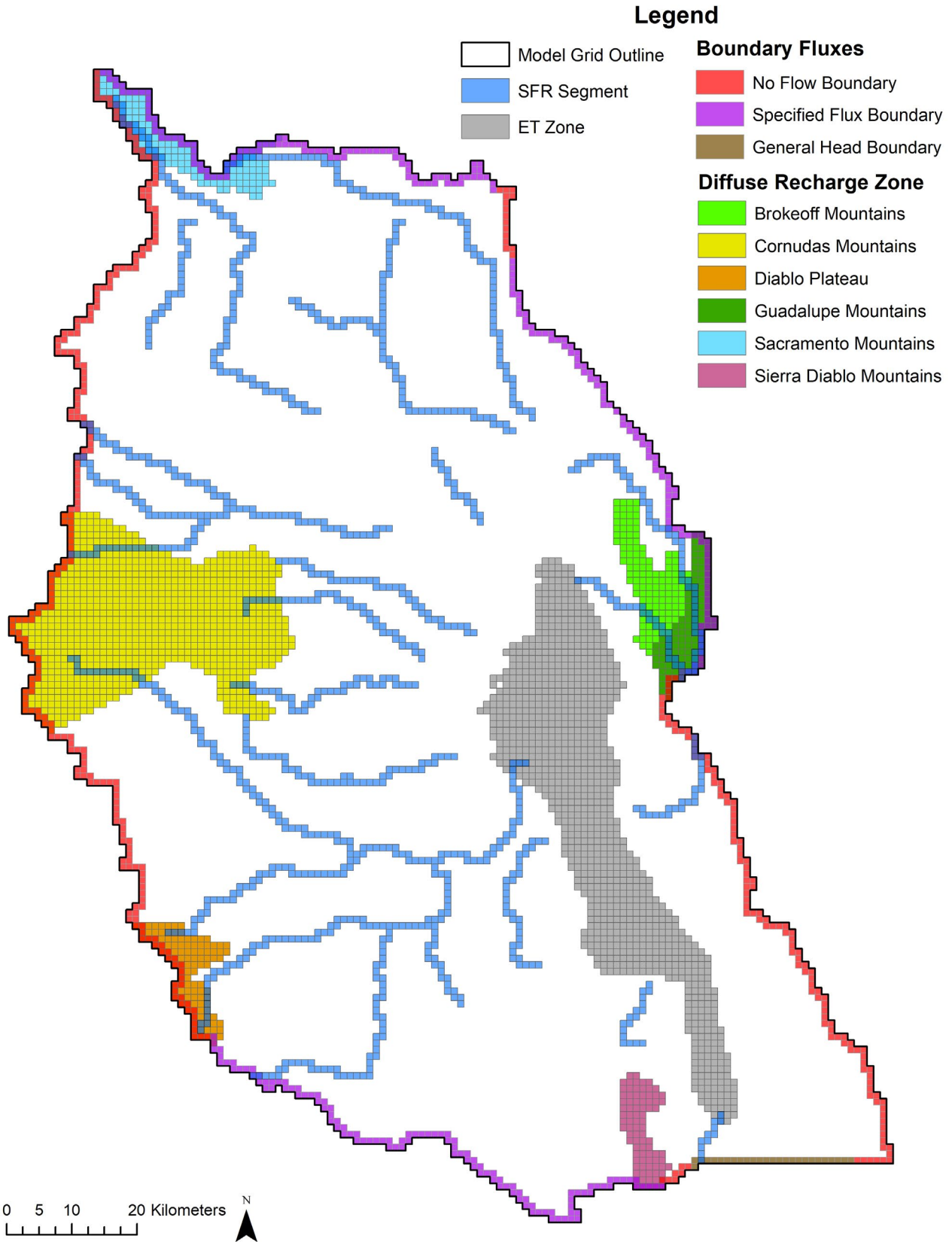


Figure 5-1. Current model grid outline with all boundary conditions symbolized by color of grid cell. Diffuse recharge (colored polygons), channel-focused recharge (derived using Streamflow Routing [SFR] package, blue lines) evapotranspiration (ET Zone, gray polygon), specified flux boundaries (purple boundary cells), general head boundaries (brown boundary cells), and no-flow boundaries (red boundary cells) are shown.

vertical anisotropy. Layers 2 through 6 are primarily made up of Permian, Paleozoic, and earlier units.

The hydrostratigraphic framework model used in this study was developed after Ritchie (2011) using structural features from geologic maps, lithologic facies, compiled data from oil and gas exploratory wells, and surface geologic exposure information. Compared to Ritchie (2011), the current model is nearly identical, except for minor changes to a “state line fault,” the addition of the Capitan Reef Complex, and minor modifications of geology zones for simplification and model calibration. The current model extends the southern boundary 50 km farther south than Ritchie (2011). The current model uses one geologic zone for each geologic unit except for the Permian geologic unit, which has many geologic subunits because of complex facies changes within the Permian units throughout the Salt Basin that affect hydraulic properties and fracture densities of the various rock units (see the Hydrogeology section of Chapter 1 and the Salt Basin Geology appendix in Evenocheck, 2021). Figure 5-2 presents the plan-view maps of the 20 geologic zones used to represent various geologic units. The large number of polygons shown in Figure 5-2 represent fault block boundaries where different lithologic units are juxtaposed against one another vertically. In many instances, the geologic zones delineate different regions of the same geologic formation; thus, permeability of a given formation can vary spatially. If the Permian unit only had one set of properties, it would be difficult to fit the observed data, and the model would be too simple to accommodate the spatial differences in hydraulic response to historical pumping stresses. There is one confining unit in the southwestern Salt Basin—the low-permeability Cretaceous unit

(Geologic Zone 2). The Proterozoic basement was lumped into the Paleozoic and earlier group, with Layer 6 completely composed of Proterozoic rocks. Faulting in the Salt Basin has increased permeability, creating flowpaths and causing the aquifers to be poorly connected across some of the fault zones. Geologic zones were spatially adjusted to improve the parameter flexibility required to better fit observed water levels during the calibration process. Each geologic zone had unique values of hydraulic conductivity, vertical anisotropy, S_y , and S_z for each model layer. Due to the lack of porosity data, a uniform value of 0.15 was used for all the geologic units, which was close to Ritchie’s (2011) average porosity model values. S_y and S_z are only used in the transient models. The geologic zone assignments and initial parameters are in Table 5-1 and Figure 5-2.

The model boundary follows the surface water divide around the entirety of the model, except for the southeastern portion, which follows the groundwater divide of the Victorio Flexure. The Victorio Flexure is a large fault that crosses the Salt Basin Graben, which lies beneath the Salt Flats (see Figure 1-1 for locations). The boundary was divided into segments based on the internal Salt Basin HUC 10 watersheds, except for the northern boundary and southeastern groundwater divide. The northern boundary and portions of the northeastern and southwestern boundary were assigned specified flux boundaries (Figure 5-1). The northern boundary had the largest flux, with an initial value of 5,000 acre-ft/yr, representing underflow from the adjacent Peñasco Basin. Flow is believed to come from the Peñasco Basin because head gradients show water flowing into the Salt Basin (Newton et al., 2012; DBS&A, 2010a).

Table 5-1. Hydraulic conductivity values and vertical anisotropies assigned to geologic zones used in model. Figure 5-2 shows the distribution of geologic zones.

Geologic Unit	Geologic Zones	Hydraulic Conductivity (m/day)	Vertical Anisotropy
Cenozoic alluvium (Layer 1)	8	25.6	8.7
Cenozoic intrusions	3	0.0001 to 0.0003	93 to 1,000
Cretaceous	105	0.037	56
Low-permeability Cretaceous	2	0.000003	92 to 1,000
Permian	6, 7, 8, 10, 107, 110, 205, 207, 210, 307, 310, 407, 410, 507, 607	0.001 to 41	10 to 100
Paleozoic and earlier	4	0.0003 to 0.03	0.36 to 1,000

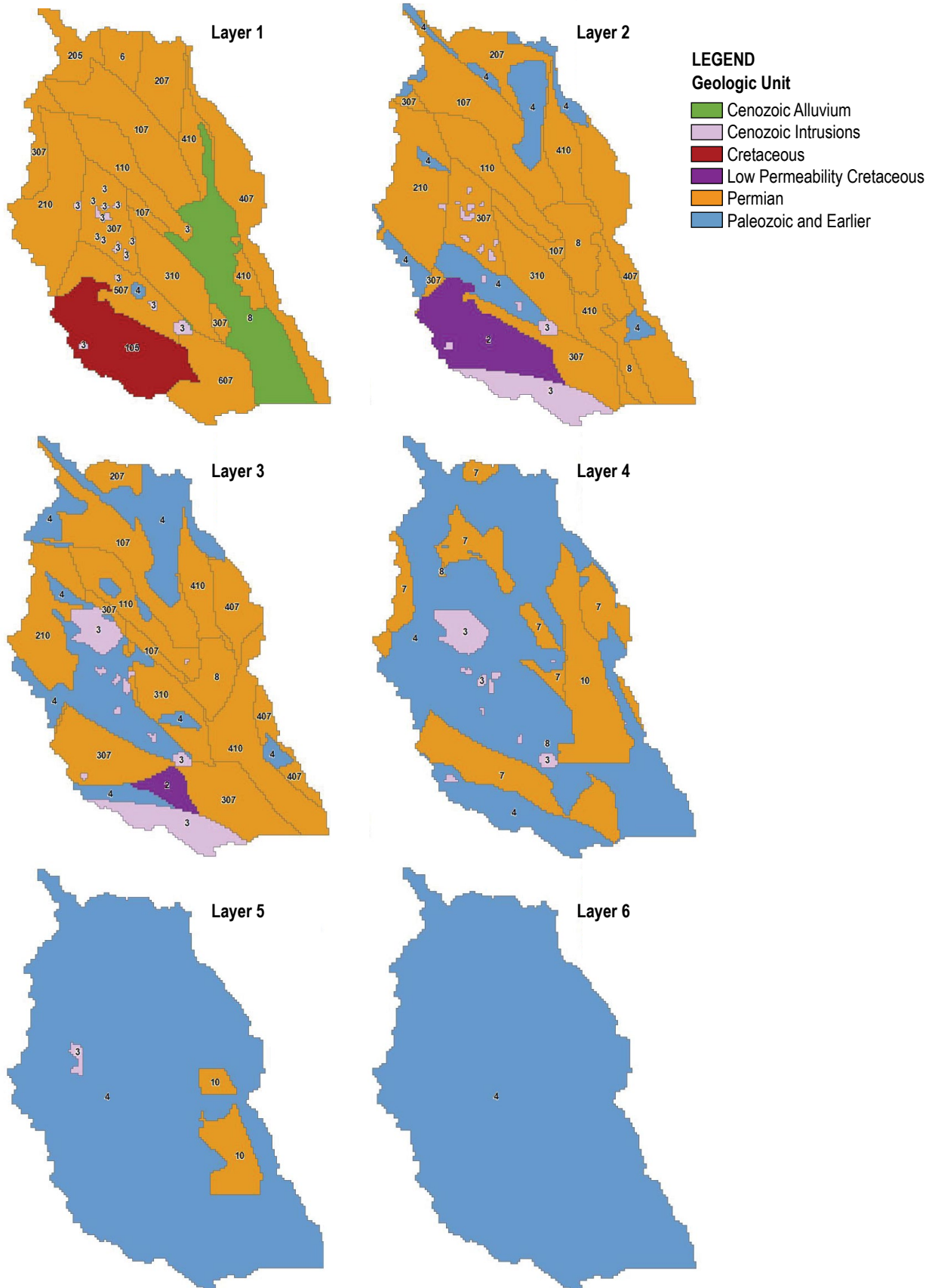


Figure 5-2. Maps of final model geologic zonation in Layers 1 through 6.

The other segments were assigned initial fluxes of about 15 acre-ft/yr and were included to represent mountain-front or slope-front recharge at the extent of the surface watershed. The southeastern groundwater divide section was represented as a general head boundary with a conductance of 0.0001 m/day (Figure 5-1). This boundary condition was imposed to help with model convergence and to assess simulated flow direction across the boundary. The goal was essentially to have no flow through the general head boundary. All perimeter boundary fluxes were applied to Layer 1. In all other layers, model cells on the perimeter of the active model domain were assigned no-flow boundary conditions.

Recharge and evapotranspiration

The model included both diffuse and focused recharge. Diffuse recharge was applied using the Recharge package in MODFLOW. We used the Python Recharge Assessment for New Mexico Aquifers (PyRANA) to determine where diffuse recharge needed to be applied in upland regions (see Chapter 4 and Cadol et al., 2020). Channel-focused recharge was applied along ephemeral streams and arroyos throughout the model domain using the Streamflow Routing (SFR2) package in MODFLOW (Niswonger and Prudic, 2005).

To determine the recharge rate in the Salt Basin, three different scenarios were considered in the predevelopment steady-state model. These scenarios estimated 40,000, 60,000, and 80,000 acre-ft/yr of recharge. These values were chosen because they span the range of prior Salt Basin model recharge rates, except for recharge estimates from Ritchie (2011), which were significantly lower. Runoff is routed based on the continuity equation, which assumes steady, uniform flow. Volumetric inflow is equal to volumetric outflow plus the net of all sources and sinks along the channel. Simulated water seepage out of a stream to the aquifer when the water table is below the stream bottom is computed by:

$$q = \frac{K}{m} (h_s - h_b)$$

where q is the infiltration rate, K is the saturated hydraulic conductivity of the streambed, h_s is the hydraulic head in the stream at the top of the

streambed, h_b is the hydraulic head at the bottom of the streambed, and m is the thickness of the streambed (Niswonger and Prudic, 2005).

Evapotranspiration is applied to the model using the MODFLOW EVT-package (Banta, 2000). Evapotranspiration is parameterized in MODFLOW using the following relationship:

$$\begin{aligned} ET &= ET_{max}; h > z_{ls} \\ ET &= ET_{max} \frac{h - (z_{ls} - z_{ext})}{z_{ext}} \quad z_{ext} \leq h < z_{ls} \\ ET &= 0; h < z_{ext} \end{aligned}$$

where z_{ls} is the land surface elevation, z_{ext} is the elevation where ET is zero, and ET_{max} is the maximum evapotranspiration rate. The maximum ET rate was provided by PyRANA. Note that in the text below we refer to the extinction depth, which is given by $z_{ls} - z_{ext}$. As the water table elevation (h) approaches the land surface, ET increases and reaches a maximum at the land surface (ET_{max}). If heads fall below the extinction depth (the depth where capillary forces can no longer draw moisture toward the land surface), evapotranspiration is zero. Evapotranspiration was only applied to the Salt Flats (Figure 5-1). This is because it was the only place that the water table was historically close enough to the surface to be available for evaporation. During high-precipitation events, surface water flows to the Salt Flats, pools on the ground surface, and evaporates. An initial maximum evapotranspiration rate of 80 in./year (288,427 acre-ft/yr) was used, with an extinction depth of 10 m, as determined by PyRANA and gridMET. The dataset gridMET contains daily meteorological data (Abatzoglou et al., 2014).

Historic pumping

In order to estimate the current pumping and water use in the model, four datasets were reviewed and combined to create a location-specific database of wells in the basin that includes New Mexico Office of State Engineer (NMOSE) well permit information, Texas Water Development Board well location information, work done by John Shomaker & Associates, Inc. (JSAI; 2010), and NDVI analysis from this study (see the Evapotranspiration section in

Chapter 4). The process of combining these different datasets into a basin-wide estimate of historical water use is discussed below.

The NMOSE well data were extracted from the list of permitted wells in the area and include well location, drill date, well use, and approved diversion amount (NMOSE, 2021). For modeling purposes, all wells with domestic, commercial, municipal, and industrial (DCMI) uses were separated from irrigation uses. For the New Mexico DCMI wells, the model assumes that pumping begins the year the well was drilled and that the effective pumping rate is half of the listed diversion amount to account for return flows. Data such as the drill date, diversion amount, and well depth were documented for New Mexico wells; however, possible plug or abandonment dates were not. Therefore, all wells were assumed to pump from their drill date to the end of the model run (1948 to 2019). The total New Mexico DCMI pumping for the entire period of simulation is 29,575 acre-ft.

Well data available on the Texas Water Development Board website included well location, drill date, and type of use but did not include specific diversion amounts. In many cases, data were incomplete for the Texas wells, so a few assumptions were required. If a well did not have a drill date, it was assumed to begin in 1975 based on a histogram of drill dates. If the well depth was not reported, the "Aquifer" attribute was used to estimate the model layer assignment. Diversion was assumed to be 3 acre-ft/yr for all Texas DCMI wells, with effective pumping at 50% for consistency with the New Mexico assumptions. The total Texas DCMI pumping for the entire period of simulation is 8,730 acre-ft.

Irrigation pumping was defined using two data sources: (1) irrigation pumping rates through 1983 were extracted from the JSAI (2010) model; (2) for rates after 1983, the model used estimates of consumptive pumping derived from the Blaney-Criddle method presented in Chapter 4. The JSAI (2010) model contained 470 wells with assigned well depths and pumping rates beginning in 1984, making input of this data into the current model fairly straightforward. Translating the Blaney-Criddle-calculated consumptive use to a pumping record required a few steps. The model grid was first compared to the NDVI analysis of historic areas

of active irrigation to determine pumping areas from 1984 through 2019. One irrigation well was added to each model grid cell that intersected the irrigated footprint, and the pumping estimate was adjusted annually. The total consumptive pumping estimate was distributed proportionally over the irrigated area polygon.

A final comprehensive irrigation dataset was created by combining the JSAI (2010) pumping records from 1948 through 1983 with the NDVI/consumptive use dataset from 1984 to 2019. This joining of datasets was determined manually by identifying which JSAI (2010) wells overlapped with the NDVI irrigation zones and adjusting the pumping record at those wells accordingly.

Model calibration

The steady-state and transient models were calibrated manually (by trial and error) and then using the parameter estimation code PEST (Doherty and Hunt, 2010). Hydraulic conductivity and streambed conductance were varied during the calibration. Observed water levels were not weighted as heavily or were excluded from PEST calibration if the water level diverged from the pattern of observed water levels around it or a lack of geologic formation data and model geology resolution made fitting the gradient of the water level too difficult. We discuss two statistical descriptors of model fit below—the root mean squared error (RMSE) and the mean error:

$$RMSE = \sqrt{\frac{\sum_m^N [h_m^{sim} - h_m^{obs}]^2}{N}}$$

$$Mean\ Error = \frac{1}{N} \sum_{m=1}^N h_m^{sim} - h_m^{obs}$$

where m is a given observation, and N is the total number of observations.

For each of the three levels of recharge, the predevelopment steady-state model has a relatively good fit between observed versus computed heads (Table 5-2 and Figure 5-3). Note that the average hydraulic conductivity and anisotropy listed in Table 5-2 represent the arithmetic mean for all active cells in the model. The R^2 values for all three levels of recharge models were above 0.992, which suggests there was a substantial correlation and therefore a

good fit of observed to computed heads. The mean error for all three recharge scenarios was negative, indicating that on average the computed heads were lower than the observed heads. A common calibration metric used to determine whether a model fit is good is an RMSE of less than 10% of the range of observed values. The range of observed heads was about 1,600 m (2,600 m to 1,100 m). For all three levels of recharge, the predevelopment steady-state model RMSE was well below the 10% observed value range. The 60,000 acre-ft/yr of recharge model had a slightly better R^2 and RMSE value compared to the other

two recharge rates. The 40,000 acre-ft/yr of recharge model had the smallest mean error.

The predevelopment steady-state model water table contours had a relatively good fit to the observed predevelopment water table contours (Figure 5-4). The observed and simulated water level contours have similar head gradients and water table mounding in the Sacramento Mountains area, the Cornudas Mountains, the Diablo Plateau, and the Sierra Diablo Mountains area. The Salt Flats water table is flat in both the observed and simulated contour maps.

Table 5-2. Spatially averaged hydraulic conductivity values and vertical anisotropies data for the three MODFLOW model recharge scenario model runs as well as statistics for the observed versus computed water levels for the predevelopment steady-state recharge model using three levels of recharge. Obs = observed and Comp = computed.

Model Scenario Recharge Rate (acre-ft/yr)	R^2	Mean Error (m) (Obs - Comp)	RMSE (m)	Hydraulic Conductivity Average (m/day)	Vertical Anisotropy Average
~40,000	0.992	-2.02	20.8	0.93	152.6
~60,000	0.993	-3.25	20.0	1.7	175.4
~80,000	0.992	-3.57	22.2	3.2	179.3

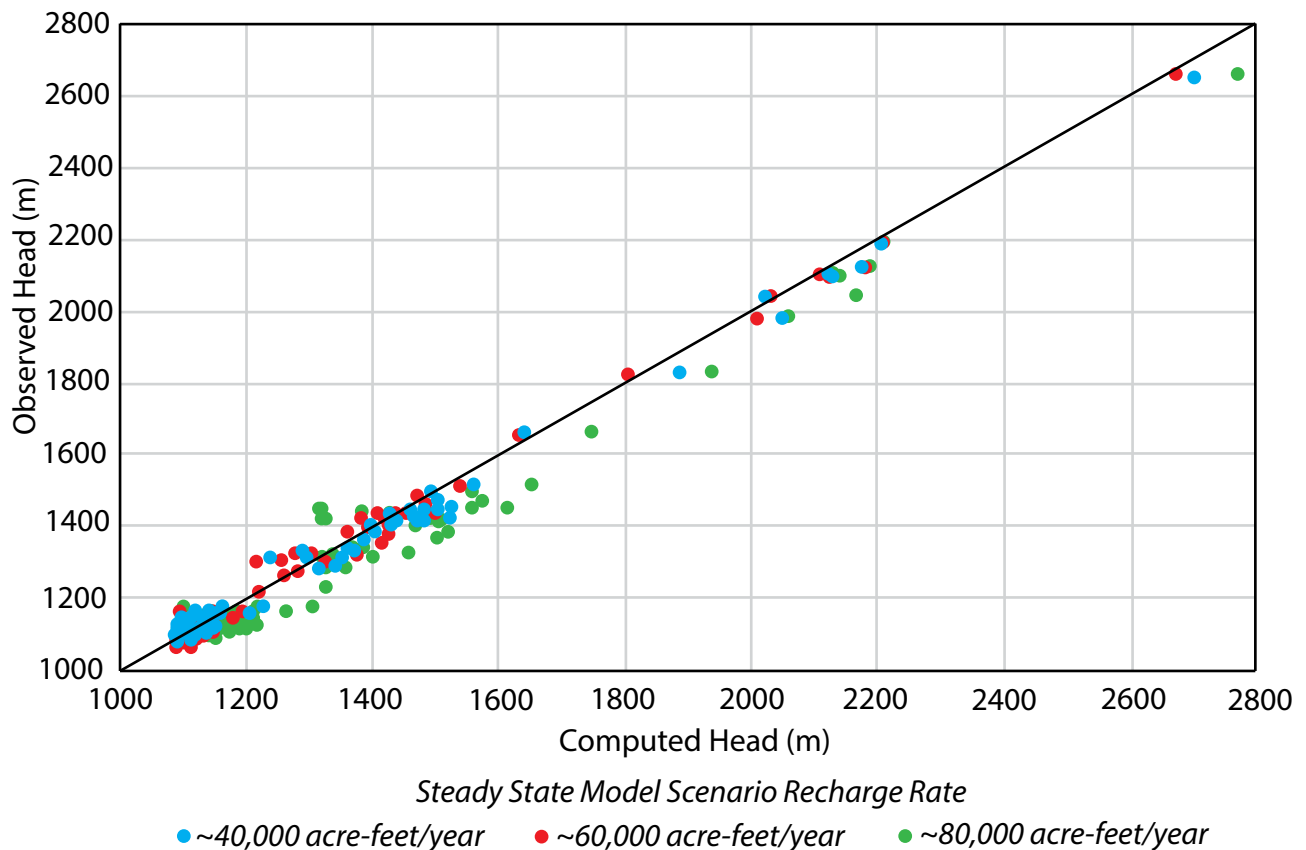


Figure 5-3. Observed versus computed water levels for the three predevelopment steady-state recharge model scenarios. Water levels not used in the PEST calibration were not used to compute the statistics.

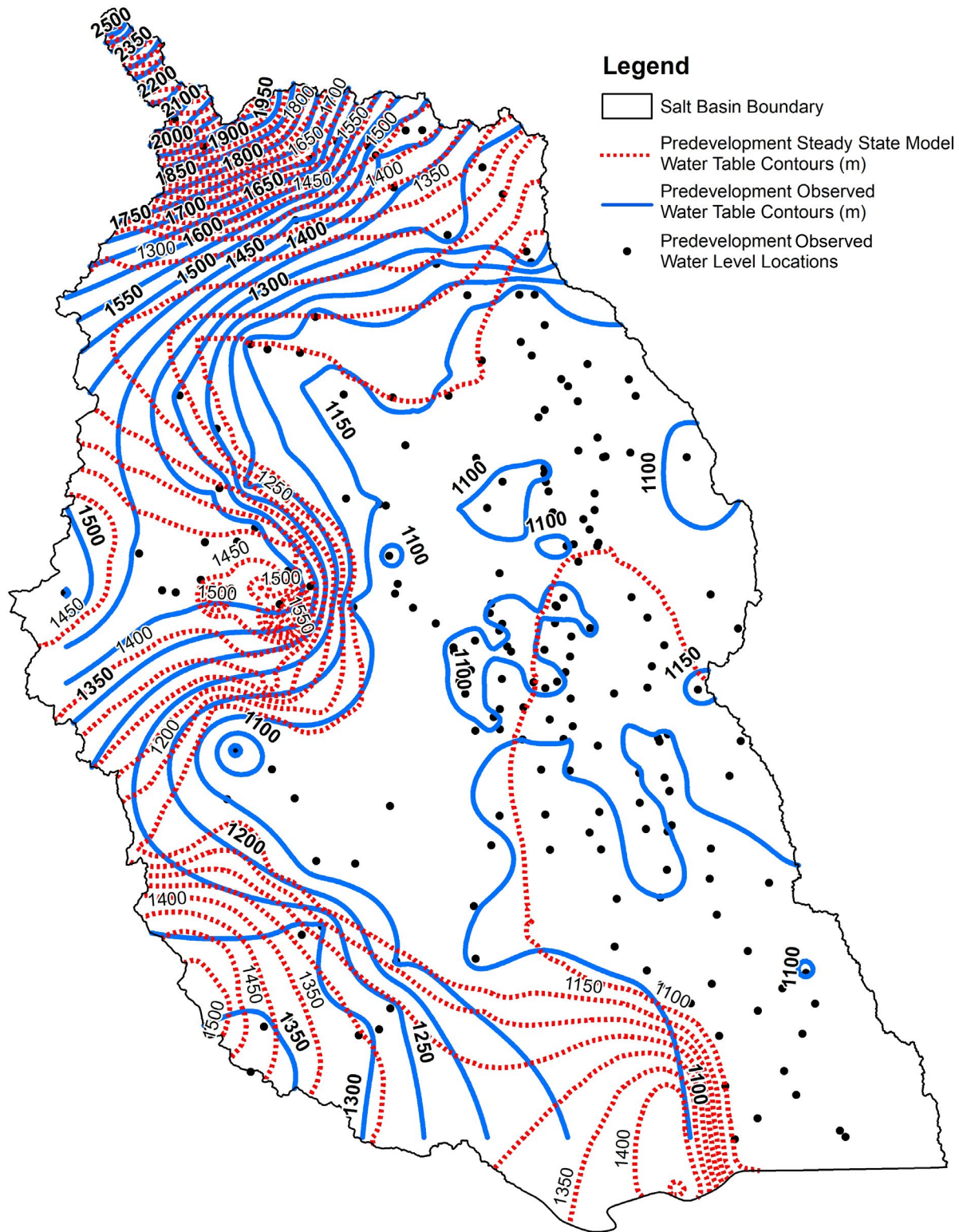


Figure 5-4. Observed and modeled predevelopment water table contour map (in meters). Observed water table contours are denoted by solid blue contour elevation; labels are in meters. Model-computed water table contours are denoted by red dashed lines. Black points are locations of observed predevelopment water levels used to create predevelopment observed water table contours. Both sets of water table contours were developed in this study. The contour interval is 50 m. This figure shows a relatively good fit between the observed and model predevelopment water tables and indicates some of the larger discrepancies may simply reflect interpolation of observed data across regions with only sparse data.

Stream conductance was calibrated using flux targets consistent with the general conceptual model of Salt Basin stream flow presented by Tillery (2011). Upstream portions of each stream tend to increase in total flow (net gains), while downstream portions tend to have net losses, with the final portion of the mapped stream channel losing virtually all remaining flow, reflecting the high infiltration capacity of the fractured Permian system in the vicinity of each stream terminus. Stream conductance values were calibrated with PEST to a model-wide maximum of 1.62 m/day, minimum of 0.0000305 m/day, average of 0.0860 m/day, and median of 0.00675 m/day. Virtually all runoff that is input to the streams enters the aquifer. Figure 5-5 gives a detailed view at the distribution of channel-focused recharge in the predevelopment steady-state model. The Sacramento River, Piñon Creek, Shiloh Draw, and sections of Antelope Gulch produce the most channel-focused recharge, with over 1,200 acre-ft/yr each (Figure 5-5).

Table 5-3 shows the flow budget for the final predevelopment steady-state model. Total recharge is made up of 67% diffuse recharge, 29% channel-focused recharge, and 4% underflow from adjacent basins. Evapotranspiration is the only discharge in the model and is approximately equivalent to total recharge. Table 5-3 also shows the distribution of diffuse recharge in the final predevelopment steady-state model. Each diffuse recharge polygon has a unique recharge rate dependent on the initial PyRANA value given and calibrations made to better fit observed water levels. The Cornudas Mountains and Sacramento Mountains have the highest percent of diffuse recharge volume. The Sierra Diablo Mountains, Brokeoff Mountains, Diablo Plateau, and Guadalupe Mountains all have similar recharge volumes of under 3,000 acre-ft/yr. Locations of recharge polygons are shown in Figure 5-1.

Despite the hydrogeochemical and geologic challenges of working with carbon-14 data in this region, as noted in Chapter 3, for discussion purposes we compared observed carbon-14 ages from Sigstedt (2010) to advective ages (Figure 5-6). Advective ages were computed using MODPATH (i.e., piston flow neglecting dispersion-diffusion). Without robust and representative porosity data for the region, the use of age data in manual or PEST calibrations was unsuccessful. For example, the R^2 values for the three steady-state models ranged

from 0.0098 to 0.012, which are unsatisfactory values. All three predevelopment steady-state models had poor statistical fits to carbon-14 ages. A poor fit of advective travel times to carbon-14 is not uncommon. In this study it could be due to inaccurate MODFLOW flowpaths or young and old water mixing in the highly fractured Salt Basin (Kreitler et al., 1987). Sanford (2011) found a poor fit between advective groundwater ages to correct carbon-14 data for his model of the Albuquerque basin.

Historical transient model

The hydraulic parameters from the steady-state model were used as a starting point for the historical transient model. PEST was used to determine the transient hydrogeologic parameters specific yield and specific storage. The historical transient model considered time-varying channel-focused recharge and pumping. The calibrated values of specific yield (S_y) varied between 0.01 and 0.1 for various layers that cropped out at the land surface. Lack of sensitivity allowed the best-fit value of specific storage (S_s) to stay at its initial assigned value of 10^{-6} m^{-1} for all units.

The transient model was calibrated to observed water level trends. Figure 5-7 shows four observed versus computed water level graphs for four wells. These wells had the longest time series of observations in the Salt Basin. The wells are all located near Dell City, Texas. No wells outside the Dell City area had a large number of water level measurements. For the wells in Figure 5-7, computed water levels were lower than observed water levels. However, the general trend of a decrease in water levels from 1948 to 1980, an increase from 1980 to 2000, then a decrease from 2000 to today was reproduced.

Figure 5-8 compares the predevelopment model computed steady-state water table versus the final water table contours at the termination of the transient model in 2020. In the predevelopment steady-state model water table contours, the lowest water levels are in the Salt Flats. In the final transient model water table contours, a cone of depression has formed under Dell City. The Dell City cone of depression suggests the potential for movement of water from the playas toward Dell City, including possibly higher salinity water often associated with the playa.

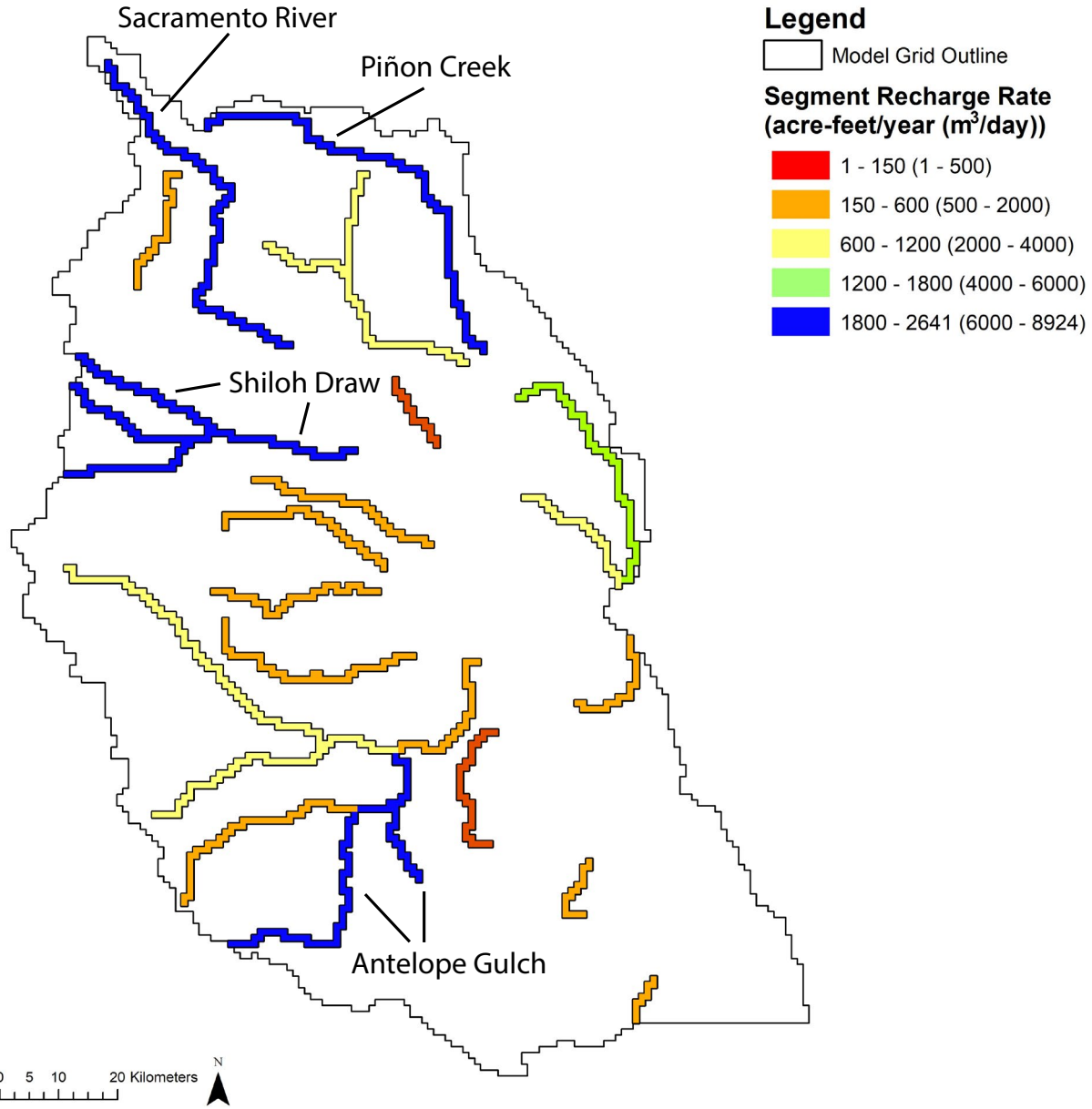


Figure 5-5. Distribution of depression-focused recharge in streamflow routing (SFR) segments in the predevelopment steady-state model. Color denotes amount of recharge from SFR segment.

Table 5-3. Diffuse recharge polygons (left columns) and net fluxes (right columns) from final predevelopment steady-state model.

Diffuse Recharge Polygon Flux (acre-ft/yr)		Basin-wide Flux (acre-ft/yr)	
Cornudas Mountains	20,617	Total Recharge	60,487
Sacramento Mountains	9,554	Total Discharge	60,474
Sierra Diablo Mountains	2,791	Diffuse Recharge	40,446
Brokeoff Mountains	2,646	Channel-Focused Recharge	17,479
Diablo Plateau	2,484	Underflow	2,562
Guadalupe Mountains	2,352	Evapotranspiration	60,474

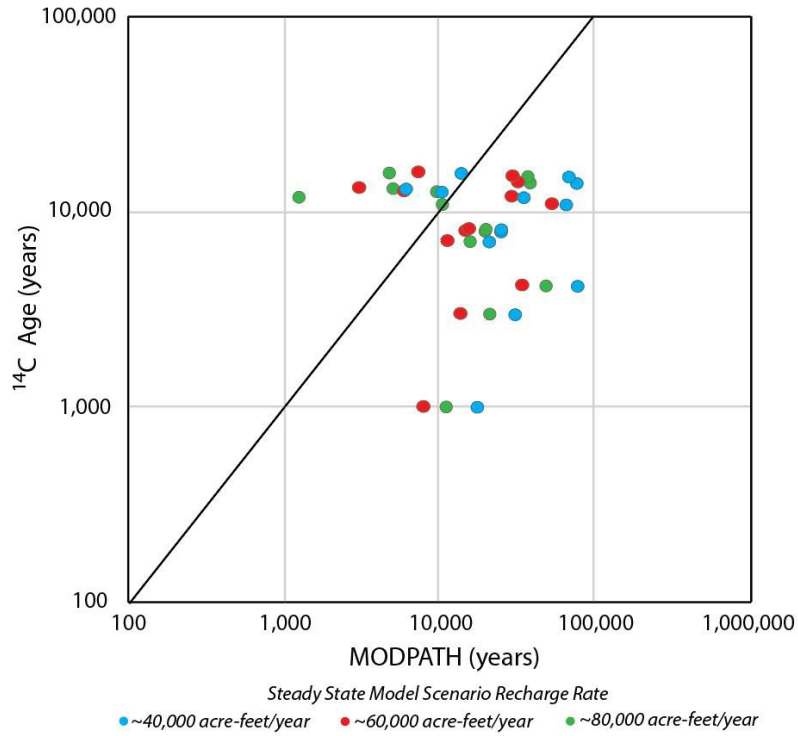


Figure 5-6. Computed versus observed carbon-14 ages for the three preliminary predevelopment steady-state model scenarios. Observed carbon-14 was measured by Sigstedt (2010).

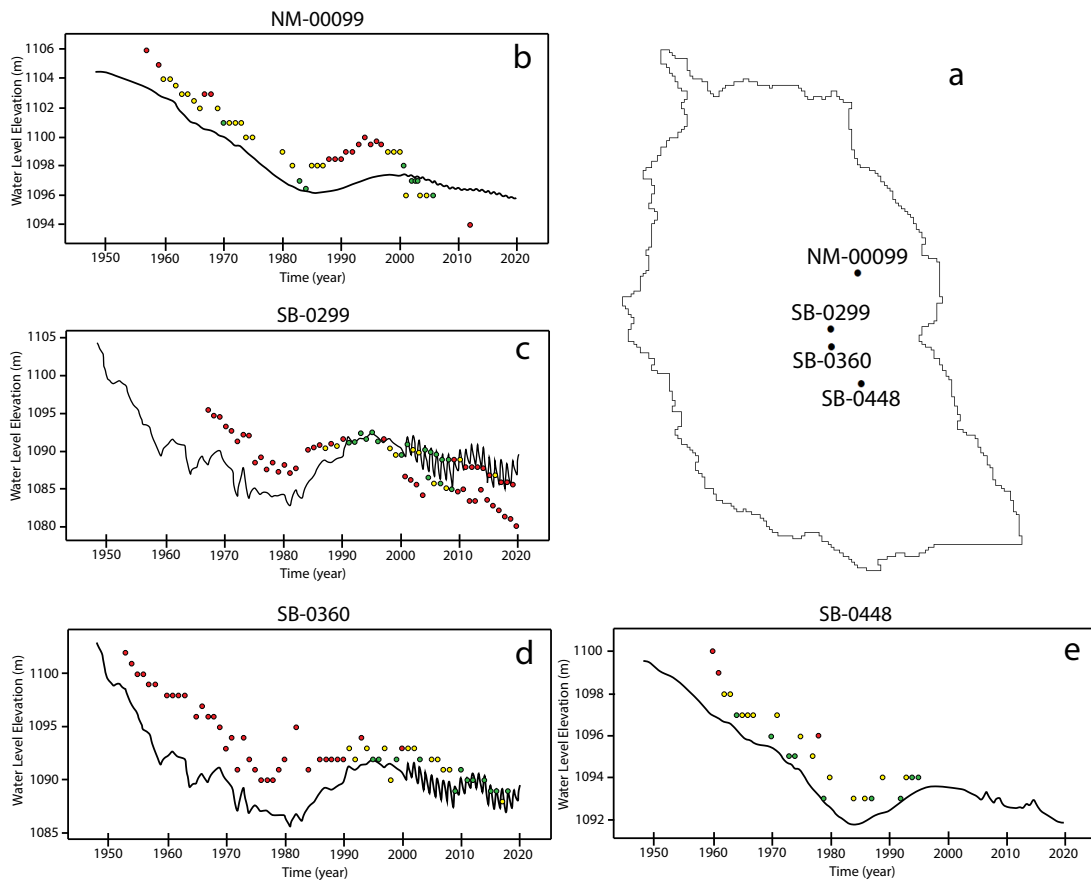


Figure 5-7. Observed versus computed well hydrographs in the Salt Basin (b–e). Locations of the four wells are displayed as black dots on the inset map (a). Black lines show computed water levels through time for each well. Points are observed water levels.

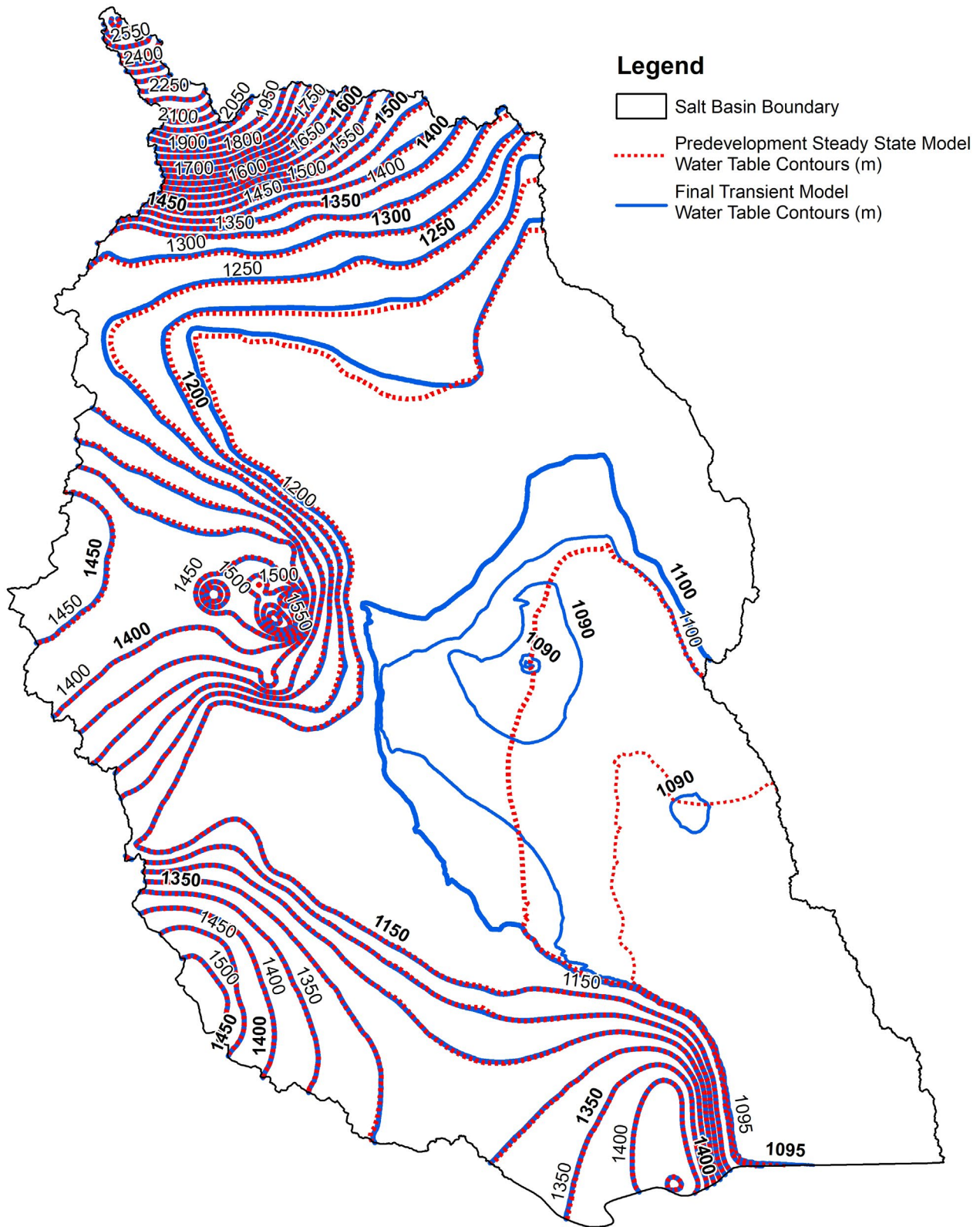


Figure 5-8. Initial 1948 (red dashed line) and final 2020 (blue and bolded labels) transient model water table contours. The initial water table contour map is from the predevelopment steady-state model. Contour intervals (50 m) change in the Salt Flats region to 5 m.

Figure 5-9 displays the water budget changes through the entire historical transient model simulation. Focused recharge and pumping vary with each annual or seasonal stress period. The evapotranspiration rate generally decreases through time, starting at 57,000 acre-ft/yr in 1948 and declining to about 3,000 acre-ft/yr at the end of the transient run in 2020. This is due to the lowering of the water table in the playa areas below the evapotranspiration extinction depth of 5 m. Transient recharge stays under 80,000 acre-ft/yr except for 5 years of high precipitation (1974, 2006, 2008, 2013, and 2014). After 1985, net storage starts to oscillate over the zero change in storage line. Between 1948 and 1984, changes in storage were predominantly negative, with a maximum annual change in storage of about -50,000 acre-ft/yr. Between 1985 and 2020, there were many years with less than 20,000 acre-ft/yr of storage declines. Some years during this period had aquifer storage changes that were positive (increased storage), which correlated to years with high recharge or low pumping. In the 32 years between 1948 and 1980, there has been a near-exponential decline in evapotranspiration. During this same time period, changes in net storage mimicked groundwater pumping. That is, during periods of increased pumping, groundwater storage decreased.

The decrease in water levels from 1985 to 2020 is also seen in observed water levels in Dell City (Figure 5-10). The pumping rate from 1985 to 2020 averaged 69,276 acre-ft/yr. There is still more net loss in storage than net gain in storage since

1985, suggesting the Salt Basin has not reached an equilibrium. This is not surprising given that the average recharge to the basin (61,259 acre-ft/yr) is less than the average pumping (79,529 acre-ft/yr). The hydrologic system has compensated for the recharge/pumping imbalance by reductions in evapotranspiration (outflow) and mining of groundwater from aquifer storage (Bredehoeft, 2002). Between 1985 and 1996, average pumping was about 60,000 acre-ft/yr and changes in storage approached zero; pumping was likely balanced by recharge.

Table 5-4 presents the average flow budget values for the historical transient model from 1948 to 2020. The average recharge rate for the historical transient model was 61,259 acre-ft/yr. This increase from the predevelopment steady-state model is due to channel-focused recharge, which varied with annual precipitation rates. Over the course of the transient simulation period, evapotranspiration decreased substantially from the predevelopment steady-state model. On average, the storage change decreased by 26,732 acre-ft/yr.

Pumping scenario results

Multiple strategies are available to evaluate proposed pumping scenarios. One approach is to run models into future alternative pumping scenarios. For the Salt Basin, this would involve making estimates of future recharge and evaporation conditions based on historical data and using current hydrologic conditions as initial conditions. However, post-audit studies have found that the uncertainty in forecasting

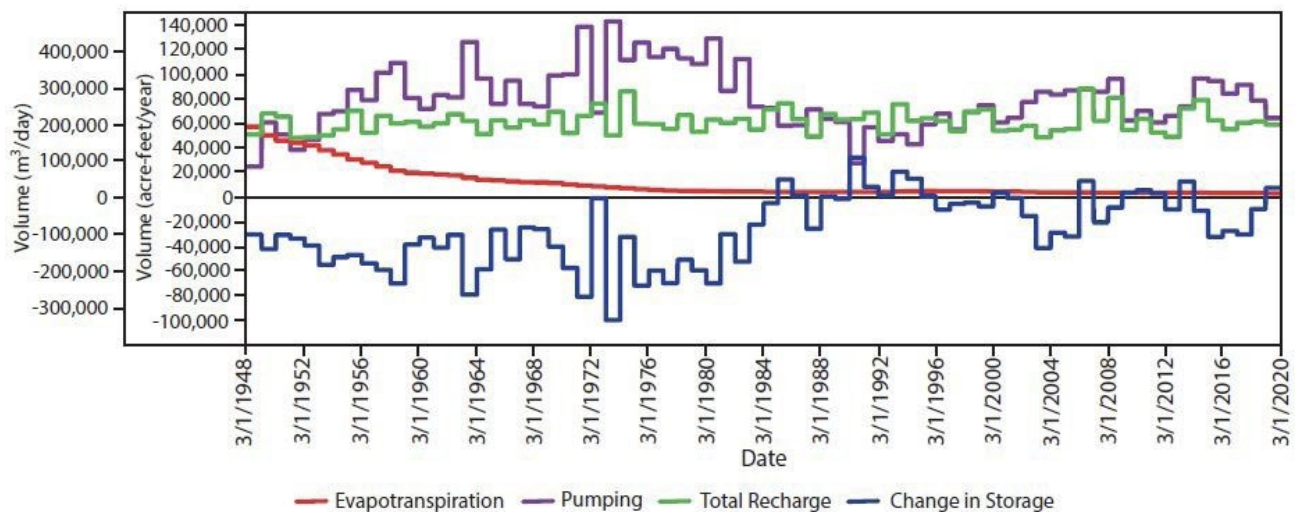


Figure 5-9. Computed changes in evapotranspiration, pumping, total recharge, and net storage within the Salt Basin between 1948 and 2020.

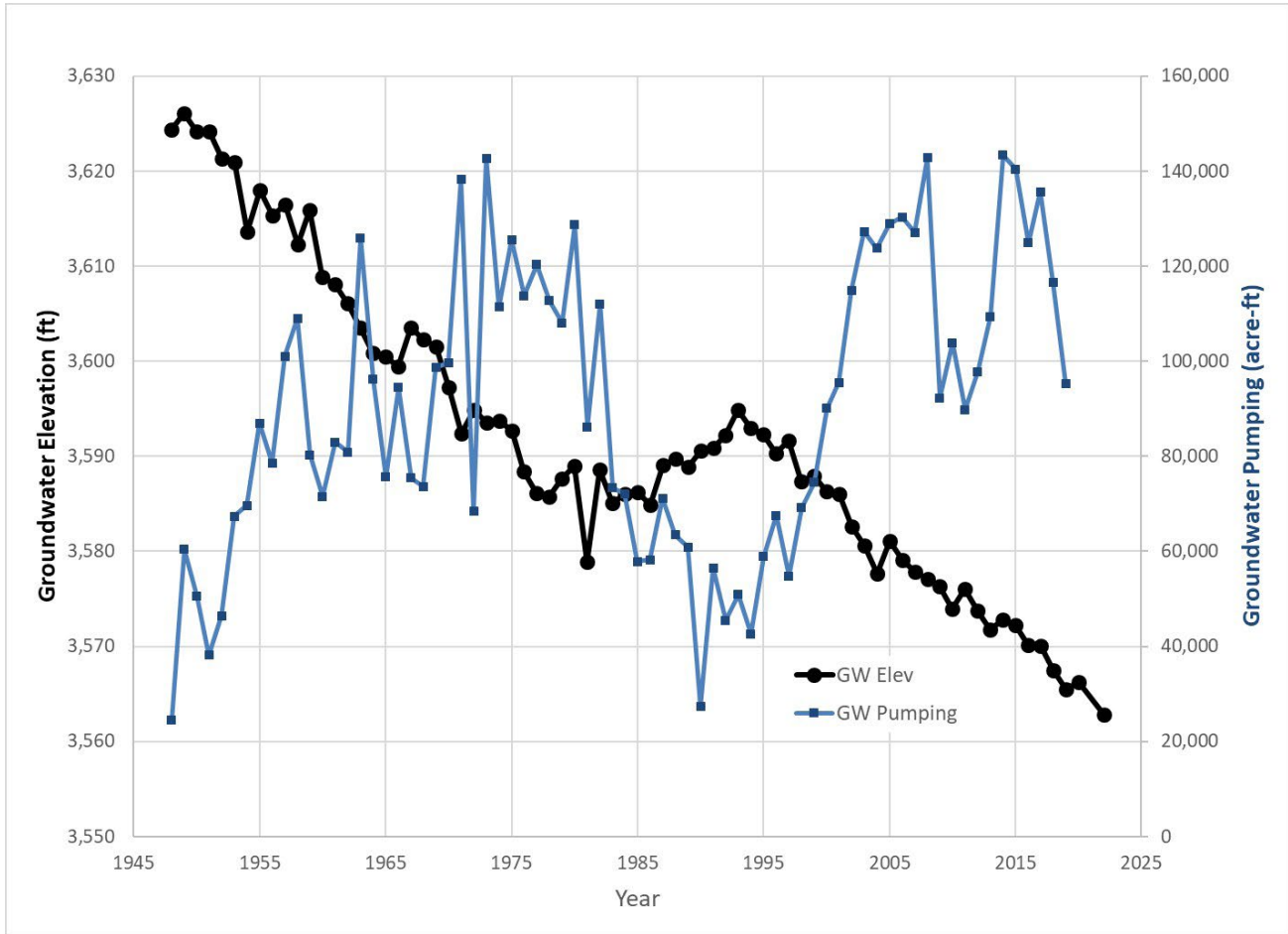


Figure 5-10. Measured water table elevations in the Dell City area compared to the modeled groundwater pumping over time. See Figure 1-8 for more details on the observed groundwater elevations.

Table 5-4. Net changes to the flow budget (in acre-ft/yr) for the historical transient model from 1948 to 2020.

Unit	Average Total Recharge	Average Total Discharge (ET + Pumping)	Average Diffuse Recharge	Average Focused Recharge	Average Underflow	Average ET	Average Pumping	Average Storage Change
acre-ft/yr	61,259	90,595	40,446	18,251	2,562	11,067	79,529	-26,732

future hydrologic stresses results in a lack of confidence in the predictions (Konikow, 1986). Here, we opted instead to evaluate proposed pumping scenarios by adding new, hypothetical well fields into the historical transient model runs.

Six hypothetical pumping simulations were performed using the historical transient model. Three well field locations were considered (Figure 5-11a), with two pumping schemes (Scenario 1 and Scenario 2) for each location, totaling six pumping scenario simulations. The well fields are located between 20 and 80 km north of the wells centered near Dell City (Fig 5-11b). In any scenario, only one of the well fields was pumped using one of the two pumping rates / time periods. The hypothetical pumping scenarios extracted additional water from the three locations. Additional pumping was set to 127,072 acre-ft and 66,345 acre-ft for Scenarios 1 and 2, respectively. The hypothetical pumping scenarios were not run into the future because of the many unknowns, including projected temperature increases and uncertainty regarding future pumping stresses (Gutzler, 2005).

The Otero Break and Crow Flats well field locations are consistent with locations previously simulated by Finch (2002) and JSAI (2002), whereas the Piñon Creek well field location was chosen because it was farther from the Texas–New Mexico border. Minor adjustments were made to Finch (2002) and JSAI (2002) well field locations to ensure the wells were in a productive geologic formation. The hypothetical Piñon Creek well field footprint consisted of five areas near Piñon Creek on New Mexico state lands. The hypothetical locations provided opportunities to examine the effects of spatial and geologic contrasts and to evaluate the simulated response. The five areas were intersected with the current model grid to assign pumping to model cells. For each of the hypothetical well fields, the well model layer was assigned based on the deepest model layer with a productive geologic formation. This was Layer 2 for the Otero Break and Piñon Creek well fields and Layer 3 for the Crow Flats well field (Figure 5-11). Pumping volumes were distributed uniformly across all of the wells in each of the hypothetical well fields.

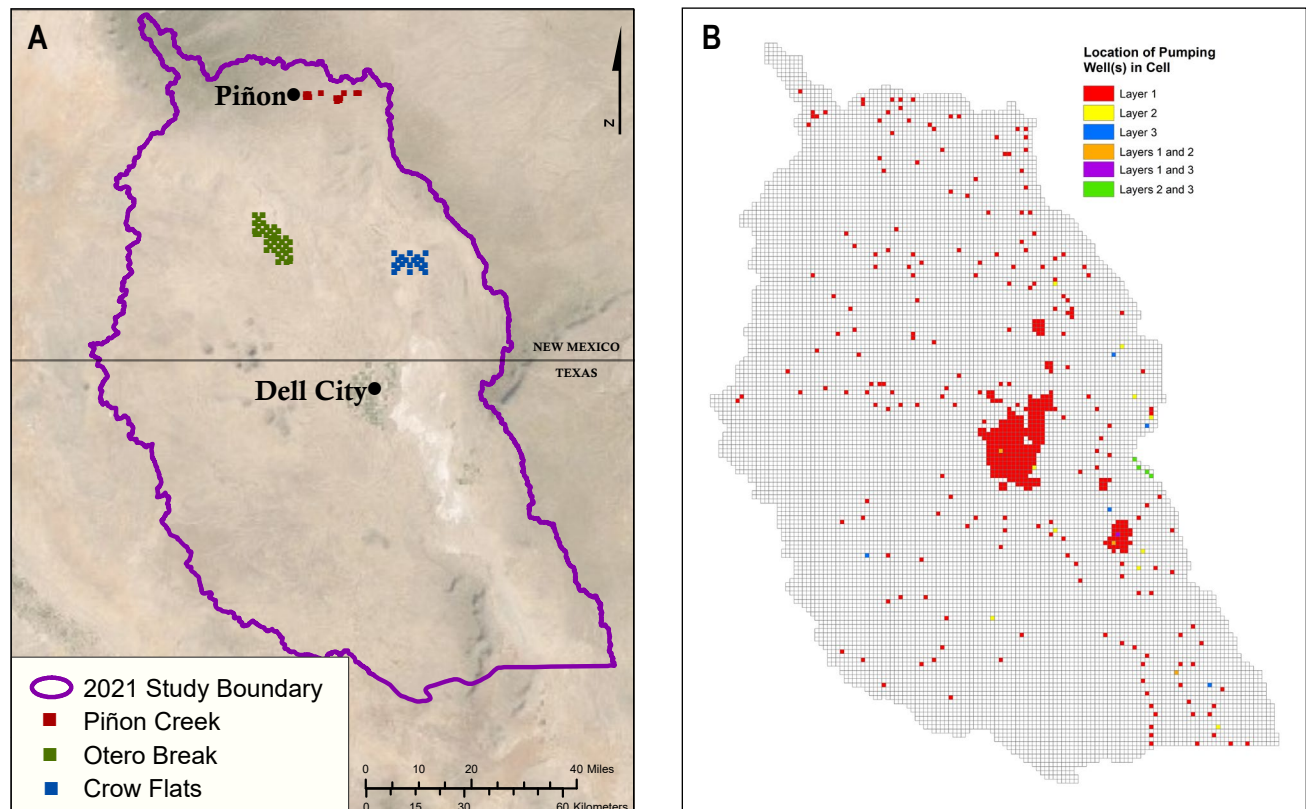


Figure 5-11. (A) Locations of hypothetical well fields used in model, and (B) locations of pumping wells in different model layers.

Pumping Scenario 1 represents the pumping volume needed to make up for the Pecos River Compact shortages of water going from New Mexico to Texas in six historical years with delivery shortfalls (1969 through 1974). The Pecos River Compact is an interstate compact between New Mexico and Texas that allocates the waters of the Pecos River between the states (Compact, 1949). In this scenario, pumped water would have to be transferred via a pipeline discharging to the Pecos River. The well fields were pumped from 1969 through 1974 with a total of 127,072 acre-ft for the entire six years of additional pumping. Limiting Scenario 1 pumping to a single 6-year time period provides the opportunity to examine long-term response from the individual 6-year augmentation effort. The pumping for Scenario 1 simulates a worst-case scenario, or pumping large volumes of water for several years in a row. Table 5-5 has the annual additional pumping rates for Scenario 1.

Pumping Scenario 2 was developed to have additional pumping in years with above-normal runoff. The pumping volumes were suggested by consultants for New Mexico Interstate Stream Commission (S.S. Papadopoulos & Associates, Inc.). The first step to determine suggested pumping volumes was summing the predevelopment steady-state runoff volumes from drainages on the New Mexico side of the Salt Basin. The total predevelopment steady-state runoff in New Mexico was 9,375 acre-ft/yr. A threshold of 20% greater than this value, or 11,000 acre-ft/yr, was chosen. Years with more than 15,100 acre-ft of runoff were selected for extra pumping. The extra pumping volume per year was the runoff exceeding the threshold of 11,000 acre-ft/yr. Based on these criteria, additional pumping was applied for Scenario 2 in 1972, 1974, 1985, 1993, 2006, 2008, 2013, and 2014, totaling 66,345 acre-ft over the entire 8 years (Table 5-6). Scenario 2 pumping represents a best-case scenario, or only pumping water volumes above a typical recharge threshold in years with high recharge.

The greatest drawdown associated with the hypothetical pumping scenarios occurs in 1974 for Scenario 1 (Figure 5-12a), which had a total of 127,072 acre-ft additional pumping. For Scenario 1, drawdown reaches over 6 m for the Crow Flats and Otero Break well fields and over 25 m for the Piñon Creek well field. For Scenario 2, maximum drawdown

occurs in 2014, resulting from the 66,345 acre-ft of additional pumping (Figure 5-12b). For Scenario 2, Crow Flats and Otero Break well fields reach a drawdown of over 2 m, and Piñon Creek well field drawdown is over 10 m. For the higher additional pumping volume (Scenario 1) in the Otero Break and Piñon Creek hypothetical well fields, the result was maximum drawdown of about 1 m. Beyond the 1 m of drawdown contour, there were decreases of less than 1 m in water levels sporadically throughout the basin for all pumping scenarios.

Figure 5-13 compares fluxes across the New Mexico–Texas state line for the six pumping simulations. All hypothetical pumping simulations have a modest annual decrease in subsurface water flowing from New Mexico into Texas. The state line flux for the entire model run decreased the most for the Crow Flats Scenario 1 simulation, which pumps

Table 5-5. Years and pumping rates of extra pumping in acre-ft/yr for Scenario 1 simulations. The pumping total for the six consecutive years of additional pumping was 127,072 acre-ft. Pumping rates were provided in Finch (2002) and JSAI (2002).

Year	Pumping Rate (acre-ft/yr)
1969	27,449
1970	24,555
1971	21,960
1972	18,372
1973	22,060
1974	12,676

Table 5-6. Years and pumping rates of extra pumping in acre-ft/yr for the hypothetical Scenario 2 simulations. A total of 66,345 acre-ft was added to the eight non-consecutive years indicated, and those years were times with above-normal runoff.

Year	Pumping Rate (acre-ft/yr)
1972	6,532
1974	11,848
1985	6,652
1993	6,341
2006	13,107
2008	9,215
2013	4,495
2014	8,152

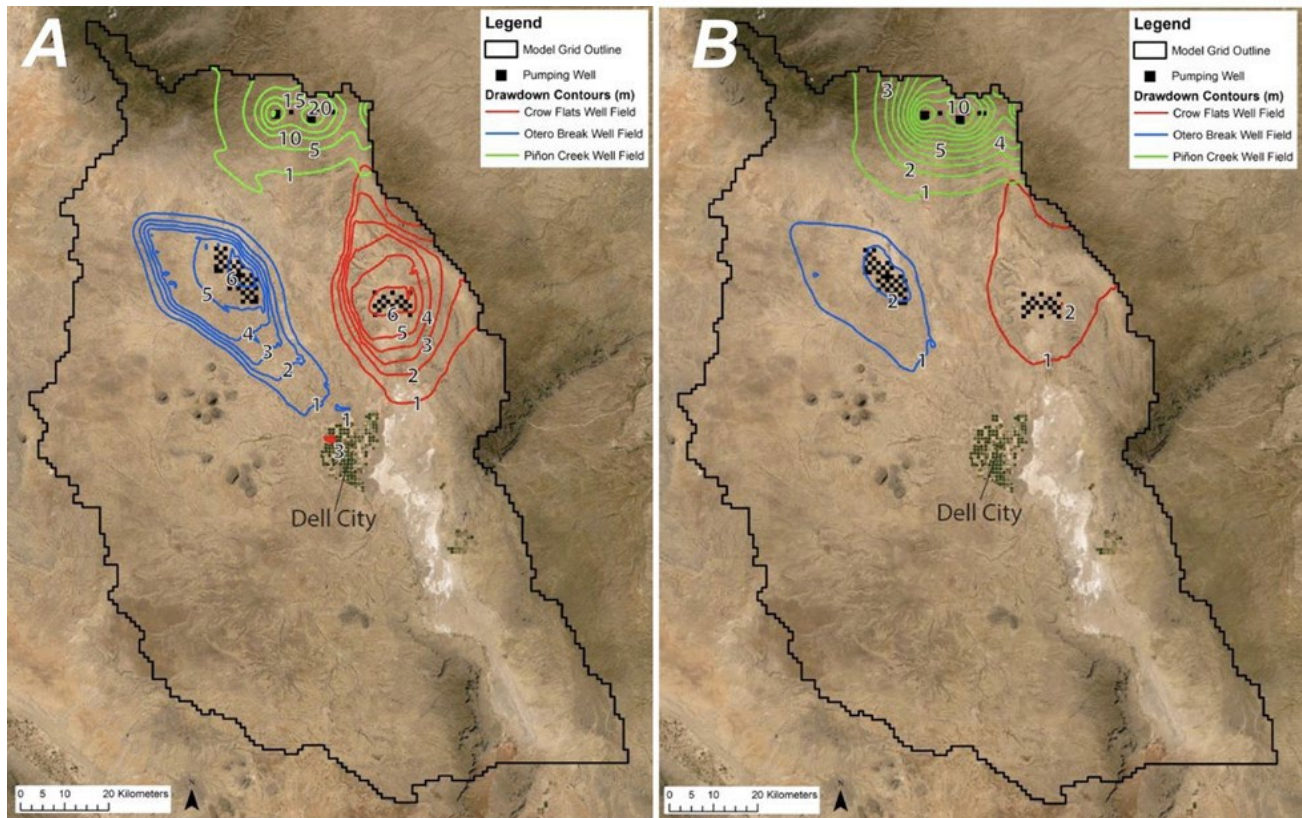


Figure 5-12. (A) Drawdown contours for Scenario 1 (127,072 acre-ft of additional pumping) for the year 1974. (B) Drawdown contours for Scenario 2 (66,345 acre-ft of additional pumping) for the year 2014. In both scenarios, the cones of depression were calculated by taking the difference between the historical transient model water table (in meters) and the water table calculated under the well field pumping scenarios.

a total additional 127,072 acre-ft with a decrease of 67,625 acre-ft across the state line into Texas. The smallest decrease was for the Piñon Creek well field, pumping a total of 66,345 acre-ft (Scenario 2) with a decrease of 1,522 acre-ft across the state line over the entire model period. From 1970 to 2008, the Crow Flats Scenario 1 and Otero Break Scenario 1 have the largest decrease in state line flux. After 2008, all model scenarios have similar decreases in state line flux. Comparisons of the maximum, minimum, and average fluxes across the New Mexico–Texas state line for the six pumping scenarios are listed in Table 5-7. This table also compares the total change in state line flux for each of the pumping scenarios to the historical baseline model. Over the 72-year modeling period, the biggest change is seen with the Crow Flats Scenario 1 simulation, with a total decrease of 67,625 acre-ft across the state line. The Piñon Creek Scenario 2 simulation showed the least change from the historical model, with a small decrease of 1,522 acre-ft across the state line after 72 years.

Model discussion

The choice of 60,000 acre-ft/yr recharge is well supported by prior studies. DBS&A (2010a) developed a basin-scale balance model that evaluated precipitation, evapotranspiration, and recharge. They used a groundwater model to estimate an average recharge of 63,000 acre-ft/yr, with recharge of 37,000 acre-ft in a low-precipitation year and 82,000 acre-ft in a high precipitation year. DBS&A (2010b) studied the evaporation from the playa deposit core samples in the Salt Flats and found an average of 28,300 acre-ft/yr of evapotranspiration. DBS&A (2010b) also described potential factors that might cause this estimate to be too low, making this estimate a minimum. PyRANA estimated the total diffuse and focused recharge to be 34,000 to 68,000 acre-ft/yr. For the predevelopment steady-state model, all of the discharge results from evapotranspiration in the Salt Flats. The maximum evapotranspiration rate for the three levels of recharge is reduced from 5.5 to 1.45 mm/day with a 10-m extinction depth.

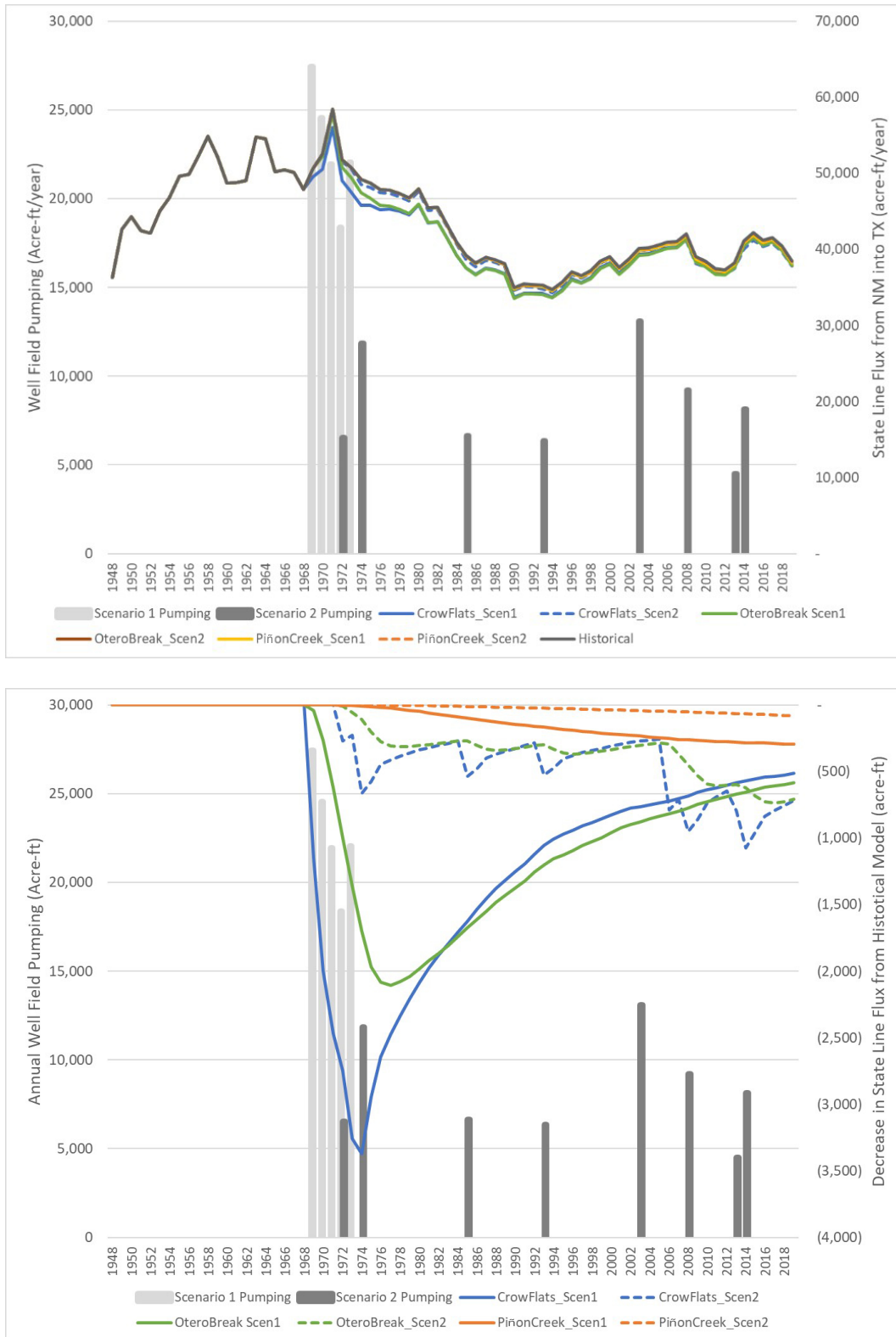


Figure 5-13. Comparison of (top) the annual subsurface flux of water across the state line from New Mexico to Texas, and (bottom) the difference in flux from the historical model for each of the well field locations pumping scenarios. Under the Crow Flats Scenario 1 pumping regime, the well field pumped approximately 25,000 acre-ft every year from 1969 to 1972. This created a near-instantaneous decrease in state line flux of 3,500 acre-ft compared to the historical model. Well field location plays a strong role in determining the timing and changes to state line flux. The Piñon Creek Scenario 1 model had no immediate impact to state line flux but continued to slowly decline 40 years after the pumping had stopped.

Table 5-7. Comparison of subsurface water flux across the state line from New Mexico into Texas for the historical baseline simulation and six pumping simulations, including the total difference in state line flux from New Mexico into Texas over the entire model run (1948–2020).

Simulation	Average annual state line flux (acre-ft)	Maximum annual state line flux (acre-ft)	Minimum annual state line flux (acre-ft)	Total (sum) difference in state line flux from historical model (1948–2020) (acre-ft)
Historical Transient Model	43,586	58,475	34,762	-
Crow Flats Scenario 1	42,647	56,007	33,683	-67,625
Otero Break Scenario 1	42,768	57,851	33,561	-58,916
Piñon Creek Scenario 1	43,473	58,474	34,587	-8,125
Crow Flats Scenario 2	43,257	58,475	34,289	-23,700
Otero Break Scenario 2	43,334	58,475	34,428	-18,102
Piñon Creek Scenario 2	43,565	58,475	34,736	-1,522

The historical transient model was unable to fit seasonal oscillations in the water table after the year 2000, but it was able to reproduce the annual trends in water levels. The historical transient model revealed that holding diffuse recharge rates constant and varying channel-focused recharge based on annual precipitation rates provided a good match to transient water level observations. Pumping reduced the water levels under the Salt Flats, significantly decreasing the evapotranspiration rate from 1948 to 2020. Between 1948 and 1980, the evapotranspiration rate dropped quickly from 57,000 to 4,500 acre-ft/yr. Then from 1980 to 2020, evapotranspiration rates decreased more slowly to 3,000 acre-ft/yr in 2020. JSAI (2010) observed a similar phenomenon in their model, which used a 9-m evapotranspiration extinction depth from the land surface. Pumping in their transient groundwater model decreased water levels under the Salt Flats, decreasing evapotranspiration rates to zero in 1980. Based on observed data, the Salt Flats should have reached zero evapotranspiration in the year 2000 (JSAI, 2010). JSAI (2010) believed that the early decrease in water levels in their model under the Salt Flats was due to overestimated consumptive pumping used in their model. Our model did not reach zero evapotranspiration for the entire transient simulation, let alone the year 2000, but the decrease down to just 3,000 acre-ft/yr from an initial value 20 times higher seems a reasonable representation of historical evapotranspiration changes.

The computed predevelopment steady-state water table compared favorably to observed conditions. The final computed 2020 water level map from the

historical transient model compared favorably to the measured cone of depression (Figure 5-8). Water table maps and model results show the water table minima shifted from under the Salt Flats to under Dell City. Following the groundwater gradient, the groundwater flow direction may be toward Dell City instead of toward the Salt Flats, providing the opportunity for lower quality water to migrate from the playa area toward Dell City wells.

The historical transient model indicates the Salt Basin has not reached equilibrium conditions since pumping started there. Rather, we observe the effects of groundwater mining in which groundwater is removed faster than it is recharged. This phenomenon can be seen in Figure 5-9 in the net storage oscillating back and forth with gains and losses since about 1985. Some fluctuations in groundwater storage are due to transient pumping / recharge rates. The simulated decrease in water levels from 1985 to 2020 is also seen in observed water levels in Dell City (Figure 5-10).

Pumping scenario discussion

The six different pumping simulations were created by adding pumping at defined intervals within the calibrated historic model from 1948 to 2020. This 72-year model simulation period may be too short to determine what the long-term effects of pumping could be. Additionally, effects from additional pumping in the hypothetical pumping scenarios could be exacerbated in the future if this additional pumping were continued using 2020 climate conditions.

The three hypothetical well fields used in the six pumping simulations are a long distance from the Dell City pumping center, ranging from 34 to 76 km away. This distance was designed to minimize drawdown in both the hypothetical well fields and Dell City. Based on the computed state line fluxes, the additional well field pumping in New Mexico had a minimal effect on annual groundwater flowing from New Mexico to Texas—typically 1,000 acre-ft or less in any given year, although the Crow Flats Scenario 1 and Otero Break Scenario 1 briefly decreased state line flux by over 3,000 and 2,000 acre-ft, respectively. When comparing cumulative totals, however, the change is larger. Pumping a total additional 127,072 acre-ft (Scenario 1) in the Crow Flats well field had the largest cumulative decrease in flux from New Mexico to Texas for all six scenarios, with a total of 67,625 acre-ft from 1948 to 2020. That decrease in state line flow is 61% of the total additional pumping volume of 127,072 acre-ft. Wells in the Salt Basin that were not directly in the well field could be affected by the additional pumping, including wells 20 km from the southern border of the basin, but this was a drawdown of less than 0.5 m. Drawdowns of less than 0.5 m are seen throughout the entire basin. The observation well in Dell City showed minimal (less than 1 m) to no changes in water levels due to the pumping scenarios. Together the flux across the New Mexico–Texas border and observation well water levels suggest that additional pumping will not have much effect on wells in Texas.

Figure 5-14 shows the extent of the drawdown for the pumping scenarios. In the pumping scenarios, wells located within the cones of depression would be affected by the hypothetical well field pumping. Outside of the 1-m contours, drawdown of less than 1 m is seen sporadically throughout the Salt Basin. Overall, pumping an additional 127,072 acre-ft (Scenario 1) creates water level drawdown that is more severe than pumping an additional 66,345 acre-ft (Scenario 2). The shape of the drawdown contours seems to be highly affected by geology in the Crow Flats and Otero Break well fields. The contours extend farther in geologic zones with higher conductivity. The Otero Break well field contours extend farther down the Otero Break toward Dell City, and the Crow Flats well field extends toward the Salt Flats. Pumping a total additional 66,345 acre-ft (Scenario 2) at the Crow Flats and Otero Break well fields does not cause water level drawdown

of more than 2 m outside the well field. Despite the small drawdown, it should be noted that the Otero Break well field has a preferential drawdown pattern oriented toward Dell City, which could cause problems if drawdown increases. Nevertheless, pumping a total additional 66,345 acre-ft (Scenario 2) at the Crow Flats and Otero Break well fields looks the most promising. Pumping a total additional 127,072 acre-ft (Scenario 1) for all three well fields or the lower pumping rate (Scenario 2) at the Piñon Creek well field will either create excessive drawdown or encroach on Dell City.

In addition, if the pumping scenarios were run for the year 2021 and into the future, they may show more negative effects, such as increased drawdown and decreased state line flux, because those years could potentially have less recharge due to climate change in the future. It is also important to note that our analysis did not consider water quality change due to pumping.

Model uncertainties and improvements

The models we constructed contain uncertainties. First, the predevelopment recharge rate of 60,487 acre-ft/yr was mostly based on prior work and is not significantly statistically better than the other recharge scenarios. Recharge values of 40,000 or 80,000 acre-ft/yr are potentially reasonable as well. Recharge and evapotranspiration are spatially and temporally variable, especially in a semiarid climate, with monsoons providing most of the water in the basin, making these parameters hard to quantify and estimate (Jovanovic and Israel, 2012; Sophocleous, 2004). The pumping rates used in our models needed to be estimated for most wells. Although the methods used to determine pumping were thorough, they still produced estimates. For the historical transient model, the water level oscillations discussed in Huff and Chace (2006) were not reproduced by the simulation. This suggests the geology zones may be too coarse and lack the spatial variability to reproduce the water level fluctuations in that portion of the Salt Basin. Thus, assumptions were made based on the short-term additional pumping to determine how additional pumping would affect the Salt Basin in the long term.

Several other studies have attempted to more or less answer the questions posed in this study. Not surprisingly, there have been a wide variety of answers. The current model is the only model of

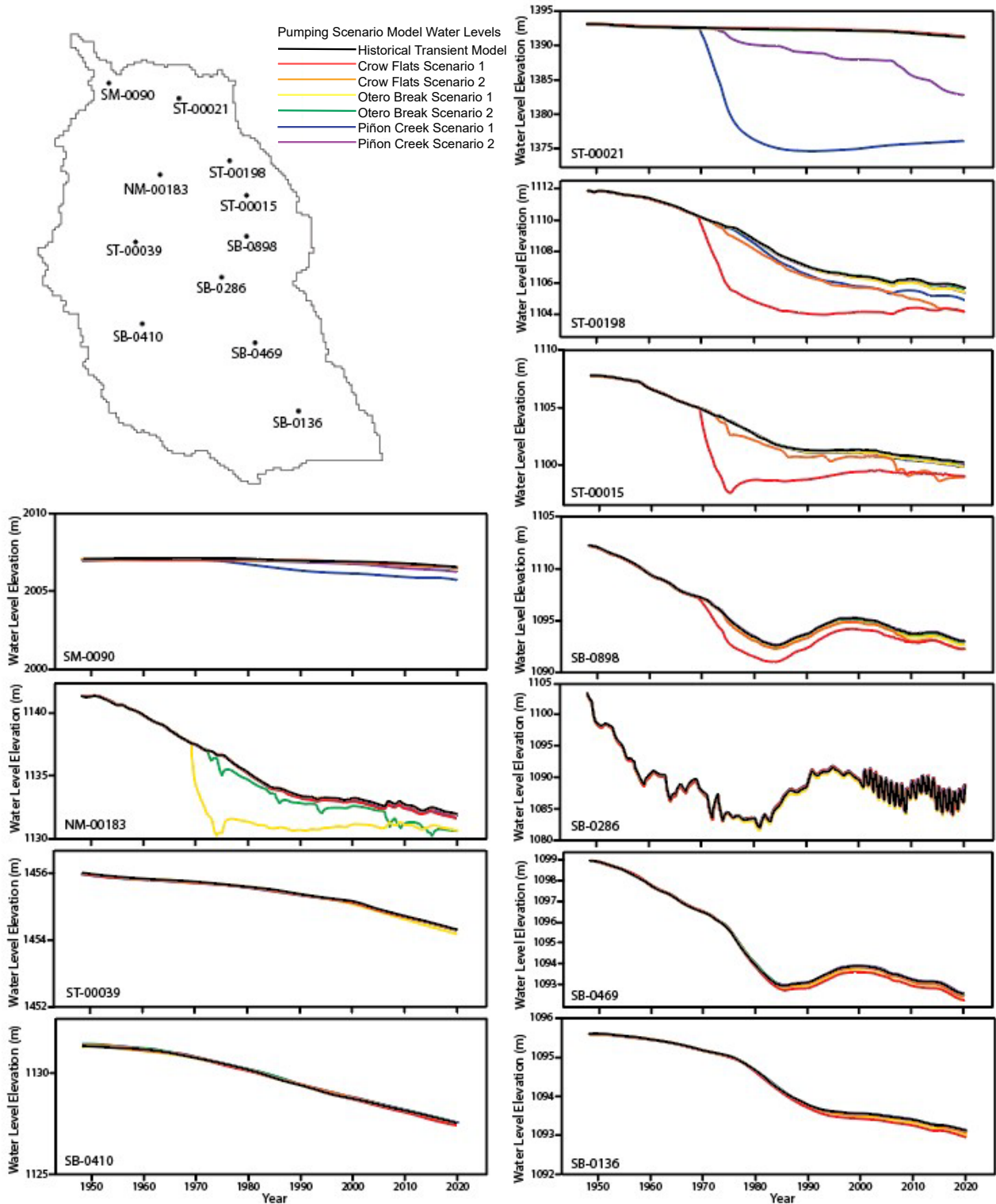


Figure 5-14. Transient water levels for the historical transient model and the six pumping simulations. Color denotes the model scenario. Well ID is at the bottom left of each graph. At top left of the figure is a map of the model grid with locations of wells plotted. Well ST-00021 was near the Piñon Creek well field. Well ST-00015 was within the Crow Flats well field. Well NM-00183 was within the Otero Break well field. Water levels are in meters.

the Salt Basin to use PEST. PEST helps determine a better fit to observed data, improving the model quality. In many instances, PEST can reveal spatial data gaps. This model improved estimates of pumping rates by using available public pumping rates, NDVI maps, the Blaney-Criddle method, and JSAI's (2010) pumping data.

Model conclusions

Using information from prior studies and the results from our predevelopment steady-state model, the recharge rate of about 60,000 acre-ft/yr best fits the data, with a possible range of 40,000 to 80,000 acre-ft/yr also providing a good fit to the data. The evapotranspiration rate matched the recharge rate in the predevelopment steady-state model. The historical transient model had an average recharge rate of 61,259 acre-ft/yr, an average evapotranspiration rate of 11,067 acre-ft/yr due to declining water table elevation, and an average pumping rate of 79,529 acre-ft/yr. Evapotranspiration rates decreased from 57,000 to 3,000 acre-ft/yr from 1948 to 2020. This decline was caused by pumping in the Salt Basin that lowered the water levels under the Salt Flats below the evapotranspiration extinction depth.

Six hypothetical pumping simulations were applied to the historical transient model. Scenario 1 applied a total of 127,072 acre-ft of additional pumping from 1969 through 1974 to each of the hypothetical New Mexico well fields. Scenario 2 applied a total of 66,345 acre-ft of additional pumping to years with higher runoff. These pumping scenarios were applied to three different hypothetical well fields—the Crow Flats well field, the Otero Break well field, and the Piñon Creek well field. Any additional pumping from the Salt Basin will result in a decrease of groundwater storage. For all six pumping simulations, the annual decrease in groundwater flowing from New Mexico to Texas is minimal, with a single-year maximum of

3,372 acre-ft for the Crow Flats well field pumping (Scenario 1). This change represents about an 8% decrease in the average annual transboundary flux. The drawdown contours showed that the 66,345 acre-ft (Scenario 2) of additional pumping in the Crow Flats and Otero Break would have a minimal effect on groundwater production around Dell City, Texas. The maximum drawdown at Crow Flats was about 6 m, while the other well fields had about 1.5 to 1.8 m of drawdown.

Future work

Future work should focus on repeating the historical and hypothetical pumping scenario transient models using 40,000 and 80,000 acre-ft/yr of recharge to determine the range of uncertainty in our model predictions. Allowing recharge to be a calibration parameter should be considered in future modeling studies. Running transient models into the future would also be useful to determine if and when dynamic equilibrium conditions occur. Installing stream gages and/or pressure transducers to the Sacramento River and arroyos during high precipitation events would provide useful ground truth on channel-focused recharge. Monitoring lake levels and underlying groundwater heads in the Salt Flats would confirm whether or not the vertical head gradients are downward and whether water is migrating away from the Salt Flats toward Dell City. This model could also be improved by creating a model ground surface directly from a digital elevation model instead of from the nodes with digital elevation model values that are currently used. Pursuing model calibration with the carbon-14 ages and analyzing flowpaths may prove fruitful if sufficient information to limit the porosity adjustment can be developed. Incorporating the geophysical results in the geologic framework, particularly expanding the extent of the Ancestral Rocky Mountain highland, would help refine the model.

GROUNDWATER STORAGE

Marissa Fichera

Quantifying the recoverable storage of groundwater in aquifers is challenging due to variability in hydraulic properties (specific yield, specific storage, porosity), in aquifer designation (confined, unconfined, semi-confined), spatial variations in water quality, unknown depths to the “base” of aquifers (in both concept and data), and changes in economic limitations related to drilling for and treating groundwater. Groundwater models with hydrogeologic frameworks and defined/calibrated hydraulic properties assist in these efforts; however, there is still a large degree of interpretation involved in calculating a reasonable estimate. This section outlines the methods, assumptions, and results of an analysis to estimate the total recoverable storage of groundwater within the Salt Basin study area. The general methodology for this calculation is structured similarly to that outlined in Boghici et al. (2014), which defines total estimated recoverable storage as the “estimated amount of groundwater within an aquifer that accounts for recovery scenarios that range between 25 percent and 75 percent of the porosity-adjusted aquifer volume.”

A handful of Salt Basin hydrogeologic studies have attempted to calculate groundwater storage (referred to as aquifer storage, aquifer volume, total volume, or recoverable volume) for aquifers within the region. Results of these studies are summarized here. Boghici et al. (2014) estimated the recoverable groundwater storage of the Bone Spring–Victorio Peak Aquifer within the Salt Basin in Texas (Figure 5-15) using the preliminary groundwater flow model for the Dell City area developed by El Paso Water Utilities (Hutchison, 2008). The model includes one layer representing the Bone Spring–Victorio Peak Aquifer. Specific yield values were obtained from a groundwater storage zones database that accompanied the model and ranged from 0.01 to 0.019. These values were assigned to cells per their respective zonation. The same study additionally estimated the groundwater storage for the Capitan Aquifer using aquifer top and base surfaces (Standen et al., 2009) and an estimated specific yield of 0.05. Livingston Associates P.C. and JSAI (2002) estimated a total groundwater volume of Salt Basin bedrock and

basin-fill aquifers in New Mexico. This estimation assumed a constant saturated thickness of 750 ft and porosity values of 0.05 and 0.2 for bedrock and basin-fill aquifers, respectively (Livingston Associates P.C. and JSAI, 2002). JSAI refined their groundwater model and consequently their groundwater storage estimate in 2010 using model-calibrated specific yield values, a saturated thickness of 1,000 ft, and a larger model domain (Figure 5-15; Ritchie, 2011; DBS&A, 2010a).

Estimates based on model

Total groundwater storage estimation for unconfined aquifers requires the following variables: aquifer area, specific yield, and saturated thickness. Storage was calculated on a cell-by-cell basis using the geologic framework, hydraulic properties, and calibrated results of Evenocheck’s (2021) groundwater model. Each model cell was defined at 1,000 m by 1,000 m, for a cell area of 1,000,000 m². Specific yield varied by zone and layer from 0.1 to 0.01. Saturated thickness is a complex variable that in previous storage estimations was assumed constant (Livingston Associates P.C. and JSAI, 2002; DBS&A, 2010a) or was calculated from geologic boundaries (Boghici et al., 2014). In an expansive, heterogenous, anisotropic aquifer system like that of the Salt Basin, saturated thickness varies to an unknown extent, with the principal unknown variable being the base of the aquifer. General lack of wells, lack of deep (>1,000 ft) wells, and consequently the lack of associated water data all contribute to this inability to accurately quantify the aquifer base. Despite these challenges, this study developed an aquifer base using TDS (total dissolved solids) data and assumed well-screen elevations in an attempt to make a data-based quantification of groundwater resources.

The aquifer base was developed as a water quality boundary rather than a geologic boundary due to the high degree of TDS variability across the study area. The objective was to include economically treatable groundwater (TDS concentration $\leq 3,000$ mg/L) in the total recoverable storage calculation and to omit high-salinity groundwater (TDS concentration $> 3,000$ mg/L). This can be done with a variety of spatial interpolation tools, but the general method is to group wells into “treatable” and “high-salinity” categories, then interpolate the well-screen elevations of each group. This results in a generalized depth of known

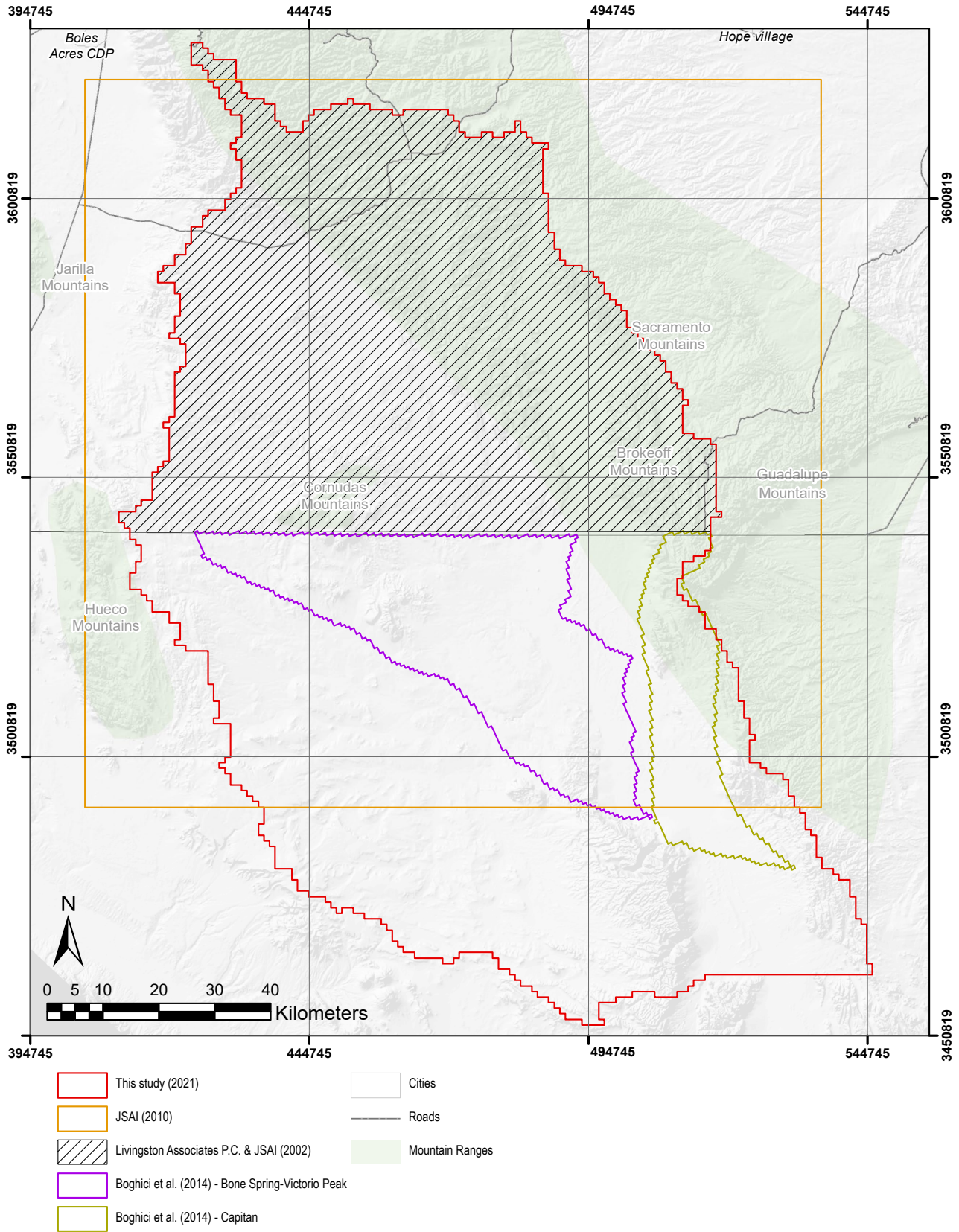


Figure 5-15. Study domains corresponding to existing groundwater storage estimates.

treatable groundwater and known high-salinity groundwater. Challenges arise when wells in close proximity to one another (areal location and well-screen depths) exhibit vastly different concentration values, as the treatable groundwater surface cannot be distinguished from the high-salinity surface. The Salt Basin study area presents such a challenge, as TDS content ranges from 253 to 139,144 mg/L, with most variability concentrated in the Bone Spring–Victorio Peak Aquifer underlying Dell City, Texas (Figure 5-16). Consequently, to delineate treatable from high-salinity groundwater, this study developed an aquifer base that was dependent on three datasets: water quality, well-screen elevation, and geologic contacts. With a continuous surface representing the base of the aquifer, a saturated thickness was calculated for every 1,000-m-by-1,000-m cell, and a total recoverable storage could be estimated.

Input data

Data used to estimate recoverable groundwater storage is outlined here:

3-D groundwater flow model (Evenocheck, 2021)—Model layer elevations and the output water level elevations from the groundwater flow model were used. These data were exported in a 1,000-m-by-1,000-m point-grid format from the Groundwater Modeling System (GMS) described in the next section, then converted to a raster format using the Topo-to-Raster and Point-to-Raster ArcGIS tools. Model layer elevations for the base of Layers 1 through 4, output water level elevations, and model-calibrated specific yield values were used in the final volume calculation. Each model layer represents multiple hydrogeologic units delineated by model zone, typically defined by specific yield (as described in previous section). Specific yield values were assigned to each cell within each layer using the corresponding model zone and model layer assignment scheme. Data were converted from polygon format to raster format with the Polygon-to-Raster tool.

3-D geologic framework (Ritchie, 2011)—The 3-D geologic framework developed by Ritchie (2011) was used in combination with TDS data to develop the aquifer base elevation surface. This framework was developed from geologic control points including formation picks from well logs, subsurface fault maps, and surficial geologic maps.

TDS data and well-screen elevation—TDS and well-screen elevation data were obtained from NMBGMR, USGS, and Texas Water Science Center databases. Well-screen elevation was assumed to be equivalent to total well depth.

Aquifer base development

Well-screen elevation, TDS concentration data, and a 3-D stratigraphic framework (Ritchie, 2011) were used to create a point dataset that represents the 3-D extent of treatable groundwater in the basin area, referred to as the aquifer base elevation dataset. A schematic of this process is shown in Figure 5-17. This was done in a multistep procedure, described below.

Geologic formations were assigned by well-screen elevation within the 3-D stratigraphic framework (Figure 5-17a). The observed TDS concentrations were then divided into two categories: (1) fresh to low-salinity brackish water, represented by a concentration less than or equal to 3,000 mg/L (referred to as treatable groundwater); and (2) brackish to saline water, represented by a concentration greater than 3,000 mg/L (referred to as high-salinity groundwater; Figure 5-17b). As determined by the TDS data, each well was identified as having either treatable or high-salinity groundwater. This designation, combined with the geologic formation assignment, provides the best estimate for the subsurface location of the aquifer base elevation point.

For treatable groundwater wells, the aquifer base elevation point was placed at the base of the well's associated geologic formation. High-salinity wells resulted in the groundwater base elevation point being placed at the top of the associated formation (Figure 5-17c). This makes the assumption that the vertical column of water within a geologic formation at the well location is of the same water quality as the well water. For the purposes of this estimation, groundwater in overlying formations is assumed to be treatable. Groundwater in underlying formations is assumed to be high salinity. This treatable groundwater elevation point dataset was then interpolated using the Topo-to-Raster ArcGIS tool to create an aquifer base elevation surface. This surface was used as the base of the aquifer in recoverable storage calculations (Figure 5-17d).

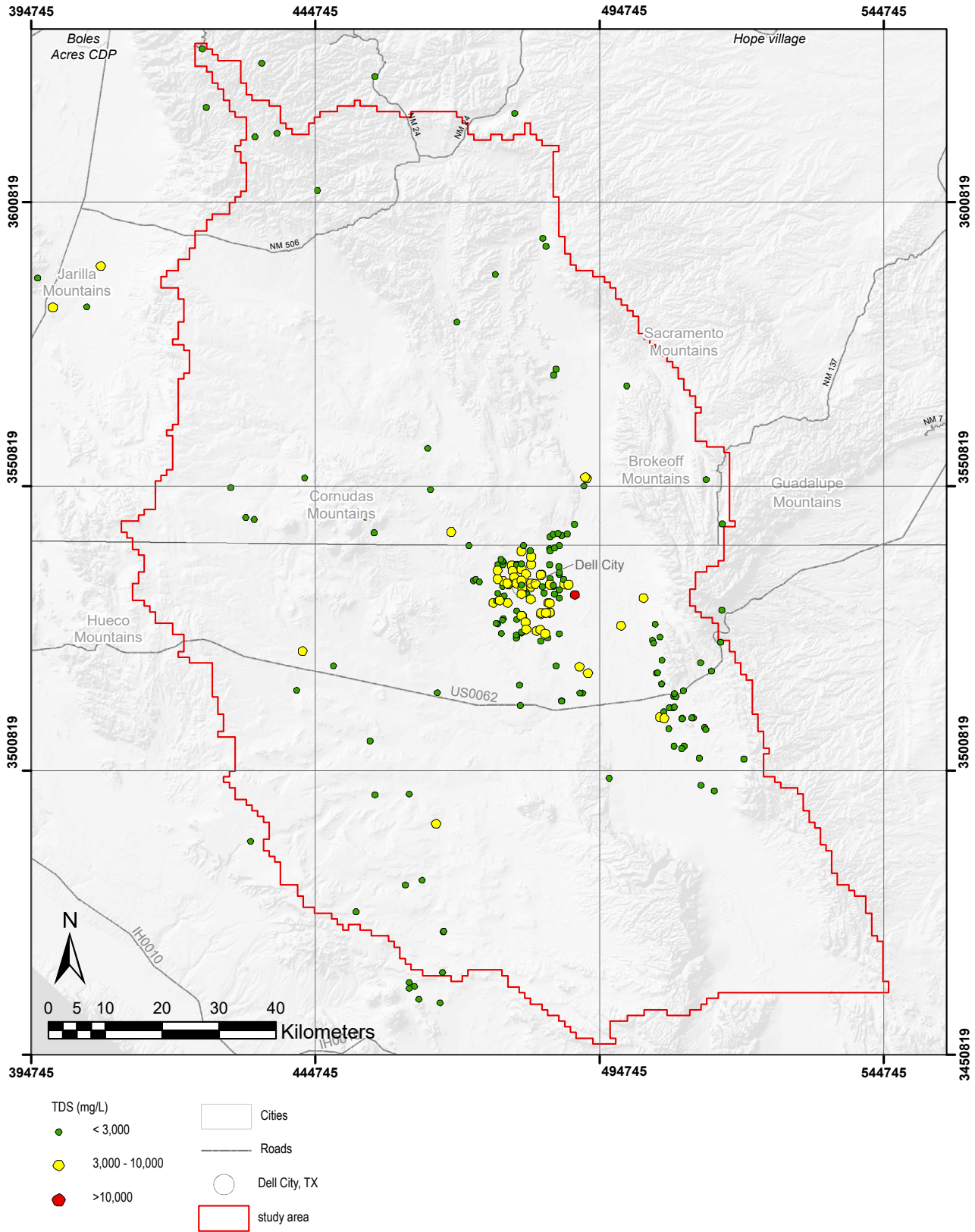


Figure 5-16. Distribution of TDS data from groundwater wells with known well depths across the Salt Basin study area. Data density is poor outside the surrounding Dell City, Texas, region. TDS concentration ranges from 253 mg/L to 139,144 mg/L. The highest concentration results are from a shallow (<5 m) well located just east of Dell City bordering the Salt Flats in the discharge zone. The TDS concentration ranges from 400 mg/L to 139,144 mg/L in Dell City, accounting for the majority of variability in the study area.

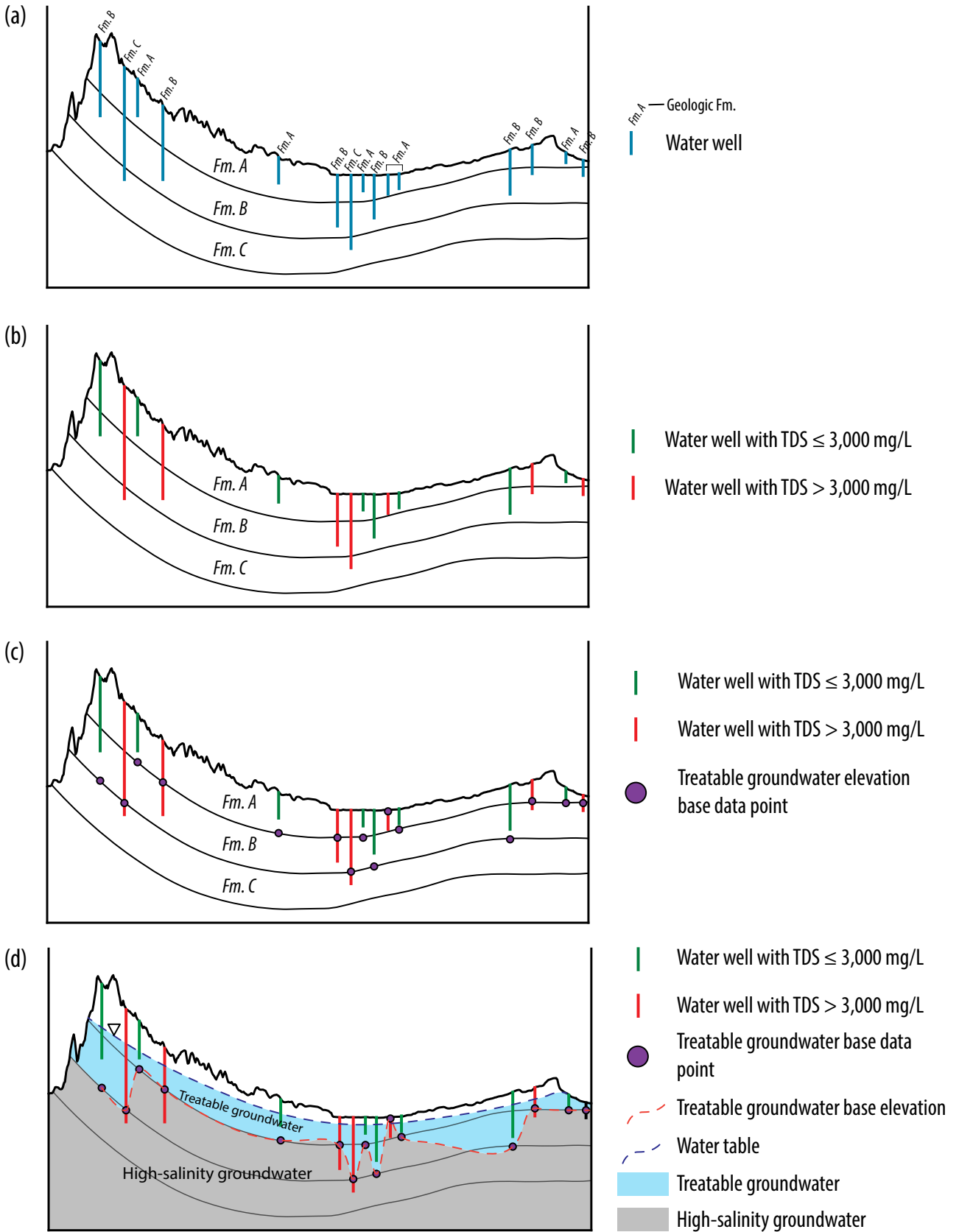


Figure 5-17. Conceptual schematic of the multistep process of developing a TDS surface including (a) geologic formation assignment, (b) well water quality designation, (c) elevation point placement, and (d) interpolation process result.

Storage calculation

Once the aquifer bases were estimated, the process of calculating the recoverable groundwater was calculated on a cell-by-cell basis using the following equation for unconfined aquifer systems (Boghici et al., 2014):

$$\text{Total Storage} = V_{\text{drained}} = A * S_y * \Delta h$$

where:

V_{drained} = storage volume due to water draining from the formation (acre-ft),

A = aquifer area (acre),

S_y = specific yield, and

Δh = saturated thickness of water column.

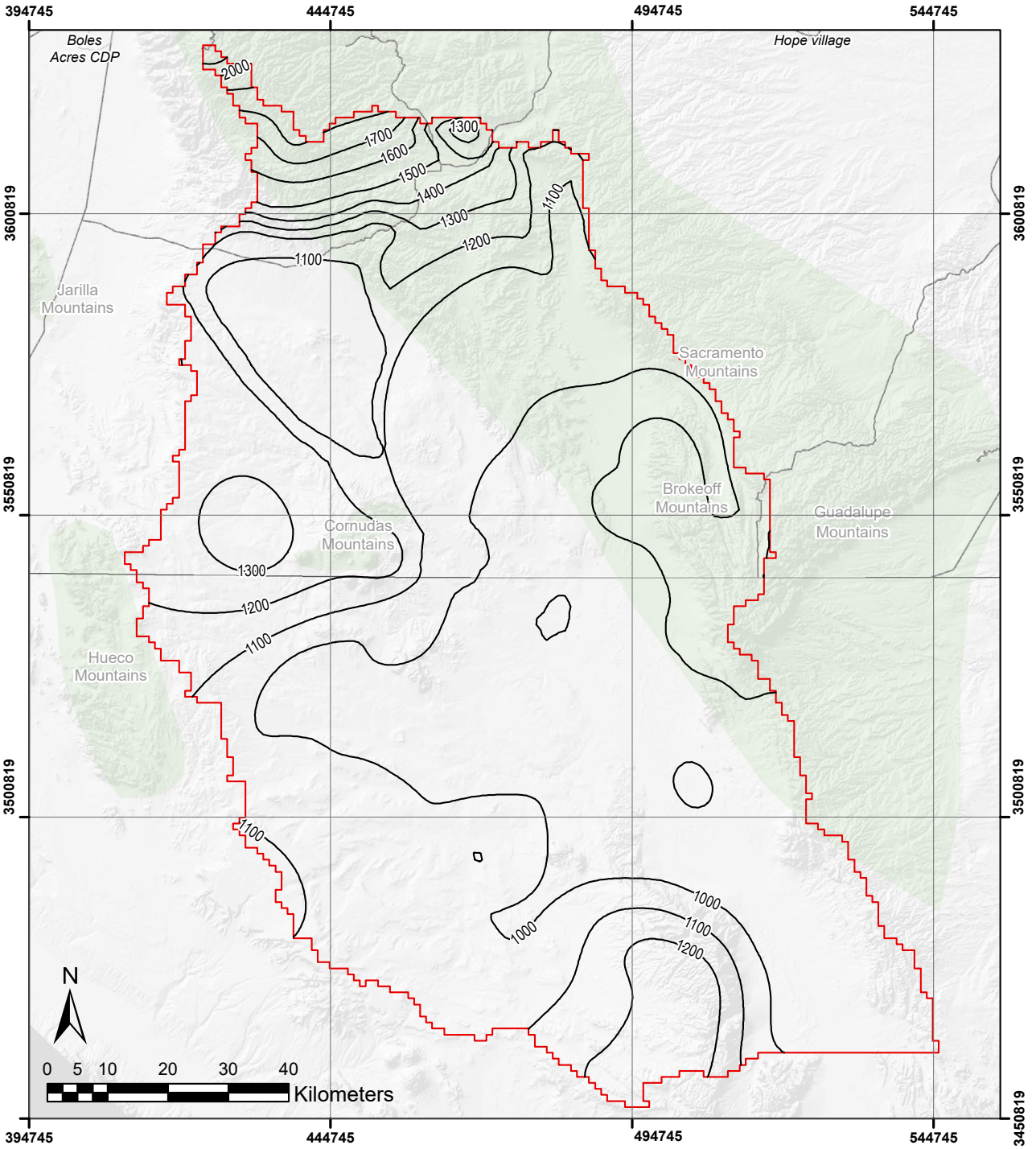
Variable Δh was equal to the difference between the computed water table elevation from the model developed in Evenocheck (2021) and the aquifer base elevation (Figure 5-18) described above. Specific yield was equal to the model-calibrated specific yield value (varied by cell and layer; Figure 5-19). Area remained constant for each cell at 1,000,000 m². A total volume was calculated for each cell in each model layer. The summation of cell volumes resulted in the estimated total basin volume.

Storage calculation results

Estimated recoverable groundwater storage volumes for the current study and previous studies are shown in Table 5-8. Previously estimated recoverable groundwater storage volumes are reported as 50% of the associated total groundwater volume for comparison purposes. Calculation area is included for this purpose also, as each study estimated volume for particular regions, some of which are significantly smaller than others (e.g., 172,000 acres for the Capitan Aquifer [Boghici et al., 2014] and 3,300,000 acres for this study's Salt Basin aquifers).

The total recoverable groundwater volume estimated for the Salt Basin study area is approximately 34.5 million acre-ft. This volume estimate covers approximately 3.3 million acres. The saturated thickness ranged from 0 to 590 m (0 to 1,900 ft) with an average value of 135 m (442 ft). Saturated thickness was below average throughout the majority of the basin and increased in higher elevation areas such as the Sacramento Mountains, Diablo Plateau, Cornudas Mountains, and Hueco Mountains. The shallow groundwater table in recharge areas combined with the thickness of associated carbonate aquifer units (Yeso Formation, San Andres Limestone) likely contribute to the increased saturated thickness values in these areas.

Additionally, the resulting recoverable volume for the New Mexico side of the Salt Basin was calculated to be 6.35 million acre-ft, or approximately 18% of the estimated recoverable groundwater volume for the entire basin, as reported in Table 5-8. It should be noted that the method presented in this report is meant to result in a minimum recoverable storage estimate using calibrated groundwater model data and known well depths. Well depth has a significant influence on the estimated saturated thickness: deep wells result in a deeper aquifer base and higher saturated thickness, while shallow wells result in a shallower aquifer base and lower saturated thickness. The general lack of high-density well coverage in New Mexico and the paucity of deep (>1,000 ft below ground surface) wells results in a lower saturated thickness estimate and consequently a relatively low groundwater storage estimation. The recoverable storage is therefore underestimated in regions with low data density and should be taken into consideration when interpreting results. It is reasonable to assume that the actual recoverable storage for the New Mexico part of the Salt Basin is larger than the estimated recoverable storage presented here, as the Sacramento Mountains are the primary source of fresh water into the basin.



Treatable groundwater base elevation (m asl)

- Contour Interval = 100m
- Cities
- ▭ study area
- Roads
- Mountain Ranges

Figure 5-18. Contoured surface representing the estimated treatable groundwater base elevation in meters above mean sea level.

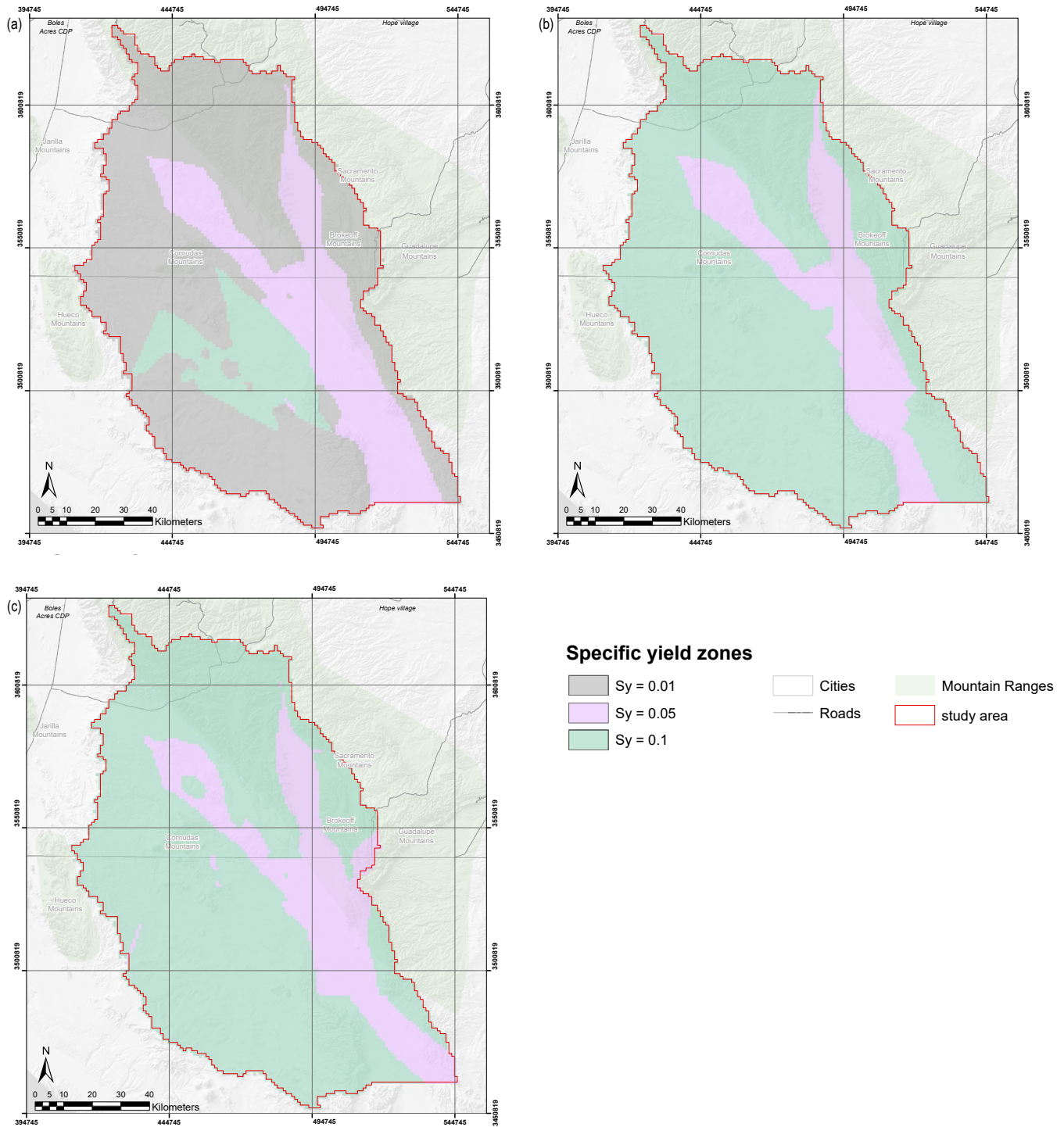


Figure 5-19. Specific yield values used in groundwater storage estimation, based on model-calibrated specific yield values (see Chapter 5 Hydrogeologic Model section for model layer descriptions). Map (a) displays the model-calibrated specific yield values for Layer 1. Maps (b) and (c) display specific yield values assumed for Layers 2 through 4 based on zone assignments for Layer 1. Simulated confined and unconfined water table results were undifferentiated (i.e., a single water table was simulated for all layers); therefore, all layers were treated as unconfined and assigned specific yield values for the purpose of calculating groundwater storage.

Table 5-8: Summary of estimated recoverable groundwater storage values calculated previously and in this study. Regions are outlined in Figure 5-15. Recoverable storage refers to 50% of the total groundwater storage reported in each study unless otherwise indicated. Calculation area is included to facilitate comparison of values, as each study calculated a recoverable storage for different and sometimes multiple areas. The assumptions involved in each calculation are summarized in this table and in this section's text.

Source	Region (see Figure 5-15)	Recoverable storage (acre-ft)	Calculation area (acres)	Assumptions
Boghici et al. (2014)	Bone Spring–Victorio Peak Aquifer	1,850,000	453,000	Hutchison (2008) groundwater flow model framework
Boghici et al. (2014)	Capitan Aquifer (Hudspeth Co., Texas)	550,000	172,000	$S_y = 0.05$, upper and lower surfaces, from Standen et al. (2009)
Livingston & JSAI (2002)	Salt Basin bedrock aquifer (New Mexico)	28,736,640*	1,500,000	Saturated thickness = 750 ft Porosity = 0.05
	Salt Basin basin-fill aquifer (New Mexico)	1,459,200*		Porosity = 0.2
DBS&A (2010a)	Salt Basin (New Mexico and Texas)	39,700,000**	2,600,000	Saturated thickness = 1,000 ft, Specific yield = model-calibrated, 0.01 and 0.1
This study	Salt Basin (New Mexico and Texas)	34,500,000	3,300,000	Saturated thickness = groundwater model and water quality-based Specific yield = layer-variable model-calibrated, range 0.01 – 0.1***

*Total recoverable volume stored in bedrock is based on the ability of the aquifer to liberate half of the total in storage to wells and on a confined storage factor equal to 0.05 (Livingston Associates P.C. and JSAI, 2002).

**Type of volume (total versus recoverable) unspecified.

***Groundwater model framework and model-calibrated specific yield values from Evenocheck (2021); geology framework for water quality boundary from Ritchie (2011).

MODEL CALIBRATION: LAST GLACIAL MAXIMUM SIMULATION

Mark Person

One way to test a calibrated hydrogeologic model is to predict heads in response to a new set of hydrologic stresses (e.g., pumping or recharge; Konikow and Person, 1985; Konikow, 1986). During the last glacial maximum (LGM), temperatures were estimated to have been at least 5°C cooler, and precipitation is thought to have doubled in New Mexico, forming a number of Pleistocene lakes (Phillips et al., 1988; Menking et al., 2004; Allen, 2005). Two lakes formed within the Salt Basin during this Pleistocene time period, including Lake King and Lake Sacramento. Wilkins and Currey (1997) used carbon-14 dating of shoreline deposits to determine Late Pleistocene lake levels within the Salt Basin (Figure 5-20a). Lake King was filled at least four times between 22.5 and 15 ka, with a periodicity of about 2,000 years of 26-m stage levels (Wilkins and Currey, 1997). Lake Sacramento reached maximum stages of 40 m above the lake bottom, but less is known about its lake level history. Lake Sacramento

was likely a perched lake not in good connection to the water table. Conversely, Lake King was likely in hydrologic connection with the Permian Bone Spring Limestone aquifer beneath it, and it received runoff from a few ephemeral streams (Figure 5-20a).

We estimated LGM evapotranspiration and recharge rates and used these as initial inputs to a suite of LGM steady-state MODFLOW models. The goal of developing these models was to determine paleo-recharge and surface runoff conditions that could account for LGM Lake King and Lake Sacramento high stands. In many of the simulations, we used the PEST parameter estimation module. In the PEST simulations, we varied the recharge rates and amounts of runoff using multipliers on the modeled 60,000 acre-ft/yr of recharge. We also constrained model results such that surface flooding was minimized.

Paleo-recharge estimates

We estimated potential evapotranspiration and recharge during the LGM in the uplands and lowlands of the Salt Basin using a modified Thornthwaite method (Thornthwaite and Mather, 1957; Knott and Olimpio, 1986). Potential

evapotranspiration (PET , in mm/mo) is calculated based on the temperature-dependent saturation vapor pressure (e_a , in kPa):

$$PET = 40.9 e_a$$

$$e_a = 0.6 \exp \left[\frac{17.3T}{T + 237.3} \right]$$

where T is mean monthly temperature in °C. Recharge (R) was then calculated to be the difference between PET and precipitation (P).

$$R = P - PET \text{ for } P > PET; \text{ if } P \leq PET, R = 0$$

Potential evapotranspiration, recharge, and precipitation were all calculated in mm/mo. We used weather station data from Dell City, Texas (lowland site), and Cloudcroft, New Mexico (upland site). We subtracted 5°C from modern monthly temperatures and doubled the monthly precipitation.

The mean monthly LGM and modern temperature/precipitation and recharge for Cloudcroft, New Mexico, and Dell City, Texas, are listed in Tables 5-9 and 5-10, and monthly recharge is plotted in Figure 5-21 at these two locations.

Our evapotranspiration model predicted nearly zero recharge at Dell City under modern climatic conditions. Inspection of Figure 5-21 suggests little recharge occurred in the lowlands during the LGM, but recharge was as much as 3.5 times higher in mountainous terrains.

Last glacial maximum model approach

We began by adding the lake package (Hunt, 2003) to the steady-state predevelopment Salt Basin MODFLOW model described above. Initially, we used the modern hydrologic stresses and hydrogeologic parameters (Run 1). In Run 2, we generally decreased the streambed hydraulic conductivity of the streamflow routing (SFR) network from the values

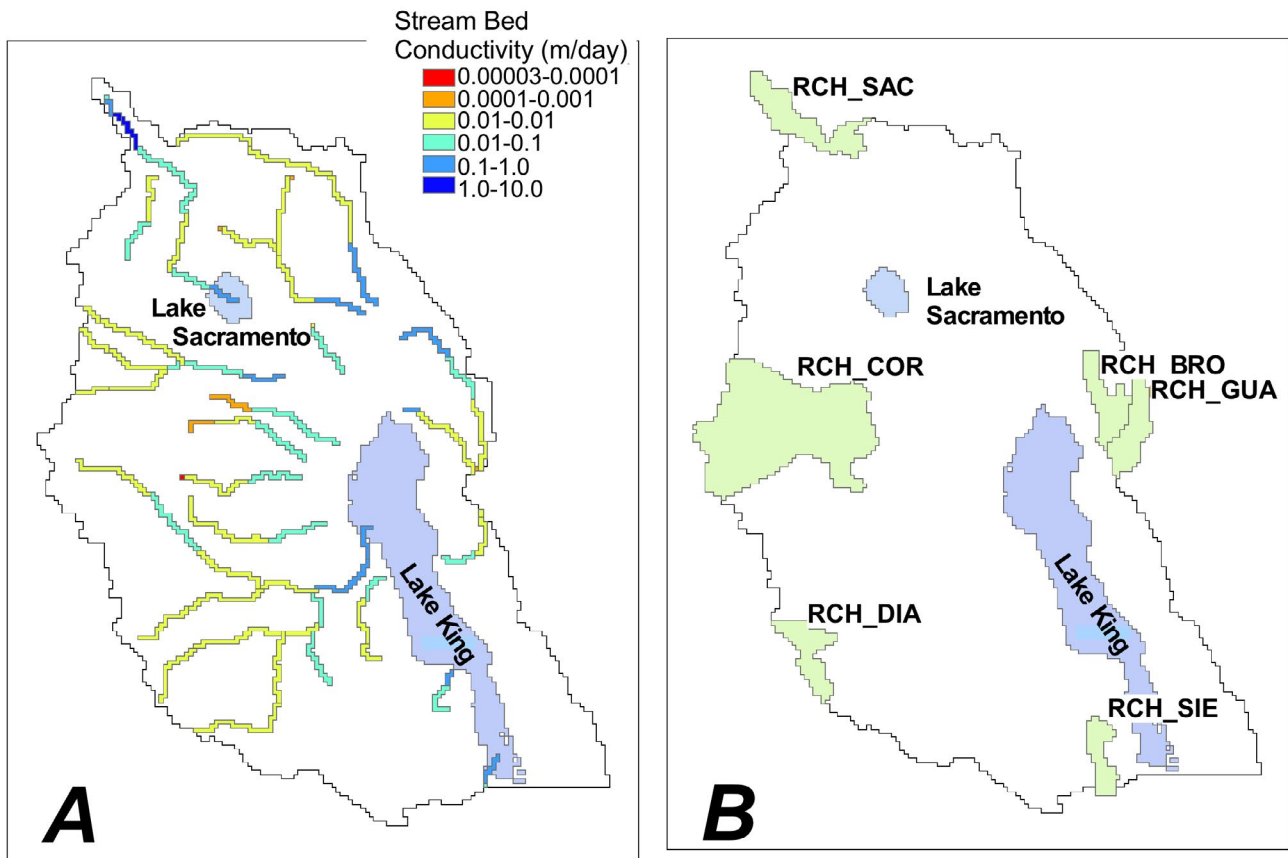


Figure 5-20. Base map of Salt Basin showing (A) stream bed hydraulic conductivity and (B) recharge zones. The location of Lake King and Lake Sacramento are also shown. The locations of these paleolakes were taken from Wilkins and Currey (1997). For Figure B, RCH is a delineated recharge area; the abbreviations used include BRO for Brokeoff Mountains, COR for Cornudas Mountains, SAC for Sacramento Mountains, DIA for Diablo Plateau, GUA for Guadalupe Mountains, and SIE for Sierra Diablo Mountains.

Table 5-9. Modern and LGM recharge estimates for Cloudcroft, New Mexico (elevation 2,645 m), using a modified Thornthwaite method. Potential evapotranspiration (PET), precipitation (Precip), and recharge (Rech) are presented in mm/mo. Temperature (Temp) is in °C.

Month	Modern				Last Glacial Maximum			
	Temp	Precip	PET	Rech	Temp	Precip	PET	Rech
1	-1.1	78.5	0.0	78.5	-6.1	157.0	0.0	157.0
2	0.3	82.6	25.5	57.0	-4.7	165.1	0.0	165.1
3	2.8	66.3	30.5	35.8	-2.2	132.6	0.0	132.6
4	6.4	30.0	39.3	0.0	1.4	59.9	27.1	32.8
5	10.8	34.5	53.2	0.0	5.8	69.1	37.2	31.9
6	15.0	64.0	69.9	0.0	10.0	128.0	49.4	78.6
7	15.0	152.1	69.9	82.2	10.0	304.3	49.4	254.9
8	14.4	141.2	67.4	73.8	9.4	282.4	47.6	234.9
9	12.2	79.5	58.3	21.2	7.2	159.0	40.9	118.1
10	7.8	54.6	43.3	11.3	2.8	109.2	30.0	79.2
11	2.8	45.7	30.5	15.2	-2.2	91.4	0.0	91.4
12	-0.8	72.1	23.5	48.6	-5.8	144.3	0.0	144.3

Table 5-10. Modern and LGM recharge estimates for Dell City, Texas (elevation 1,128 m), using a modified Thornthwaite method. Potential evapotranspiration (PET), precipitation (Precip), and Recharge are presented in mm/mo. Temperature (Temp) is in °C.

Month	Modern				Last Glacial Maximum			
	Temp	Precip	PET	Recharge	Temp	Precip	PET	Recharge
1	5.6	10.4	36.5	0.0	0.6	20.8	25.6	0.0
2	8.3	13.0	44.1	0.0	3.3	25.9	31.2	0.0
3	12.2	8.6	57.3	0.0	7.2	17.3	40.9	0.0
4	16.4	7.9	75.0	0.0	11.4	15.7	54.2	0.0
5	21.7	22.9	104.3	0.0	16.7	45.7	76.4	0.0
6	25.8	29.2	134.1	0.0	20.8	58.4	99.1	0.0
7	26.9	39.6	143.2	0.0	21.9	79.2	106.1	0.0
8	25.8	49.8	134.1	0.0	20.8	99.6	99.1	0.4
9	22.2	42.7	107.9	0.0	17.2	85.3	79.1	6.2
10	16.9	25.9	77.7	0.0	11.9	51.8	56.2	0.0
11	10.0	13.0	49.4	0.0	5.0	25.9	35.1	0.0
12	5.6	11.2	36.5	0.0	0.6	22.4	25.6	0.0

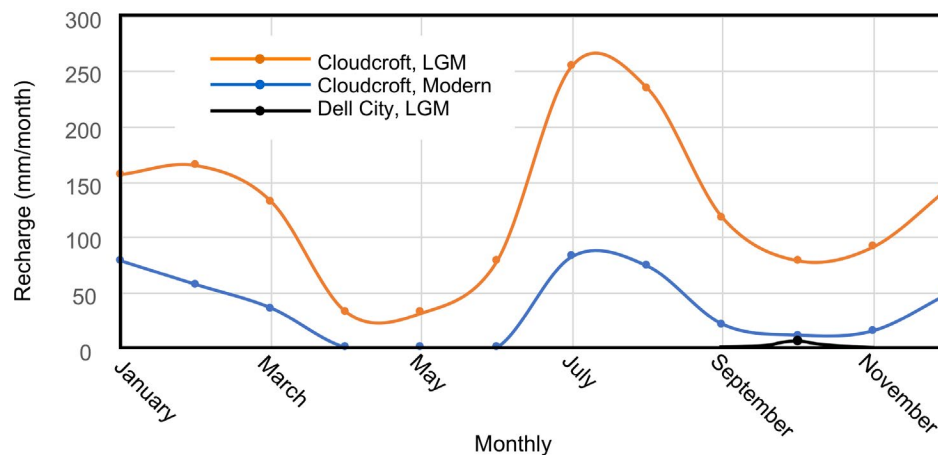


Figure 5-21. Comparison of estimated modern and last glacial maximum recharge for Cloudcroft, New Mexico, and Dell City, Texas. For this visualization, the lines are approximate recharge estimates, created using a spline fit.

shown in Figure 5-20, improving connections to the lake cells still using modern recharge/runoff forcing (Table 5-11). We ran a total of nine LGM simulations (Runs 3–11) varying diffuse recharge and surface runoff (channel-focused recharge). We used the decreased streambed hydraulic conductivity in some of the LGM simulations (Table 5-11), which resulted in more stable numerical solutions and lower lake package mass balance errors. In Runs 3–8, we used the hydraulic properties from the predevelopment Salt Basin model. The calibration targets for these LGM runs included minimizing cell flooding in Layer 1 cells, as well as matching maximum lake levels for Lake King in the lowlands and Lake Sacramento in the uplands.

As indicated above, Lake Sacramento was likely a perched lake and not hydrologically well-connected with the water table. Thus, we do not expect to see any ponded cells at the terminus of the Sacramento River. The hydrologic budget for Lake Sacramento includes stream inflow from the SFR network as well as lake losses from groundwater seepage and evapotranspiration. The hydrologic budget for Lake King, on the other hand, included groundwater inflow as well as SFR runoff. All outflow from Lake King is related to evapotranspiration losses.

For LGM Runs 5–11, we used PEST to try to improve model fit to lake levels. We modified the amount of diffuse recharge by allowing PEST to individually alter the diffuse recharge multipliers (Table 5-11, last column) as well as an SFR multiplier. The diffuse recharge and SFR multipliers were allowed to vary between 1 to 100, 0.1 to 100, 0.1 to 10, and 0.1 to 3.5 in Runs 5–11.

In Runs 9–11, we allowed PEST to also vary hydraulic conductivity (HK) and vertical anisotropy (VA) of the six model layers. Table 5-12 quantifies computed versus observed lake levels as well as the sum of flooded upland cells in Layer 1. The sum of flooded cells was calculated as follows:

$$sum = \sum_{n=1}^{N_{upland}} h_n - z_n; \text{ for } h_n > z_n$$

where h_n is the nodal upland heads in Layer 1, and z_n is the associated land surface elevations.

Results

All model runs show some degree of flooding in the lowlands, which is to be expected since evapotranspiration is the primary way water leaves the Salt Basin. The computed water table elevations and flooded cells (blue triangles) for all nine LGM model runs are graphically presented in Figures 5-22 and 5-23. Runs 7–8 had the lowest model residual with respect to simulated lake levels. Negative values of error in Table 5-12 denote under-prediction of lake levels. Runs 7–8 had similar levels of upland flooding compared to the predevelopment model runs (Runs 1–2). Runs 9–11 had similar goodness of fit to observed LGM lake level targets but with reduced levels of cell flooding.

A common feature of Runs 7-8 was increased surface runoff (~20x to 29x) and modest decreases in diffuse recharge (0.1x to 0.80x). In Runs 9-11, some recharge zones in the southern portion of the Salt Basin had much higher multipliers (up to 10x), whereas the central diffuse recharge zones were somewhat lower than modern rates (as low as 0.41x). To some degree, the best fit values of diffuse recharge in these runs was constrained by the upper limits imposed by PEST (e.g., SFR_RUNOFF, Runs 10–11).

Runs 9–11 allowed for modifications to HK and VA as well as recharge using PEST. Table 5-13 presents a comparison of the range of HK and VA for Run 1 (predevelopment, modern hydrologic forcing) and Runs 9–11. For some layers, the maximum HK and VA were higher in Runs 9–11 than in Run 1. Figure 5-24 graphically compares HK values for Run 1 and Run 10 within the top two layers. While the overall patterns do not change much, some adjustments occur within various HK zones.

Discussion and conclusions

We cannot point to one specific model run that best recreates paleo-lake levels during the LGM (although Runs 8 and 10–11 are the most likely candidates). However, a common feature of the LGM models is that runoff and channel-focused recharge was much higher (between 10x and 30x) than it is today. Increases in runoff would be consistent with more frequent episodic precipitation events exceeding the soil hydraulic conductivity and more frequent

Table 5-11. Description of LGM model parameters. HK = hydraulic conductivity; VA = vertical anisotropy; SFR = Streamflow Routing module.

Run Number	Comments	Revised SFR conductivity used?	Calibrate HK/VA?	PEST used?	Multipliers on modern focused and diffuse recharge
1	Modern (~60,000 acre-ft focused and diffuse recharge)	No	No	No	1
2	Modern, revised SFR	Yes	No	No	1
3	LGM 3.5	No	No	No	3.5
4	LGM 3.5, revised SFR	Yes	No	No	3.5
5	Diffuse recharge and focused SFR runoff multipliers allowed to vary from 1 to 100	No	No	Yes	SFR_RUNOFF = 1 RCH_SAC_MU = 1 RCH_COR_MU = 1 RCH_DIA_MU = 1 RCH_BRO_MU = 1 RCH_GUA_MU = 34.7 RCH_SIE_MU = 1
6	Diffuse recharge and focused SFR runoff multipliers allowed to vary from 1 to 100, revised SFR	Yes	No	Yes	SFR_RUNOFF = 26.8 RCH_SAC_MU = 1 RCH_COR_MU = 1 RCH_DIA_MU = 1 RCH_BRO_MU = 1 RCH_GUA_MU = 1 RCH_SIE_MU = 1
7	Diffuse recharge and focused SFR runoff multipliers allowed to vary from 0.1 to 100	No	No	Yes	SFR_RUNOFF = 19.8 RCH_SAC_MU = 0.1 RCH_COR_MU = 0.1 RCH_DIA_MU = 0.122 RCH_BRO_MU = 0.1 RCH_GUA_MU = 0.1 RCH_SIE_MU = 0.652
8	Diffuse recharge and focused SFR runoff multipliers allowed to vary from 0.1 to 100, revised SFR	Yes	No	Yes	SFR_RUNOFF = 29.2 RCH_SAC_MU = 0.703 RCH_COR_MU = 0.795 RCH_DIA_MU = 0.653 RCH_BRO_MU = 0.256 RCH_GUA_MU = 0.404 RCH_SIE_MU = 0.629
9	Calibrate HK/VA, diffuse recharge and focused SFR runoff multipliers allowed to vary from 0.1 to 100, revised SFR	Yes	Yes	Yes	SFR_RUNOFF = 15.6 RCH_SAC_MU = 0.807 RCH_COR_MU = 0.853 RCH_DIA_MU = 0.119 RCH_BRO_MU = 32.2 RCH_GUA_MU = 33.5 RCH_SIE_MU = 13
10	Calibrate HK/VA, diffuse recharge and focused SFR runoff multipliers allowed to vary from 0.1 to 10, revised SFR	Yes	Yes	Yes	SFR_RUNOFF = 10 RCH_SAC_MU = 0.95 RCH_COR_MU = 1.31 RCH_DIA_MU = 0.119 RCH_BRO_MU = 10 RCH_GUA_MU = 10 RCH_SIE_MU = 10
11	Calibrate HK/VA, diffuse recharge and focused SFR runoff multipliers allowed to vary from 0.1 to 3.5, revised SFR	Yes	Yes	Yes	SFR_RUNOFF = 3.5 RCH_SAC_MU = 0.414 RCH_COR_MU = 1.32 RCH_DIA_MU = 0.119 RCH_BRO_MU = 2.74 RCH_GUA_MU = 2.93 RCH_SIE_MU = 3.5

Table 5-12. Simulated lake levels, errors in simulated versus observed lake levels, and sum of flooding errors for Layer 1. Target lake elevations are 1,347 m and 1,114 m for Lake Sacramento and Lake King, respectively.

Run	Computed Lake Sacramento elevation (m)	Computed Lake King elevation (m)	Error Lake Sacramento (m)	Error Lake King (m)	Sum computed water table minus land surface elevation (m)
1	Dry	1102.5	-40	-11.5	667
2	1308.9	1105	-38.1	-9	640
3	1313.8	1104.9	-33.2	-9.1	168,000
4	1315.5	1104.2	-31.5	-9.8	216,000
5	Dry	1104.2	-40	-9.8	695
6	1323.4	1107	-23.6	-7	942
7	1316.7	1114.3	-30.3	0.3	766
8	1324	1114.3	-23	0.3	816
9	1317.7	1113.3	-29.3	-0.7	511
10	1314.8	1106.3	-32.2	-7.7	13
11	1310.2	1103.9	-36.8	-10.1	0

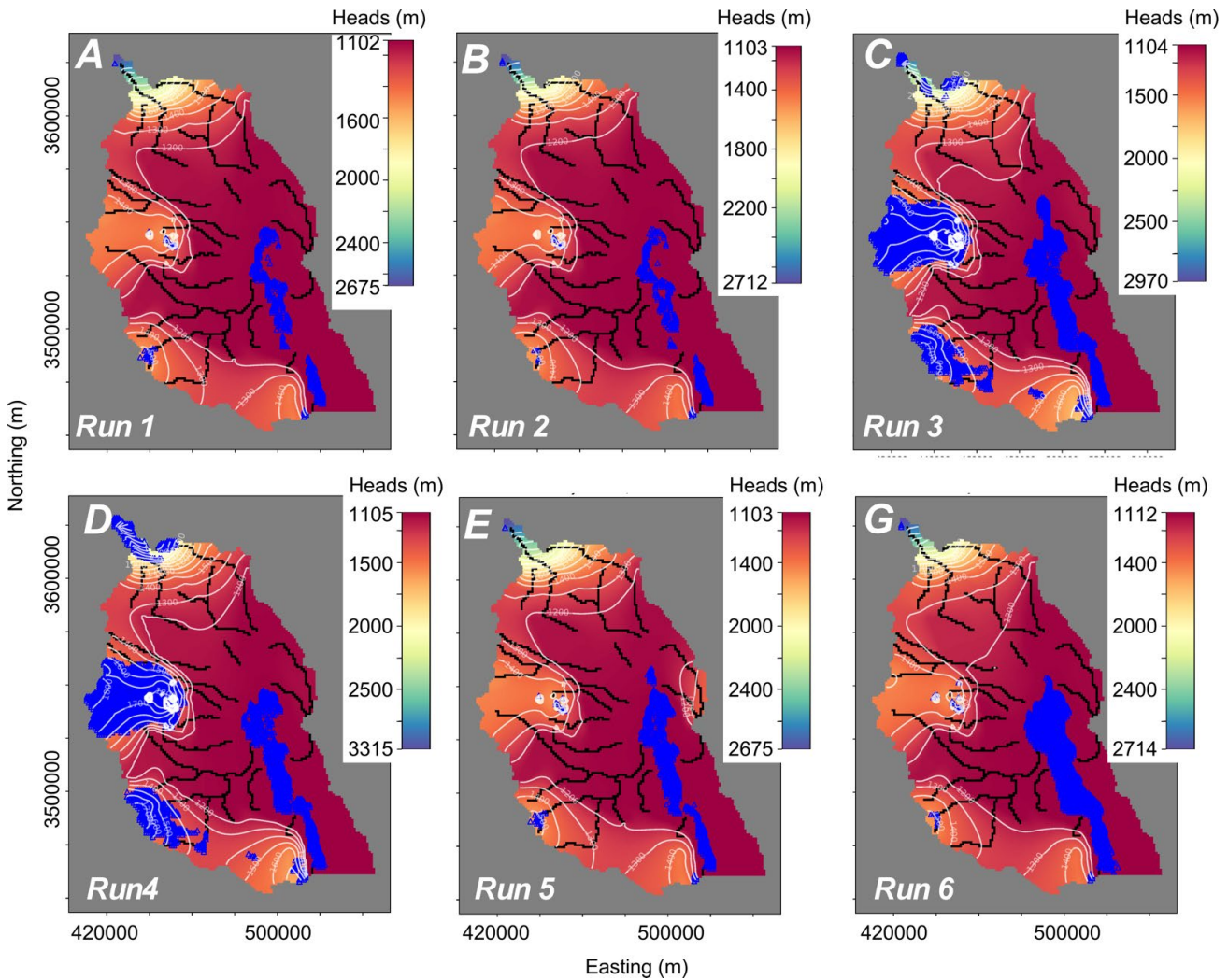


Figure 5-22. Simulated heads (red to blue shaded patterns) and flooded cells in Layer 1 (blue triangles) for last glacial maximum simulation Runs 1 through 6 (subplots A through G). 100-ft head contours are shown in white; the shallowest contour on each model run is the 1200-ft contour.

Table 5-13. Summary of hydraulic conductivity (m/day) and vertical anisotropy (unitless) range for Layers 1–6, model Runs 1 and 9–11.

Layer Number	Min HK	Max HK	Min VA	Max VA	Min HK	Max HK	Min VA	Max VA
	Run 1				Run 9			
1	0.00031	41	8.7	2,100	0.0046	210	1	10,000
2	0.000003	13	8.4	1,700	0.000004	3	1	9,400
3	0.000003	17	7.8	1,900	0.000003	87	1	3,500
4	0.0001	13	8.2	360	0.000089	15	7.6	1,700
5	0.0001	2.2	0.36	1,000	0.000093	1.2	1	880
6	0.00031		0.36		0.000045		1	
	Run 10				Run 11			
1	0.0029	87	1	1,800	0.0026	130	1	10,000
2	0.000004	1.9	1	10,000	0.000004	1.1	1.1	10,000
3	0.000003	75	1	3,600	0.000003	78	1	10,000
4	0.000079	15	7.7	1,600	0.000093	15	7.6	1,800
5	0.000093	1.1	1.1	880	0.000093	1.2	1.1	880
6	0.00023		1		0.00073		1	

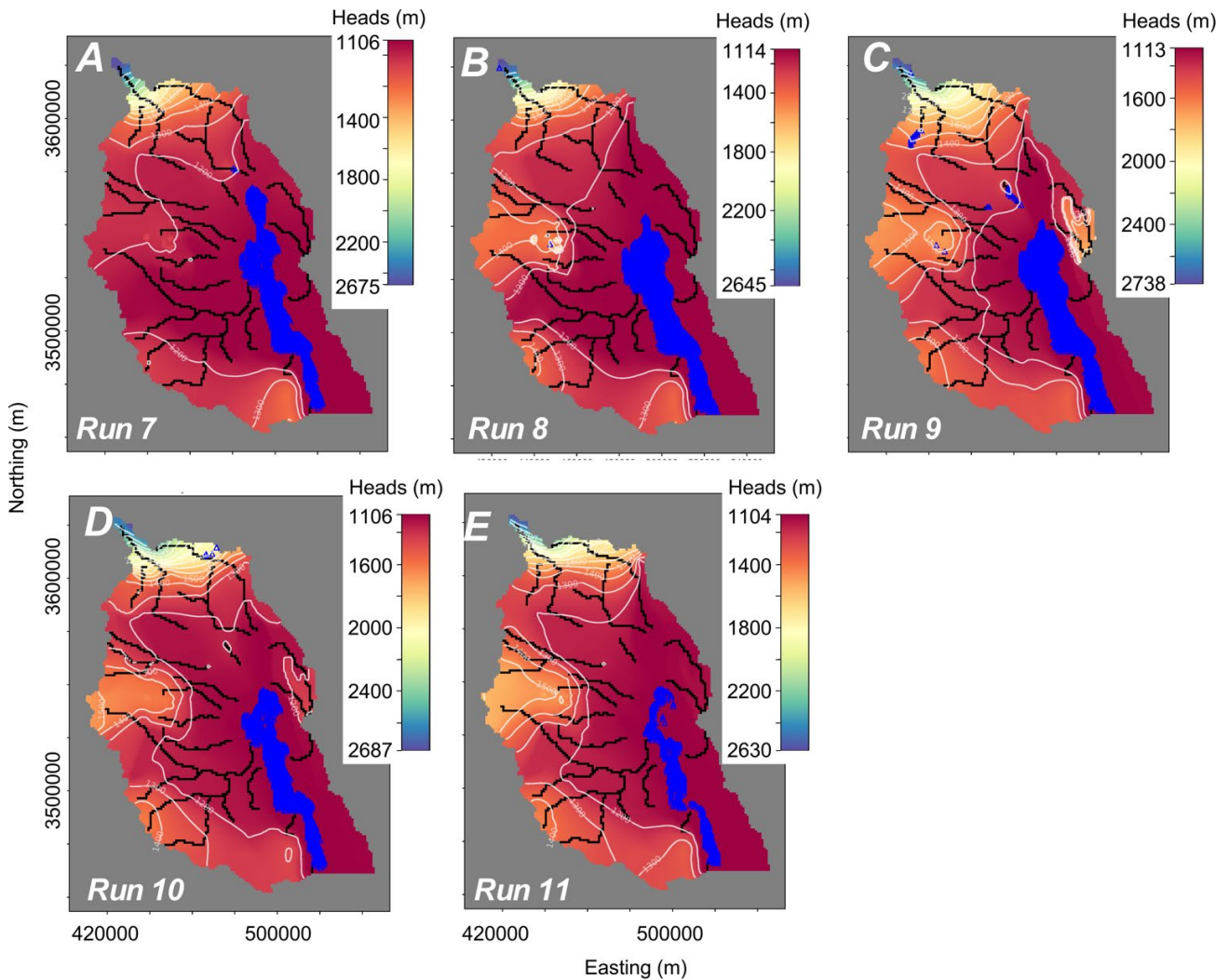


Figure 5-23. Simulated heads (red to blue shaded patterns) and flooded cells in Layer 1 (blue triangles) for last glacial maximum simulation Runs 7 through 11. 100-ft head contours are shown in white; the shallowest contour on each model run is the 1200-ft contour.

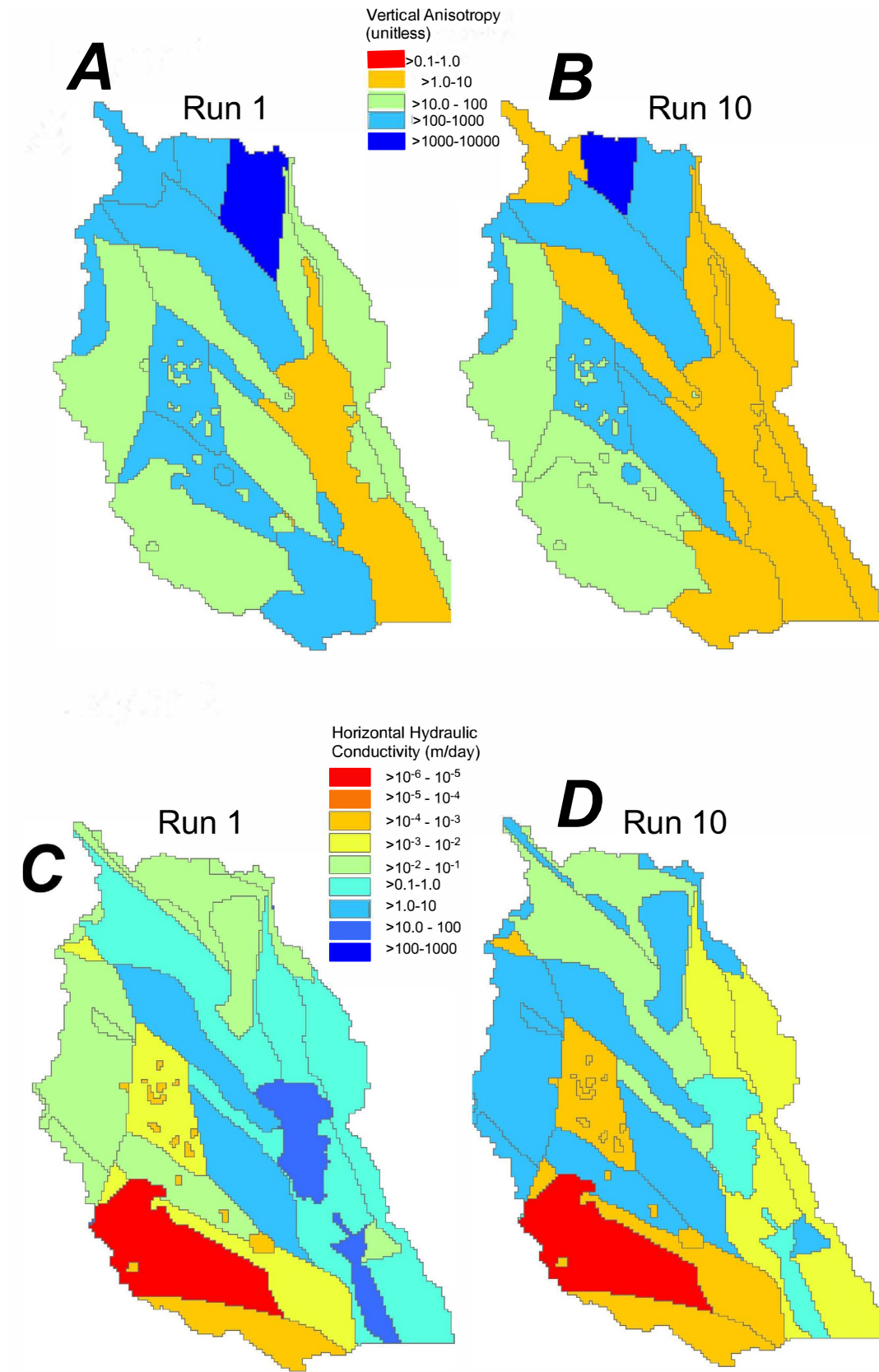


Figure 5-24. Graphic comparison of vertical anisotropy (A and B) and horizontal hydraulic conductivity (C and D) values in Layer 1 for Runs 1 and 10.

instances of water-saturated soils. For PEST Runs 9-11, diffuse recharge may have been higher to the south than it is today. In some simulations such as Run 8, the 1,200-m contour migrated down toward the playas, indicating enhanced filling of the upper aquifer (Figure 5-23). This seems reasonable given that the present-day water levels within the Salt Basin are quite deep (i.e., underfit; Sigstedt et al., 2016). Sigstedt et al. (2016) also noted that stable isotopic composition of Pleistocene-age groundwater within the Salt Basin likely experienced lower evapotranspiration rates. Our LGM recharge calculations in the uplands indicates that evapotranspiration rates decreased from about 510 to 280 mm/mo between modern and LGM times.

There is uncertainty in the LGM steady-state model runs. The values of hydraulic conductivity and recharge are non-unique. LGM surface elevations in the lake regions were likely lower during the LGM. This is due to the effects of sediment avulsion into the lakes over the past 20,000 years. A lower lake bed would have required more runoff to fill the lakes.

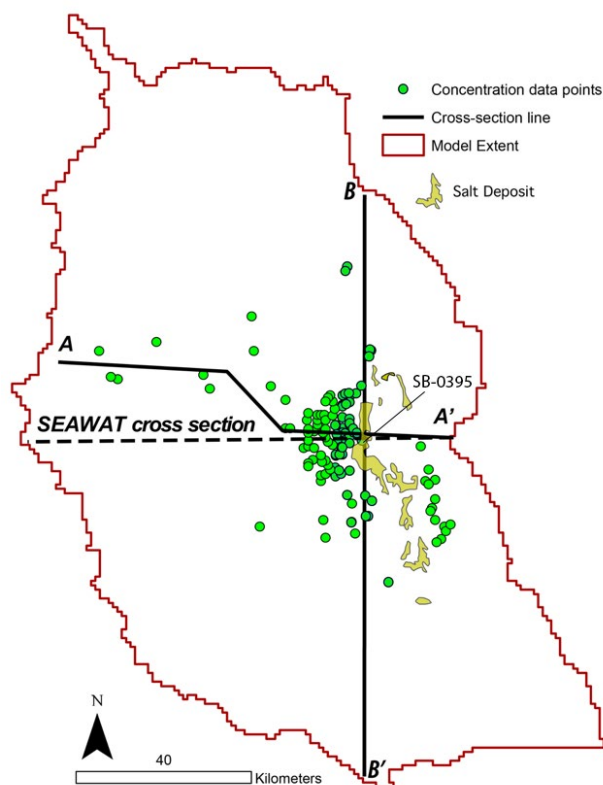


Figure 5-25. Base map showing the location of north-south ($B-B'$) and west-east ($A-A'$) salinity profiles (solid black lines), halite salt deposits (yellow pattern), and well locations (green dots) having salinity data (after DBS&A, 2010b).

EFFECTS OF FLUID DENSITY VARIATIONS ON GROUNDWATER FLOW AND SALINE WATER MIGRATION

Mark Person

Introduction

In this study so far, we have focused on groundwater flow within the Salt Basin assuming that constant fluid-density conditions prevail. The presence of halite deposits reported in playa sediment cores (the yellow pattern in Figure 5-25; DBS&A, 2010b) suggests that hypersaline conditions (TDS concentration >200 g/L) occurs within some portion of the lowland groundwater flow system. In addition, the Yeso Formation contains anhydrite, which could result in elevated groundwater salinities of up to 10 g/L.

Within an arid, hydrologically closed basin, saline fluids sink due to density effects (Duffy and Al-Hassan, 1988; Fan et al., 1997; Davis et al., 1986; Fig. 5-26). Saline groundwater acts as a barrier to overlying freshwater groundwater flow. Figure 5-26 illustrates this by comparing hydraulic head and flow patterns associated with a freshwater system (density = $1,000$ kg/m³; Figure 5-26d-e) with one where dense brines ($1,200$ kg/m³) are present (Figure 5-26c-e). For the freshwater system, groundwater discharges along the right top edge of the model domain, consistent with a hydrologically open basin. However, when brine density conditions are imposed along the right edge of the system, discharge is shifted to the left. Where normalized concentrations exceed 0.1, a hydrodynamic barrier forms, forcing fresh water upwards towards the land surface. We hypothesize that variable-density conditions occur within the lowlands of the Salt Basin, forcing discharge westward and northward of the playas.

Much of the well salinity data within the Salt Basin is centered in the lowlands near Dell City, Texas (green dots in Figure 5-25), at shallow depth (<400 m). Beneath Dell City, brackish conditions prevail (1 to 4 g/L). Salinity data were interpolated onto north-south ($B-B'$; Figure 5-27) and west-east ($A-A'$; Figure 5-27) cross sections. Outside of the Dell City area, groundwater salinity at shallow units is brackish (1 to 7 g/L; Figure 5-27). However, one well near the playas has a salinity that is about 4 times that of seawater (139 g/L; Figure 5-27).

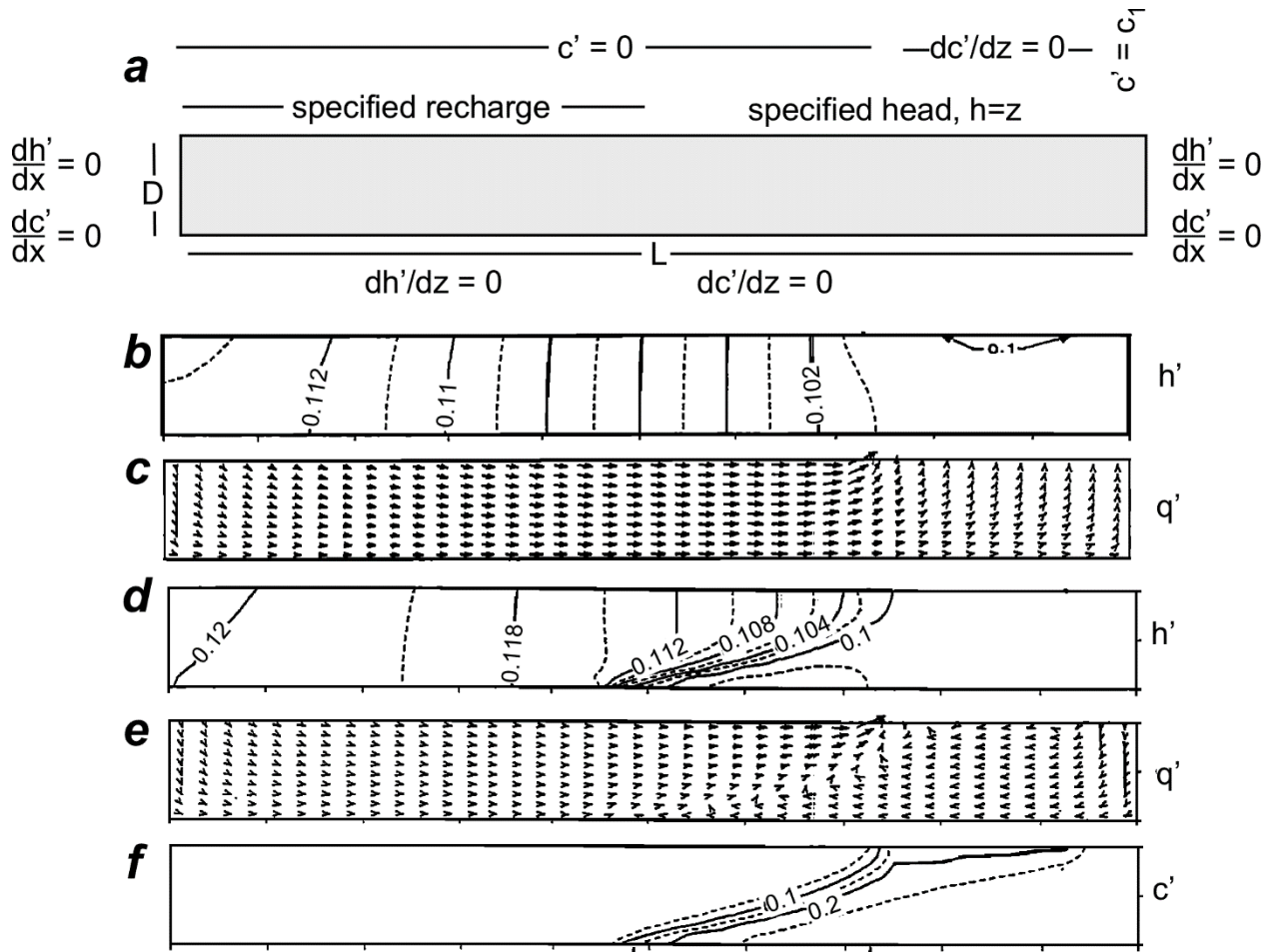


Figure 5-26. Idealized simulation of variable-density groundwater flow in an arid, hydrologically closed basin (from Duffy and Al-Hassan, 1988). (a) Boundary conditions imposed on an idealized closed-basin model domain having a width of L and height of D . There is a modest slope to the right imposed along the top surface. The variables h' , q' , and c' denote normalized heads, fluxes, and concentrations, respectively. Where $c' = 1$, fluid density is 1200 kg/m^3 , consistent with brine conditions. (b) Computed normalized heads for a freshwater system (i.e., no variable-density effects). (c) Computed normalized velocity vectors for freshwater flow system. The length of the vector shaft is proportional to the magnitude of the velocity. (d) Computed normalized heads for a variable-density system. (e) Computed normalized velocity vectors for a variable-density system. (f) Computed normalized concentrations and associated freshwater/saline-water interface.

DBS&A (2010b) report both halite and anhydrite deposits within the playas, suggesting a salinity range for the playas between about 10 and 230 g/L. Variable-density effects are important under these salinity conditions.

Results from the transient MODFLOW model that included agricultural pumping discussed above (Figure 5-14) revealed a trend of increasing drawdown in the Dell City area. Over time, the computed water table minimum shifted from the playas westward to the cone of depression near Dell City (blue lines, Figure 5-8). This suggests that saline groundwater from the playas may be migrating toward Dell City.

In this section, we investigate predevelopment salinity conditions as well as the formation of a regional cone of depression on the migration of

saline water from the Salt Flats region toward Dell City, Texas. Predevelopment hydrologic conditions refer to the groundwater flow system prior to irrigation-related pumping that began during the late 1940s around Dell City. We developed an east-west cross-sectional model (Fig. 5-28) using SEAWAT. SEAWAT is a companion code to MODFLOW used to study coastal hydrogeologic problems (Langevin et al., 2003) and capable of simulating variable-density groundwater flow. We relied on cross-sectional models because of the high discretization requirements needed to accurately simulate variable-density groundwater flow and solute transport. We increased vertical discretization from 6 to 23 layers.

We also explored predevelopment conditions along a NW–SE transect from the Sacramento Mountains down to the playa (A–A', Figure 5-29). Also shown in Figure 5-29 are the corrected

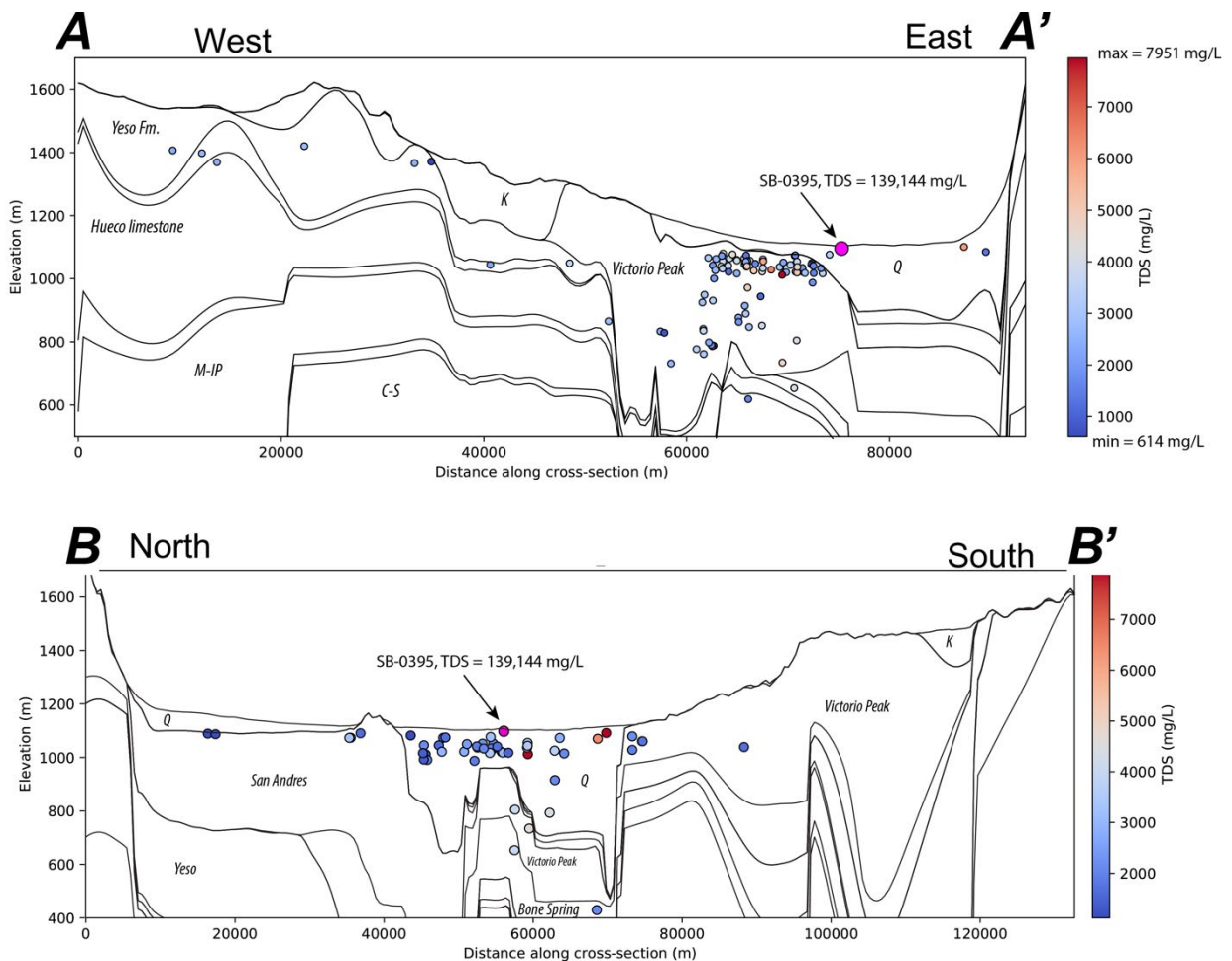


Figure 5-27. Salinity of Salt Basin wells along cross sections A–A' and B–B'. See Figure 5-25 for the location of the Salt Basin profiles.

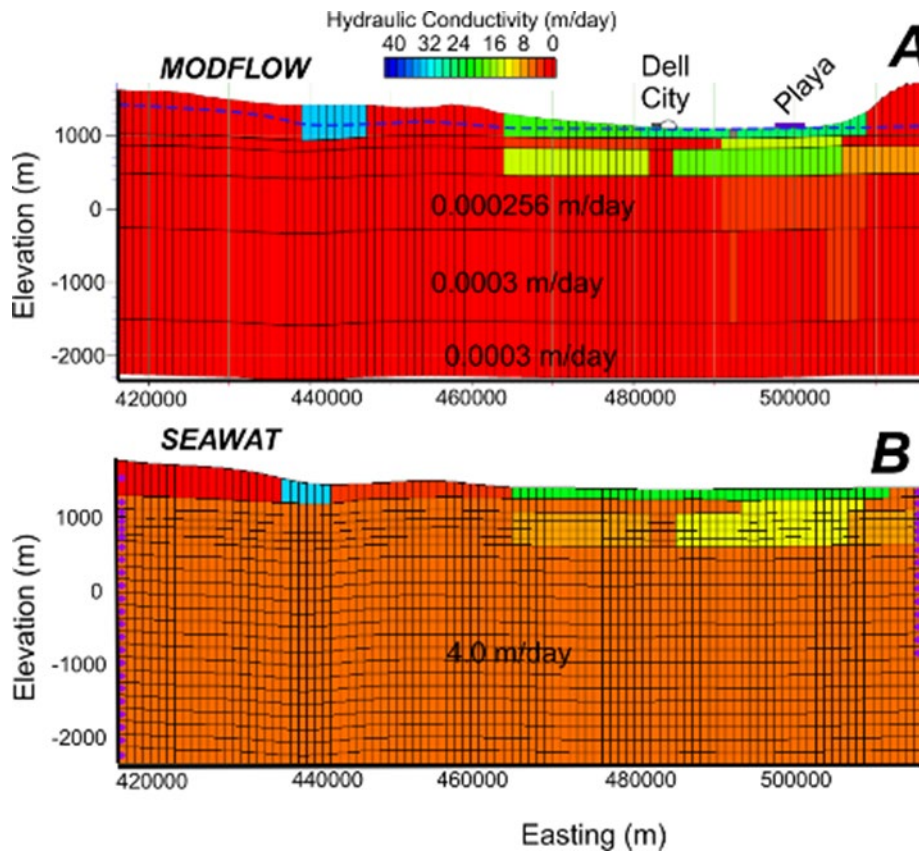


Figure 5-28. Hydraulic conductivity distribution used in east-west 6-layer MODFLOW (A) and 23-layer SEAWAT (B) model grids.

carbon-14 ages from Sigstedt et al. (2016), which indicate an increase in groundwater age from the Sacramento Mountains down to the Salt Flats, with a maximum age of about 19,000 years. The hydrostratigraphic units used along this cross section are presented in Figure 5-30. For the NW–SE model, we used the variable-density groundwater flow, heat, and solute transport model FEMOC (Person et al., 2007). This code also computes advective-dispersive groundwater residence times (Goode, 1996). The code uses the equations of state of Batzle and Wang (1992), which relate fluid density and viscosity to fluid pressure, temperature, and salinity.

Using these cross-sectional models of variable-density groundwater flow and solute transport, we addressed the following questions: (1) What is the likely predevelopment salinity distribution within the Salt Basin? (2) Will the present-day cone of depression centered on Dell City, Texas, result in saline water migrating into irrigation wells? (3) How

long could it take for saline water to migrate from the Salt Flats to Dell City?

SEAWAT cross-sectional model setup

We initially used the hydraulic conductivity values largely consistent with Layers 1–6 from the MODFLOW steady-state model runs presented in Table 5-14 (MODFLOW predevelopment model parameters). However, we found that using the predevelopment hydrogeologic parameters resulted in high-salinity conditions beneath Dell City (10 to 20 g/L). As shown in Figures 5-29 and 3-1, salinity conditions underlying Dell City range between about 1 and 4 g/L. For the purposes of this investigation, we decided to elevate the hydraulic conductivity of hydrostratigraphic Layers 3–6 from about 0.0003 to 4.0 m/day in these SEAWAT model runs (Table 5-14, Adjusted model parameters). This reduced the permeability difference between the shallow and deeper hydrostratigraphic layers and resulted in

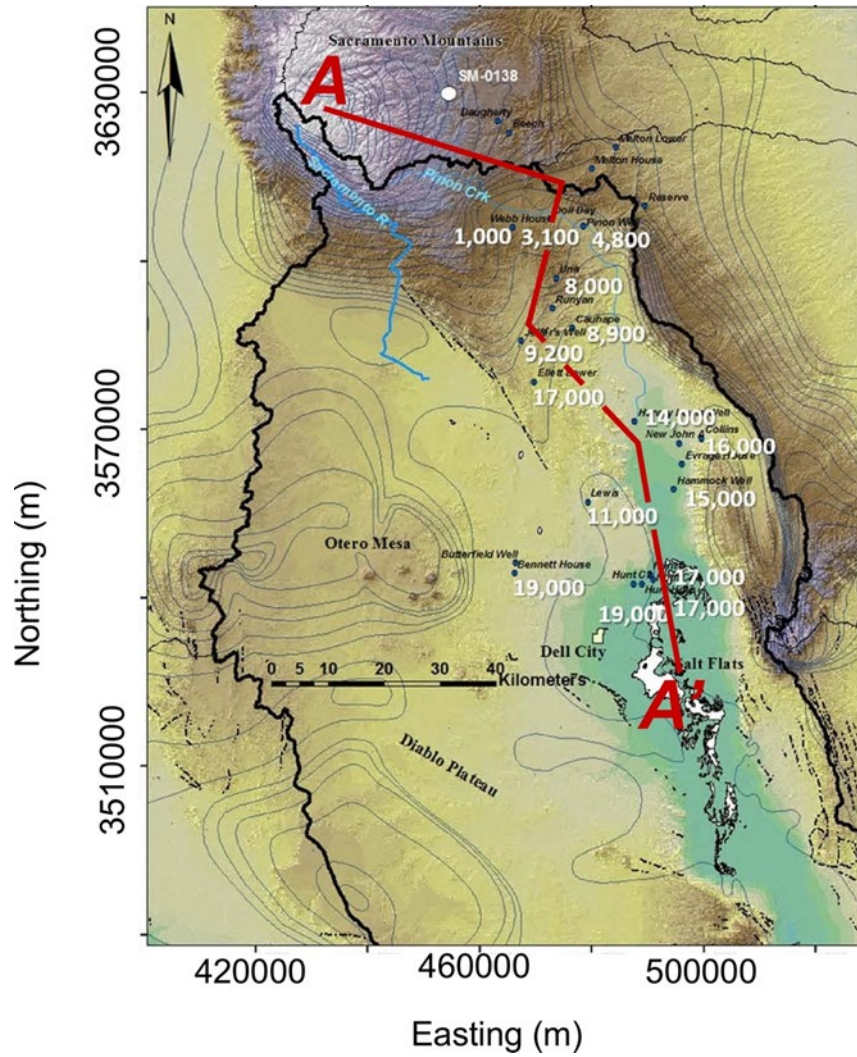


Figure 5-29. Location of NW–SE hydrostratigraphic cross section and corrected carbon-14 age dates (from Sigstedt et al., 2016).

Table 5-14. Comparison of hydraulic conductivity ranges between MODFLOW and SEAWAT model runs.

Layer Number	MODFLOW predevelopment model parameters		Adjusted model parameters	
	Min HK	Max HK	Min HK	Max HK
1	0.21	25	0.0046	210
2	0.0011	12.8	0.000004	3
3	0.0095	17.3	0.000003	87
4	0.000256	0.000256	4	4
5	0.0003	0.0001	4	4
6	0.0003	0.0003	4	4

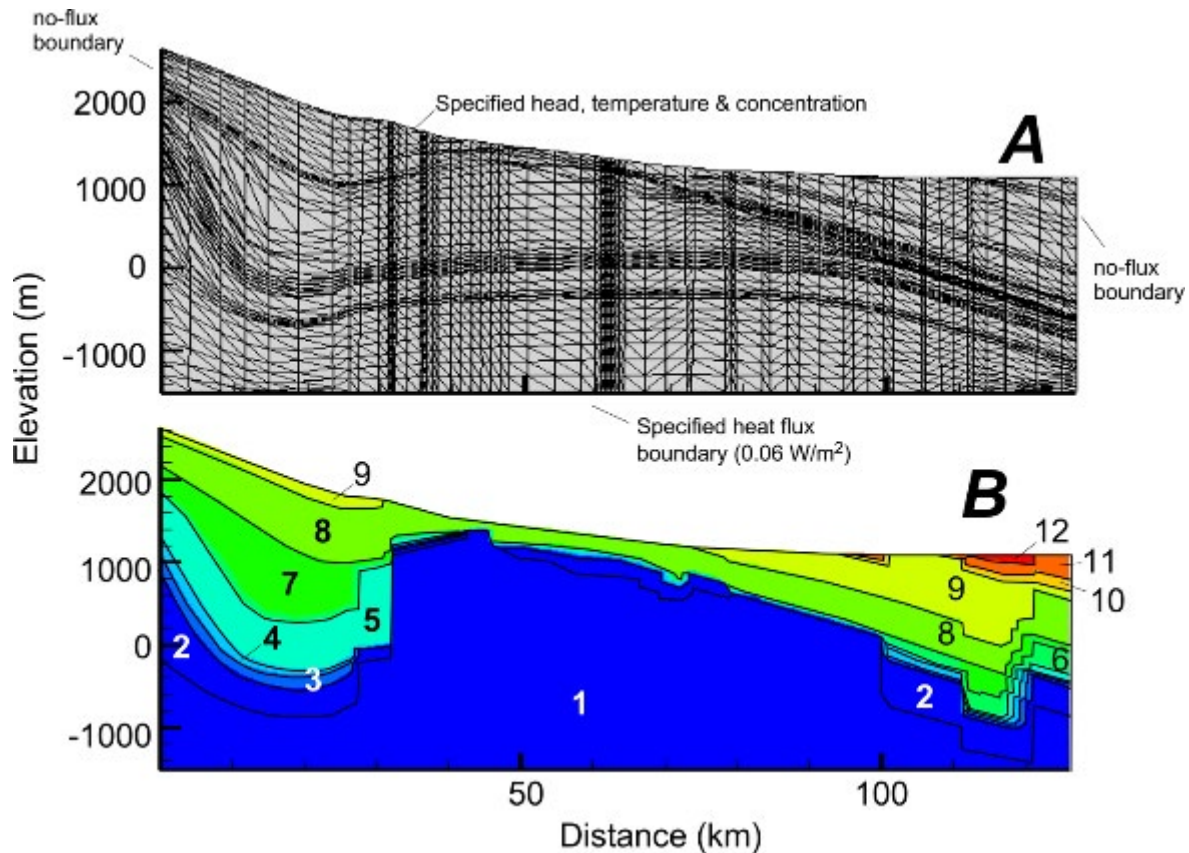


Figure 5-30. (A) FEMOC finite element mesh and (B) hydrostratigraphic units used in FEMOC model.

what we consider to be more realistic salinity patterns beneath Dell City prior to pumping. We used a uniform vertical anisotropy of 100 (K_x/K_z). For this idealized simulation, we applied a porosity and longitudinal dispersivity of 0.15 and 100 m, respectively. Transverse dispersivity was assumed to be 10% of longitudinal dispersivity.

We built the east–west cross-sectional SEAWAT model using 98 cells in the easting direction and 23 cells in the vertical direction (Figure 5-28). This relatively high number of layers is necessary to accurately represent variable-density groundwater flow (Post and Kooi, 2003). The position of this cross section was at a projected UTM northing of 3534497 m. The total width of the model was about 93.5 km, and the lateral discretization was 954.5 m. The vertical discretization varied between about 70 m near the bottom of the grid and 390 m in the uppermost layer. The top of Layer 1 was the simulated water table elevation taken from the 3-D model run (dashed line in Figure 5-25).

We imposed a combination of specified recharge, constant head, and drain boundary conditions in order to approximate the water table geometry from the MODFLOW model (Figure 5-31). In the region where salt deposits are found, we explored imposing a specified concentration of 35 g/L within the top 6 layers. While it would have been desirable to set the playa concentrations equal to a brine (~200 g/L), SEAWAT did not converge when we used this boundary condition. On the edges of the model domain, we imposed constant head and constant concentration (0 g/L) boundary conditions to the bottom of the model domain on the western (left) edge and down 16 model grid layers on the east (right) side of the model domain (purple lines, Figure 5-31).

We ran the SEAWAT for 100,000 years using a time step size of 100 years with no pumping. As an initial condition, we set all cells in the model to 35 g/L. During the simulation, fresh water infiltrated into the model, displacing salt water and forming freshwater/salt-water mixing at depth. This allowed

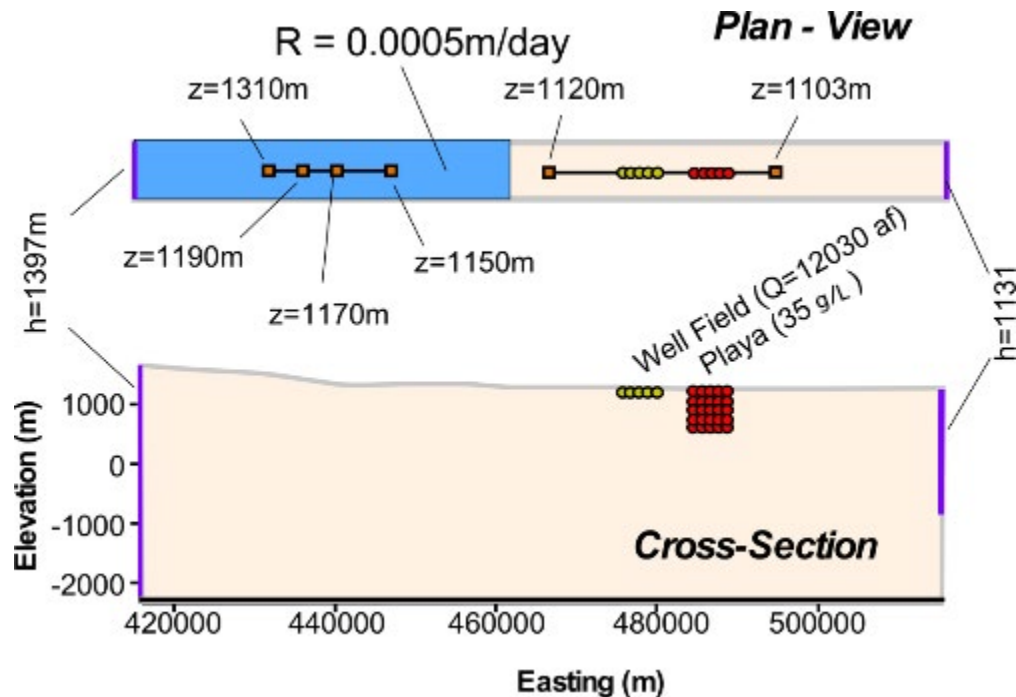


Figure 5-31. Plan-view and cross-sectional schematic diagrams showing boundary conditions imposed along the land surface. The red squares denote the elevation of surface drains that pin the water table. Specified heads are denoted by the purple lines. Pumping wells are indicated with gold circles. Yellow squares represent input head values, with z equal to input head in meters.

us to create predevelopment concentration initial conditions prior to pumping. We used four cells in Layer 1, imposing a net pumping rate of 12,030 acre-ft per year near Dell City (Figure 5-31). The pumping simulations were run for 200 years. We used a time step size of 2 years for these model runs. This amount of pumping represents about 16% of the average historical pumping rate ($\sim 80,000$ acre-ft/year).

FEMOC NW–SE cross-sectional model setup

We developed a finite element mesh along a northwest–southeast cross-sectional transect across the Salt Basin (Figure 5-30) using the basin-scale transport code FEMOC (Person, et al., 2007). The mesh consisted of 2,362 nodes and 4,513 elements (Figure 5-30a). The lateral triangular element dimensions varied between about 500 to 2000 m in the x direction and 15 to 200 m in the z direction. The orientation and stratigraphy for this cross section was taken from Sigstedt et al. (2016). The model is about 126 km long and is more or less perpendicular

to the water table contours. The total thickness of the model domain was over 3 km. We used a total of 12 hydrostratigraphic units (Figure 5-30b) in this model. The hydraulic conductivity assigned to these units (Table 5-15) are similar to those used in the SEAWAT cross-sectional model (Figure 5-28). The hydraulic conductivity value of 4 m/day, which corresponds to a rock permeability of $10^{-11.3}\text{ m}^2$, assigned to the lower layers is on the high side of the fractured rocks properties presented in Ingebritsen and Manning (2010). On the other hand, it is lower than the crystalline basement permeability measure in the town of Truth or Consequences ($10^{-9.3}\text{ m}^2$) along the Rio Grande rift (Person et al., 2019). Thermal and transport parameters not varied in the FEMOC simulations are presented Table 5-16. The porosity used in the FEMOC model (0.2) is slightly higher than what was used in the MODFLOW models (0.15) for particle-tracking purposes.

We assigned the playa concentration at 200 g/L. For the top boundary, we set hydraulic heads to equal the land surface elevation along the top surface.

Table 5-15. Hydraulic conductivity used in the FEMOC model.

Unit	Name	K _x (m/day)
1	Basement	4
2	Silurian	4
3	Devonian	4
4	Mississippian	4
5	Pennsylvanian	4
6	Pow Wow	4
7	Abo	0.26
8	Yeso	0.026
9	San Andres	3.1
10	Goat Seep	432
11	Alluvium	432
12	Lacustrine	0.0026

Table 5-16. Transport parameters held constant in the FEMOC model runs.

Parameter	Value
Sediment thermal conductivity	2.5 W/m-°C
Fluid thermal conductivity	0.58 W/m-°C
Porosity	0.2
Fluid heat capacity	4180 J/kg-°C
Solid heat capacity	1000 J/kg-°C
Longitudinal dispersivity	100 m
Transverse dispersivity	10 m

For groundwater flow, solute transport, and groundwater residence times, the side and base of the model domain were set as no-flux boundaries. Away from the playas, the concentration at the water table was set at 0 g/L. We assigned a land surface temperature of 10°C. We imposed a basal heat flux of 0.06 W/m². We set concentrations within the Yeso Formation at 10 g/L. The code was run for 1 million years using a time step size of 100 years.

SEAWAT model results

We ran a predevelopment cross-sectional model assuming constant-density (Figure 5-32a, d) and variable-density conditions using the original hydrogeologic parameters from the steady-state calibrated model (Figure 5-32b, e) and using higher permeability conditions within the lower four layers (Figure 5-32c, f). Simulated heads for the constant-density simulation were highest in the upland region to the west and lowest near the Salt Flats

(Figure 5-32a). Under constant-density conditions, the initial high-salinity conditions (35 g/L) were swept out of the model domain (Figure 5-32d). Only a small region to the east of the specified concentration cells exceeded background salinity. Some remnant saline water is found in the lower right corner of the model domain of Figure 5-32d. This is because the low groundwater velocity conditions in the corners of the model resulted in a diffusion-dominated system. The saline water in the lower left corner would eventually disappear if the simulation were run longer by solute diffusion. Using the predevelopment calibrated hydraulic conductivity parameters from the MODFLOW model (Figure 5-32e), a tongue of saline water mounded at the base of Layer 3 and migrated laterally beneath Dell City (Figure 5-32e). This is not consistent with modern salinity data in the Dell City area. For the SEAWAT run using elevated hydraulic conductivity in the lower layers, saline fluids extended downward but did not migrate laterally toward Dell City (Fig.5-32f). Freshwater/saline-water mixing zones developed on either side of the Salt Flats (Figure 5-32e, f).

How do simulated predevelopment concentrations in Figure 5-32e and 5-32f compare to observed concentrations in and around Dell City? Figure 5-33 presents temporal trends in well salinity data (mg/L) to the east and west of Dell City. All of the wells presented were located within 10 km of Dell City. The data used in Figure 5-33 are listed in Table 5-17. Wells in and around Dell City had salinity levels that ranged between 0.1 and 4.5 g/L. Observed well salinity data are inconsistent with predicted salinity conditions from the SEAWAT model run that used predevelopment hydraulic conductivity data (Figure 5-32e). The results are more consistent with the SEAWAT model run using a relative permeability of Paleozoic and Proterozoic units (Figure 5-32f). That is, salinity conditions under Dell City are fresh.

The mean, maximum, and minimum salinity levels to the east and west of Dell City are presented in Table 5-18. Again, salinity levels varied between about 0.1 and 4 g/L, which is not consistent with the SEAWAT model runs that used predevelopment permeability data.

Next, we imposed pumping at the wells near Dell City as a means of assessing whether or not saline groundwater would flow into the Dell City region due to historical irrigation practices. Four cells

about 4 km to the west of the playa deposits were assigned as pumping nodes extracting groundwater. The SEAWAT model output is presented for 50-, 100-, and 200-year time slices. Using the hydraulic conductivity field from the predevelopment model (Figure 5-34d–f), saline water migrated laterally into the irrigation region at 50 to 200 years (Figure 5-34d–f). On the western edge of the wells, fresh water was drawn into the water table aquifer (Figure 5-34f). For the model run using relatively high hydraulic conductivity values for the lower four layers, brackish water migrated into the irrigation region at 50 and 200 years. After 200 years, brackish water with a concentration of 14 g/L began to encroach on the well field (Figure 5-34c). The western side of the wells remained fresh.

How do computed temporal trends in solute concentrations around Dell City compare to observed water quality conditions? Figures 5-33b and c present temporal trends in salinity to the east and

west of Dell City. The trends are consistent with the hypothesis that the Dell City cone of depression could pull saline water toward the irrigation region to the east of Dell City, while to the west relatively fresh groundwater is drawn eastward.

FEMOC model results

Figure 5-35 presents FEMOC model output including computed freshwater heads (Figure 5-35a), concentrations (Figure 5-35b), groundwater residence times (Figure 5-35c), temperatures (Figure 5-35d), and stream functions (Figure 5-35e). Elevated water-table-topography-driven flow within the Sacramento Mountains to the northwest drives groundwater flow toward the Salt Flats on the lowland portion of the flow system to the southeast (Figure 5-35e). Variable-density effects clearly influence regional flow patterns within the lowland, forcing an upflow zone in front of the playas. Vertical flow rates beneath the Sacramento Mountains varied between 5 and 0.5 m/year, which

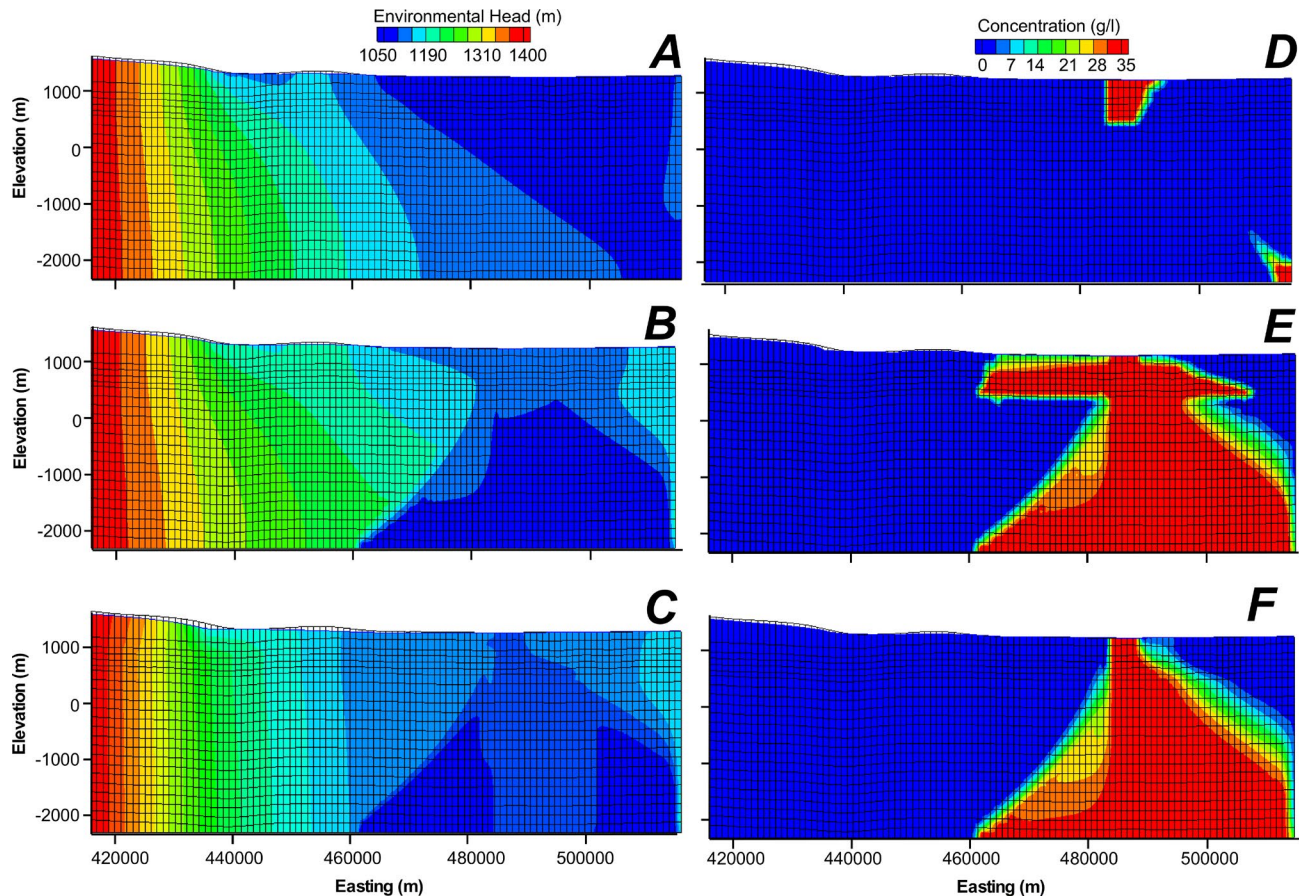


Figure 5-32. Computed heads for (A) constant-density, (B) variable-density using hydrogeologic parameters from calibrated steady-state SEAWAT model, and (C) SEAWAT model using elevated hydraulic conductivity. Computed concentrations for (D) constant-density using hydrogeologic parameters from calibrated steady-state model, (E) SEAWAT model, and (F) SEAWAT model using elevated hydraulic conductivity.

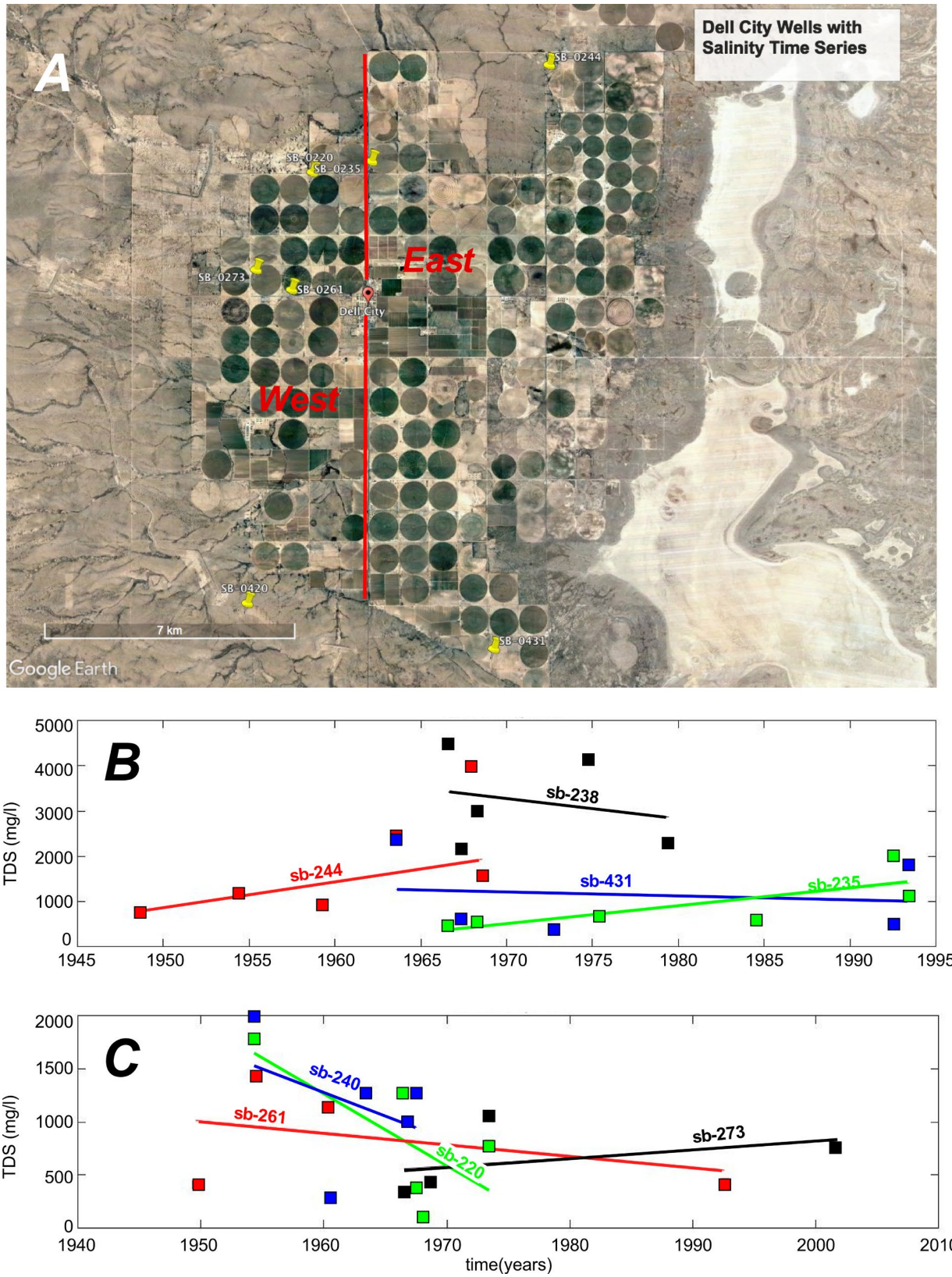


Figure 5-33. (A) Location of pumping wells within 10 km of Dell City. (B) Salinity time series for wells to the east of Dell City. (C) Salinity time series for wells to the west of Dell City.

Table 5-17. Temporal records of salinity for wells within 10 km of Dell City, Texas.

East Well Name	Date	Salinity (mg/L)	West Well Name	Date	Salinity (mg/L)	
SB-0244	8/12/1948	752	SB-0220	6/24/1954	1767	
	5/25/1954	1196		7/27/1966	1257	
	3/31/1959	923		5/16/1967	238	
	7/25/1963	2448		3/18/1968	100	
	8/6/1968	1577		5/22/1973	790	
SB-0238	8/1/1966	4501	SB-0420	6/8/1954	2005	
	5/16/1967	2163		7/2/1960	280	
	4/9/1968	2988		7/26/1963	1277	
	10/7/1974	4127		8/1/1966	1002	
	6/5/1979	2307		7/24/1967	1276	
SB-0431	7/25/1963	2367	SB-0261	8/9/1949	408	
	4/26/1967	645		5/20/1954	1433	
	9/28/1972	384		7/2/1960	1140	
	7/14/1992	494		7/8/1992	429	
	6/8/1993	1810				
SB-0235	7/27/1966	450	SB-0273	7/27/1966	339	
	4/9/1968	563		8/6/1968	434	
	5/28/1975	670		5/22/1973	1043	
	7/11/1984	594		9/14/2001	750	
	7/8/1992	2021				
	6/8/1993	1133				

Table 5-18. Statistical analysis of well salinity data to the east and west of Dell City. See Figure 5-33 for well locations.

	East	West
mean	1624	887
maximum	4501	2005
minimum	384	99.6

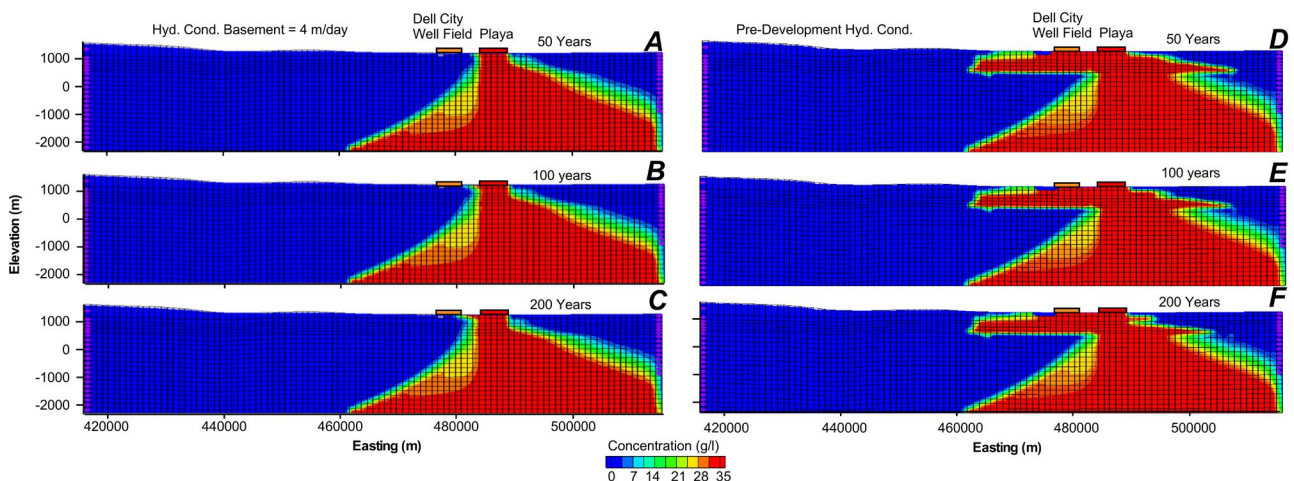


Figure 5-34. SEAWAT computed concentrations after (A) 50 years, (B) 100 years, and (C) 200 years of pumping for relatively high-permeability basement (4 m/day). Computed concentrations using calibrated steady-state hydraulic parameters after (D) 50 years, (E) 100 years, and (F) 200 years of pumping. Purple diamonds along the left and right edges of the model domain denote specified head and concentration boundary conditions.

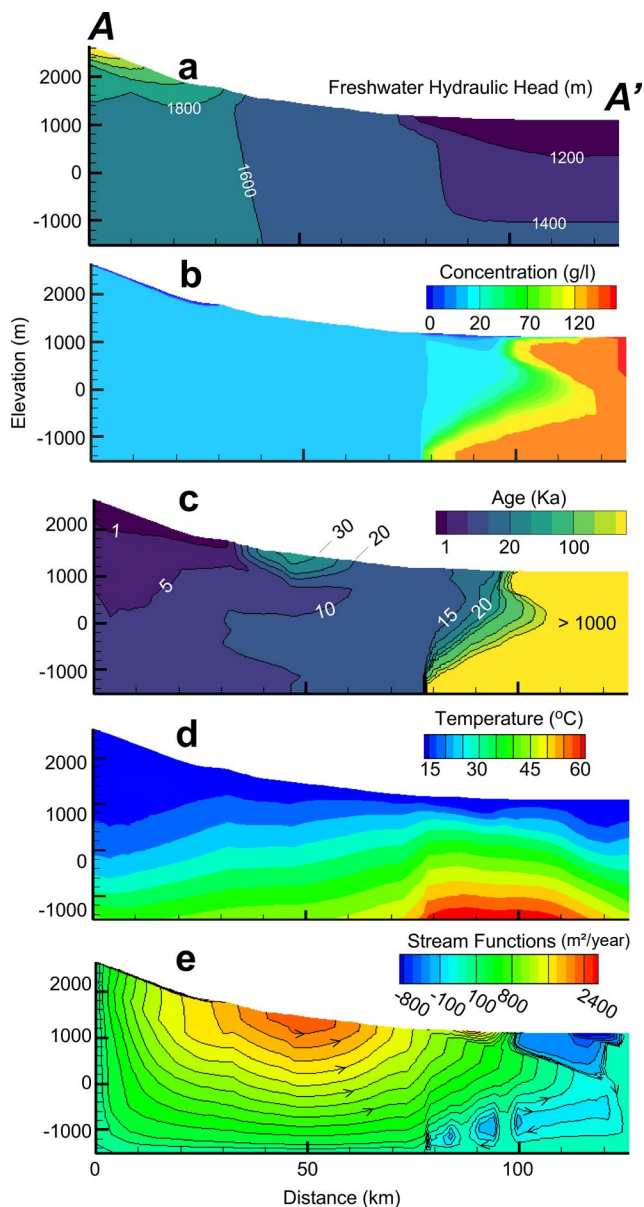


Figure 5-35. FEMOC model output including simulated (a) equivalent freshwater hydraulic heads, (b) salinity, (c) groundwater age, (d) temperatures, and (e) stream functions. Negative values of stream functions denote flow from right to left.

seems unrealistically high given the relatively low recharge rates presented in prior sections. This is the result of the specified head boundary conditions imposed along the top surface of the model domain. A recirculation cell developed in the high salinity region within the playas in the southern portion of the model domain dominated underneath the Salt Flats (Figure 5-35e). As in the SEAWAT model, saline water sinks to the base of the model domain under the Salt Flats due to relatively high bedrock permeability. Computed groundwater residence times (Figure 5-35c) varied in the lowlands between about 10,000 and 20,000 years, consistent with carbon-14 ages reported by Sigstedt et al. (2016; Figure 5-29). There is a region of a shallow local flow system near the foothills of the Sacramento Mountains where groundwater ages reach 30 ka (Figure 5-35c, 30-ka contour at top of contour). Older groundwater occurs within a shallow local flow cell within the Yeso Formation, which was assigned relatively low-permeability conditions. Sigstedt et al. (2016) also observed older carbon-14 groundwater ages in this region (Figure 5-29). Computed concentrations throughout most of the model domain at depth are about 10 g/L due to the effects of the Yeso-Formation-specified salinity condition (0.10 g/L). This resulted in brackish conditions existing across much of the basin. Near the Salt Flats and within the Sacramento Mountains, there is a layer of low-salinity fluids 100 to 200 m thick overlying brackish water.

Discussion

Since there is no pumping test data available to constrain the basement permeability used, the SEAWAT and FEMOC model results should be viewed as conceptual. In addition, the boundary conditions used in this chapter do not match the MODFLOW predevelopment steady-state model. Including pumping wells in a cross-sectional model is incorrect due to the 3-D patterns pumping induces on groundwater flow. Under these 2-D conditions, there is no possibility of radial flow.

As noted, the uniform high permeability (4 m/day) assigned to lower layers is much higher than what was used in the MODFLOW models. While this value of hydraulic conductivity is relatively high, it is not unrealistic. Ingebritsen and Manning (2010) present a global compilation of basement permeability with depth for tectonically active and quiescent regions. A permeability value of about 10^{-10}

m^2 (~ 100 m/day) has been observed at depths of 5 km in tectonically active basins. The Salt Basin is considered to form the eastern edge of the Basin and Range Provinces, with over 100 active Quaternary faults (Goetz, 1980). Further support for relatively high-permeability ($10^{-11.3}$ m^2) fractured Paleozoic and crystalline basement rocks is provided by Kreitler et al. (1987). Finally, as noted above, the value $10^{-11.3}$ m^2 is lower than the crystalline basement permeability measured in the town of Truth or Consequences ($10^{-9.3}$ m^2) along the Rio Grande rift (Person et al., 2019). It would have been useful to vary porosity with depth as well as impose a recharge boundary condition in the uplands of the FEMOC model.

Other limitations of the cross-sectional models presented above include the observation that fine-grained playa/evaporite deposits typically have low permeability (Nicot and Bennett, 1998; Beauheim and Roberts, 2002). A relatively high hydraulic conductivity (>20 m/day) was assigned to the upper layer in the SEAWAT model that contained the playa/evaporite units, allowing saline fluids to migrate downward by advection. There was reasonable agreement between the computed groundwater residence times from the FEMOC model and those presented by Sigstedt et al. (2016). FEMOC models that considered lower permeability in the Paleozoic bedrock resulted in much older computed residence times (not shown).

The transient SEAWAT models suggest that saline water will be drawn from the playa deposits into the eastern portion of the Dell City wells between 100 and 200 years from now (Figure 5-34). This suggests that water quality may become an important issue for safe aquifer yield in the Dell City area.

Conclusions

The cross-sectional SEAWAT and FEMOC models indicated that high-salinity conditions within the Salt Basin have an effect on deep groundwater flow patterns within the fractured Paleozoic bedrock and the crystalline basement, especially near the playas. Regional groundwater flow is forced up toward the land surface above the saline-water/freshwater interface. Comparison of observed and simulated salinity conditions suggest that the Paleozoic and Proterozoic rocks within the Salt Basin are permeable. Using the permeability conditions from the MODFLOW models for the lower four layers

resulted in unrealistic salinity conditions beneath Dell City. Both model results and salinity time series data collected within 10 km of Dell City more or less support the hypothesis that salinity conditions are increasing between the irrigation region and the playas. Future work should consider using salinity data as an additional model calibration tool. Increased salinity within the Dell City irrigation region could have important consequences to consider with estimates of safe aquifer yield within the Salt Basin.

We do not have aquifer test data to confirm or refute the 4-m/day hydraulic conductivity assigned to these units. There is permeability information from global hydraulic tests carried out in deep boreholes that supports the assignment of relatively high crystalline basement permeability conditions (Ingebritsen and Manning, 2010). There was a reasonable fit between observed and simulated salinity conditions from the SEAWAT models along the east-west transect within the lowlands. Temporal trends in salinity conditions from wells generally support the hypothesis that salinity conditions are increasing between the playas and the irrigation region.

A 3-D model calibration exercise that included the effects of variable-density flow and solute transport in 3-D would provide more constraints on the overall Salt Basin model fit. Such an endeavor would probably require at least twice the time and effort of the modeling work presented in this study. Utilization of high-performance, variable-density groundwater flow and solute transport models (e.g., Cohen et al., 2010) would probably be required due to the large number of anticipated nodes.



The sun sets on Otero Mesa. Two of the Cenozoic intrusions in the Cornudas Mountains are on the skyline. *Photo by Shari Kelley*

REFERENCES

- Abatzoglou, J.T., Rupp, D.E., and Mote, P.W., 2014, Seasonal climate variability and change in the Pacific Northwest of the United States: *Journal of Climate*, v. 27, no. 5, p. 2125–2142, <https://doi.org/10.1175/JCLI-D-13-00218.1>.
- Allen, B.D., 2005, Ice age lakes in New Mexico, *in* Lucas, S.G., Morgan, G.S., and Zeigler, K.E., eds., *New Mexico's Ice Ages: New Mexico Museum of Natural History and Science Bulletin* 28, p. 107–114.
- Allen, R.G., and Pruitt, W.O., 1986, Rational use of the FAO Blaney-Criddle formula: *Journal of Irrigation and Drainage Engineering*, v. 112, no. 2, p. 139–155, [https://doi.org/10.1061/\(ASCE\)0733-9437\(1986\)112:2\(139\)](https://doi.org/10.1061/(ASCE)0733-9437(1986)112:2(139)).
- Allen, R.G., Tasumi, M., Morse, A., and Trezza, R., 2005, A Landsat-based energy balance and evapotranspiration model in western U.S. water rights regulation and planning: *Irrigation and Drainage Systems*, v. 19, no. 3-4, p. 251–268, <https://doi.org/10.1007/s10795-005-5187-z>.
- Anderholm, S.K., 1994, Ground-water recharge near Santa Fe, north-central New Mexico: U.S. Geological Survey Water Resources Investigations Report 94-4078, 68 p., <https://doi.org/10.3133/wri944078>.
- Anderson, M.C., Norman, J.M., Mecikalski, J.R., Otkin, J.A., and Kustas, W.P., 2007, A climatological study of evapotranspiration and moisture stress across the continental United States based on thermal remote sensing: 1. Model formulation: *Journal of Geophysical Research: Atmospheres*, v. 112, no. D10, <https://doi.org/10.1029/2006JD007506>.
- Angle, E.S., 2001, Hydrogeology of the Salt Basin, *in* Mace, R.E., Mullican, W.F., III, and Angle, E.S., eds., *Aquifers of West Texas: Texas Water Development Board Report* 356, p. 232–247, https://www.twdb.texas.gov/publications/reports/numbered_reports/doc/R356/Chapter17.pdf.
- Ashworth, J.B., 1995, Ground-water resources of the Bone Spring-Victorio Peak Aquifer in the Dell Valley Area, Texas: *Texas Water Development Board Report* 344, 42 p., https://www.twdb.texas.gov/publications/reports/numbered_reports/doc/R344/R344.pdf.
- Back, W., Hanshaw, B.B., Plummer, L.N., Rahn, P.H., Rightmire, C.T., and Rubin, M., 1983, Process and rate of dedolomitization: Mass transfer and ^{14}C dating in a regional carbonate aquifer, *in* *Geological Society of America Bulletin* 94, no. 12, p. 1415–1429.
- Banta, E.R., 2000, MODFLOW-2000, The U.S. Geological Survey modular ground-water model—documentation of packages for simulating evapotranspiration with a segmented function (ETS1) and drains with return flow (DRT1): U.S. Geological Survey Open-File Report 00-466, 131 p., <https://water.usgs.gov/nrp/gwsoftware/modflow2000/ofr00-466.pdf>.
- Barnes, C.J., Jacobson, G., and Smith, G.D., 1992, The origin of high-nitrate ground waters in the Australian arid zone: *Journal of Hydrology*, v. 137, no. 1–4, pp. 181–197, [https://doi.org/10.1016/0022-1694\(92\)90055-Z](https://doi.org/10.1016/0022-1694(92)90055-Z).
- Barnes, M.A., Anthony, E.Y., Williams, I., Asquith, G.B., 2002, Architecture of a 1.38–1.34 Ga granite-rhyolite complex as revealed by geochronology and isotopic and elemental geochemistry of subsurface samples from west Texas, USA: *Precambrian Research*, v. 119, no. 1–4, p. 9–43, [https://doi.org/10.1016/S0301-9268\(02\)00116-X](https://doi.org/10.1016/S0301-9268(02)00116-X).
- Barnes, V.E., compiler, 1992, *Geologic map of Texas: University of Texas at Austin, Bureau of Economic Geology, State Map SM 3, scale 1:500,000, 4 sheets.*
- Bastiaanssen, W.G., Menenti, M., Feddes, R.A., and Holtslag, A.A.M., 1998, A remote sensing surface energy balance algorithm for land (SEBAL). 1. Formulation: *Journal of Hydrology*, v. 212–213, p. 198–212, [https://doi.org/10.1016/S0022-1694\(98\)00253-4](https://doi.org/10.1016/S0022-1694(98)00253-4).
- Batzle, M., and Wang, Z., 1992, Seismic properties of pore fluids: *Geophysics*, v. 57, no. 11, p. 1396–1408, <https://doi.org/10.1190/1.1443207>.
- Beauheim, R.L., and Roberts, R.M., 2002, Hydrology and hydraulic properties of a bedded evaporite formation: *Journal of Hydrology*, v. 259, no. 1-4, p. 66–88, [https://doi.org/10.1016/S0022-1694\(01\)00586-8](https://doi.org/10.1016/S0022-1694(01)00586-8).

- Bibby, H.M., Caldwell, T.G., and Brown, C., 2005, Determinable and non-determinable parameters of galvanic distortion in magnetotellurics: *Geophysical Journal International*, v. 163, no. 3, p. 915–930, <https://doi.org/10.1111/j.1365-246X.2005.02779.x>.
- Bjorklund, L.J., 1957, Reconnaissance of ground-water conditions in the Crow Flats area Otero County, New Mexico: State of New Mexico, State Engineer Office Technical Report Number 8, <https://www.ose.state.nm.us/Library/TechnicalReports/TechReport-008.pdf>.
- Black, B.A., 1976. Tectonics of the northern and eastern parts of the Otero platform, Otero and Chaves Counties, New Mexico, in Woodward, L.A., and Northrop, S.A., eds., *Tectonics and mineral resources in southwestern North America*: New Mexico Geological Society, Special Publication 6, p. 39–45.
- Blaney, H.F., and Criddle, W.D., 1950, Determining water requirements in irrigated areas from climatological and irrigation data: U.S. Department of Agriculture Technical Paper SCS-TP-96, 48 p., <https://ia800300.us.archive.org/4/items/determiningwater96blan/determiningwater96blan.pdf>.
- Blaney, H. F., and Criddle, W. D., 1962, Determining consumptive use and irrigation water requirements: U.S. Department of Agriculture Technical Bulletin No. 1275, 59 p., <https://naldc.nal.usda.gov/download/CAT87201264/PDF>.
- Boghici, R., Jones, I., Bradley, R., Shi, J., Goswami, R.R., Thorkildsen, D., and Backhouse, S., 2014, GAM task 13-028: Total estimated recoverable storage for aquifers in Groundwater Management Area 4: Texas Water Development Board, 33 p., <https://www.twdb.texas.gov/groundwater/docs/GAMruns/Task13-028.pdf>.
- Booker, J.R., 2014, The magnetotelluric phase tensor: A critical review: *Surveys in Geophysics*, v. 35, p. 7–40, <https://doi.org/10.1007/s10712-013-9234-2>.
- Boyd, F.M., 1982, Hydrogeology of the northern Salt Basin of west Texas and New Mexico [M.A. thesis]: University of Texas at Austin, 135 p.
- Bredehoeft, J.D., 2002, The water budget myth revisited: Why hydrogeologists model: *Groundwater*, v. 40, no. 4, p. 340–345, <https://doi.org/10.1111/j.1745-6584.2002.tb02511.x>.
- Cadol, D., Parish, G., Reuter, S., Newton, B.T., Philips, F.M., and Hendrickx, J.M.H., 2020. Estimating soil water holding capacity and runoff in New Mexico to improve modeled recharge rates: New Mexico Water Resources Research Institute Technical Completion Report No. 384, 26 p., <https://nmwri.nmsu.edu/wp-content/uploads/TR/tr384.pdf>.
- Caldwell, T.G., Bibby, H.M., and Brown, C., 2004, The magnetotelluric phase tensor: *Geophysical Journal International*, v. 158, p. 457–469, <https://doi.org/10.1111/j.1365-246X.2004.02281.x>.
- Caselle, C., Bonetto, S., and Comina, C., 2019, Comparison of laboratory and field electrical resistivity measurements of a gypsum rock for mining prospection applications: *International Journal of Mining Science and Technology*, v. 29, no. 6, p. 841–849, <https://doi.org/10.1016/j.ijmst.2019.09.002>.
- Chave, A., and Jones, A., eds., 2012, *The Magnetotelluric Method: Theory and Practice*: Cambridge, United Kingdom, Cambridge University Press, 570 p.
- Cohen, D., Person, M., Wang, P., Gable, C.W., Hutchinson, D., Marksamer, A., Dugan, B., Kooi, H., Groen, K., Lizarralde, D., and Evans, R.L., 2010, Origin and extent of fresh paleowaters on the Atlantic continental shelf, USA: *Groundwater*, v. 48, no. 1, p. 143–158, <https://doi.org/10.1111/j.1745-6584.2009.00627.x>.
- Compact, Pecos River, 1949, U.S. 81st Cong., 1st sess., S. Doc. 109. Public Law, 91.
- Craig, H., 1961, Isotopic variations in meteoric waters: *Science*, v. 133, p. 3702–3703, <https://www.science.org/doi/10.1126/science.133.3465.1702>.
- Daniel B. Stephens and Associates, Inc., 2010a, Recharge modeling study, Salt Basin of southeastern New Mexico: Report prepared for New Mexico Interstate Stream Commission, June 30, 2010, 75 p.
- Daniel B. Stephens and Associates, Inc., 2010b, Salt Basin historical playa evaporation study: Report prepared for New Mexico Interstate Stream Commission, June 30, 2010, 71 p.

- Davis, J.R., Friedman, I., and Gleason, J.D., 1986, Origin of the lithium-rich brine, Clayton Valley, Nevada: U.S. Geological Survey Bulletin 1622, 8 p., https://data.nbmng.unr.edu/public/Geothermal/GreyLiterature/Davis_ClaytonVlly_LiBrine_1986.pdf.
- Davis, S.N., Whittemore, D.O., and Fabryka-Martin, J., 1998, Uses of chloride/bromide ratios in studies of potable water: *Groundwater*, v. 36, no. 2, p. 338–350, <https://doi.org/10.1111/j.1745-6584.1998.tb01099.x>.
- Denison, R.E., and Hetherington, E.A., Jr., 1969. Basement rocks in far west Texas and south-central New Mexico, *in* Kottowski, F.E., and Lemone, D.V., eds., *Border Stratigraphy Symposium*: New Mexico Bureau of Mines and Mineral Resources Circular 104, p. 1-16, <https://geoinfo.nmt.edu/publications/monographs/circulars/downloads/104/Circular-104.pdf>.
- Doherty, J.E., and Hunt, R.J., 2010, Approaches to highly parameterized inversion: A guide to using PEST for groundwater-model calibration: U.S. Geological Survey Scientific Investigations Report 2010-5169, 37 p., <https://doi.org/10.3133/sir20105169>.
- Donegan, B., 1961, Oil and gas possibilities in southeastern Otero County, New Mexico: Preliminary report: Unpublished report on file in the New Mexico Bureau of Geology and Mineral Resources Petroleum Records Library, 16 p.
- Duffy, C.J., and Al-Hassan, S., 1988, Groundwater circulation in a closed desert basin: Topographic scaling and climatic forcing: *Water Resources Research*, v. 24, no. 10, p. 1675–1688, <https://doi.org/10.1029/WR024i010p01675>.
- Eastoe, C.J., Watts, C.J., Ploughe, M., and Wright, W.E., 2012, Future use of tritium in mapping pre-bomb groundwater volumes: *Groundwater*, v. 50, no. 1, p. 87–93, <https://doi.org/10.1111/j.1745-6584.2011.00806.x>.
- Eberle, B.A., 2021, Evaluation of groundwater recharge in the Salt Basin, NM/TX [M.S. thesis]: New Mexico Institute of Mining and Technology, 127 p., <https://www.proquest.com/docview/2639230891>.
- Evenocheck, E., 2021, Assessment of safe aquifer yield within the Salt Basin in New Mexico and Texas [M.S. thesis]: New Mexico Institute of Mining and Technology, 71 p., <https://www.proquest.com/openview/eb48a32b3eedfebd2a3b7db6d7a835ab/1?pq-origsite=gscholar&cbl=18750&diss=y>.
- Fan, Y., Duffy, C.J., and Oliver, D.S., Jr., 1997, Density-driven groundwater flow in closed desert basins: Field investigations and numerical experiments: *Journal of Hydrology*, v. 196, no. 1–4, p. 139–184, [https://doi.org/10.1016/S0022-1694\(96\)03292-1](https://doi.org/10.1016/S0022-1694(96)03292-1).
- Finch, S.T., 2002, Hydrogeologic framework of the Salt Basin and development of three-dimensional ground-water flow model: John Shomaker & Associates, Inc. report prepared for the New Mexico Interstate Stream Commission, 60 p.
- Fisher, J.B., Tu, K.P., and Baldocchi, D.D., 2008, Global estimates of the land-atmosphere water flux based on monthly AVHRR and ISLSCP-II data, validated at 16 FLUXNET sites: *Remote Sensing of Environment*, v. 112, no. 3, p. 901–919, <https://doi.org/10.1016/j.rse.2007.06.025>.
- Fontes, J.C., and Garnier, J.M., 1979, Determination of the initial ¹⁴C activity of the total dissolved carbon: A review of the existing models and a new approach: *Water Resources Research*, v. 15, no. 2, p. 399–413, <https://doi.org/10.1029/WR015i002p00399>.
- Fritz, P., and Fontes, J.Ch., eds., 1980, *Handbook of environmental isotope geochemistry*, *in* Fritz, P., and Fontes, J.Ch., eds., *The Terrestrial Environment A*, Volume 1: Amsterdam, Elsevier Science, p. II, <https://doi.org/10.1016/B978-0-444-41780-0.50001-8>.
- Gates, J.S., White, D.E., Stanley, W.D., and Ackermann, N.D., 1978, Availability of fresh and slightly saline ground water in the basins of westernmost Texas: U.S. Geological Survey Open-File Report 78-663, 115 p., <https://doi.org/10.3133/ofr78663>.
- George, P. G., Mace, R. E., & Mullican, W. F. (2005). *The Hydrogeology of Hudspeth County, Texas*. Texas Water Development Board.
- Gerritse, R.G., and George, R.J., 1988, The role of soil organic matter in the geochemical cycling of chloride and bromide: *Journal of Hydrology*, v. 101, no. 1–4, p. 83–95, [https://doi.org/10.1016/0022-1694\(88\)90029-7](https://doi.org/10.1016/0022-1694(88)90029-7).

- Goetz, L.K., 1980, Quaternary faulting in Salt Basin Graben, west Texas, *in* Dickerson, P.W., Hoffer, J.M., and Callender, J.F., eds., *Trans Pecos Region (West Texas): New Mexico Geological Society 31st Annual Fall Field Conference Guidebook*, p. 83–92, https://nmgs.nmt.edu/publications/guidebooks/downloads/31/31_p0083_p0092.pdf.
- Goode, D.J., 1996. Direct simulation of groundwater age: *Water Resources Research*, v. 32, no. 2, p. 289–296, <https://doi.org/10.1029/95WR03401>.
- Gorelick, N., Hancher, M., Dixon, M., Ilyushchenko, S., Thau, D., and Moore, R., 2017, Google Earth Engine: Planetary-scale geospatial analysis for everyone: *Remote Sensing of Environment*, v. 202, p. 18–27, <https://doi.org/10.1016/j.rse.2017.06.031>.
- Groeneveld, D.P., and Baugh, W.M., 2002, Mapping and estimating evapotranspiration for Dell Valley, Texas: *HydroBio Advanced Remote Sensing report prepared for El Paso Water Utilities*, 52 p., *in* Hutchison, W.R., 2008, Preliminary groundwater flow model, Dell City area, Hudspeth and Culberson Counties, Texas: EPWU Hydrogeology Report 08-01, p. 385–411, https://www.twdb.texas.gov/groundwater/models/gam/bsvp/bsvp_report.pdf.
- Guinea, A., Playá, E., Rivero, L., Ledo, J.J., and Queralt, P., 2012, The electrical properties of calcium sulfate rocks from decametric to micrometric scale: *Journal of Applied Geophysics*, v. 85, no. 10, p. 80–91, <https://doi.org/10.1016/j.jappgeo.2012.07.003>.
- Gutzler, D.S., 2005, New Mexico's changing climate: *Natural Resources Journal*, v. 45, no. 2, p. 277–282, <https://digitalrepository.unm.edu/nrj/vol45/iss2/2>.
- Harbaugh, A.W., 2005, MODFLOW-2005: The U.S. Geological Survey modular ground-water model--the ground-water flow process: U.S. Geological Survey Techniques and Methods 6-A16, <https://doi.org/10.3133/tm6A16>.
- Hayes, P.T., 1964, *Geology of the Guadalupe Mountains, New Mexico*: U.S. Geological Survey Professional Paper 446, 69 p., <https://doi.org/10.3133/pp446>.
- Huff, G.F., and Chace, D., 2006, Knowledge and understanding of the hydrogeology of the Salt Basin in south-central New Mexico and future study needs: U.S. Geological Survey Open-File Report 2006–1358, 17 p., https://pubs.usgs.gov/of/2006/1358/pdf/of06-1358_508.pdf.
- Hunt, R., 2003, Ground water-lake interaction modeling using the LAK3 package for MODFLOW 2000: *Groundwater*, v. 41, no. 2, p. 114–118, <https://doi.org/10.1111/j.1745-6584.2003.tb02575.x>.
- Hutchison, W.R., 2006, *Groundwater management in El Paso, Texas [Ph.D. dissertation]*: University of Texas at El Paso, 328 p., <https://scholarworks.utep.edu/dissertations/AAI3214009>.
- Hutchison, W.R., 2008, Preliminary groundwater flow model, Dell City area, Hudspeth and Culberson Counties, Texas: EPWU Hydrogeology Report 08-01, 435 p., https://www.twdb.texas.gov/groundwater/models/gam/bsvp/bsvp_report.pdf.
- Ingebritsen, S.E., and Manning, C.E., 2010, Permeability of the continental crust: Dynamic variations inferred from seismicity and metamorphism: *Geofluids*, v. 10, no. 1–2, p. 193–205, <https://doi.org/10.1111/j.1468-8123.2010.00278.x>.
- John Shomaker & Associates, Inc., 2002, Hypothetical well fields in Salt Basin and pipeline to Pecos River: Draft report prepared for New Mexico Interstate Stream Commission, 17 p.
- John Shomaker & Associates, Inc., 2010, Revised hydrogeologic framework and updated groundwater model of the Salt Basin, New Mexico: Draft report prepared for the New Mexico Interstate Stream Commission, 68 p.
- Jovanovic, N., and Israel, S., 2012, Critical review of methods for the estimation of actual evapotranspiration in hydrological models, *in* Irmak, A., ed., *Evapotranspiration: Remote Sensing and Modeling*: InTech, p. 329–350, <https://doi.org/10.5772/21279>.
- Kalin, R.M., 2000, Radiocarbon dating of groundwater systems, *in* Cook, P.G., and Herczeg, A.L., eds., *Environmental Tracers in Subsurface Hydrology*: Boston, Kluwer Academic Publishers, p. 111–144, https://doi.org/10.1007/978-1-4615-4557-6_4.

- Kelley, S., Fichera, M., Evenocheck, E., Eberle, B.A., Person, M., Cadol, D., Newton, B.T., Timmons, S., and Pokorny, C., 2020, Assessment of water resources in the Salt Basin Region of New Mexico and Texas, data summary report: New Mexico Bureau of Geology and Mineral Resources Open-File Report 608, 63 p., https://geoinfo.nmt.edu/publications/openfile/downloads/600-699/608/OFR-608_Salt_Basin_revised_Oct_2020.pdf.
- Ketchum, D., 2016, High-resolution estimation of groundwater recharge for the entire state of New Mexico using a soil-water-balance model [M.S. thesis]: New Mexico Institute of Mining and Technology, <https://www.proquest.com/docview/1867024747>.
- King, W.E., and Harder, V.M., 1985, Oil and gas potential of the Tularosa Basin–Otero platform–Salt Basin graben area, New Mexico and Texas: New Mexico Bureau of Mines and Mineral Resources Circular 198, 36 p., <https://geoinfo.nmt.edu/publications/monographs/circulars/downloads/198/Circular-198.pdf>.
- Klein, D.P., and Rodriguez, B.D., 1997, Electrical resistivity survey in the Cornudas Mountains area, Otero County, New Mexico: U.S. Geological Survey Open-File Report 97-149, 25 p., <https://doi.org/10.3133/ofr97149>.
- Knott, J.F., and Olimpio, J.C., 1986, Estimation of recharge rates to the sand and gravel aquifer using environmental tritium, Nantucket Island, Massachusetts: Denver, Colorado, U.S. Geological Survey, 26 p.
- Konikow, L.F., 1986, Predictive accuracy of a ground-water model—Lessons from a postaudit: *Groundwater*, v. 24, no. 2, p. 173–184, <https://doi.org/10.1111/j.1745-6584.1986.tb00993.x>.
- Konikow, L.F., and Person, M., 1985, Assessment of long-term salinity changes in an irrigated stream-aquifer system: *Water Resources Research*, v. 21, no. 11, p. 1611–1624, <https://doi.org/10.1029/WR021i011p01611>.
- Kreitler, C.W., Raney, J.A., Nativ, R., Collins, E.W., Mullican, W.F., III, Gustavson, T.C., and Henry, C.D., 1987, Siting a low-level radioactive waste disposal facility in Texas, volume four - geologic and hydrologic investigations of state of Texas and University of Texas lands: The University of Texas at Austin, Bureau of Economic Geology, report prepared for the Texas Low-Level Radioactive Waste Disposal Authority under Interagency Contract No. IAC (86-87), 330 p., <https://www.beg.utexas.edu/files/publications/contract-reports/CR1987-Kreitler-2.pdf>.
- Krieger, L., and Peacock, J.R., 2014, MTpy: A Python toolbox for magnetotellurics: *Computers and Geosciences*, v. 72, p. 167–175, <https://doi.org/10.1016/j.cageo.2014.07.013>.
- Land, L., and Veni, G., 2018, Karst hydrogeology scoping investigation of the San Solomon Spring Area: Culberson, Jeff Davis, and Reeves Counties, Texas: National Cave and Karst Research Institute Report of Investigation 8, 20 p., <https://www.nckri.org/wp-content/uploads/2021/03/nckri-report-of-investigations-08.pdf>.
- Langevin, C.D., Shoemaker, W.B., and Guo, W., 2003, Modflow-2000, the U.S. Geological Survey modular ground-water model—Documentation of the SEAWAT-2000 version with the variable-density flow process (VDF) and the integrated MT3DMS transport process (IMT): U.S. Geological Survey Open-File Report 03-426, 43 p., https://fl.water.usgs.gov/PDF_files/ofr03_426_langevin.pdf.
- Livingston Associates, P.C., and John Shomaker & Associates, Inc., 2002, Tularosa Basin and Salt Basin: Regional Water Plan 2000 – 2040: South Central Mountain RC&D Council, Inc. Executive Summary, 33 p., https://www.ose.state.nm.us/Planning/RWP/05_Tularosa/2004/tularosa_execsummaryr.pdf.
- Longworth, J.W., Valdez, J.M., Magnuson, M.L., Albury, E.S., and Keller, J., 2008, New Mexico water use by categories 2005: New Mexico Office of the State Engineer Technical Report 52, 111 p., <https://www.ose.state.nm.us/Library/TechnicalReports/TechReport-052.pdf>.

- Longworth, J.W., Valdez, J.M., Magnuson, M.L., and Richard, K., 2013, New Mexico water use by categories 2010: New Mexico Office of the State Engineer Technical Report 54, 128 p., <https://www.ose.state.nm.us/Library/TechnicalReports/TechReport%2054NM%20Water%20Use%20by%20Categories%20.pdf>.
- Lowrie, W., 2007, Fundamentals of Geophysics: New York, Cambridge University Press, 381 p.
- MacInnes, S., 2010a, MTEdit documentation: Zonge Engineering and Research Organization, 14 p., http://www.zonge.com/legacy/PDF_DatPro/MtEdit.pdf.
- MacInnes, S., 2010b, TEMAVGW documentation: Zonge Engineering and Research Organization, 29 p.
- MacInnes, S., 2014, MTFT24 documentation: Zonge Engineering and Research Organization, 23 p.
- MacInnes, S., and Raymond, M., 2009, STEMINV documentation: ZONGE data processing, smooth-model TEM inversion: Zonge Engineering and Research Organization, 29 p., http://www.zonge.com/legacy/PDF_Modeling/Steminv.pdf.
- Magnuson, M.L., Valdez, J.M., Lawler, C.R., Nelson, M., and Petronis, L., 2018, New Mexico water use by categories 2015: New Mexico Office of the State Engineer Technical Report 55, 126 p., https://www.ose.state.nm.us/WUC/wucTechReports/2015/pdf/2015%20WUR%20final_05142019.pdf.
- Mayer, J.R., and Sharp, J.M., Jr., 1998, Fracture control of regional ground-water flow in a carbonate aquifer in a semi-arid region: Geological Society of America Bulletin, v. 110, no. 2, p. 269–283, [https://doi.org/10.1130/0016-7606\(1998\)110<0269:FCORGW>2.3.CO;2](https://doi.org/10.1130/0016-7606(1998)110<0269:FCORGW>2.3.CO;2).
- Melton, F.S., et al., 2012, Satellite irrigation management support with the terrestrial observation and prediction system: A framework for integration of satellite and surface observations to support improvements in agricultural water resource management: IEEE Journal of Selected Topics in Applied Earth Observations and Remote Sensing, v. 5, no. 6, p. 1709–1721, <https://doi.org/10.1109/JSTARS.2012.2214474>.
- Menking, K.M., Anderson, R.Y., Shafike, N.G., Syed, K.H., and Allen, B.D., 2004, Wetter or colder during the Last Glacial Maximum? Revisiting the pluvial lake question in southwestern North America: Quaternary Research, v. 62, no. 3, p. 280–288, <https://doi.org/10.1016/j.yqres.2004.07.005>.
- Morse, J., 2010, The hydrogeology of the Sacramento Mountains using environmental tracers [unpublished M.S. thesis]: New Mexico Institute of Mining and Technology, 120 p.
- National Centers for Environmental Information, 2021, xmACIS2: <https://xmaccis.rcc-acis.org/> (accessed January 2021).
- New Mexico Manufacturing Extension Partnership, 2018, New Mexico MEP agriculture review, 75 p., <https://webnew.ped.state.nm.us/wp-content/uploads/2018/10/New-Mexico-Agriculture-Report.pdf>
- New Mexico Office of the State Engineer, 2021, Water rights reporting system, <https://www.ose.state.nm.us/WRAB/> (accessed April 2021).
- Newton, B.T., Rawling, G.C., Timmons, S., Land, L., Johnson, P.S., Kludt, T.J., and Timmons, J.M., 2012, Sacramento Mountains hydrogeology study: New Mexico Bureau of Geology and Mineral Resources Open-File Report 543, 77 p., https://geoinfo.nmt.edu/publications/openfile/downloads/500-599/543/OFR-543_HR.pdf.
- Nicot, J.-P., and Bennett, P.C., 1998, Shallow subsurface characterization of gas transport in a playa wetland: Journal of Environmental Engineering, v. 124, no. 11, p. 1038–1046, [https://doi.org/10.1061/\(ASCE\)0733-9372\(1998\)124:11\(1038\)](https://doi.org/10.1061/(ASCE)0733-9372(1998)124:11(1038)).
- Nielson, P.D., and Sharp, J.M., Jr., 1985, Tectonic controls on the hydrogeology of the Salt Basin, Trans-Pecos Texas, *in* Dickerson, P.W., and Muehlberger, W.R., eds., Structure and Tectonics of Trans-Pecos Texas: West Texas Geological Society Field Conference Publication 85-81, p. 231–235.
- Niswonger, R.G., Panday, S., and Ibaraki, M., 2011, MODFLOW-NWT, A Newton formulation for MODFLOW-2005: U.S. Geological Survey Techniques and Methods 6-A37, 44 p., <https://doi.org/10.3133/tm6A37>.

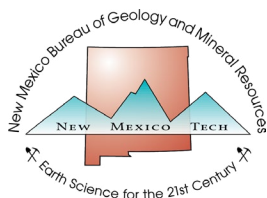
- Niswonger, R.G., and Prudic, D.E., 2005, Documentation of the Streamflow-Routing (SFR2) Package to include unsaturated flow beneath streams - A modification to SFR1: U.S. Geological Survey Report 2328-7055, 51 p., <https://doi.org/10.3133/tm6A13>.
- Peacock, J.R., Mangan, M.T., McPhee, D., and Ponce, D.A., 2015, Imaging the magmatic system of Mono Basin, California, with magnetotellurics in three dimensions: *Journal of Geophysical Research: Solid Earth*, v. 120, no. 11, p. 7273–7289, <https://doi.org/10.1002/2015JB012071>.
- Pellerin, L., and Hohmann, G.W., 1990, Transient electromagnetic inversion: A remedy for magnetotelluric static shifts: *Geophysics*, v. 55, no. 9, p. 1242–1250, <https://doi.org/10.1190/1.1442940>.
- Person, M., Mulch, A., Teyssier, C., and Gao, Y., 2007, Isotope transport and exchange within metamorphic core complexes: *American Journal of Science*, v. 307, no. 3, p. 555–589, <https://doi.org/10.2475/03.2007.01>.
- Person, M.A., Pepin, J.D., Peacock, J., Kelley, S., Butler, J.J., Jr., and Sion, B.D., 2019, Assessment of the deep plumbing of the Truth or Consequences geothermal system using magnetotelluric surveys, groundwater residence time tracers, and hydrologic modeling: Abstract GP12A-01 presented at 2019 Fall Meeting, AGU, San Francisco, California, 9 December.
- Phillips, F.M., Mattick, J.L., Duval, T.A., Elmore, D., and Kubik, P.W., 1988, Chlorine 36 and tritium from nuclear weapons fallout as tracers for long-term liquid and vapor movement in desert soils: *Water Resources Research*, v. 24, no. 11, p. 1877–1891, <https://doi.org/10.1029/WR024i011p01877>.
- Popp, C.J., Ohline, R.W., Brandvold, D.K., Brandvold, L.A., 1984, Nature of precipitation and atmospheric particulates in central and northern New Mexico, *in* Hicks, B.B., ed., *Deposition Both Wet and Dry: Acid Precipitation Series, Volume. 4*: London, Butterworth Publishers, p. 79–95.
- Post, V.E., and Kooi, H., 2003, Rates of salinization by free convection in high-permeability sediments: Insights from numerical modeling and application to the Dutch coastal area: *Hydrogeology Journal*, v. 11, no. 5, p. 549–559, <https://doi.org/10.1007/s10040-003-0271-7>.
- PRISM Climate Group, 2014 February 4, PRISM climate data: <https://prism.oregonstate.edu> (accessed 2021).
- R Core Team, 2018, R: A language and environment for statistical computing (version 3.5.2): Foundation for Statistical Computing, <https://www.R-project.org> (accessed on 11 September 2020).
- Rawling, G.C., and Newton, B.T., 2016, Quantity and location of groundwater recharge in the Sacramento Mountains, south-central New Mexico (USA), and their relation to the adjacent Roswell Artesian Basin: *Hydrogeology Journal*, v. 24, no. 4, p. 757–786, <https://doi.org/10.1007/s10040-016-1399-6>.
- Reuter, S., Cadol, D., Phillips, F.M., and Newton, B.T., 2021, Evaluating focused aquifer recharge in the Jornada Experimental Range, NM, using chloride profile analysis: *New Mexico Water Resources Research Institute Technical Completion Report No. 392*, 36 p., <https://nmwrri.nmsu.edu/wp-content/uploads/TR/tr392.pdf>.
- Richter, B.C., and Kreitler, C.W., 1986, Geochemistry of salt water beneath the Rolling Plains, north-central Texas: *Groundwater*, v. 24, no. 6, p. 735–742, <https://doi.org/10.1111/j.1745-6584.1986.tb01689.x>.
- Ritchie, A.B.O., 2011. Hydrogeologic framework and development of a three-dimensional finite difference groundwater flow model of the Salt Basin, New Mexico and Texas [M.S. thesis]: New Mexico Institute of Mining and Technology, 445 p., http://www.ees.nmt.edu/outside/alumni/papers/2011t_ritchie_ab.pdf.
- Sajil Kumar, P.J., and James, E.J., 2016, Identification of hydrogeochemical processes in the Coimbatore district, Tamil Nadu, India: *Hydrological Sciences Journal*, v. 61, no. 4, p. 719–731, <https://doi.org/10.1080/02626667.2015.1022551>.
- Sandvig, R.M., and Phillips, F.M., 2006, Ecohydrological controls on soil moisture fluxes in arid to semiarid vadose zones: *Water Resources Research*, v. 42, no. 8, <https://doi.org/10.1029/2005WR004644>.
- Sanford, W., 2011, Calibration of models using groundwater age: *Hydrogeology Journal*, v. 19, no. 1, p. 13–16, <https://doi.org/10.1007/s10040-010-0637-6>.

- Scanlon, B.R., 1991, Evaluation of moisture flux from chloride data in desert soils: *Journal of Hydrology*, v. 128, p. 137–156, [https://doi.org/10.1016/0022-1694\(91\)90135-5](https://doi.org/10.1016/0022-1694(91)90135-5).
- Scanlon, B.R., Goldsmith, R.S., and Paine, J.G., 1997, Analysis of focused unsaturated flow beneath fissures in the Chihuahuan Desert, Texas, USA: *Journal of Hydrology*, v. 203, no. 1, p. 58–78, [https://doi.org/10.1016/S0022-1694\(97\)00086-3](https://doi.org/10.1016/S0022-1694(97)00086-3).
- Scholle, P.A., 2003, Geologic map of New Mexico: New Mexico Bureau of Geology and Mineral Resources, scale 1: 500,000, 2 sheets, <https://geoinfo.nmt.edu/publications/maps/geologic/state/home.cfm>.
- Senay, G.B., Bohms, S., Singh, R.K., Gowda, P.H., Velpuri, N.M., Alemu, H., and Verdin, J.P., 2013, Operational evapotranspiration mapping using remote sensing and weather datasets: A new parameterization for the SSEB approach: *Journal of the American Water Resources Association*, v. 49, no. 3, p. 577–591, <https://doi.org/10.1111/jawr.12057>.
- Sigstedt, S.C., 2010, Environmental tracers in ground water of the Salt Basin, New Mexico, and implications for water resources [M.S. thesis]: New Mexico Institute of Mining and Technology, 202 p.
- Sigstedt, S.C., Phillips, F.M., and Ritchie, A.B.O., 2016, Groundwater flow in an ‘underfit’ carbonate aquifer in a semiarid climate: Application of environmental tracers to the Salt Basin, New Mexico (USA): *Hydrogeology Journal*, v. 24, no. 4, p. 841–863, <https://doi.org/10.1007/s10040-016-1402-2>.
- Simpson F., and Bahr, K., 2005, *Practical Magnetotellurics*: Cambridge, United Kingdom, Cambridge University Press, 254 p., <https://doi.org/10.1017/CBO9780511614095>.
- Solomon, D.K., and Sudicky, E.A., 1991, Tritium and helium-3 isotope ratios for direct estimation of spatial variations in groundwater recharge: *Water Resources Research*, v. 27, no. 9, p. 2309–2319, <https://doi.org/10.1029/91WR01446>.
- Sophocleous, M.A., 2004, Groundwater recharge, *in* Silveira, L., and Usunoff, E.J., eds., *Groundwater*, Volume 1: Oxford, United Kingdom, UNESCO-EOLSS, p. 126–163, <https://www.eolss.net/sample-chapters/c07/E2-09-01-05.pdf>.
- Standen, A., Finch, S., Williams, R., and Lee-Brand, B., 2009, Capitan Reef Complex structure and stratigraphy: Texas Water Development Board Report for Contract Number 0804830794, 53 p., https://www.twdb.texas.gov/groundwater/models/gam/crcx/CapitanReefComplex_Framework_finalwErrata.pdf.
- Stone, J.J., Nichols, M.H., Goodrich, D.C., and Bruno, J., 2008, Long-term runoff database, Walnut Gulch Experimental Watershed, Arizona, United States: *Water Resources Research*, v. 44, no. 5, W05S05, <https://doi.org/10.1029/2006WR005733>.
- Texas Water Science Center, 2014, Geologic database of Texas: <https://data.tnris.org/collection?c=79a18636-3419-4e22-92a3-d40c92eced14#4.67/31.32/-100.08> (accessed 2020).
- Thornthwaite, C.W., and Mather, J.R., 1957, Instruction and tables for computing potential evapotranspiration and the water balance, *in* *Publications in Climatology*, Volume 10, Number 3: Centerton, New Jersey, Drexel Institute of Technology, p. 185–311.
- Tillery, A.C., 2011, Estimates of mean-annual streamflow and flow loss for ephemeral channels in the Salt Basin, southeastern New Mexico, 2009: U.S. Geological Survey Scientific Investigations Report 2011–5062, 20 p., <https://pubs.usgs.gov/sir/2011/5062/pdf/SIR11-5062.pdf>.
- U.S. Census Bureau, 1960, Number of inhabitants: Texas, 52 p., <https://www2.census.gov/prod2/decennial/documents/33255142v1p45ch02.pdf>.
- U.S. Census Bureau, 2021, 2020 decennial census, <https://www.census.gov/programs-surveys/decennial-census/decade/2020/2020-census-results.html>.
- U.S. Geological Survey, 2021, Normalized difference vegetation index: <https://espa.cr.usgs.gov/> (accessed spring 2021).
- Walvoord, M.A., and Phillips, F.M., 2004, Identifying areas of basin-floor recharge in the Trans-Pecos region and the link to vegetation: *Journal of Hydrology*, v. 292, no. 1–4, p. 59–74, <https://doi.org/10.1016/j.jhydrol.2003.12.029>.

- Wilkins, D.E., and Currey, D.R., 1997, Timing and extent of late quaternary paleolakes in the Trans-Pecos closed basin, west Texas and south-central New Mexico: *Quaternary Research*, v. 47, no. 3, p. 306–315, <https://doi.org/10.1006/qres.1997.1896>.
- Wilson, B.C., 1992, Water use by categories in New Mexico counties and river basins, and irrigated acreage in 1990: New Mexico Office of the State Engineer Technical Report 47, 141 p., <https://www.ose.state.nm.us/Library/TechnicalReports/TechReport-047.pdf>.
- Wilson, B.C., and Lucero, A.A., 1997, Water use by categories in New Mexico counties and river basins, and irrigated acreage in 1995: New Mexico Office of the State Engineer Technical Report 49, 149 p., <https://www.ose.state.nm.us/Library/TechnicalReports/TechReport-049.PDF>.
- Wilson, B.C., Lucero, A.A., Romero, J.T., and Romero, P.J., 2003, Water use by categories in New Mexico counties and river basins, and irrigated acreage in 2000: New Mexico Office of the State Engineer Technical Report 51, 164 p., <https://www.ose.state.nm.us/Library/TechnicalReports/TechReport-051.pdf>.
- Wood, W.W., 1999, Use and misuse of the chloride-mass balance method in estimating ground water recharge. *Groundwater*, v. 37, no. 1, p. 2–3, <https://doi.org/10.1111/j.1745-6584.1999.tb00949.x>.
- Xu, F., 2018. Estimation of focused recharge for New Mexico using a soil-water-balance model: PyRANA [M.S. thesis]: New Mexico Institute of Mining and Technology, 73 p.
- Zaidi, F.K., Nazzal, Y., Jafri, M.K., Naeem, M., and Ahmed, I., 2015, Reverse ion exchange as a major process controlling the groundwater chemistry in an arid environment: A case study from northwestern Saudi Arabia: *Environmental Monitoring and Assessment*, v. 187, article number 607, <https://doi.org/10.1007/s10661-015-4828-4>.
- Zhu, J., and Liu, Z., 2003, Long-range persistence of acid deposition: *Atmospheric Environment*, v. 37, no. 19, p. 2605–2613.

Disclaimer:

The data, views, and conclusions included in this report are those of the authors and should not be interpreted as necessarily representing the official policies, either expressed or implied, of the New Mexico Bureau of Geology and Mineral Resources or the State of New Mexico. All data are for informational purposes only, and the user bears all responsibility in determining whether these data are fit for the user's intended use.



New Mexico Bureau of Geology and Mineral Resources
A Research Division of New Mexico Tech

geoinfo.nmt.edu

801 Leroy Place
Socorro, NM 87801
(575) 835-5490